Silicon and oxygen stable isotopes in chert as indicators of diagenesis and ocean paleo-environmental conditions

Dissertation

zur Erlangung des Grades eines

Doktors der Naturwissenschaften (doctor rerum naturalium)

am Fachbereich Geowissenschaften

der Freien Universität Berlin

vorgelegt von

Michael Tatzel

Berlin, 2016

Erstgutachter: Prof. Friedhelm von Blanckenburg

Zweitgutachter: Prof. Louis A. Derry

Tag der Disputation: 14.04.2016

Eidesstattliche Erklärung

Hiermit versichere ich, die vorliegende Dissertation selbstständig und ohne unerlaubte Hilfe angefertigt zu haben. Bei der Verfassung der Dissertation wurden keine anderen als die im Text aufgeführten Hilfsmittel verwendet. Beiträge von Koautoren zu publizierten und zur Publikation vorbereiteten Manuskripten sind im ‚Preface' dieser Arbeit dargelegt. Ein Promotionsverfahren zu einem früheren Zeitpunkt an einer anderen Hochschule oder bei einem anderen Fachbereich wurde nicht beantragt.

Berlin, 18. Januar 2016

READ WRITE THINK DREAM

(Geisel Library, UCSD)

Who has no time to read the summary is referred to the twitter format version:

When flint forms, silicon may keep its atomic mass and record sponge abundance. Oxygen loses heavy isotopes and records temperatures in the crust.

Summary

The conversion of amorphous opaline sediment to quartz chert is a very slow process that occurs on geological time scales of up to 20 million years. This diagenetic silicon dioxide (silica) phase transformation entails the conversion from opal-A (amorphous opal) via opal-CT (cristobalite-tridymite opal) to quartz and does not depend on whether silica was deposited as biogenic opal or precipitated inorganically from silicon-rich water. The involved early diagenetic dissolution and later diagenetic dissolution-precipitation reactions affect the silicon (Si) stable isotope composition of quartz, but the underlying isotope fractionation processes are largely unknown. This lack of knowledge hampers the interpretation of the silicon isotope composition of chert, the topic of this thesis.

The first diagenetic reaction that occurs during opal maturation is the phase transformation of opal-A to opal-CT. This transformation is forming layered sedimentary rock referred to as porcellanite and commonly occurs during burial diagenesis at temperatures between 30 to 60°C. In pure, i.e., clay-free siliceous sediment (composed dominantly of opal-A), porcellanite layers can form already during early diagenesis. Such porcellanite layers are present in Pleistocene and Pliocene sediment of the Southern Ocean. These layers as well as their surrounding siliceous sediment were analyzed for their silicon isotope composition. I measured silicon stable isotope ratios of these sediments by multicollector ICP-MS after sample dissolution, and measured the silicon stable isotope ratios of porcellanite layers by femtosecond laser ablation multicollector ICP-MS (fs-LA-ICP-MS). Porcellanite layers are significantly enriched in heavy silicon isotopes (1.7 to 2.3‰ δ^{30}Si, the normalized ^{30}Si/^{28}Si isotope ratio) relative to the surrounding siliceous sediment (-0.3 to 1.5‰ δ^{30}Si). Scanning electron microprobe analyses following sequential NaOH extractions of three sediment samples reveal the preferential dissolution of diatoms relative to radiolarians. The preferential dissolution of diatoms that are enriched in isotopically heavy Si relative to Si from radiolarians and aluminum-silicate phases causes the depletion of ^{30}Si in sediment and enrichment of ^{30}Si in pore water relative to ^{28}Si. Early diagenetically formed porcellanite layers precipitate from pore water as soon as the opal-CT solubility is exceeded. *In situ* Si isotope analyses of porcellanite layers using fs-MC-ICP-MS show anti-correlating Al/Si and δ^{30}Si, documenting that early diagenetic aluminum silicate precipitation depletes pore water in light isotopes. These processes cause a shift of the initial bulk sediment Si isotope composition during early diagenesis. Therefore, the Si isotope composition of chert will also be shifted away from that of the initial bulk sediment. In the Precambrian, however, early diagenetic selective dissolution of opal was suppressed through high seawater Si concentrations. Precambrian cherts should therefore reflect the primary bulk Si isotope composition of the opaline precursor. Furthermore, isotopic shifts through diagenetic phase transformations will be minimal as exchange of Si between sedimentary layers is impeded in the presence of variable amounts of detrital minerals. The reason is that the solubility of siliceous sediment is reduced in the presence of detrital minerals.

Therefore, Si stable isotopes can be used to study paleo-environmental conditions in marine successions of Ediacaran through Cambrian times. Chert and siliceous shales from the 'Lijiatuo' section, Hunan, South China, were analyzed for stable Si isotopes, and major-and trace element concentrations. An overall decreasing trend of $\delta^{30}Si$ values throughout the section is compatible with shifting proportions of the Si sources. We infer that high $\delta^{30}Si$ values of up to 1.1‰ in the bottom part of the section (Late Ediacaran) represent dominant contribution of inorganic Si precipitation from seawater. Values decreasing down to -0.5‰ I assume to reflect an increasing contribution of light Si from siliceous sponge spicules. The relative proportion of sponges was quantified by mass balance calculations and geochemical inversion. An inferred late Ediacaran increase in sponge abundance correlates with Ce-anomalies, P- and Ba- enrichment in sediment. These geochemical proxy data suggests that seawater oxygenation occurred concurrently with the increased colonization of the continental slope by siliceous sponges. This multi-proxy evidence supports the hypothesis that the Late Neoproterozoic oxygen rise in seawater was significantly controlled by sponges. Sponges reduce dissolved and fine particulate organic matter from seawater through filter feeding. This way of feeding changes the redox structure of seawater and sediments and make sponges 'ecosystem engineers'. Thus, the respiratory oxygen consumption is shifted towards greater water depths and shallow water habitats are becoming oxygenated. As another consequence the nutrient availability for other species is affected by changed fluxes of chemical elements between seawater and sediment. This mechanism called 'ecosystem engineering', possibly facilitated the Cambrian 'explosion', the rapid evolution of higher life on Earth.

The oxygen (O) isotope composition ($^{18}O/^{16}O$) of chert is frequently used to reconstruct paleo-seawater temperatures. However, for most chert samples, oxygen isotope thermometry yields implausibly high temperatures. Two physico-chemical characteristics allow scrutinizing whether oxygen isotopes retain a diagenetic fingerprint. These are i) the strong effect of detrital minerals on the silica solubility, and by inference on the timing of silica phase transformations during sediment burial; and ii) the temperature-dependent equilibration of silica $\delta^{18}O$ during dissolution-precipitation reactions. The set of Ediacaran to Cambrian chert and siliceous shale samples from 'Lijiatuo' section as introduced above was used to explore these dependencies. The normalized $^{18}O/^{16}O$ ratios of bulk chert ranges from 17.1 to 24.0‰, and the detrital mineral content is estimated to range from ca. 1 to 75 wt%. A mass balance calculation shows that the oxygen isotope composition of authigenic quartz ranges between 17.1 and 29.8‰. This result was verified by SIMS analyses of three detrital-rich samples. The $\delta^{18}O$ value of quartz is correlated with the detrital mineral abundance. Raman spectroscopy of carbonaceous material reveals peak diagenetic temperatures around 260°C. The correlation between detrital mineral abundance and quartz $\delta^{18}O$ provides evidence that chert $\delta^{18}O$ records the temperature during opal-CT to quartz phase transformation. The preservation of this signature, despite burial to high diagenetic temperatures, confirms evidence that chert is resistant to isotopic exchange. A calculation of quartz formation rates at different temperature gradients suggests that the global

trend of increasing chert $\delta^{18}O$ through the Proterozoic results from quartz formation at increasing depths and decreasing temperatures as consequence of a decreasing geothermal gradient through cooling of the solid Earth.

Zusammenfassung

Die Umwandlung von amorphem Opal zu kristallinem Quarz-Chert (ein Silicium-reiches Sedimentgestein) ist ein sehr langsamer Prozess, der über geologische Zeiträume von mehr als 20 Millionen Jahren andauern kann. Die diagenetischen Phasenumwandlungen von Opal-A über Opal-CT zu Quarz finden dabei unabhängig davon statt, ob Silica (SiO_2) als biogener Opal oder anorganisch aus Silicium (Si)-reichem Meerwasser ausgefällt wurde. Die Auswirkungen von frühdiagenetischer Opal-Auflösung und von diagenetischen Lösungs-Fällungsreaktionen auf die Silicium-Isotopensignatur von Quarz sind weitgehend unbekannt. Dieses fehlende Wissen erschwert die Interpretation der Si-Isotopenzusammensetzung von Chert als Paläo-Umwelt Indikator.

Die erste diagenetische Reaktion, die bei der Opal Reifung stattfindet, ist die Opal-A Phasenumwandlung zum metastabilen Silica-Polymorph Opal-CT, welches das Sedimentgestein Porzellanit bildet. Diese Phasenumwandlung findet gewöhnlich zwischen 30 und 60°C statt. In sehr reinen, d.h. tonmineral-freien opalinen Sedimenten können Porzellanit-Lagen bereits bei der Frühdiagenese entstehen. Derartige Porzellanit-Lagen wurden in pleistozänen und pliozänen Sedimenten des Südpolarmeeres gefunden. Ich habe die Si-Isotopenzusammensetzung solcher Lagen sowie die des umgebenden Sediments analysiert. Dabei wurden Si Isotopenverhältnisse dieser Sedimente nach deren Auflösung mit Multicollector ICP-MS bestimmt. Si-Isotopenverhältnisse in Porzellanit-Lagen wurden mittels Femtosekunden-Laser Ablations-ICP-MS (fs-LA-ICP-MS) gemessen. Porzellanit ist im Vergleich zum umgebenden opalinem Sediment (-0.3 bis 1.5‰ $\delta^{30}Si$, dem normalisierten $^{30}Si/^{28}Si$ Verhältnis) deutlich an schweren Si-Isotopen angereichert (1.7 bis 2.3‰ $\delta^{30}Si$). Raster-elektronenmikroskopische Analysen dreier Sedimentproben, die sequenziell NaOH ausgesetzt wurden, zeigen eine präferentielle Auflösung von Diatomeen gegenüber Radiolarien. Die präferentielle Auflösung von Diatomeen, welche eine schwerere Si-Isotopenzusammensetzung gegenüber Radiolarien und Al-Si-Phasen aufweisen, führt zu einer Abreicherung von ^{30}Si im Sediment und zu einer Anreicherung von ^{30}Si im Porenwasser. Frühdiagenetisch gebildete Porzellanit-Lagen präzipitieren aus Porenwasser, sobald die Löslichkeit von opal-CT überschritten wird. *In situ* Si-Isotopenanlysen mittels fs-MC-ICP-MS zeigen eine Antikorrelation von Al/Si und $\delta^{30}Si$, die belegt, dass frühdiagenetische Ausfällungen von Al-Si-Phasen das Porenwasser zusätzlich an leichten Si-Isotopen abreichern. Diese frühdiagenetischen Prozesse führen zu einer Verschiebung der initialen Si-Isotopenzusammensetzung. Als Folge wird die Si-Isotopenzusammensetzung von Chert relativ zur ursprünglichen Isotopenzusammensetzung des opalinen Sediments verschoben. Im Gegensatz zum phanerozoischen Ozean wurde in präkambrischem Meerwasser die frühdiagenetische, selektive Auflösung von Opal durch hohe Si-Konzentrationen unterdrückt. Daher sollten präkambrische Cherts die primäre Isotopenzusammensetzung des Opals erhalten. Außerdem werden mögliche Verschiebungen der primären Si-Isotopenzusammensetzung durch diagenetische Silica Phasenumwandlungen minimiert, wenn aufeinanderfolgende Sedimentschichten variable Detritus-Gehalte besitzen. Der Grund dafür ist, dass die Gegenwart von Detritus die Silica-Löslichkeit reduziert.

Aus diesem Grund können Si-Isotope ediakarischer bis kambrischer mariner Cherts zur Rekonstruktion von Paläo-Umweltbedingungen genutzt werden. Die Si-Isotopenzusammensetzung sowie die Haupt- und Spurenelementzusammensetzung von Cherts und silifizierten Tonsteinen aus dem ‚Lijiatuo' Profil in Hunan (Süd China) wurden analysiert. Insgesamt zeigt das Profil einen abnehmenden Trend in δ^{30}Si, der sich durch verschiebende Proportionen von Si-Quellen erklären lässt. Ich interpretiere dies so, dass hohe δ^{30}Si-Werte von bis zu 1.1‰ im unteren Bereich des Profils (spätes Ediakarium) hauptsächlich anorganische Silica Präzipitation aus Meerwasser repräsentieren. Die auf bis zu -0.5‰ abnehmenden δ^{30}Si-Werte könnten einen zunehmenden Anteil von isotopisch leichtem Si aus Schwammnadeln anzeigen. Die relativen Anteile von silikatischen Schwämmen wurden mittels Massenbilanz und geochemischer Inversion berechnet. Der berechnete Anstieg der relativen Häufigkeit von Schwämmen korreliert mit Cer-Anomalien und mit Phosphor- und Barium- Anreicherungen im Sediment. Diese geochemischen Proxy-Daten deuten darauf hin, dass die Oxygenierung des Meerwassers gleichzeitig mit der Verbreitung von silikatischen Schwämmen auf dem Kontinentalabhang stattfand. Diese Ergebnisse unterstützen die Hypothese, dass der Spät-Neoproterozoische Sauerstoffanstieg in Meerwasser in bedeutendem Maße von Schwämmen verursacht wurde. Schwämme verringern durch die Filtration von Meerwasser zur Nahrungsaufnahme die Konzentration gelöster- und feinpartikulärer organischer Materie. Diese Ernährungsweise ändert die Redoxstruktur des Wasserkörpers und macht Schwämme zu ‚Ökosystemingenieuren'. Der respirative Verbrauch von Sauerstoff wird dadurch in größere Wassertiefen verschoben, Flachwasserhabitate werden oxygeniert und die Nährstoffverfügbarkeit für andere Spezies wird durch geänderte Stoffflüsse zwischen Meerwasser und Sediment beeinflusst. Dieser Mechanismus war möglicherweise der Auslöser der kambrischen ‚Explosion', der schnellen Entwicklung höheren Lebens auf der Erde.

Die Sauerstoff-Isotopenzusammensetzung von Cherts wird häufig zur Rekonstruktion von Paläo-Meerwassertemperaturen benutzt. Allerdings ergibt die Berechnung mittels O-Isotopenthermometrie unrealistisch hohe Meerwassertemperaturen für die meisten Chert-Proben. Zwei physiko-chemische Eigenschaften ermöglichen die Überprüfung, ob O-Isotope in Chert einen diagenetischen ‚Fußabdruck' besitzen. Diese sind i) der starke Einfluss von Detritus auf die Silica-Löslichkeit und somit auf die Geschwindigkeit der Silica Phasenumwandlungen bei der Versenkungsdiagenese und ii) die temperaturabhängige Equilibrierung der O-Isotopenzusammensetzung von Silica bei Lösungs-Fällungs-Reaktionen. Hierzu wurde der gleiche Probensatz ediakarischer bis kambrischer Cherts und silifizierter Tonsteine des ‚Lijiatuo' Profils untersucht. Die O-Isotopenzusammensetzung von Chert liegt zwischen 17.1 und 24.0‰ δ^{18}O und der Gehalt detritischer Minerale wurde auf ca. 1 bis 75 Gew.-% berechnet. Eine Massenbilanzrechnung zeigt, dass der authigene Quarz eine O-Isotopenzusammensetzung zwischen 17.1 und 29.8‰ δ^{18}O besitzt. Dieses Ergebnis wurde durch SIMS-Analysen verifiziert. Die δ^{18}O-Werte des authigenen Quarzes korrelieren mit dem Detritus-Gehalt. Raman-spektrometrische Analysen von kohlenstoffhaltigen Material zeigen, dass die diagenetischen Maximaltemperaturen bei etwa 260°C lagen. Die Korrelation

zwischen $\delta^{18}O$ und Detritus-Gehalt liefert den Nachweis, dass $\delta^{18}O$ in Chert Temperaturen bei der Phasenumwandlung von Opal-CT nach Quarz anzeigen. Der Erhalt dieser Signatur trotz hoher Temperaturen bei der Versenkungsdiagenese bestätigt, dass Chert resistent gegenüber Isotopenaustausch ist. Eine Berechnung von Quarz-Bildungsraten bei unterschiedlichen Temperatur-Gradienten zeigt, dass der globale Trend zunehmender $\delta^{18}O$ Werte in Chert über das Proterozoikum durch Quarzbildung bei zunehmenden Tiefen und bei abnehmenden Temperaturen als Konsequenz abnehmender geothermischer Gradienten durch Abkühlung der Erde erklärt werden kann.

Acknowledgements

Many thanks are due to Prof. Friedhelm von Blanckenburg for supervising my doctoral thesis. In particular I am grateful for the advancing scientific discussions during early morning train rides to Bremen, late office hours in Potsdam, or even later (CET) between Berlin and Palo Alto. Thanks for the freedom to develop my research focus independently, but at the same time for guiding ideas. I am grateful for funding by the DFG (grant no. BL 562/11-2) through Prof. Christoph Heubeck's research group FOR 736 "The Precambrian–Cambrian Ecosphere (R)evolution: Insights from Chinese microcontinents". Being member of this group was a lot of fun and I am thankful for discussions, the introduction to the Ediacaran and Cambrian periods, common conferences and field work. I also thank Dorothee Hippler and Prof. Gerhard Franz for providing samples and for discussions. For field work in Hunan and Hubei I would like to acknowledge funding by the National Science Foundation of China, NSFC.

I thank my colleagues of the 'Earth Surface Geochemistry' group in Potsdam for, seminars, discussions and cakes. I benefited from the well maintained ICP laboratory at GFZ. In this respect I would like to thank Jan Schuessler for his support with (fs-laser-) MC-ICP-MS analyses and his helpful advice in case of uncertainty. Special thanks are due to my stable, stable isotope discussion pal Marcus Oelze whose doubtful attitude about new interpretations fueled our discussions. Thanks to Daniel Frick for discussions on technical matter and reliable supply of great coffee. Thanks to Ralf Oeser and Maria Stuff for common lab work, discussions and great BSc and MSc theses. I thank Birgit Plessen for analyses of carbon and nitrogen isotopes and discussions. Many thanks are also to Simon Hohl for day-long scientific discussions and writing sessions at the Staatsbibliothek zu Berlin.

Many thanks to my family for their constant support and to my girlfriend Stefanie for her support and commuting 420 km every day.

Preface

This cumulative PhD thesis summarizes my research work in form of three manuscripts. These manuscripts have either been accepted for publication, are in the review process, or are in a final preparation stage for submission. Below I briefly summarize the individual chapters of this thesis and indicate the contribution from co-authors to the respective manuscripts.

- **Chapter 1** is an introduction into silicon- and oxygen stable isotope Geochemistry and the Ediacaran period in Earth's history.

- **Chapter 2** reports on early diagenetic processes that affect the silicon isotope composition of deep-sea siliceous sediment and the implications for the reconstruction of past biogeochemical cycles using silicon stable isotopes in chert. This study is published in *Earth and Planetary Science Letters* ('The silicon isotope record of early silica diagenesis' by Michael Tatzel, Friedhelm von Blanckenburg, Marcus Oelze, Jan A. Schuessler and Gerhard Bohrmann; doi: 10.1016/j.epsl.2015.07.018).

  During early diagenesis of silica, the bulk sediment's silicon isotope composition is shifted by two fundamental processes, namely by i) preferential dissolution of isotopically distinct, labile opal in solutions undersaturated in Si and ii) aluminum silicate precipitation. The results imply that chert formed from siliceous sediment deposited in environments with high Si concentrations (such as the Precambrian ocean) will faithfully record paleo-environmental conditions because dissolution is suppressed by high Si levels.

  GB, FvB and I have sampled piston cores in the core repository of the Alfred Wegener Institut, Helmholz Zentrum für Polar- und Meeresforschung; these cores were recovered from sediments in the Atlantic sector of the Southern Oceans during Polarstern cruise ANT-IX/3. Bulk sample Si isotope MC-ICP-MS analyses, leaching experiments and data evaluation were conducted by me. Femtosecond laser ablation MC-ICP-MS Si isotope analyses were conducted by JS and me. The data were discussed between all co-authors, especially between Mo, FvB and me. I interpreted the data and wrote the manuscript with input from all co-authors. The manuscript was reviewed by all co-authors, especially by FvB, Gregory de Souza and two anonymous journal reviewers.

- **Chapter 3** reports on stable silicon isotopes and supporting geochemical data in Ediacaran to Cambrian cherts and siliceous shales that yield implications for the mechanism of the Neoproterozoic seawater oxygenation. A manuscript on this study, entitled 'Ecosystem engineering as driver for the Late Neoproterozoic ocean oxygenation' is prepared for submission. Co-authors on this manuscript are Friedhelm von Blanckenburg, Julien Bouchez, Marcus Oelze and Dorothee Hippler.

In this study a well-preserved section of Precambrian/Cambrian cherts and siliceous shales is reported ('Lijiatuo', South China) in which the silicon stable isotope composition records an increasing abundance of siliceous sponges during the Precambrian-Cambrian transition. Redox-sensitive elements reveal that the oxygenation of sea water and benthos occurred simultaneously with the increase in sponge abundance. These results provide evidence that filter feeding by sponges led to rising oxygen concentrations in shallow ocean basins, and might have facilitated the Cambrian 'explosion', the sudden increase in the number of metazoan phyla.

The research was planned by FvB and DH. Some samples were collected during field work in 2008 by Jörg Trappe. I collected additional samples during field work in 2012 and carried out Si isotope analyses. Major- and trace elements were analyzed commercially by Actlabs, Canada. The mass balance calculation was done by me and JB ran the inversion model. The data was interpreted by me with input from FvB and MO. I wrote the manuscript with contribution from FvB and input from JB, MO, and DH.

- **Chapter 4** reports oxygen isotope evidence from Ediacaran to Cambrian cherts and siliceous shales that the chert oxygen isotope composition represents diagenetic temperatures. A model calculation shows that the cooing of the Earth's crust entails an increase in chert $\delta^{18}O$.

This chapter reports a preliminary scientific synthesis summarized in a manuscript. Analytic work was supported by Daniel Herwartz, Keno Lünsdorf and Michael Wiedenbeck.

Cherts and siliceous shales from 'Lijiatuo' section preserve a relation between detrital mineral abundance and $\delta^{18}O$ of authigenic quartz. Since $\delta^{18}O$ records the temperature of quartz equilibration and the underlying phase transformation in turn depends on the detrital mineral abundance, quartz chert $\delta^{18}O$ records the temperature of the diagenetic phase transformation from opal-CT to quartz. This signature is preserved despite burial to high temperatures of ca. 260°C. The indicated robustness of the oxygen isotope composition together with a model calculation show that $\delta^{18}O$ of chert increases with decreasing geothermal gradients, implying that the secular chert $\delta^{18}O$ trend preserves a record of the cooling history of the solid Earth.

DH and I conducted oxygen isotope analyses by laser fluorination gas mass spectrometry. KL conducted the Raman spectrometric analyses with my contribution, MW conduced the SIMS analyses.

Content

1. Introduction

In form of their chemical and isotopic composition sedimentary rocks disclose information about environmental conditions prevailing at the time their pre-diagenetic precursors were deposited. The distribution of chemical elements and isotopes in the environment and their accumulation in sediments is controlled by chemical, physical and biological processes. Therefore, they can be used as 'geochemical proxies' that 'translate' the chemical and isotopic composition of a rock or a mineral into environmental conditions of the past and thus disclose the geological record. Chemical elements and isotope ratios that react sensitively to the presence of free oxygen are used as proxies for paleo-redox conditions. Examples include the rare earth element Ce that in seawater is depleted relatively to Pr and Nd under oxic conditions (e.g. Bau and Koschinsky, 2009), Ba that is immobilized in barite at the sulfide/sulfate redox boundary (e.g. Torres et al., 1996), and Mo isotopes that fractionate to a degree that depends on redox controlled rates of precipitation (e.g. Chen et al., 2015). The oxygen isotope composition of minerals contained in sediments is a proxy for the temperature of mineral precipitation (Knauth and Epstein, 1976). The stable isotopes of silicon contain information about biological Si utilization (Egan et al., 2012), the source of Si and distribution of sedimentary Si sinks (André et al., 2006; Geilert et al., 2014b; Marin-Carbonne et al., 2012; Steinhoefel et al., 2010; van den Boorn et al., 2007), and, in specific cases, sea water temperatures (Marin-Carbonne et al., 2014). The underlying principle is that during biological Si utilization ^{28}Si is preferred over ^{29}Si and ^{30}Si (De La Rocha et al., 1997; Ding et al., 1996; Wille et al., 2010) and the light isotopes are similarly preferred during the rapid Si attachment at chemical disequilibrium (Oelze et al., 2015, 2014).

However, this wealth of information might be obliterated when sediment is buried to great depth and re-exposed at the surface where fluid interaction alters the chemical and isotopic composition of sediments. A prominent example is the process of silicification, the secondary precipitation or exchange of silica. The O- and Si isotope composition was found to increase with the degree of silicification of basalt (Abraham et al., 2011). Thus, to interpret these geochemical proxies in terms of paleo-environmental conditions we require knowledge about the influence of such secondary processes. To take this consideration further, if a geochemical rock record is affected by post-depositional alteration, the chemical and isotopic composition might even be exploited to derive information about the process that induced these geochemical changes.

1.1. Silicon and oxygen stable isotopes in chert

Quartz chert formation is a diagenetic process (Calvert, 1974). At surface conditions, silicon dioxide commonly forms primarily as amorphous, water-rich opal. Sedimentary burial and/or heating of siliceous sediment eventually transforms the metastable, amorphous silica into crystalline silica in which silicon is bound in form of a network of linked SiO_4 tetrahedra. The strong Si-O bonds provide quartz with a high physical strength and its chemical resistance adds to its overall high robustness against alteration. Therefore, quartz is commonly well-preserved over long geological time scales and with it a record of past conditions on Earth in form of its stable silicon- and oxygen isotope composition. However, the diagenetic nature of chert means that the interpretation of the isotope composition requires two questions to be answered. First, does chert preserve the isotope composition of the initial amorphous silica despite diagenetic transformation? And second, if so, what information do the oxygen- and silicon isotope compositions disclose in the context of the silica cycle at the time of deposition?

Regarding the first question, it is largely unknown whether the silicon- and oxygen isotope records are preserved during silica diagenesis. Many previous studies assume that the original isotope composition is inherited by quartz during diagenetic phase transformation, and thus disclose paleo-environmental significance. These diagenetic phase transformation reactions, however, proceed through dissolution-reprecipitation and are therefore prone to isotope exchange. The effect of diagenesis on the silicon isotope composition was addressed only in a few studies that overall yield an ambiguous notion of isotope shifts during diagenesis. A lower $\delta^{30}Si$ of quartz (0‰) compared to higher $\delta^{30}Si$ in associated diatoms (1.4‰) suggests equilibration of diagenetic fluids with isotopically light shales (Ziegler et al., 2011). On the other hand, silicification of magadiite [$(NaSi_7O_{13}(OH)_3 \cdot 3(H_2O)$] was found not to be associated with isotope fractionation of silicon (Ziegler and Marin-Carbonne, 2012). Dissolution-reprecipitation produces a high variability in O- and Si- isotope composition on the micro-scale (Marin-Carbonne et al., 2012).

An overall disagreement exists about the preservation of the original oxygen isotope composition of chert. Some studies suggest that some chert preserves its original isotope composition (Hren et al., 2009; Knauth and Lowe, 2003; Knauth, 2005). In contrast, decreasing $\delta^{18}O$ in buried deep-sea siliceous sediment during diagenetic phase transformation to opal-CT and quartz has been observed (Kolodny and Epstein, 1976; Murata et al., 1977; Pisciotto, 1981). This observation suggests temperature- dependent equilibration of the chert oxygen isotope composition with ambient fluids during dissolution-reprecipitation.

Regarding question two, it must be noted that i) the amorphous silica precursor of chert has potentially multiple sources of which the significance also shifted through Earth history and that ii) silicon concentrations in seawater shifted significantly over time Figure 1-1). On the ancient Earth surface, silica precipitation occurred inorganically where massive Banded Iron Formation deposits formed from Si-rich, hydrothermal fluids. During most of the Precambrian time, no biological silicon withdrawal mechanism

existed (Kidder and Erwin, 2001), leaving seawater silica concentrations at high levels estimated at estimated ≈60 ppm (Siever, 1992) or even >110 ppm (Grenne and Slack, 2003). Under these conditions, silica precipitation as opal-CT occurred in the sediment's pore space following Si diffusion or by precipitation at the seawater-sediment interface (Siever, 1992). The ecological success of sponges and radiolarians in the Paleozoic and of diatoms since the Jurassic led to a stepwise decrease in silicon concentrations in seawater (Racki and Cordey, 2000). Si levels dropped beneath the equilibrium solubility (the equilibrium Si solubility is the concentration of silicon in solution at which neither net dissolution nor (abiotic) precipitation of the associated silica polymoph occurs) of opal-A and opal-CT, and to a declining importance of inorganic silicon precipitation (Kidder and Erwin, 2001) (Figure 1-1). The equilibrium solubility of opal-A is 60 to 130 ppm SiO_2, that of opal-CT is between 20 to 30 ppm SiO_2 and that of quartz 6 to 10 ppm SiO_2 (Williams et al., 1985 and references therein) (Figure 1-1). It follows that decreasing seawater Si concentrations decrease the preservation efficiency of siliceous deposits. Therefore, the mass presence of silica secreting organisms, in particular diatoms, fundamentally changed the silica cycle due to recycling of silica by dissolution in seawater and shallow sediment. These secular changes of the silica cycle indicate that both the fractionation factor of Si isotopes and the mass balance of silicon shifted through time. Thus, the interpretation of the silicon isotope composition of silica requires i) an understanding of the silicon mass balance and ii) knowledge of isotope fractionation under different geochemical conditions.

The information disclosed by the oxygen isotope composition of chert crucially depends on whether $\delta^{18}O$ is reset during diagenesis, or whether the $\delta^{18}O$ of the original precipitate is preserved. In the former case $\delta^{18}O$ will depend on ambient temperature and the $\delta^{18}O$ of the source fluid. In the frequently presumed latter case, the temperature dependence of oxygen isotope fractionation can be exploited to estimate paleo-surface temperatures.

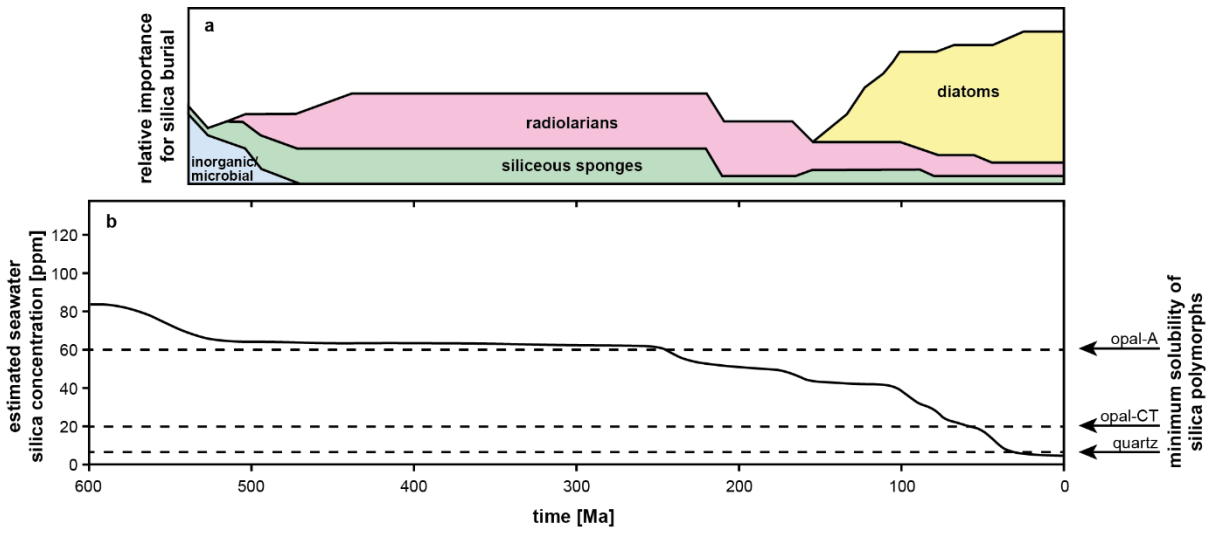

Figure 1-1: (a) Importance of siliceous organisms for silica burial (modified after Kidder and Erwin, 2001) and (b) estimated seawater silica concentrations during the Phanerozoic (modified after Racki and Cordey, 2000). In the Precambrian, seawater silicon concentrations were controlled by inorganic precipitation and was as high as between ≈60 and >110 ppm SiO_2 (Siever, 1992; Grenne and Slack, 2003). In the Paleozoic and the Mesozoic, seawater silicon concentrations dropped slightly due to the establishment of siliceous sponges and radiolarians. With the emergence of diatoms in the Jurassic, silicon concentrations dropped significantly to modern levels between 0.6 and 10.8 ppm SiO_2 (Tréguer et al., 1995).

1.2. The Ediacaran Period

The Ediacaran is the final period of the Proterozoic eon (2500 – 541 Ma) and its end marks the beginning of the Phanerozoic eon (541 Ma to today). The definition of the Ediacaran in the rock record is based on the fact that at this time the surface environment and life were subjected to vast changes. It begins at ca. 635 Ma with the end of the global, low-latitude 'Marinoan' glaciation (a 'snowball Earth', 650 – 635 Ma; Kirschvink, 1992). It terminates at 541 Ma with the first appearance of *Trichophycus pedum*, a feeding trace in sediment left by an unknown animal. During this time, two fundamental and unidirectional developments occurred on Earth: i) Concentrations of molecular oxygen increased significantly in the ocean and atmosphere for the second time in Earth history, following ca. 1900 Ma at low levels between 0.01-10% of the present atmospheric level (PAL) (Lyons et al., 2014; Planavsky et al., 2014); and ii) Large and architecturally complex organisms evolved (Narbonne, 2005) that required a minimum concentration of oxygen (Nursall, 1959) estimated to between 1 and 10% PAL (Budd and Jensen, 2000).

The deglaciation of Marinoan ice has likely been triggered by super greenhouse conditions where volcanic degassing resulted in atmospheric CO_2 accumulation to ca. 350-fold PAL (Hoffman et al., 1998). Warm temperatures, high atmospheric CO_2 and an intense hydrological cycle have caused high rates of continental weathering, resulting in high seawater alkalinity and the rapid precipitation of carbonates (Hoffman et al., 1998). These are preserved in the rock record as globally occurring cap carbonate layers

overlying Marinoan glacial till. The post-glacial increase in weathering fluxes led to an increase in bioavailable phosphorous, which limits primary productivity on geological time scales (Howarth, 2013). Therefore, post-glacial weathering is believed to have increased primary productivity and organic carbon burial, leading to the oxygenation of the atmosphere (Planavsky et al., 2010). Se isotope evidence suggests that deep ocean oxygenation took ≈100 Ma and started at the latest with the termination of the Marinoan glaciation (Pogge von Strandmann et al., 2015). However, the carbon isotope composition of carbonates and organic matter suggest that the size of the organic carbon reservoir might have increased already during the early, and mid-to-late Neoproterozoic in a stepwise manner (Des Marais et al., 1992). These discrete steps coincide with phases of continental rifting and orogeny that are believed to have triggered atmospheric oxygenation through enhanced organic carbon burial by way of higher clastic sedimentation rates (Des Marais et al., 1992). A new evaluation of the global carbon isotope database reveals a significant and permanent increase in organic carbon burial since the Proterozoic-Phanerozoic boundary (Krissansen-Totton et al., 2015) that implies a concomitant increase in oxygen (Derry et al., 1992).

Alternative trigger mechanisms for this Neoproterozoic Oxygenation Event have been proposed in recent years. These hypotheses suggest that life itself has led to the oxygenation of Earth. Triggers in the terrestrial environment include the development of primitive land biota which enhances pedogenic clay production and marine organic carbon burial (Kennedy et al., 2006), where mineral weathering was accelerated by fungi and other soil biota (Derry, 2006). Soil formation through the development of the terrestrial fungi-lichen ecosystem would also have enhanced organic carbon burial through restricted supply of oxygen to the weathering environment (Kump, 2014). In the marine realm, enhanced organic carbon burial is suggested to result from an increased efficiency of the biological pump through the evolution of large eukaryotes (Logan et al., 1995), seawater filtration by sponges (Lenton et al., 2014), and the appearance of Eumetazoa (Butterfield, 2009).

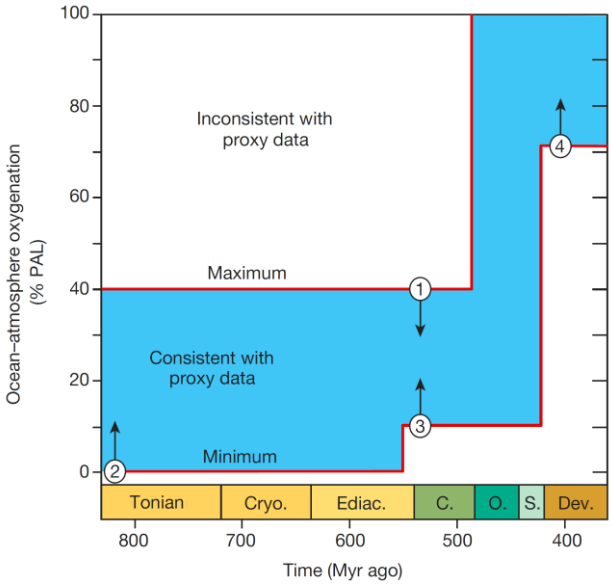

Figure 1-2: Constraints on the evolution of atmospheric and seawater oxygenation (Sperling et al., 2015). A moderate Late Ediacaran increase in oxygen levels is suggested based on (2) low minimum O_2 levels (0.5 to 1% PAL) required for the appearance of mass-dependent sulfur isotope fractionation and (1) anoxic surface waters and (3) oxygen requirements of the Cambrian biota on the other hand. High levels of ca. 70% PAL in the Devonian are inferred from the presence of fires (4). Such modest Neoproterozoic oxygen increase might, however, have been sufficient to exceed a threshold oxygen concentration that triggered the Cambrian animal evolution.

Remaining ambiguity in the exact timing and the spatial evolution of seawater redox conditions impedes on the exploration of trigger mechanisms of the Late Neoproterozoic oxygenation event and the timing of animal evolution in relation to surface

oxygenation. Mo concentration data suggest that the deep oceans were oxygenated in the Late Ediacaran (Fike et al., 2006), whereas Mo, S and Fe isotope evidence supports anoxia in deep seawater (e.g. Kurzweil et al., 2015). Such delayed full oxygenation is supported by a recent statistical analysis of iron geochemical data, which suggests that the Ediacaran oxygenation was relatively modest and that oxygenation continued into the Paleozoic (Sperling et al., 2015) (Figure 1-2).

However, even a slight increase in oxygen levels might have been the critical environmental trigger for the Cambrian bioradiation (Sperling et al., 2015).It must be noted that despite the presence of oxygen-rich, shallow seawater in a stratified Ediacaran ocean (Li et al., 2010), the distribution of eukaryotic algae might have been limited by the presence of sulfidic deep water (Anbar and Knoll, 2002). This is because bioessential metals including Fe, Mo, Cu and Zn would have been withdrawn from seawater through sulfide formation and Fe- and Mo scarcity would have limited the N availability (Anbar and Knoll, 2002). New Mo isotope data provide evidence that the Cambrian bioradiation coincided with the extent of bottom water oxidation (Chen et al., 2015). Bottom water oxygenation in the Cambrian might reflect the development of a modern ocean like redox structure with intermediate oxygen minimum zones (Wen et al., 2015). Contrary to the view that low oxygen concentrations delayed animal evolution, a recent study of redox sensitive metals in Mesoproterozoic sediments indicate that deep ocean oxygen levels had reached oxygen concentrations >4% PAL around 1.4 Ga, suggesting that animal evolution might not have been limited by oxygen itself (Zhang et al., 2016).

1.3. Silicon stable isotopes

Silicon is the second most abundant chemical element in the Earth's crust with approximately 27 wt%. Silicon is an important constituent in most solid compartments of the Earth. It occurs in high abundances in most rock- and sediment types with up to ≈47 wt% in pure silica minerals like quartz (SiO_2).

Silicon consists of 14 protons and 14 electrons. These determine its chemical properties. Three stable configurations of its nucleus exist with 14, 15, and 16 neutrons, representing the stable isotopes of silicon with atomic masses 28, 29 and 30. Their average natural abundances of 92.2297% (^{28}Si), 4.6832% (^{29}Si) and 3.0872% (^{30}Si) result in an average atomic mass of 28.0855. This mass, however, is variable on the fifth decimal place due to slight variations in the abundance of Si isotopes in various compartments.

Absolute abundances of isotopes and absolute natural isotope ratios cannot be analytically determined. Therefore, relative isotope ratios are reported as the isotope composition which is the deviation of an isotope ratio of a sample from that of a reference material. For silicon, the reference material is the quartz sand NIST 8546, also known as NBS 28 and the isotope composition of silicon is reported as:

$$\delta^{(x/28)}Si = \left[\frac{\left(\frac{x}{^{28}Si}\right)_{sample} - \left(\frac{x}{^{28}Si}\right)_{NBS\ 28}}{\left(\frac{x}{^{28}Si}\right)_{NBS\ 28}} \right]$$

Where x denotes either ^{29}Si or ^{30}Si.

As variations in isotope ratios occur on the per mil scale, $\delta^{(x/28)}Si$ is commonly multiplied by 1000 and abbreviated as $\delta^{29}Si$ and $\delta^{30}Si$. Natural materials reveal a maximum range between ca. -6 and +6‰ $\delta^{30}Si$ and between ca. -3 and +3‰ $\delta^{29}Si$.

1.3.1. Silicon stable isotope measurements

Stable silicon isotopes can be measured using fluorination gas mass spectrometry, multi collector-inductively coupled plasma-mass spectrometry (MC-ICP-MS) and secondary ion mass spectrometry (SIMS). In the course of the present PhD work, Si isotope analyses were performed using a Thermo Neptune MC-ICP-MS equipped with a Neptune Plus Jet interface. Samples were analyzed either from aerosols after laser ablation of solid material or in liquid form after wet chemical digestion and chromatographic ion separation.

1.3.1.1. Solution MC-ICP-MS analysis

For solution analyses samples are prepared using method of Georg et al. (2006) with slight modifications. Approximately 15 mg of pulverized, homogenized sediment sample are digested for 15 min at 750°C in a

muffle furnace by NaOH fusion (400 mg NaOH pellets, Merck, p.a. grade) in Ag-crucibles. After the dissolution of the fusion cake in Milli-Q water (>18 MΩ) and 1.5mM HCl (pH 1.5), the sample solution is diluted to <30 ppm SiO_2 and acidified to pH 1.5 with HCl. Aliquots of ca. 50 µg Si of this solution are loaded onto cation exchange columns (DOWEX AG 50W-X8, 200–400 mesh) from which silicon is eluted with 5 ml Milli-Q water. Sample aliquots are analyzed by ICP-OES (Varian 720-ES with an uncertainty of about 5%) before isotope analyses to check for column recovery and for purity of the Si sample solution. Samples and standards are diluted in 0.1 M HCl to <1 ppm Si. Mg (Alfa Aesar Specpure 14430) is added to sample solutions to match Si concentrations.

Samples are taken up in diluted acid and introduced into the plasma using a PFA nebulizer connected to either a stable sample introduction (SSI) cyclonic / scott dual spray chamber or a desolvation unit (here an ESI APEX). The ICP torch consists of three concentric quartz tubes; through the inner tube (injector) the sample is introduced into the plasma. The second tube feeds the auxiliary gas (ca. 1 L/min Ar), which sustains the plasma. Through the outer tube, ca. 15 L/min Ar are flushed to prevent the torch from melting. The sample enters the plasma where it vaporizes, atomizes and ionizes. The ions are transferred from atmospheric pressure, through two consecutive cones into high vacuum (10^{-4} mbar). The motorized positioning allows centering the plasma torch relative to the water-cooled interface. Optimization of the gas flow rates allows maximizing the sample nebulization and ion formation. In the transfer lens system, ions are accelerated to 5 kV, the pressure is further reduced down to 10^{-7} mbar by turbo molecular pumps and the ion beam is focused by electrical lenses to maximize transmission through the entrance slit of the electrostatic analyzer (ESA). Three different source slit sizes are available that have high-, medium- and low resolution, where mass resolution (Δm/m) increases with decreasing width of the slit. Si isotope analyses require a mass resolution of at least Δm/m≈ 3000 to resolve the isobaric interference of $^{14}N^{16}O$ on ^{30}Si. In the ESA, an electric field focusses the ions with different kinetic energies onto a first focal point in the intermediate slit. Subsequently ions are further accelerated to 10 kV before they enter the magnet. Ions are separated according to mass/charge in the magnet, after which further zoom lenses focus the ions before they enter the detection system. The multicollector detection system is aligned along the focal plane of the ion optics to allow simultaneous detection of up to 12 isotopes. Detector platforms are equipped with Faraday cups that are connected to voltage amplifiers to increase the electronic signal generated by the incoming ions. Silicon isotopes are measured by Faraday detectors connected to 10^{11} Ω resistors.

True absolute isotope ratios cannot be measured directly, due to instrumental mass bias, i.e., the deviation of a measured isotope ratio from the true isotope ratio. Mass bias results from effects in the ICP, from sample introduction, and ion transmission through the mass spectrometer. Space charge effects during ion transmission cause the mutual repulsion of ions and preferential outward deflection of lighter isotopes, resulting in the preferential transmission of heavy isotopes. As long as the resulting mass bias is constant, measured isotope ratios can be corrected for this offset by two means. One method is isotope dilution, where

a double spike of known isotope composition and element concentration is mixed with a sample. The measured ratio is then corrected for the spike to obtain the isotope ratio of the sample. The alternative approach is standard-sample-bracketing, which is used for Si isotope ratio measurements. The alternating measurements of standards (i.e., homogenous material with uniform isotope composition, such as NBS 28) and samples yields normalized sample isotope ratios. Mass bias for Si isotopes can furthermore be reduced by $^{25}Mg/^{24}Mg$ and $^{26}Mg/^{24}Mg$ drift correction employing the exponential mass fractionation law (Cardinal et al., 2003; Engström et al., 2006; Zambardi and Poitrasson, 2011). This approach requires the addition of Mg to Si sample solutions and standards and has two further advantages. First, Mg addition (at equal concentrations to Si around 0.3 to 1 µg/g) serves as matrix modifier that suppresses differences in mass bias. Such effects would result from even minor variation in the sample matrix due to imperfectly separated solutions. In particular, matrix effects are caused by the presence of anions such as SO_4^{2-} and PO_4^{3-}. These cannot be separated with cation-exchange columns, which are used to separate Si from cations. Second, Mg addition causes an approximately threefold signal intensity boost, due to an increased rate of atom-electron collisions, enhancing ionization (Barling and Weis, 2012; Beauchemin et al., 1987). The uncertainty of the entire solution MC-ICP-MS method is estimated to be ±0.07‰ (2SD) for $\delta^{29}Si$ and ±0.10‰ (2SD) for $\delta^{30}Si$. Details on the specific measurement conditions are found in chapters 2 and 3.

1.3.1.2. Femtosecond laser ablation MC-ICP-MS analysis

High-spatial resolution analysis of stable silicon isotope ratios by laser ablation MC-ICP-MS requires an ablation technique that reduces shifts in elemental and isotopic fractionation. Such conditions can be achieved using a femtosecond laser ablation systems that generates short-length pulses (Russo et al., 2002). The very short interaction time of the femtosecond pulse with the material significantly reduces melting of the sample during ablation. For analysis of translucent samples, such as silicates, the system needs to operate in the deep UV wavelength in order to increase the absorbance.

The laser system used for sample analysis is a custom-built system (fem2; Schuessler and von Blanckenburg, 2014). This system combines a Ti:sapphire femtosecond seed laser (Spectra Physics, MaiTai) coupled to a high energy Nd:YLF pump laser system (Spectra Physics, Empower-30) in order to obtain short pulses with Millijoule intensities. Amplification of low-energy laser pulses of the seed laser occurs through a regenerative amplifier containing a Ti:sapphire crystal. The output IR-wavelength (785 nm) light is converted to UV-wavelength (196 nm) using nonlinear optics, consisting of three Barium Beta Borate crystals (BBO). The first BBO crystal doubles the frequency of the incident beam to obtain a wavelength of 393 nm (second harmonic). The second crystal generates the third harmonic (262 nm), and the third BBO crystal combines non-linearly the 262 nm pulses with the 785 nm pulses to produce the 196 nm wavelength (fourth harmonic) used for laser ablation. The laser beam is directed by dielectric mirrors through an iris aperture into a microscope and focused into the ablation cell onto the sample surface. Aerosol is produced by particle

transport through a helium carrier gas which is mixed with Ar and H_2O from a 50 µL/min PFA nebulizer before entering the plasma torch. To obtain signal intensity matching of different materials, the repetition rate of the laser can be adapted to rates between 1 Hz and 1000 Hz. The spot size can be varied between 10 and 80 µm, where resulting energy densities are between 0.1 and 50 J/cm². Precise Si isotope analyses with an uncertainty of <0.23‰ δ^{30}Si (2SD) can be obtained when areas >50 x 50 µm are analyzed in the raster mode or when geometric features of similar surface area are analyzed using a laser spot diameter of >20 µm. Reference materials for calibration (NBS 28 quartz sand) and for analytical quality control (USGS BHVO-2G basalt glass, IRMM-017 Si single crystal) are prepared as polished epoxy grain mounts and placed together with samples into the ablation cell for analysis. To allow automated isotope ratio measurements, the laser and the mass spectrometer are synchronized through a trigger sent by the laser system with the onset of ablation.

1.4. Oxygen stable isotopes

Oxygen is the most abundant element in the Earth's crust with approximately 49wt% and is also a major constituent in the hydrosphere and atmosphere.

Oxygen has three stable isotopes with masses 16, 17 and 18. Their natural average abundances are 99.762% (^{16}O), 0.038% (^{17}O), and 0.2% (^{18}O), giving oxygen an average mass of 15.9994. The isotope composition is reported as the deviation of the sample's isotope ratio from that of the PeeDee Belemnite (PDB) for carbonates, and relative to that of Vienna Standard Mean Ocean Water (VSMOW) for other material:

$$\delta^{(x/16)}O = \left[\frac{\left(\frac{x}{^{16}O}\right)_{sample} - \left(\frac{x}{^{16}O}\right)_{VSMOW}}{\left(\frac{x}{^{16}O}\right)_{VSMOW}} \right]$$

Where x denotes either ^{17}O or ^{18}O.

Absolute oxygen isotope ratios of silicates are commonly calibrated relative to the reference material quartz sand NIST 8546, (NBS 28), which is at 9.57 ± 0.10‰ δ^{18}O (1SD) (IAEA, 2007) and are back-calculated to the VSMOW scale.

Natural variations in oxygen isotope composition occur on the per mil scale, therefore $\delta^{(x/16)}O$ is multiplied by 1000 and abbreviated as $\delta^{17}O$ and $\delta^{18}O$. Atmospheric H_2O shows the largest variability in oxygen isotope composition, ranging between ca. 0 and -45‰ $\delta^{18}O_{VSMOW}$ (Hoefs, 2009). Rocks reveal a

smaller range, where carbonates yield between ca. 0 to -20‰ $\delta^{18}O_{PDB}$, i.e., approx. 10 to 30‰ $\delta^{18}O_{VSMOW}$, and cherts between 10 and 35‰ $\delta^{18}O_{VSMOW}$ (Jaffrés et al., 2007).

1.4.1. Oxygen stable isotope analysis

Stable oxygen isotopes in silicates can be analyzed by laser fluorination combined with gas source mass spectrometry or by secondary ion mass spectrometry (SIMS). Oxygen isotope measurements acquired during this thesis work were done using both methods.

1.4.1.1. Laser fluorination gas source mass spectrometry

Oxygen isotope analyses by laser fluorination gas source mass spectrometry (Sharp, 1990) were performed in continuous flow mode at the University of Göttingen. Following evacuation and heating of the sample chamber to 70°C overnight, sample and NBS 28 standard powders were fused in a 18-pit Ni sample holder to glass beads using a SYNRAD 50 W CO_2-laser. Oxygen is liberated from solid samples by the reaction of 0.2 mg powdered rock with ≈10 mbar purified F_2 using the same laser. Condensable reaction products (e.g. SiF_4) are trapped in a first liquid nitrogen cold trap. Excess F_2 is reacted with NaCl at 180°C, where the Cl_2 produced is removed in a second liquid nitrogen cold trap. Oxygen is trapped in a liquid nitrogen- cooled U-trap containing a 5 Å molecular sieve. Following O_2 collection for 8 to 10 minutes, the sample is heated to ca. 120°C and transported by He-carrier gas into a final 5 Å molecular sieve trap, where a fraction of the sample is cryofocused at -196°C. Oxygen is released by rapid heating in a water bath at ca. 92°C and transported with the carrier gas stream to a Thermo Gas Bench-II. There the O_2 gas is purified in a ca. 10 m capillary gas chromatography column lined with a 5 Å molecular sieve to remove residual trace gasses other than O_2. Sample O_2 is then analyzed using a Thermo MAT 253 mass spectrometer operating in continuous flow mode. Two reference O_2 gas peaks are injected prior to the sample and used as internal reference. Oxygen isotopes were simultaneously detected on m/z 32 ($^{16}O^{16}O$) and m/z 34 ($^{16}O^{18}O$) on Faraday cups and yielded sample signal intensities of ca. 25V. Absolute $\delta^{18}O$ values are normalized relative to the NBS 28 quartz standard.

1.4.1.2. Secondary ion mass spectrometry

Oxygen isotope analyses by secondary ion mass spectrometry (SIMS) were conducted on a Cameca 1280-HR at GFZ Potsdam. In SIMS, secondary ions, produced by sputtering primary ions onto a solid sample surface, are measured mass spectrometrically (van der Heide, 2014). A primary 2.5 nA Gaussian $^{133}Cs^+$ beam is focused to a beam diameter of ca. 8 µm on the sample surface. Charge compensation on the surface is accomplished by low energy electron flooding. The secondary ion beam is transmitted through an analyzer system and ions are detected with Faraday cups, similarly to MC-ICP-MS. During data acquisition, a 10 x 10 µm area is rastered to reduce drift in isotopic composition. To resolve isobaric interferences, the mass spectrometer is operated

at a mass resolution of Δm/m≈2000. ^{16}O is measured on the L2 Faraday cup connected to an amplifier with a 10^{10} Ω resistor; ^{18}O is measured on the H2 cup connected to an amplifier with a 10^{11} Ω resistor. Drift in mass bias is corrected for by measurement of 'drift monitors' between sample measurements, i.e., homogenous standard materials with known isotope composition. For analysis of quartz samples, NBS 28 quartz is used to monitor and correct mass bias drift and to calibrate absolute $\delta^{18}O$ values.

1.5. Isotope fractionation

Variations in stable isotope ratios are the result of isotope fractionation, i.e., the disproportional transfer of isotopes of between two compartments. Physical grounds for this isotope partitioning are mass differences and variable strengths of chemical bonds that relate to different vibrational-, translational- and rotational motions in atoms of different isotopes of a chemical element. One distinguishes between two types of fractionation. On the one hand, there is 'equilibrium isotope fractionation', meaning that the cause of the isotope distribution between two compartments is that the lowest possible zero point energy is obtained in the present distribution of stable isotopes in chemical bonds. This type of fractionation requires chemical equilibrium. However, isotopic equilibrium is not always attained in chemical equilibrium. Equilibrium isotope fractionation is commonly observed in high temperature systems.

'Kinetic isotope fractionation' on the other hand commonly occurs at low temperatures and is caused by either i) transport effects or by ii) chemical reactions. Isotopes are fractionated when a chemical element with multiple stable isotopes is transported, for example along a diffusion gradient. Here, diffusion rates of stable isotopes differ according to mass differences. Kinetic isotope fractionation also occurs in ii) chemical reactions: The energy barrier that needs to be overcome in a chemical reaction varies for different isotopes due to differences in zero point energy, i.e., differences in the depth of the 'energy well'. This 'reaction-limited' kinetic effect occurs during rapid attachment of constituents to a surface at chemical disequilibrium (DePaolo, 2011; Oelze et al., 2015, 2014).

Isotope fractionation is expressed as the *isotopic fractionation factor* α_{A-B} , i.e., the quotient of isotope ratios R in two compartments A and B between which isotopes are exchanged in a chemical reaction:

$$\alpha_{A-B} = \frac{R_A}{R_B} \qquad \textbf{Equation 1-1}$$

This ratio differs at the fourth decimal place and therefore isotope fractionation is also commonly reported as $10^3 \ln \alpha$.

The isotopic fractionation between two compartments A and B is approximated by the *isotopic difference*, Δ_{A-B}:

$$\Delta_{A-B} = \delta_A - \delta_B \qquad \textbf{Equation 1-2}$$

The isotopic difference does not only depend on the fractionation factor, but also on the style of separation of compartments. If compartments A and B remain in physical contact, the isotopic difference equals the isotopic fractionation factor (closed system; Johnson et al., 2004). If the two compartments are separated, and no exchange takes place, the isotope composition δ and the isotopic difference $\delta_A - \delta_B$ will shift with ongoing chemical reaction and hence depend on mass balance ('open system fractionation' or 'Rayleigh fractionation'). This fractionation style commonly occurs during low-temperature precipitation reactions. Therefore, any quantitative inference from the (silicon) isotope record requires i) means to assess mass balance and ii) knowledge about isotope fractionation. In contrast the difference in oxygen isotopes between distinct compartments rarely depends on mass balance, as oxygen is mostly ubiquitous in any solid Earth compartment.

1.6. Scope

The main objectives of this thesis are i) to obtain an understanding whether and under what conditions the silicon- and oxygen isotope composition of chert records primary, environmental conditions at the time of silica deposition and ii) to evaluate effects of diagenesis on the isotope records. This understanding is derived from the youngest diagenetic products of silica and is applied to Late Precambrian chert (Figure 1-3).

The first major goal is to constrain the preservation potential of the initial silicon isotope composition of sedimentary silica in quartz chert and to identify early diagenetic processes that affect diagenetic products. This question is addressed by studying silicon isotopes in the youngest diagenetically formed porcellanite layers and their surrounding siliceous sediment layers. These sediments are Pliocene- to Pleistocene in age and occur in the Atlantic sector of the Southern Ocean (Bohrmann et al., 1994). This research is relevant for the interpretation of the silicon isotope composition of ancient chert and is reported in Chapter 2.

With an understanding of early diagenetic processes that affect the Si isotope composition, this thesis further aims at deriving information for conditions of ancient chert formation. The goal is to assess the source of silicon in chert and siliceous shale that were deposited during the Precambrian-Cambrian transition. The sediments studied were deposited on a continental slope and are now exposed on Yangtze Craton in South China, and belong to the best preserved marine sections of the time. Paleo-environmental implications are derived from the Si-isotope record in combination with major- and trace element data. Chapter 3 reports this part of the research.

Within the framework of silica phase transformation, the paleo-environmental significance of oxygen isotopes in chert is examined. The conceptual frame for such evaluation is developed from existing studies on the kinetics of silica phase transformation rates. Samples used are from the same, Ediacaran-Cambrian section and are basis for the evaluation of supposedly elevated surface temperatures in deep geological time. This part is reported in chapter 4.

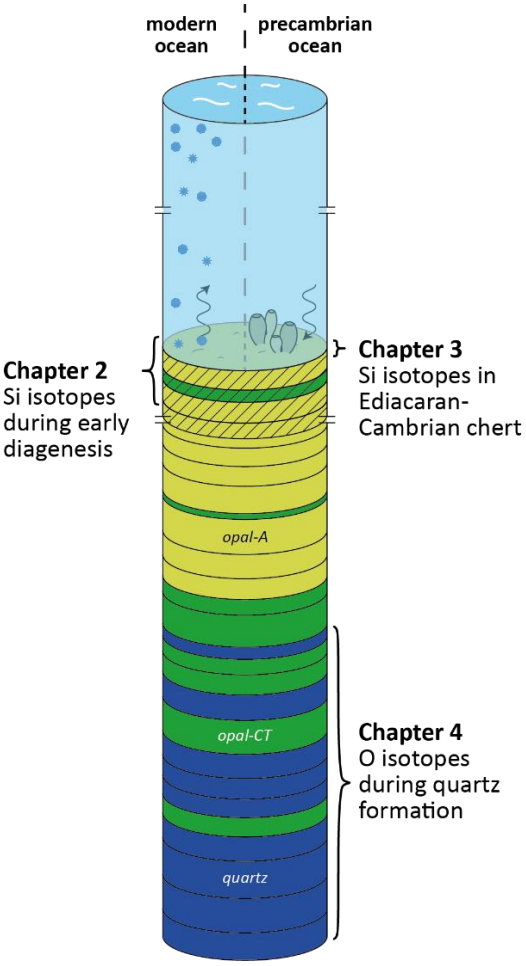

Figure 1-3: Schematic representation of the Late Precambrian and modern environments of chert formation. The modern ocean is distinguished from the Precambrian ocean by Si concentrations and therefore by Si fluxes out of/into shallow sediment. Diagenetic phase transformation occurs during burial. Topics addressed in this thesis are indicated next to the column.

2. The silicon isotope record of early silica diagenesis

Abstract

The heavy isotopes of silicon are strongly enriched in some of the youngest, early diagenetically formed porcellanite layers from the Southwest Indian Ridge (Pleistocene) and the Maud Rise (Pliocene). These porcellanite layers are composed of opal-CT and were formed by the conversion of amorphous silica (opal-A) from siliceous sediment via dissolution-reprecipitation. Their bulk δ^{30}Sivalues range between 1.7 and 2.3‰. Detritus-poor siliceous sediment surrounding these layers is significantly lower at -0.3 to 1.5‰. Sequential chemical extractions of bulk siliceous sediment show (i) preferential dissolution of diatoms featuring higher δ^{30}Si than radiolaria and Al–Si components. The detailed investigation of porcellanite layers by micro-scale Si isotope and Al/Si analyses using UV femtosecond laser ablation ICP mass spectrometry show that (ii) precipitation of authigenic aluminum silicates enriched in light Si isotopes drives pore waters to even higher δ^{30}Si. We suggest that the same processes redistributed stable silicon isotopes in precursor siliceous sediments of ancient chert. We infer that past environmental conditions can be reconstructed with high fidelity from the stable Si isotope composition of chert when initial seawater Si concentrations were high (such as in the Precambrian). Exchange of Si between layers during phase transformation (from opal-A to opal-CT and from opal-CT to quartz) is impeded when variable amounts of detrital minerals are present, because they control rates of silica phase transformation and hence the timing of dissolution–reprecipitation during burial.

This chapter is published in:

Earth and Planetary Science Letters Vol. 428, Pages 293-303

Michael Tatzel, Friedhelm von Blanckenburg, Marcus Oelze, Jan A. Schuessler, Gerhard Bohrmann (2015); doi:10.1016/j.epsl.2015.07.018

2.1. Introduction

Today the stable isotopes of silicon are successfully employed to quantify the present and past oceans' environmental conditions and marine biogeochemical cycles. In the modern ocean for example biological silicic acid utilization is inferred from the Si isotope composition of seawater (Cardinal et al., 2005; De La Rocha et al., 1997; Reynolds et al., 2006) or from biogenic silica in diatoms sampled in core top sediments (Egan et al., 2012). This information is crucial for estimating export rates of organic carbon from surface waters and its burial that affects atmospheric carbon dioxide concentrations. In the geologic record the stable Si isotope composition of chert and silicified rocks is used to reconstruct for example the weathering and hydrothermal sources of Si and the distribution of sedimentary Si sinks (e.g. André et al., 2006; Chakrabarti et al., 2012; Fan et al., 2013; Marin-Carbonne et al., 2013, 2012, 2011; Steinhoefel et al., 2010, 2009; van den Boorn et al., 2010, 2007). In spite of this progress we lack an understanding of whether the measured isotope compositions of sedimentary chert deposits do indeed record primary environmental conditions. This difficulty arises because chert forms by diagenetic dissolution-reprecipitation reactions. The effect of diagenetic overprint on sedimentary Si isotope compositions was testified for example in a study of the Miocene Monterrey Formation. There, Ziegler et al. (2011) found that the stable Si isotope composition ($\delta^{30}Si$) of diagenetic quartz ($\delta^{30}Si$= 0‰) was much lower than that of the amorphous silica in associated diatoms ($\delta^{30}Si$= 1.4‰). The authors attributed this difference to a late diagenetic fluid that had equilibrated with the Monterrey shales. Another result of such dissolution of amorphous precursor silica and reprecipitation of quartz was found in the form of highly variable Si and O isotope compositions measured by micro-scale SIMS analyses of microquartz in Precambrian chert, in which $\delta^{30}Si$ varied by 2.8‰ on the micrometer scale (Marin-Carbonne et al., 2012). However, such overprinting of isotope compositions is not ubiquitous on the bulk scale. Isotope fractionation was found to be absent during the formation of chert by the silicification of magadiite ($NaSi_7O_{13}(OH)_3 \cdot 3(H_2O)$) (Ziegler and Marin-Carbonne, 2012). Progress in synthesizing these disparate observations into a fundamental understanding of the underlying processes is hampered by our lack of knowledge of the isotope effects associated with diagenetic processes that convert amorphous opal into quartz.

Diagenesis of siliceous sediment means that the abundance of the crystalline SiO_2 polymorphs cristobalite and tridymite (opal-CT) and quartz increases with burial depth at the expense of amorphous silica (opal-A) where time and temperature exert the dominant control over the rate of diagenesis. The slow kinetics of these dissolution–reprecipitation processes explains why most chert deposits found are at least 20 Ma in age (Hesse, 1988). Besides time and temperature, the host sediment's chemical composition exerts a first-order control over rates of diagenesis. Such control is expressed in form of localized porcellanite beds (made up of opal-CT) and chert beds (made up of quartz) in unconsolidated siliceous sediment comprised predominantly of opal-A of the Monterrey Formation (Bramlette, 1946). Porcellanite layers as young as 430ka

were found in siliceous sediments of the Southern Ocean (Kerguelen Plateau: Schlich et al., 1989; Weaver and Wise, 1973; Maud Rise: Barker et al., 1988; Bohrmann et al., 1994 and Southwest Indian Ridge (Bohrmann et al., 1994, 1990) and were formed at temperatures of only 0 to 4°C as inferred from their oxygen isotope composition (Botz and Bohrmann, 1991).

The phase transformation from opal-A to opal-CT does not re-quire elevated temperature and can rather be explained by solubility changes of silica polymorphs (Williams et al., 1985). In early marine diagenesis opal-CT forms if the equilibrium solubility of silicon (setting pore water Si concentration with respect to the host sediment) exceeds that of opal-CT (ca. 25 ppm SiO_2 for cristobalite in aqueous solutions at 20°C and standard pressure; Walther and Helgeson, 1977). At the seawater-sediment interface solutions are dominated by the low seawater Si concentrations (in the modern ocean between 0.6 and 10.8 ppm SiO_2; Tréguer et al., 1995) and are thus strongly undersaturated in Si. With increasing depth, Si concentrations increase gradually and attain equilibrium concentrations asymptotically at about 10 cm sediment depth, i.e., the 'asymptotic pore water concentration' (Van Cappellen and Qiu, 1997a, 1997b). These equilibrium solubilities depend on the composition of the sediment. Pure opal-A has an equilibrium solubility of ca. 60–130 ppm SiO_2 (Williams and Crerar, 1985; Williams et al., 1985). However, this value is significantly modified by pore water pH, the presence of carbonates and Mg-hydroxides in the sediment (Kastner et al., 1977), organic matter (Hinman, 1990), and Na, Mg, K, Al and Fe in solution (Hinman, 1998). Dissolved aluminum, promoted by the dissolution of detrital minerals at the water-sediment interface (van Beusekom et al., 1997), has a particularly strong impact on the solubility of biogenic silica (Dixit et al., 2001). It has been found that the equilibrium solubility of siliceous sediment is reduced by the structural incorporation of Al into opal during biosynthesis (Dixit et al., 2001; Gehlen et al., 2002; van Bennekom et al., 1991) and by the formation of authigenic aluminum silicates (Dixit et al., 2001; Van Cappellen and Qiu, 1997a). Aluminum silicates, i.e., poorly crystalline Al-Si phases containing various amounts of K, Fe, Mg and Cl (Michalopoulos et al., 2000) readily form in the sediment during early diagenesis and can form coatings on biogenic silica, e.g. diatom frustules (Michalopoulos and Aller, 2004; Rickert et al., 2002). In this case the solubility of biogenic silica is reduced and the asymptotic pore water Si concentration is lower than that of the biogenic silica (Hurd, 1973). Thus, during early diagenesis it is the geochemical environment that determines the timing of the phase transformations.

Stable silicon isotope ratios are likely to shift during these phase transformations. In the most simple terms the isotope composition of the pore water Si and the solids precipitated thereof can be affected by i) selective dissolution of silicon sources of variable isotope composition, ii) isotope fractionation during precipitation into solids that differ in their isotope fractionation factor, and iii) the mass balance between dissolution and precipitation. We are now in the position to unravel these effects as recent experimental work has shed light on the isotope fractionation accompanying Si precipitation with unprecedented detail. The precipitation of aluminum silicates is associated with a range of negative isotope fractionation factors

($\alpha^{30}Si_{solid/solution}$) of up to -4.5‰ (Oelze et al., 2015), while the adsorption onto gibbsite is associated with fractionation factors that range between -1.8 and -3.2‰ (Oelze et al., 2014). Both depend on the net solid formation or adsorption rate. In contrast, precipitation of Si from Al-free and low-Al solutions shows that silicon does not fractionate its isotopes upon precipitation, i.e., $\alpha^{30}Si_{solid/solution}$= 0 (Oelze et al., 2015). Furthermore, experimental studies show that preferential precipitation of light silicon isotopes occurs if chemical disequilibrium prevails, and that isotope fractionation is absent at equilibrium (Geilert et al., 2014a; Roerdink et al., 2015). This view is supported by absence of Si isotope fractionation during chert formation (Ziegler et al., 2011).

To evaluate the fidelity of chert as a paleo-environmental archive we explored stable Si isotope fractionation accompanying early marine diagenesis. We sampled the youngest porcellanite found to date. Porcellanites (opal-CT) and the adjacent siliceous sediments (mainly opal-A) were sampled in piston cores from the Southwest Indian Ridge (PS2089-2, Pleistocene) and the Maud Rise (PS2070-1, Pliocene) (Bohrmann et al., 1994). The porcellanite found in these cores was preserved undisturbed in contact with its host sediment. We compared the Si isotope composition of the early diagenetic porcellanite with that of the precursor material. To determine the differential solubility of primary silica sources and to constrain their isotope composition we conducted sequential leaching experiments on bulk, unconsolidated siliceous sediments. To resolve the temporal evolution of opal-CT precipitation the porcellanite layers were investigated in detail by micro-scale silicon isotope analyses using UV femtosecond laser ablation ICP mass spectrometry (fs-LA-MC-ICP-MS). We model the effect that dissolution and precipitation processes have on pore water and porcellanite $\delta^{30}Si$ and Al/Si. Finally, we explore the implications for the use of Si isotopes to derive past biogeochemical fluxes from ancient chert.

2.2. Materials and methods

2.2.1. Samples

Two cores were recovered with a piston corer during Polarstern cruise ANT-IX/3 at the Southwest Indian Ridge (PS2089-2: Pleistocene; 53°11.3'S, 03°19.7'E; water depth 2618 m) and Maud Rise (PS2070-1: Pliocene; 65°06.3'5, 03°37 'E; water depth 2611 m), respectively (Figure 2-1). These sediments were deposited during Marine Isotope Stages 11 and 12 (ca. 470 - 360 ka BP: PS2089-2) and be-tween ca. 4.7 and 3.6 Ma (PS2070-1) as deduced from diatom and radiolarian assemblages (Bohrmann et al., 1994). Both cores comprise very pure siliceous ooze, and contain porcellanite layers of a few centimeter thickness. Siliceous sediment was sampled from sediment depths between 7.3 and 5.4 m (PS2089-2), and 6.1 and 4.2 m (PS2070-1), respectively. Each sediment sample represents about one centimeter (Supplementary Table 2-1). We sampled the porcellanite layers that are intercalated with the siliceous ooze at depths of ca. 6.0 m (PS2089-2) and 4.7 m (PS2070-1). The Pliocene porcellanite layer in core PS2070-1 has a wide regional extent and covers large parts of Maud Rise, as inferred from seismic data (Bohrmann et al., 1992).

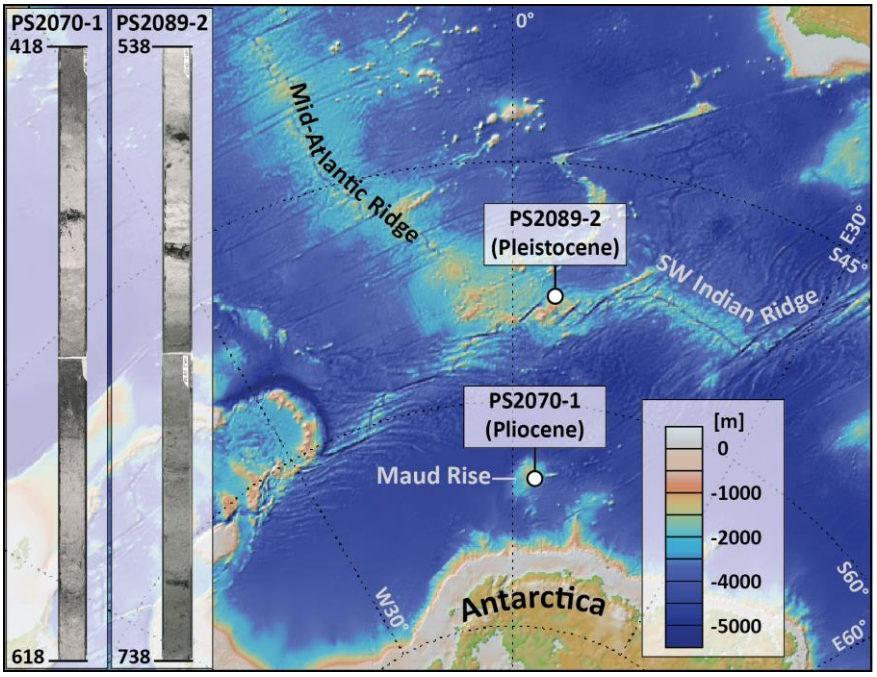

Figure 2-1: Map (www.geomapapp.com; Ryan et al., 2009) showing the sample locations in the Southern Ocean and photographs of the sampled piston cores (insets). Color coding refers to the depth below sea level.

Sediment from the Pleistocene piston core (PS2089-2) in vicinity of the porcellanite layer has high opal-A contents of up to 90%, is dominated by diatom frustules, and has TOC contents of 0.1 to 0.3% (Bohrmann et al., 1994). Siliceous sediment surrounding the porcellanite layer in PS2070-1 (Pliocene) has opal-A contents of up to 90%, contains variable amounts of mostly diatoms and radiolarians and very minor silicoflagellates,

and low TOC contents of <0.05% (Bohrmann et al., 1994). The grain size ranges from <1µmfor shards of broken diatom frustules to ca. 40 µm for undamaged frustules. Radiolarians typically range in size from 50 to 100 µm. Finely dispersed xenomorphic particles are found in variable abundance and constitute detrital as well as authigenic phases (Supplementary Figure 2-1).

The porcellanite layer from the Pleistocene piston core is comprised of a porous part (sublayer1) characterized by about 5 µm large opal-CT lepispheres that are only in parts intergrown and a dense part (sublayer2) that has little void space (Figure 2-2a). Opal-CT lepispheres from the Pliocene core cover a size range of <1 µm to ca. 5 µm. The porcellanite layer is irregularly layered and characterized by different coloring that distinguishes the two major sublayers (Figure 2-2). In close vicinity to this porcellanite we found an animal burrow of 3.5 to 7 mm thickness and ca. 3.3 cm length that is filled with opal-CT (Figure 2-2c).

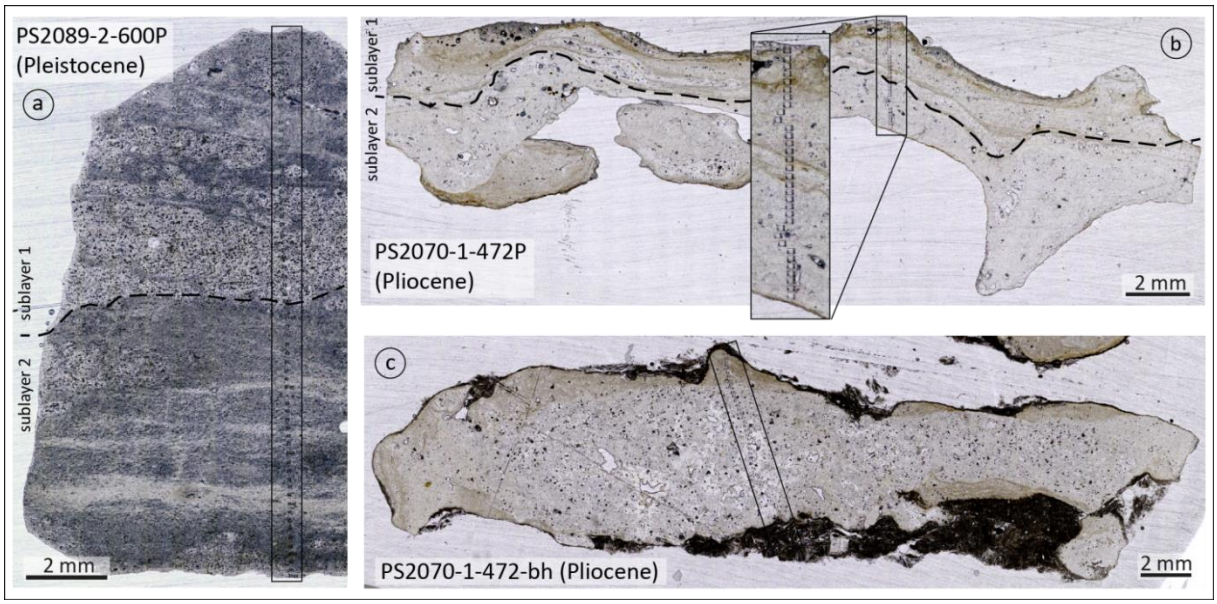

Figure 2-2: Overview images of thin sections of analyzed porcellanite samples in transmitted light. Frames highlight transects of laser ablation craters from Si isotope analyses (Figure 2-5). (a) Porcellanites PS2089-2-600P (Pleistocene) and (b) PS2070-1-472P (Pliocene) are comprised of distinct sublayers (separated by dashed lines) and bear variable amounts of impurities as indicated by their color. The inset shows a blow-up of laser craters. (c) Sample PS2070-472-bh is a cut through an animal burrow filled with opal-CT preserved in contact with adjacent siliceous ooze. The concentric texture and color variation indicates that impure precipitates have formed first.

2.2.2. Methods

2.2.2.1. Leaching experiments

To identify the Si isotope composition and Al/Si mass ratio of the most soluble component, two types of leaching experiments were conducted on three different bulk sediment samples. Conditions of the experiment are summarized in Supplementary Table 2-8. Experiment I was done at 70°C in a pre-cleaned 50

ml PP tube filled with ca. 5.3 mg sediment sample (PS2070-1-423) to which 50 ml 1.6 mm NaOH solution were added. Solutions were sampled in 30 min intervals (ca. 0.2–15 ml each time) for 5 h after which the concentration of the remaining NaOH solution was increased to 1 M. Another two solution samples were taken after 6.5 and 22.5 h. When Si amounts were too low for individual Si isotope analyses, samples of individual leach steps were combined (Supplementary Table 2-9). In experiments IIa and IIb, 12 splits of each 2.6 to 3.0 mg sediment of PS2070-1-493 (experiment IIa) and PS2089-2-639 (experiment IIb), respectively, were leached separately at room temperature in 25 ml 1.6 mm NaOH in separate pre-cleaned 50 ml PP tubes on a roller mixer. The supernatant solution of each individual tube was sampled after leach durations of 0.5, 1, 1.5, 2, 2.5, 3, 3.5, 4, 5, 6, 8 and 22.5 h and centrifugation. One sample for both experiments, IIa and IIb, was heated to 70°C for 24 h, where sediment was leached with 1.6 mm NaOH in a Teflon beaker on a hotplate. Solutions were prepared for analyses of Si and Al concentrations and for Si isotopes. Selected remaining sediments were recovered for SEM analyses (Supplementary Figure 2-1). Previous studies noted a degradation of the PP tubes by 5 mm NaOH and formation of a white gelatinous-seeming precipitate (Baah and Baah, 2002; Brzezinski and Nelson, 1995). We did not observe such precipitates during the entire leaching procedure.

2.2.2.2. Sample digestion and Si purification

Samples were prepared for Si isotope analyses using the method of Georg et al. (2006) with slight modifications. Approximately 15 mg of pulverized, homogenized sediment sample were digested for 15 min at 750°C in a muffle furnace by NaOH fusion (400 mg NaOH pellets, Merck, p.a. grade) in Ag-crucibles. After the dissolution of the fusion cake in Milli-Q water (>18 MΩ) and 1.5mM HCl (pH 1.5), the sample solution was diluted to <30 ppm SiO_2 and acidified to pH 1.5 with HCl. An aliquot of about 50 µg Si of this solution was loaded onto a column (DOWEX AG 50W-X8, 200–400 mesh) from which silicon was eluted with 5 ml Milli-Q water. Solutions sampled during leaching experiments were processed with the same procedure, but silicon amounts were as low as 5 µg in some samples. Samples were analyzed by ICP-OES (Varian 720-ES with an uncertainty of about 5%) before isotope analyses to check for column recovery which amounted to >92% Si in all cases, and for purity of the Si sample solution (>95% Si). The fusion/dissolution procedure blank contributed to <0.1% of total Si, and the blank of the Si column procedure was <50 ng Si. Element concentrations were determined on diluted sample aliquots after solid sample digestions (as described above) using an axial ICP-OES (Varian 720-ES). See Supplement S1.3 for details.

2.2.2.3. Solution MC-ICP-MS silicon isotope analyses

Isotope ratios were determined in medium or high resolution mode on a Thermo Neptune multi-collector inductively coupled plasma mass spectrometer (MC-ICP-MS) equipped with a Neptune Plus Jet Interface (using a Pfeiffer OnToolBooster interface pump; Jet sample and H skimmer cones, Apex desolvating

nebulizer). Details of the method are described in Supplement S1.1. We report the $^{29}Si/^{28}Si$ and $^{30}Si/^{28}Si$ isotope ratios in the delta notation as per mill deviation ($\delta \times 10^3$) from the international reference material NBS 28:

$$\delta^{(x/28)}Si = \left[\frac{\left(\frac{^{x}Si}{^{28}Si} \right)_{sample}}{\left(\frac{^{x}Si}{^{28}Si} \right)_{NBS28}} - 1 \right] \qquad \textbf{Equation 2-1}$$

where x denotes either ^{29}Si or ^{30}Si.

We report average $\delta^{30/28}Si$ values, abbreviated as $\delta^{30}Si$ obtained from 1 to 6 replicate measurements of the same analyte solution together with their 95% confidence interval (= $t \cdot SD/\sqrt{n}$), which indicates the instrument repeatability (Supplementary Table 2-1). Based on evaluation of accuracy and precision of the sample repeat measurements and comparison of results obtained on reference materials with published data compiled in Jochum et al. (2005; Supplementary Table 2-1, Supplementary Table 2-6), the uncertainty of the entire solution MC-ICP-MS method is estimated to be ± 0.07‰ (2SD) for $\delta^{29}Si$ and ± 0.10‰ (2SD) for $\delta^{30}Si$ (see Supplement for details). The same estimate was obtained by statistical evaluation according to equation 2 in Schoenberg and von Blanckenburg, (2005) based on repeat analyses of all samples analyzed in this study. This uncertainty is used for data interpretation in this study.

2.2.2.4. Femtosecond LA-MC-ICP-MS analyses

The micro-scale silicon isotope composition and Al/Si ratios were determined on three samples (PS2089-2-600P, Pleistocene; PS2070-1-472P, Pliocene and PS2070-1-472-bh, Pliocene) of porcellanite (opal-CT) by UV femtosecond laser ablation MC-ICP-MS (UV fs LA-MC-ICP-MS, Fem2) at GFZ Potsdam. Instrumentation and analytical conditions are described in Supplement S.1.2 and in Schuessler and von Blanckenburg, (2014). Laser ablation was performed along transects across porcellanite layers with a spatial resolution at each analysis location of about 100 ×100 µm surface area with less than 10 µm crater depth. We report results in the δ-notation as per mil deviation relative to NBS 28 together with the internal standard error of the mean (2SE at 95% confidence) of single sample measurements (Supplementary Table 2-3, Supplementary Table 2-4, Supplementary Table 2-5), which is typically <0.1‰ for $\delta^{30}Si$ as calculated by error propagation from measurements of one sample and the two bracketing NBS 28 standards. The uncertainty of the fs LA-MC-ICP-MS method (external long-term repeatability) is ± 0.15‰ (2SD) for $\delta^{29}Si$ and ± 0.23‰ (2SD) for $\delta^{30}Si$, respectively (Schuessler and von Blanckenburg, 2014). These uncertainties should be applied for geological interpretation and comparison to results obtained by other laboratories. In this study, accuracy was verified by repeat measurements on reference materials during each analytical session (Supplementary Table 2-7).

2.3. Results

2.3.1. Bulk sample Si isotope and Al/Si ratios

SiO_2 concentrations of siliceous sediment in the Pleistocene core range from 52 to 76 wt% and from 68 to 76 wt% in the Pliocene core. Porcellanites contain 87 to 92 wt% SiO_2. Other major element concentrations of bulk sediment samples are reported in Supplementary Table 2-5. and comprise mainly Al, Fe, Mg and Ca. In the vicinity of the porcellanite layers, the concentration of all measured cations is lower than in the surrounding sediments. Al/Si ratios are shown as indicator for detrital minerals and are low in porcellanite layers and adjacent siliceous sediment layers (Figure 2-3).

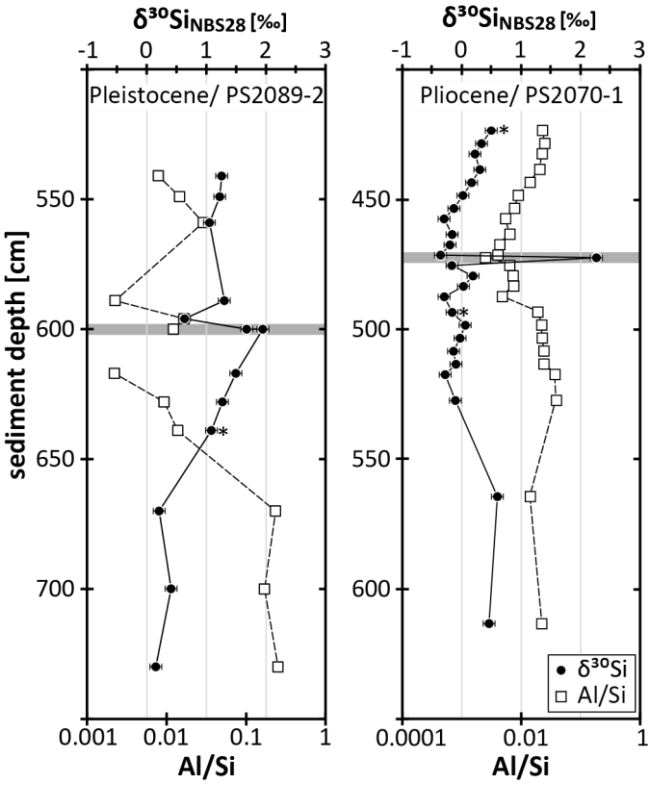

Figure 2-3: Bulk sediment $\delta^{30}Si$ (solid circles) and Al/Si mass ratios (open squares) in Pleistocene (PS2089-2) and Pliocene (PS2070-1) siliceous sediments and porcellanite (indicated by horizontal gray bar). Error bars on $\delta^{30}Si$ represent uncertainty of the solution MC-ICP-MS method (± 0.10‰, 2SD). Uncertainties on Al/Si mass ratios are smaller than the symbol size. See Supplementary Table 2-1 and Supplementary Table 2-5 for data. Samples used in leaching experiments (Figure 2-4, Supplementary Table 2-8, and Supplementary Table 2-9) are indicated by ∗.

In samples from the Pleistocene core between 730 and 541 cm sediment depth, bulk sediment $\delta^{30}Si$ ranges from 0.16 to 1.50‰. The dense part of the porcellanite (sublayer 2, Figure 2-2a) has a bulk $\delta^{30}Si$ of 1.96‰ (n= 3; Supplementary Table 2-1, Figure 2-3). In the more porous part (sublayer 1, Figure 2-2a) $\delta^{30}Si$ is at 1.69‰. In the Pliocene core bulk sediment samples from depths between 613 and 423 cm range between -0.34 and 0.61‰. The bulk analysis of the Pliocene porcellanite layer (PS2070-1-472P) yielded $\delta^{30}Si$ of 2.28‰.

2.3.2. Results from leaching experiments

We describe the results of the leaching experiments as measured in the supernatant solutions after separation from the remaining solutions. The silicon concentrations obtained in experiment I (PS2070-1-423) show that the fraction of Si dissolved during the extractions increased from ca. 0.6 to 68% of the total initial solids Si with increasing run duration (Figure 2-4). The $\delta^{30}Si$ values and Al/Si ratios in the solutions are generally higher than the bulk sediment, with the exception of two samples that were extracted after switching from 1.6 mm to 1M NaOH. In experiment IIa (PS2070-1-493) 1.5 to 43 wt% of the total silicon was

dissolved. Solutions yielded δ^{30}Si values from 0.55 to 1.08‰, which is considerably heavier than the bulk sediment (-0.15‰). Al/Si ratios are systematically higher than that of the bulk sediment.

In experiment IIb (PS2089-2-639; Pleistocene) between ca. 1.4 and 27 wt% of the initial solid silicon was dissolved. In contrast to the other experiments, the solutions' δ^{30}Si evolved from 0.28 to 1.00‰ and is thus systematically lower than the bulk sediment sample (1.09‰). As in leaching experiments I and IIa, Al/Si ratios in the solutions sampled in 1.6 mm NaOH are higher than Al/Si in the bulk sediment.

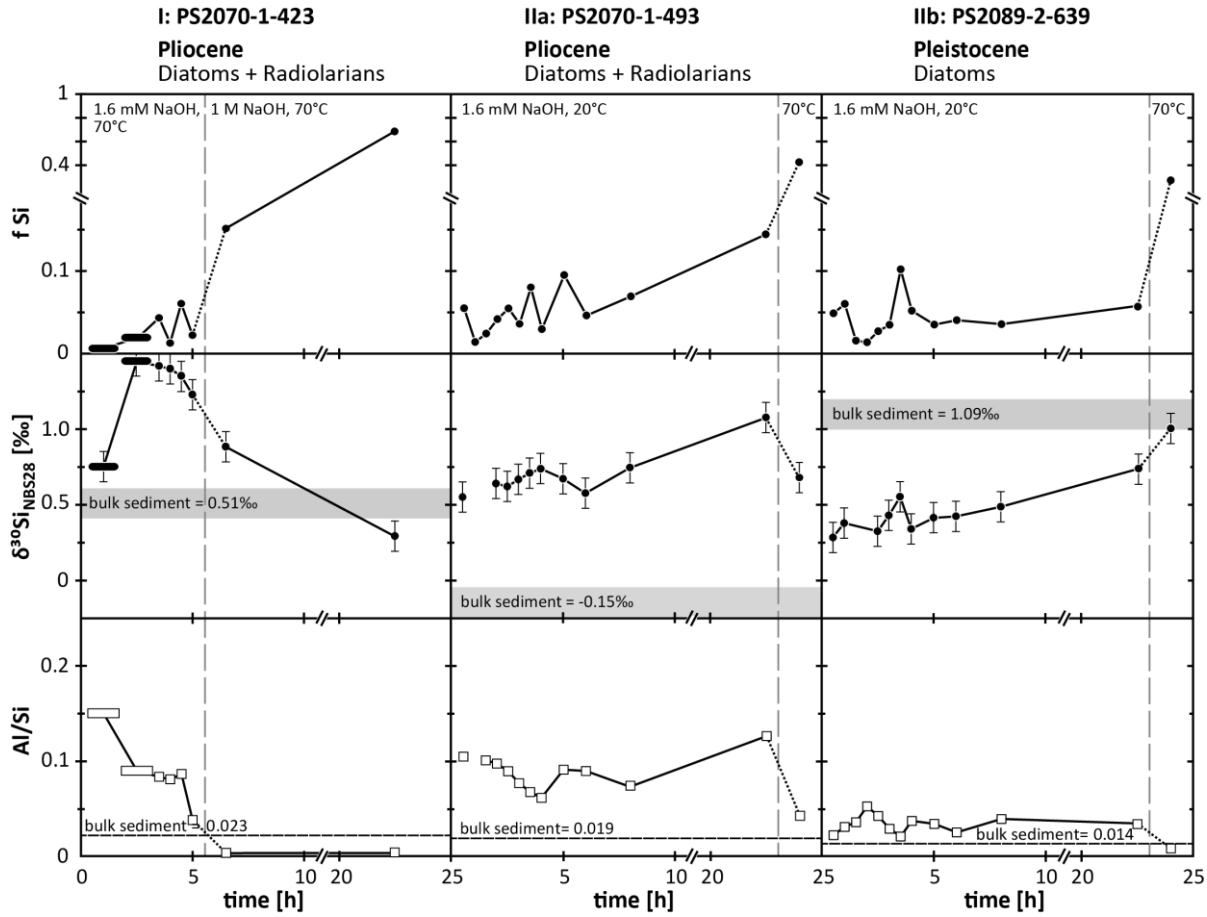

Figure 2-4: Results from leaching experiments showing relative amounts of dissolved silicon, expressed as fraction Si dissolved relative to the total Si in the sediment (f Si), δ^{30}Si of dissolved Si and Al/Si mass ratios in leachates for both experiments I (sequential extractions) and IIa +IIb (batch extractions). Samples PS2070-1-423 and 493 (Pliocene) contain mostly diatoms and radiolarians and PS2089-2-639 (Pleistocene) contains mostly diatoms. Error bars on δ^{30}Sirepresent uncertainty of the solution MC-ICP-MS method (± 0.10, 2SD). Horizontal gray lines indicate the bulk sediment Al/Si mass ratio and δ^{30}Si. Vertical dashed lines indicate the time at which experimental conditions were switched with respect to NaOH molarity or temperature.

Common to all leaching experiments is that Si in the first sampled solutions is lower in δ^{30}Si than that sampled at a later point in time (Figure 2-4). This observation is made regardless of whether the sediment samples are comprised of both diatoms and radiolarians (experiments I and IIa) or mainly diatoms (experiment IIb). These first solutions are also characterized by Al/Si ratios greater than that of their respective bulk sediment, suggesting that aluminum silicates are dominating the first leaching steps. This observation is supported by

SEM analyses and EDS spectra reported in Rickert et al. (2002) and Michalopoulos et al. (2000), who report aluminum silicate formation on diatom opal. SEM images (Supplementary Figure 2-1) of PS2070-1-493 show that radiolarians are dominating the residual sediment after leaching experiment I. Therefore radiolarians are less soluble and appear to contain Si that is lower in δ^{30}Si than di- atoms as indicated by higher δ^{30}Si in experiment IIa. Low δ^{30}Si and high Al/Si ratios in experiment IIb (mostly diatoms) reveal that the first dissolving components are aluminum silicates that have likely formed from early diagenetic solutions. Only when a high mass fraction of the sediment (here 27 wt%) is dissolved, the δ^{30}Si of the leachate approaches that of the bulk sediment, which is mainly comprised of diatoms. Consequently, diatoms and covering early diagenetic aluminum silicates preferentially dissolved in all leaching experiments. Owing to the dominance of diatoms, the Pleistocene sample (PS2089-2-639) reveals no apparent differences in its composition following the treatment (Supplementary Figure 2-1).

2.3.3. Results from micro-scale Si isotope analyses

δ^{30}Si from micro-scale Si isotope analyses are in good agreement with those from bulk analyses by solution ICP-MS. Analyses of silicon isotope ratios and the Al concentration on a thin section across porcellanite sample PS2089-2-600P (Pleistocene) yielded δ^{30}Si between 1.21 and 2.07‰ and Al concentrations from 447 to 3843 ppm (Supplementary Table 2-2). Opposing trends of Al/Si and δ^{30}Si characterize this porcellanite layer. A pronounced drop in δ^{30}Si matches increased Al concentrations and occurs at the interface of two distinct sublayers (Figure 2-5a and Figure 2-2a).

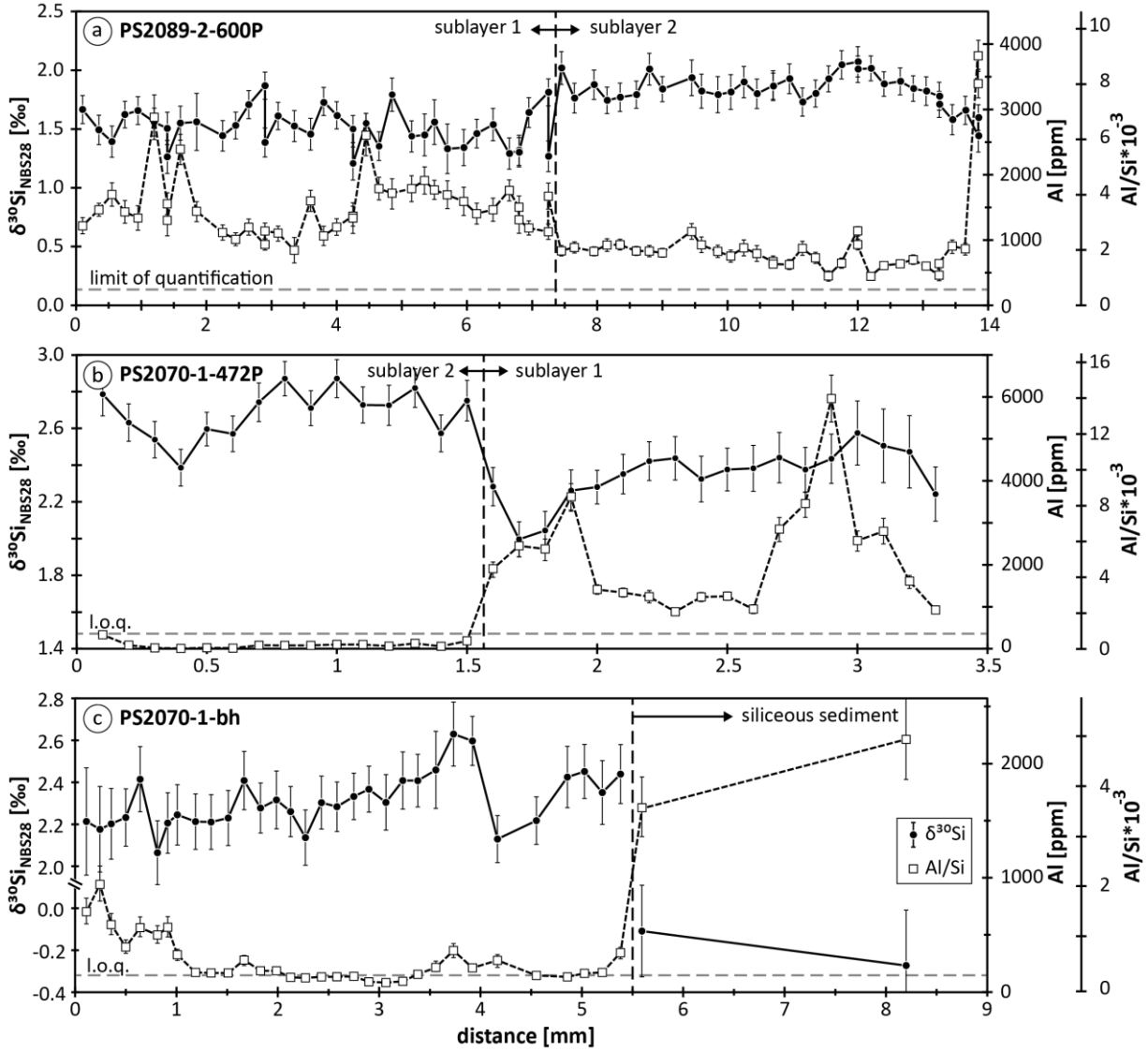

Figure 2-5: Micro-scale silicon isotope ratios (black circles), Al/Si mass ratios and derived Al concentrations [ppm] (open squares) on transects across porcellanite layers by femtosecond laser ablation MC-ICP-MS analysis from (a) Pleistocene (PS2089-2-600P; Supplementary Table 2-2), and (b) Pliocene (PS2070-1-472P; Supplementary Table 2-3) porcellanite layers as well as (c) the opal-CT filled animal burrow (PS2070-1-472-bh; Supplementary Table 2-4). The vertical dashed line delineates sublayers of the porcellanite (a, b; cf. Figure 2-2) and the contact to the surrounding siliceous sediment (c). The horizontal dashed line represents the lower limit of quantification for Al concentration measurements. Error bars represent the internal standard error of mean values (2SE for n ≈80 integrations at 1s).

In PS2070-1-472P $\delta^{30}Si$ ranges from 2.12 to 2.95‰ and Al concentrations vary between 878 and 5931 ppm where for some analyses Al concentrations were below limits of quantification (<350 ppm) (Supplementary Table 2-3). At the interface of two distinct sublayers there is a significant increase in Al concentrations which coincides with a drop in $\delta^{30}Si$ (Figure 2-5b and Figure 2-2b). We regard the sections in which $\delta^{30}Si$ and Al/Si correlate to denote simultaneous precipitation of opal-CT and authigenic Al-silicates. Layers featuring Al concentrations >2000 ppm and no correlation of $\delta^{30}Si$ and Al/Si are possibly due to the presence of Al-bearing phases.

Within an opal-CT filled, tube-shaped animal burrow (PS2070-1-472-bh) δ^{30}Si ranges from 2.06 to 2.63‰ (Supplementary Table 2-4). Al concentrations range between 145 and 910 ppm, where for some analyses Al concentrations were below limits of quantification (<130 ppm) and are elevated towards the rims, where also δ^{30}Si values are lower (Figure 2-5c). Two analyses of adjacent siliceous sediments yield δ^{30}Si of -0.11 and -0.27‰ and Al concentrations of 1580 and 2181 ppm. Micro-scale Si isotope analyses show an internal variability of less than 0.3‰ in δ^{30}Si within porcellanite layers of both cores and reveal a systematic negative correlation of Al concentrations with the isotope composition of silicon.

2.4. Discussion

2.4.1. Processes setting the Si isotope ratios and Al/Si in early diagenetic porcellanite

The unique features of our studied cores are 1) that they contain some of the youngest porcellanites found to date, 2) that these porcellanites are isotopically heavier than the bulk surrounding sediments, and 3) that δ^{30}Si in porcellanite increases with decreasing Al/Si (Figure 2-6). Unraveling the processes underlying these observations are key to understanding the behavior of Si isotopes during diagenesis in general.

Regarding 1), early diagenetic porcellanite is rare and forms apparently exclusively in very pure siliceous oozes (Bohrmann et al., 1994; Murata and Nakata, 1974). It forms from solutions in which the SiO_2 concentrations exceed ca. 25 ppm, i.e., the solubility of cristobalite at 20°C (Walther and Helgeson, 1977) which is the estimated minimum equilibrium solubility of opal-CT (Williams et al., 1985). This condition is rarely found in siliceous deep-sea sediments that typically contain significant abundances of detrital minerals. The presence of detrital minerals reduces the pore water Si concentrations that will therefore remain below the opal-CT equilibrium solubility.

Finding 2), the enrichment of ^{30}Si in porcellanite, can be explained in different ways: (i) isotope fractionation partitioning preferentially heavy Si isotopes into solution during incipient stages of dissolution of opal-A particles; (ii) heavy isotopes are enriched in opal-CT during precipitation (α >1); (iii) the solubilized component from sediment comprising multiple components with different solubilities and isotope compositions is isotopically heavy; (iv) light silicon isotopes are removed from solution by precipitation prior to precipitation of opal-CT.

With respect to explanation (i), isotope fractionation during dissolution of biogenic silica particles, only the preferential release of light isotopes due to kinetic isotope fractionation was reported for basalt and phytoliths (Ziegler et al., 2005), pedogenic clay minerals (Cornelis et al., 2014), and diatoms (Demarest et al., 2009). However, Wetzel et al., (2014) showed the absence of Si isotope fractionation during dissolution of diatom silica. Our leaching experiment IIb supports their observation. Even though release of light Si isotopes is observed in the early phase of dissolution, we interpret the preferential release of light Si to show the light

Si isotope composition of the first dissolving aluminum silicates. (ii) Enrichment of heavy isotopes ($\alpha > 1$) during silica precipitation in low temperature environments has not been observed to date and is thus considered unlikely. Rather, secondary silica precipitation typically enriches the solid in ^{28}Si (Basile-Doelsch et al., 2005; Cornelis et al., 2014; Geilert et al., 2014a; Roerdink et al., 2015; Ziegler et al., 2005) where isotope fractionation during precipitation depends on the net solid formation rate and can also occur with $\alpha = 1$ (e.g., Oelze et al., 2015, 2014). We therefore regard (iii) preferential dissolution of isotopically distinct sediment components as a first likely explanation. In siliceous sediment that comprises both radiolarians and diatoms, diatoms are expected to dissolve at higher rates. This expectation is indicated from relative enrichment of radiolarians over diatoms in sediment traps and on the seafloor (Abelmann and Gersonde, 1991). Also, the $\delta^{30}Si$ of radiolarians is considerably lower than that of diatoms as demonstrated by Egan et al. (2012). This is for two main reasons: 1) The fractionation factor of silicon isotopes is biologically controlled and varies between different Si-secreting organisms. For example, $\varepsilon^{30}Si_{diatom\text{-}water}$ is species dependent and varies between -0.5 and -2.1 (Sutton et al., 2013). 2) Diatoms exclusively dwell in the photic zone where intensive silicon utilization induces high surface water $\delta^{30}Si$. In contrast, radiolarians dwell at all water depths and thus take up silicon from water masses that are enriched in light silicon isotopes relative to surface waters through the dissolution of sinking biogenic silica (Ehlert et al., 2012; Reynolds et al., 2006). Consequently, diatoms will commonly be heavier in $\delta^{30}Si$ than radiolarians. Our leaching experiments support this prediction. The Pliocene piston core shows increased modal abundances of radiolarians after the leaching experiment (Supplementary Figure 2-1), suggesting that diatoms are more soluble than radiolarians. The decrease in the solutions' $\delta^{30}Si$ in the later stages of the leaching sequence (Figure 2-4, experiments I, IIa) is due to the increasing proportion from silicon of dissolving radiolarians, suggesting that diatoms are enriched in ^{30}Si relative to radiolarians.

Explanation (iv), the initial removal of light silicon isotopes by precipitation of aluminum silicates enriched in light Si isotopes that shifts the pore water $\delta^{30}Si$ to higher values, is the second likely cause for the isotopically heavy Si in porcellanite. The latter explanation also explains finding 3), that $\delta^{30}Si$ in porcellanite increases with decreasing Al/Si (Figure 2-6). We note that during simultaneous sedimentation and early diagenesis these processes will not proceed in a steady manner: they will shift with changing composition of the deposited sediment, and hence with sediment depth and time. We proceed to explore the evolution of pore water in a simple box model (Figure 2-7) to scrutinize whether the measured $\delta^{30}Si$ vs. Al/Si trend in porcellanite layers follows vectors in $\delta^{30}Si$ vs. Al/Si space predicted by a mass balance model.

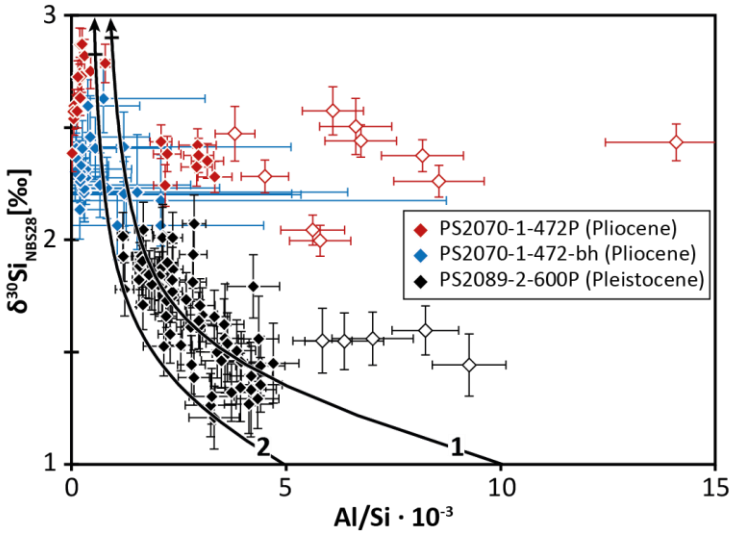

Figure 2-6: The shift of porcellanite $\delta^{30}Si$ with Al/Si mass ratio (solid symbols). Open symbols represent outliers in which laser ablation analyses were likely affected by the presence of detrital Al-rich phases contained within porcellanite (see Section 3.3). The overall negative trend is suggested to present pore water evolution driven by ongoing precipitation of aluminum silicates enriched in isotopically light Si that shifts the residual pore water towards higher δ^{30}Sivalues. Two trends of pore water evolution were modeled based on Equation 2-2 and Equation 2-3 and the assumptions reported in section 2.4.2.

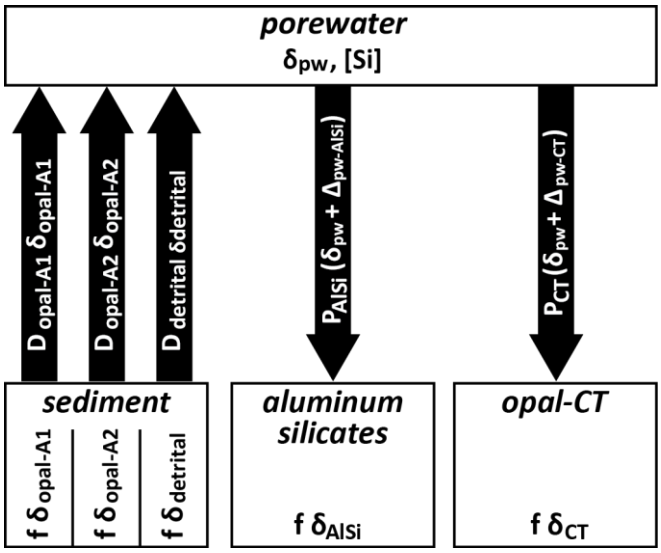

Figure 2-7: Simple box model showing the principal components involved in early diagenesis of silica. The relative mass fraction of each component is *f*, their isotope composition δ. Dissolution fluxes are represented by *D*, precipitation fluxes by *P*. Δ are the Si isotope fractionation factors for silica precipitation. [Si] is the silicon concentration in pore water. In the present case opal-A1 and opal-A2 are represented by diatoms and radiolarians, respectively. Equation 2-2 describes this box model.

2.4.2. Si mass fluxes and isotope fractionation during early diagenesis

The mass fluxes and associated Si isotope fractionation when pore waters exchange with sedimentary compartments during selective opal dissolution, and simultaneous aluminum silicate- and opal-CT

precipitation during early diagenesis are shown in Figure 2-7. The pore water mass balance can be quantified by a differential equation that describes the change in the mass of dissolved pore water Si and its isotope composition:

$$\frac{d}{dt}(M_{pw}\delta_{pw}) = D_{opal-A1}\,\delta_{opalA1} + D_{opal-A2}\,\delta_{opalA2} + D_{detrital}\,\delta_{detrital} - P_{AlSi}\,(\delta_{pw} + \Delta_{pw-AlSi}) - P_{CT}\,(\delta_{pw} + \Delta_{pw-CT}) \quad \textbf{Equation 2-2}$$

where M_{pw}[mass] is the mass of dissolved silicon in pore water (pw) and δ_{pw} [‰] its isotope composition; $D_{opal\text{-}A1}$ [mass/time] is the dissolution flux of opal-A component 1 with an isotope composition $\delta_{opal\text{-}A1}$ [‰]; D_{opalA2}[mass/time], $\delta_{opal\text{-}A2}$ [‰] and $D_{detrital}$ [mass/time], $\delta_{detrital}$ [‰] are the dissolution fluxes and isotope compositions of opal-A component 2 and detrital minerals, respectively; P_{AlSi} [mass/time] is the precipitation flux between pore water and precipitated aluminum silicates; $\Delta^{30}Si_{AlSi\text{-}pw}$ [‰] the isotope fractionation factor between pore water and aluminum silicates; P_{CT} [mass/time] is the precipitation flux from pore water into opal-CT; and $\Delta^{30}Si_{CT\text{-}pw}$ [‰] is the isotope fractionation factor between pore water and opal-CT. Aluminum silicate precipitation from pore water will shift its Al/Si ratio. Equation 2-2 can be recast accordingly for Al/Si ratios:

$$\frac{d}{dt}\left(M_{pw}\frac{Al}{Si_{pw}}\right) = D_{opal-A1}\left(\frac{Al}{Si}\right)_{opal-A1} + D_{opal-A2}\,(Al/Si)_{opal-A2} + D_{detrital}\,(Al/Si)_{detrital} - P_{AlSi}\left((Al/Si)_{pw}\cdot K_{pw/AlSi}\right) - P_{CT}\left((Al/Si)_{pw}\cdot K_{pw/CT}\right)\Big) \quad \textbf{Equation 2-3}$$

where $K_{pw/AlSi}$ and $K_{pw/CT}$ [(mass/mass)/(mass/mass)] are elemental fractionation factors for aluminum silicate and opal-CT precipitation from pore water, respectively. The time dependence in both equations arises through continuous sedimentation over depth *z*, where *dt*= (*dz*/sedimentation rate). We assign fractional dissolution fluxes to the different source components. We model the approach to steady state by first-order rate constants describing P_{AlSi} and P_{CT} as a function of the pore solutions' inventories.

We model two scenarios where 1) represents possible conditions for the Pleistocene porcellanite (PS2089-2) and 2) for Pliocene porcellanite (PS2070-1). For 1) we assume almost exclusive diatom dissolution ($D_{opal\text{-}A1}$contributes 99.5%) because this sediment is comprised almost entirely of diatoms. Their isotope composition we constrain from bulk sediment to be δ^{30}Si= 1.5‰ (Section 3.2). The detrital mineral dissolution flux $D_{detrital}$ was assumed to contribute 0.5% and was assigned δ^{30}Si= -0.5‰ as commonly measured in clay. For 2) we assume dominant diatom dissolution with $D_{opal\text{-}A1}$contributing 89% with δ^{30}Si= 1.7‰, as estimated from leaching experiments (Section 3.2). Detrital mineral dissolution was assumed to contribute 1% with δ^{30}Si= -0.5‰. Because the Pliocene core also features radiolarians we assume that these contribute a flux

$D_{opal\text{-}A2}$ of 10%. Their $\delta^{30}Si$ must be negative as shown by leaching experiments (Section 3.2); here we use $\delta^{30}Si$= -1‰. For simplicity, in both scenarios we assume $(Al/Si)_{opalA1}$= 0, $(Al/Si)_{opalA2}$= 0, $(Al/Si)_{detrital}$= 0.5, which is typical for clays. We assume that opal-CT precipitation has a negligible leverage to shift pore water Al/Si ratio which is governed to a large extent by $D_{detrital}$ and P_{AlSi}; hence we set P_{CT} to be zero. A test of this assumption is possible if the sequence of precipitation of opal-CT can be reconstructed. Fortunately, such a sequence is preserved in the form of an opal-CT filled burrow (Figure 2-2c), which reveals elevated Al-concentrations at the upper rim (where precipitation occurred first) and virtually Al-free opal-CT in its center. This finding indicates that opal-CT precipitation did not affect the opal-CT Al/Si because the ratio would otherwise increase during precipitation, i.e., towards the center of the burrow. Thus, silicon is precipitated in preference to aluminum and we therefore assume that $(Al/Si)_{pw}$ is changing only by the precipitation of aluminum silicates.

The silicon isotope fractionation factor $\Delta_{pw\text{-}AlSi}$ is assumed in both scenarios to be = -2‰, in agreement with estimates from Oelze et al. (2015, 2014). We assume the initial pore water compositions to represent those of deep seawater (i.e., $\delta^{30}Si$= 1‰, $[SiO_2]$= 2.2ppm; De La Rocha et al., 2000). We estimate $K_{pw/AlSi}$ from the highest $(Al/Si)_{CT}$ measured in porcellanite which are 0.005 (scenario 2) and 0.01 (scenario 1) and measured $(Al/Si)_{pw}$ in pore water of Southern Ocean cores which is between ca. 0.00015 and 0.0015 (van Beusekom et al., 1997). For the two scenarios specific $K_{pw/Al}$ were found by fitting to be 4 and 10 for the two scenarios. We note that while we model pore water $\delta^{30}Si$ and Al/Si, our data is obtained on porcellanite (Figure 2-6). Our porcellanites' temporal evolution nevertheless records pore water $\delta^{30}Si$ because during pure opal-CT precipitation $\Delta_{pw\text{-}CT}$ is likely zero (Oelze et al., 2015; Roerdink et al., 2015). As the initial $(Al/Si)_{pw}$ is not known we evaluate relative trends in $(Al/Si)_{CT}$ instead, and assume that these reflect relative trends in $(Al/Si)_{pw}$.

The dominant processes that control pore water $\delta^{30}Si$ and hence $\delta^{30}Si$ of opal-CT are selective dissolution of isotopically heavy diatom silica and ongoing precipitation of isotopically light aluminum silicates. Trends explored by the model are compatible with the microscale $\delta^{30}Si$ and Al/Si record (Figure 2-5 and Figure 2-6) where within porcellanite layers, the Si isotope composition co-varies with Al/Si ratios (Figure 2-6).

2.4.3. How early diagenetic opal-CT forms

Whether early diagenetic opal-CT can form is dominantly controlled by the detritus content of siliceous sediments. The detritus content determines early diagenetic reactions that control the equilibrium solubility of the bulk sediment (Dixit et al., 2001). Detritus-poor sediments can be formed under conditions of high opal sedimentation rates (e.g., diatom blooms) (Ragueneau et al., 2000) that dilute simultaneously deposited detritus. Upon shallow burial, the dissolution of opal-A in silicon-undersaturated pore water successively

increases the pore water silicon concentration until the asymptotic pore water concentration is attained (Figure 2-8a). Depending on the detrital content, the solubility of opal-CT will be exceeded (Figure 2-8a, c) and early diagenetic opal-CT will begin to form a few centimeters beneath the sea floor. Over the same depth interval, leachable detrital minerals partially dissolve and authigenic aluminum silicate minerals will form as suggested by pore water Al/Si (Figure 2-8b).

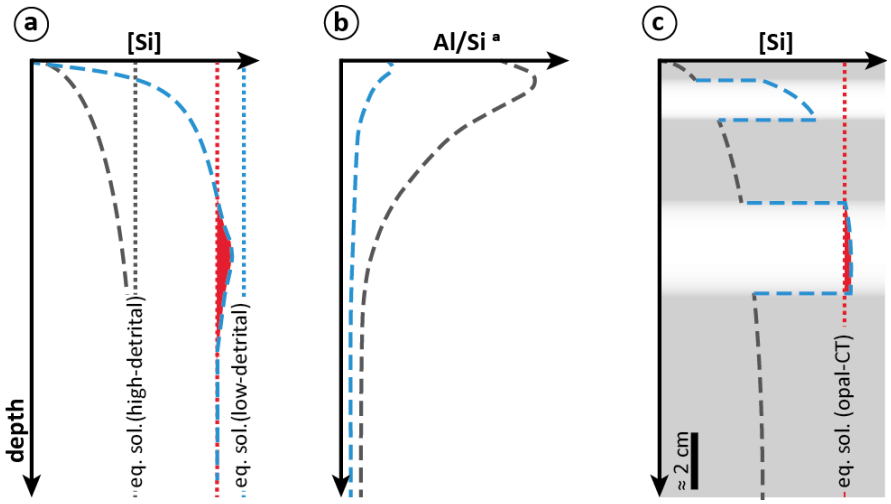

Figure 2-8: Conceptual model of early diagenetic porcellanite formation in siliceous sediment. Shown are (a) pore water silicon concentration depth profiles for high-detrital (gray) and low-detrital (blue) siliceous sediment. Their corresponding Si equilibrium solubilities are shown with dotted lines in the same color. The equilibrium solubility of opal-CT is shown as a red dotted line and sites of opal-CT precipitation are shown as a red shade. (b) Pore water Al/Si ratio depth profiles (simplified after Van Cappellen and Qiu, 1997a) for high-detrital (gray) and low-detrital (blue) sediment; (c) a schematic stack of siliceous sediment with variable detritus-contents (gray: high, white: low) and the corresponding pore water silicon concentrations. Early diagenetic opal-CT formation occurs in sections with low detritus-contents.

2.5. Implications for the use of sedimentary Si isotope records in the reconstructions of past biogeochemical cycles

Finally, we use the processes derived above to draw conclusions on the preservation potential of the sedimentary silicon isotope record in chert. The best preservation is attained if the bulk chert δ^{30}Si will reflect that of the original δ^{30}Si of the sediment once deposited. The preservation potential depends on a) depositional conditions including the Si concentration in sea water, the sedimentation rate, and the detrital mineral content, as well as on b) properties of the deposited silica including the number of sedimentary silica components, their isotopic difference, and their difference in susceptibility to dissolution.

2.5.1. Bulk sediment δ^{30}Si modification during early silica diagenesis

The strongest control on the preservation of the original δ^{30}Si in bulk chert appears to be the sea water silicon concentration. Sea water Si concentrations decreased over the Phanerozoic through the ecological success

of radiolarians and sponges in the Paleozoic and diatoms in the Jurassic (Kidder and Erwin, 2001). We therefore expect that the potential to preserve the original $\delta^{30}Si$ in bulk chert decreases through geological time, and with it, the record of past biogeochemical cycles.

Chert that formed from sediment deposited in environments with low dissolved Si concentrations will commonly not record the original bulk sediment $\delta^{30}Si$ because of effective recycling of predominantly labile silica to sea water. Exceptions are conditions where 1) only one silica component was present at sedimentation, 2) the difference in isotope composition between components was negligible, 3) the difference in dissolution susceptibility is negligible, and 4) the fraction of soluble silica is low. Therefore, most Mesozoic and Cenozoic chert that formed from siliceous sediment with more than one silica component and with different isotope compositions and susceptibility to dissolution (most commonly radiolarians and diatoms) will have a bulk $\delta^{30}Si$ value that is shifted towards the $\delta^{30}Si$ of the less soluble component (Figure 2-9a). Chert that formed from only one opal component, such as pure diatom ooze, is expected to have shifted only minimally from the sedimentary bulk $\delta^{30}Si$.

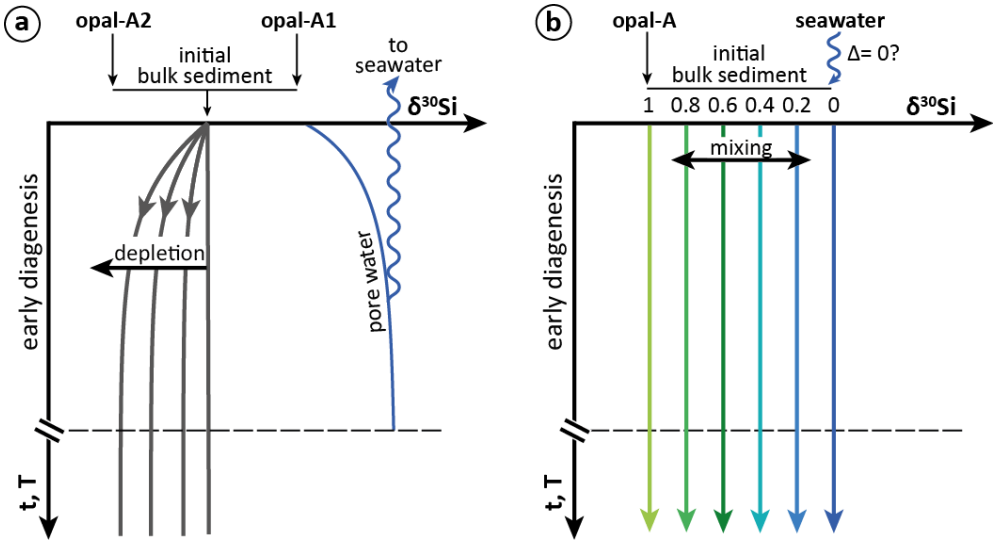

Figure 2-9: Conceptual presentation of the diagenetic change in Si isotope composition of siliceous sediment under conditions of Si-poor seawater like in the modern ocean (a) and Si-rich seawater like in the Precambrian ocean (b). (a) Sediment consists of two opal components that differ in $\delta^{30}Si$. Pore water is isotopically heavy because the isotopically heavy component (opal-A1) dissolves preferentially and be-cause aluminum silicates enriched in light Si isotopes precipitate. This pore water escapes to seawater. The bulk sediment is depleted in the more soluble component (opal-A1) to a degree that depends on initial mixing proportions of opal-A1 and opal-A2 and their difference in dissolution intensity. No further selective Si isotope loss is expected to occur after early diagenesis (shown beneath the dashed line). (b) Under conditions of high Si concentrations in seawater, the bulk sediment $\delta^{30}Si$ will represent a mixture of sedimentary opal-A components that are not selectively dissolved as in scenario (a) due to the high dissolved Si concentrations. During early diagenesis Si precipitated from seawater is added to the opal (the final relative proportions of which are shown by the numbers). The isotope composition of the resulting mixture is preserved during both early and late diagenesis.

Early diagenetic dissolution of silica is inhibited by high dissolved Si. Chert that formed from siliceous sediment deposited in environments characterized by high dissolved Si concentrations have a high potential to preserve the original $\delta^{30}Si$ (Figure 2-9b). Precambrian cherts likely preserve the original $\delta^{30}Si$ because sedimentation occurred when sea water was still Si-rich. For example the isotopic fingerprint of the earliest forms of biogenic silica, i.e,. that in radiolarians and sponges, is likely preserved in Neoproterozoic to Paleozoic chert.

2.5.2. Late diagenetic modification of bulk chert $\delta^{30}Si$ during phase transformation

Siliceous sediments will be subject to conversion to opal-CT through increasing temperature during sediment burial. Sedimentary layers will convert to chert at different times and depth that depend on the detrital mineral contents (Isaacs, 1982). We suggest that independently of the timing of opal-CT formation, opal-CT likely carries the $\delta^{30}Si$ of the pore water at the moment of supersaturation. Early diagenetically formed opal-CT (from pure siliceous sediment) will record the pore water composition of the most soluble silica whereas later formed opal-CT (from less pure siliceous sediment) will record the isotope composition of less soluble silica that did not dissolve during early diagenesis. Pore water will be locally mobile and hence affect the micro-scale silicon isotope composition. However, on the bulk sediment scale, chemically distinct layers of opal will transform in isolation from each other, precluding isotopic exchange between layers and leaving the bulk (post-early diagenesis) silicon isotope composition likely unaffected. While the oxygen isotope composition of opal-CT and chert is equilibrated at ambient temperatures where dissolution–reprecipitation occurs (Murata et al., 1977), the silicon isotope composition is predicted to be insensitive against isotopic overprinting by such diagenetic fluids because Si concentrations in solution are comparably low. The same considerations hold for the conversion from opal-CT to quartz.

2.6. Conclusions

Porcellanite layers (made of opal-CT) that form during early diagenesis of siliceous sediment record the Si isotope composition of pore water from which they form. In Si-poor seawater, two fundamental processes affect the isotope composition of both the pore water and the residual siliceous sediment: (i) selective dissolution of (isotopically distinct) sedimentary biogenic silica and (ii) precipitation of authigenic aluminum silicates enriched in light Si isotopes. A corollary is that the pore water isotope composition first is not identical to the bulk sediment (and thus differs from that of opal-CT) and second changes with time during early diagenesis at an extent that is determined by a) the silicon concentration in sea water, b) the sedimentation rate (because it controls the residence time of sediment in the zone of Si undersaturation), and c) the detrital mineral content (because it controls the equilibrium solubility). Sign and magnitude of the offset between bulk sediment $\delta^{30}Si$ and pore water $\delta^{30}Si$ is furthermore controlled by properties of the

deposited opal including d) the number of isotopically different sedimentary opal components, e) their difference in solubility, and f) their relative mass fractions. We infer that opal-CT formed from siliceous sediment deposited in environments with high Si concentrations (such as the Precambrian ocean) will faithfully record paleo-environmental conditions because dissolution is suppressed by high Si levels. We predict that the Si isotope record of opal-CT – regardless of the degree of modification by early silica diagenesis – will be preserved during the late diagenetic conversion to quartz chert.

2.7. Acknowledgements

The first author is grateful for funding provided by the DFG through FOR736 “The Precambrian–Cambrian Ecosphere (R)evolution: Insights from Chinese microcontinents” (grant no. BL 562/11-2). We greatly appreciate the support from scientists and technicians of the Alfred-Wegener-Institut, Helmholtz-Zentrum für Polar-und Meeresforschung during the sampling of the cores in the AWI core repository. We thank J. Evers for supporting SEM analyses. Comments by G.F. de Souza, two anonymous reviewers and AE G. Henderson were highly appreciated and helped to improve the clarity of the manuscript.

2.8. Supplementary information

The supplementary information includes detailed descriptions of analytical conditions (SI 1), Si isotope data of samples and reference materials (SI 2).

2.8.1. Analytical Methods (SI 1)

2.8.1.1. Solution MC-ICP-MS silicon isotope analyses (SI 1.1)

Isotope ratios were determined in either medium or high resolution mode on a Thermo Neptune multi-collector inductively coupled plasma mass spectrometer (MC-ICP-MS) equipped with a Neptune Plus Jet Interface (using a Pfeiffer OnToolBooster interface pump; Jet sample and H skimmer cones). Samples and standards were diluted in 0.1 M HCl to between 0.35 and 0.7 ppm Si. In order to correct for mass bias drift, Mg (Alfa Aesar Specpure 14430) was added and adjusted to match Si concentrations. The solutions were aspirated by a PFA nebulizer with uptake rates of 80 to 120 µL/min and introduced into an ESI APEX desolvator. Silicon isotope signals ($^{28}Si^{+}$, $^{29}Si^{+}$, $^{30}Si^{+}$) were measured simultaneously on the interference-free low mass side of the peak for 30 cycles, alternating between Si isotopes and Mg isotopes in dynamic mode (with idle time of 3 s between magnet jumps) with an integration time of 4 s for each cycle. These conditions yielded sample signal intensities of 15 to 20 V for ^{28}Si at resolution of 3700 to 7700 (mass resolving power $\Delta m/m$) on a Faraday cup (10^{11} Ω) and 32-42 V for ^{24}Mg. Background intensities (typically 15 to 30 mV ^{28}Si) were measured on-peak in 0.1 M HCl containing Mg at a concentration matched to the samples and were subtracted from sample Si signal intensities. Temporal changes in instrumental mass bias on Si isotope ratios were corrected by $^{25}Mg/^{24}Mg$ drift correction employing the exponential mass bias law (Cardinal et al., 2003) and subsequent mass bias correction by sample-standard bracketing using concentration-matched NBS 28 as measurement standard. Measured isotope ratios were rejected when the mass bias drift, i.e., the change in the isotope ratio between two bracketing NBS 28 measurement, exceeded 0.2‰ in $^{30}Si/^{28}Si$ or $^{29}Si/^{28}Si$. In every measurement session, the Si isotope composition of several reference materials including BHVO-2, Diatomite, IRMM-017, and BigBatch was determined to evaluate precision and accuracy (The quantification limits were determined taking sample dilution factors and lowest concentration of the calibration standards into account.

Supplementary Table 2-6). We report isotope ratios as per mill deviation ($\delta \cdot 10^3$) from the international reference material NBS 28 in the delta notation:

$$\delta^{(x/28)}Si = \left[\frac{\left(\frac{xSi}{28Si}\right)_{sample}}{\left(\frac{xSi}{28Si}\right)_{NBS28}} - 1 \right]$$

Supplementary Equation 2-1

where x denotes either ^{29}Si or ^{30}Si.

We report average δ-values obtained from 1 to 6 replicate measurements of the same analyte solution together with their 95% confidence interval (= t·SD/√n), which indicates the instrument repeatability (Supplementary Table 2-1). However, the uncertainty associated with the reported Si isotope results also contains uncertainty contributions from sample preparation, dissolution, column separation, and MC-ICP-MS analyses, which was evaluated as follows. In every measurement session, the Si isotope composition of several reference materials including BHVO-2, Diatomite, IRMM-017, and BigBatch was determined (Supplementary Table 2-7). The δ-values and their 95%CI are 0.64 ± 0.01‰ δ^{29}Si, 1.24 ± 0.02‰ δ^{30}Si for Diatomite (n= 13); -0.68 ± 0.02‰ δ^{29}Si, -1.34 ± 0.03‰ δ^{30}Si for IRMM-017 (n= 14); -5.45 ± 0.01‰ δ^{29}Si, -10.69 ± 0.03‰ δ^{30}Si for Big Batch (n= 18); -0.06 ± 0.02‰ δ^{29}Si, -0.14 ± 0.03‰ δ^{30}Si for 'Herasil' SiO_2 glass (an in-house standard); n= 15); -0.15 ± 0.03‰ δ^{29}Si, -0.30 ± 0.05‰ δ^{30}Si for BHVO-2 (n= 7). Based on evaluation of accuracy and precision of the sample repeat measurements and comparison of results obtained on reference materials during this study with published data compiled in Jochum et al. (2005; The quantification limits were determined taking sample dilution factors and lowest concentration of the calibration standards into account.

Supplementary Table 2-6), the uncertainty of the entire solution MC-ICP-MS method is estimated to be ± 0.07‰ (2SD) for $\delta^{29}Si$ and ± 0.10‰ (2SD) for $\delta^{30}Si$. The same estimate was obtained by statistical evaluation according to equation 2 in Schoenberg and von Blanckenburg (2005), based on repeat analyses of all samples analyzed in this study. This uncertainty is used for data interpretation in this study.

2.8.1.2. Femtosecond-LA-MC-ICP-MS analyses of Si isotopes and Al/Si (S1.2)

The micro-scale silicon isotope composition was determined on three samples (PS-2089-2-600P, PS2070-1-472P and PS2070-1-472-bh) of porcellanite (opal-CT) by UV femtosecond laser ablation MC-ICP-MS (UV fs-LA-MC-ICP-MS, *Fem2*) at GFZ Potsdam. Analytical conditions are briefly described below and further details on the instrumentation and analytical method are described in Schuessler and von Blanckenburg (2014).

Porcellanite samples were embedded in epoxy resin and polished thin sections of 30 µm thickness were prepared for laser ablation analyses. Reference materials for calibration and for analytical quality control (NIST 8546 aka NBS 28 quartz, USGS BHVO-2G basalt glass, IRMM-017 Si single crystal) were prepared as polished epoxy grain mounts and placed together with samples into the ablation cell. Helium was used as carrier gas for the ablated material, which was mixed with Ar/H_2O from spraychamber nebulization of Milli-Q-H_2O before entering the ICP source of the mass spectrometer.

The UV laser beam (196 nm, <200 fs pulses) was focused beneath the sample surface to obtain a spot diameter between 18 and 25 µm at a fluence of 3 to 1.5 J/cm². At each location ablation was done in raster scanning mode (40 µm/s scan speed), ablating a surface area of about 100 x 100 µm with less than 10 µm crater depth, representing a volume of less than 10^{-4} mm^3. Due to the more irregular shape of NBS 28 quartz crystals, line scans were used to ablate an equivalent volume for analyses. Laser pulse repetition rates between 5 and 50 Hz were employed, depending the Si concentrations and ablation properties of the different materials to obtain Si signal intensities of 5 to 8 V on ^{28}Si (10^{11} Ω amplifiers), matched within 20% relative to signals from NBS 28 ablation, which was used for standard-sample-standard bracketing. The Faraday multi collector setting of the Neptune mass spectrometer was aligned to simultaneously detect $^{28}Si^+$, $^{29}Si^+$, $^{30}Si^+$, and $^{27}Al^+$, and to resolve interferences produced by molecular oxides.

Each individual Si isotope ratio measurement consists of the mean of 80 1-second integration cycles corrected by on-peak subtraction of the background measured at the beginning of a sequence (< 43 mV ^{28}Si). Data evaluation followed the protocol described in Schuessler and von Blanckenburg (2014). All time-resolved data were screened to detect potentially occurring irregular mass bias drift, and interferences (in a three-isotope-plot). Outliers beyond the 3σ limits of a Gaussian normal distribution were excluded, typically affecting no more than five of 80 cycles. We report results in the δ notation as per mil deviation relative to NBS 28 together with the internal standard error of the mean (2SE) of single sample measurements (Supplementary Table 2-2, Supplementary Table 2-3, Supplementary Table 2-4), which is typically <0.1‰ for

$\delta^{30}Si$ as calculated by error propagation from measurements of one sample and two bracketing NBS 28 standards. In the analytical session in which sample PS2089-2-600P was analyzed, we experienced a higher signal of $^{16}O^{14}N^+$ (close to the mass of $^{30}Si^+$) as compared to the other analytical sessions. In medium mass resolution mode of the Neptune, $^{30}Si^+$ can be accurately measured on the interference-free peak shoulder, where $^{30}Si^+$ is resolved from $^{16}O^{14}N^+$ (Schuessler and von Blanckenburg, 2014). However, if the signal intensity of $^{16}O^{14}N^+$ becomes unfavorably high relative to the $^{30}Si^+$ signal, tailing of the $^{16}O^{14}N^+$ peak towards $^{30}Si^+$ leads to a much narrower $^{30}Si^+$ plateau and small magnet instabilities then result in inaccuracies in the $^{30}Si/^{28}Si$ ratio and also higher uncertainties in this ratio associated with the on-peak blank correction (Schuessler and von Blanckenburg, 2014). Therefore, we chose not to use the $\delta^{30}Si$ values from this analytical session for sample PS2089-2-600P, but instead evaluated the $\delta^{29}Si$ values. $\delta^{29}Si$ was not affected by tailing from increased molecular interference signals because the $^{14}N^{14}N^1H^+/^{29}Si^+$ signal ratio was < 0.3, $^{14}N^{14}N^+/^{28}Si^+$ signal ratio was < 0.02, compared to a $^{14}N^{16}O^+/^{30}Si^+$ signal ratio of > 30. For this session we have converted measured $\delta^{29}Si$ values into $\delta^{30}Si$ following the mass-dependent isotope fractionation law $\delta^{30}Si$ (calculated) = 1.96 · $\delta^{29}Si$ (Supplementary Table 2-2). For these measurements we estimated the internal uncertainty in individual $\delta^{30}Si$ (calculated) values by multiplication of the internal standard error of the mean (2SE) of measured $\delta^{29}Si$ by 1.5 (see Supplementary Table 2-2). As the count-statistical uncertainties in $\delta^{29}Si$ and $\delta^{30}Si$ ratios are correlated (Schuessler and von Blanckenburg, 2014), we obtained this factor of 1.5 from the two other independent analytical sessions reported in Supplementary Table 2-3 and Supplementary Table 2-4. This approach is supported by comparing the measured $\delta^{30}Si$ values with $\delta^{30}Si$ (calc) values in Supplementary Table 2-2 which gave differences typically less than 0.1‰, which is within uncertainty of the fs-LA-MC-ICP-MS method. The uncertainty of the fs-LA-MC-ICP-MS method (external long-term repeatability) is ± 0.15‰ (2SD) for $\delta^{29}Si$ and ± 0.23‰ (2SD) for $\delta^{30}Si$, respectively (Schuessler and von Blanckenburg, 2014), and these uncertainties should be applied for geological interpretation and comparison to results obtained in other laboratories. Accuracy was verified by measurements of reference materials during each analytical session (Supplementary Table 2-7). During this study we obtained a mean $\delta^{30}Si$ of -0.24 ± 0.34‰ (2SD, n= 26) for BHVO-2 and -1.28 ± 0.26‰ (2SD, n= 17) for IRMM-017, respectively, which agrees well within uncertainties to previously published values (e.g. Reynolds et al., 2007; Savage et al., 2014; Chmeleff et al., 2008; Schuessler and von Blanckenburg, 2014).

To determine Al concentrations along the LA transects in the porcellanite and opal-CT samples, $^{27}Al/^{28}Si$ ratios were measured simultaneously with Si isotope ratios at a precision of about 2% (2SD). To obtain Al/Si mass ratios, calibration was done by measurements on BHVO-2G, having an Al/Si mass ratio of 0.3123 ± 0.0061 (GeoReM compiled value; Jochum et al., 2005) and Si was used as internal reference element to determine Al concentrations. The fs-LA-MC-ICP-MS repeatability of Al/Si weight ratios on the reference material BHVO-2G is 0.3131 ± 0.0081 (2SD, n= 30). However, the major uncertainty contribution for Al quantification in the porcellanites stems from spatial variability in Si contents (used as internal standard),

which was estimated for different samples to be 1% (PS2089-2-600P), 7% (PS2070-1-472P), and 15% (PS2070-1-472-bh), derived by comparison of LA Si signal intensities at different parts of the porcellanite layers. Thus, the *in-situ* Al concentration can be determined with a relative precision of up to 6% (PS2089-2-600P), 9% (PS2070-1-472P), and 16% (PS2070-1-472-bh) at 95% confidence level, using the Si concentration of the bulk porcellanite (determined by ICP-OES after dissolution) as internal reference.

2.8.1.3. Concentration measurements by ICP-OES (S1.3)

Element concentrations were determined on diluted sample aliquots after solid sample digestions (as described in the main text section 2.2.2) using an axial ICP-OES (Varian 720-ES). The instrument was calibrated using 5 multi-element ICP standard solutions in 0.3 M HNO_3 matrix, ranging from 0.01 ppm to 10 ppm Si and from 0.002 to 1 ppm of other elements. The matrix of the calibration standards was matched to Na concentrations in sample solutions. The instrumental precision of ICP-OES analyses on diluted solutions is typically better than 5% relative. However, in this study the overall uncertainty in reported concentration data for solid samples can be higher due to the sample preparation method designed specifically for Si isotope ratio measurements, where precise knowledge of sample weight is not necessary. For example, sample amounts of <15 mg, that have not been dried to remove adsorbed ambient water lead to imprecise weighing and hence inferior relative uncertainties of up to 15% for reported element concentrations. This level of uncertainty was estimated from measurements of reference materials (e.g., BHVO-2G, NBS 28) following the same dissolution procedure as for the samples.

2.8.2. Silicon isotope data (SI 2)

Supplementary Table 2-1: Solution MC-ICP-MS silicon isotope data of bulk Pleistocene (PS2089-2) and Pliocene (PS2070-1) siliceous sediments and porcellanites. Each sample is representative of ca. 1 cm sediment. Average δ-values of n replicate measurements and their 95% confidence intervals (= t·SD/√n) are reported. 95%CI indicates the intermediate precision of the mass spectrometric method (instrument repeatability). The overall uncertainty of the solution MC-ICP-MS method is estimated to be ± 0.07‰ (2SD) for $\delta^{29}Si$ and ± 0.10‰ (2SD) for $\delta^{30}Si$.

sample	depth below seafloor [cm]	$\delta^{29}Si$ [‰]	95%CI	$\delta^{30}Si$ [‰]	95%CI	n
PS2089-2 541	541	0.67	0.04	1.27	0.04	4
PS2089-2 549	549	0.62	0.07	1.23	0.06	5
PS2089-2 559	559	0.57	0.07	1.06	0.07	4
PS2089-2 589	589	0.70	0.06	1.31	0.06	4
PS2089-2 596	596	0.34	0.05	0.64	0.06	5
PS2089-2 600P	600	0.88	0.02	1.69	0.07	4
PS2089-2 600P dense	600	0.99	0.07	1.96	0.07	3
PS2089-2 617	617	0.76	0.02	1.50	0.06	5
PS2089-2 628	628	0.65	0.06	1.28	0.08	4
PS2089-2 639	639	0.55	0.04	1.09	0.05	4
PS2089-2 670	670	0.11	0.05	0.22	0.18	3
PS2089-2 700	700	0.21	0.06	0.42	0.10	5
PS2089-2 730	730	0.07	0.03	0.16	0.06	4
PS2070-1-423	423	0.26	0.05	0.51	0.07	5
PS2070-1-428	428	0.18	0.04	0.35	0.12	4
PS2070-1-432	432	0.12	0.05	0.24	0.11	6
PS2070-1-438	438	0.16	0.05	0.32	0.08	4
PS2070-1-443	443	0.10	0.01	0.18	0.07	4
PS2070-1-448	448	0.01	0.04	0.03	0.04	4
PS2070-1-453	453	-0.09	0.02	-0.12	0.05	4
PS2070-1-457	457	-0.15	0.05	-0.28	0.04	4
PS2070-1-463	463	-0.08	0.04	-0.15	0.08	3
PS2070-1-467	467	-0.11	0.09	-0.18	0.12	5
PS2070-1-471	471	-0.17	0.03	-0.34	0.05	5
PS2070-1-472P	472	1.17	0.06	2.28	0.14	4
PS2070-1-475	475	-0.08	0.05	-0.15	0.06	4
PS2070-1-479	479	0.11	0.05	0.20	0.05	5
PS2070-1-483	483	0.03	0.03	0.04	0.06	5
PS2070-1-487	487	-0.15	0.03	-0.28	0.06	6
PS2070-1-493	493	-0.08	0.06	-0.15	0.08	5
PS2070-1-498	498	0.05	0.05	0.07	0.10	5
PS2070-1-503	503	-0.03	0.07	-0.01	0.07	3
PS2070-1-508	508	-0.08	0.05	-0.13	0.05	3
PS2070-1-513	513	-0.03	0.02	-0.08	0.06	4
PS2070-1-517	517	-0.12	0.10	-0.26	0.13	3
PS2070-1-527	527	-0.04	0.05	-0.09	0.07	4
PS2070-1-564	564	0.29	0.07	0.61	0.08	5
PS2070-1-613	613	0.22	0.08	0.47	0.09	5

Supplementary Table 2-2: fs-LA-MC-ICP-MS silicon isotope and Al/Si data of porcellanite layer PS2089-2-600P. $\delta^{30}Si$ values were calculated from $\delta^{29}Si$ (assuming $\delta^{30}Si = 1.96\ \delta^{29}Si$, see text above). The internal standard error of the mean (2SE) is given for each individual sample measurement (n= 80 integrations á 1 second). The uncertainty of the fs-LA-MC-ICP-MS method (external long-term repeatability) is ± 0.15‰ (2SD) for $\delta^{29}Si$ and ± 0.23‰ (2SD) for $\delta^{30}Si$, respectively.

analysis ID	dist. [mm]	$\delta^{29}Si$ [‰]	2SE	$\delta^{30}Si$ calc. [‰]	2SE calc	$\delta^{30}Si$ [‰]	$^{27}Al/^{28}Si * 10^{-3}$	2SE [a] $*10^{-3}$	Al [ppm]	± [b]	Al/Si $*10^{-3}$ [wt%/wt%]
600P_1.1	0.10	0.85	0.08	1.67	0.12	1.52	6.6	0.56	1227	1	2.9
600P_2	0.35	0.76	0.08	1.49	0.13	1.66	7.9	0.42	1473	1	3.5
600P_3	0.55	0.71	0.09	1.39	0.13	1.62	9.1	0.81	1707	1	4.1
600P_4	0.75	0.83	0.08	1.62	0.11	1.60	7.7	0.81	1441	1	3.4
600P_5	0.95	0.84	0.08	1.66	0.12	1.72	7.2	0.51	1346	1	3.2
600P_6	1.20	0.79	0.08	1.56	0.12	1.62	15.5	1.68	2897	3	6.9
600P_7	1.40	0.77	0.09	1.51	0.14	1.44	8.4	0.69	1565	1	3.7
600P_7.1	1.40	0.64	0.09	1.26	0.14	1.30	7.0	1.19	1310	2	3.1
600P_8	1.60	0.79	0.10	1.55	0.14	1.46	12.9	1.10	2405	2	5.7
600P_9	1.85	0.79	0.16	1.56	0.24	1.46	7.8	0.73	1450	1	3.4
600P_11	2.25	0.73	0.09	1.44	0.13	1.62	6.0	0.51	1121	1	2.7
600P_12	2.45	0.78	0.08	1.53	0.11	1.61	5.5	0.38	1018	8	2.4
600P_13	2.65	0.87	0.08	1.71	0.12	1.81	6.5	0.57	1205	1	2.9
600P_14	2.90	0.95	0.08	1.87	0.12	2.04	5.0	0.31	939	7	2.2
600P_14.1	2.90	0.71	0.08	1.39	0.12	1.40	6.1	0.63	1145	1	2.7
600P_15	3.10	0.82	0.08	1.61	0.12	1.61	6.0	0.55	1114	1	2.6
600P_16	3.35	0.78	0.09	1.53	0.13	1.66	4.6	1.00	850	1	2.0
600P_17	3.60	0.74	0.09	1.46	0.13	1.57	8.6	0.80	1609	1	3.8
600P_18	3.80	0.88	0.08	1.73	0.12	1.74	5.7	0.70	1070	1	2.5
600P_19	4.00	0.82	0.08	1.62	0.12	1.73	6.5	0.66	1206	1	2.9
600P_20	4.25	0.76	0.08	1.50	0.12	1.58	7.4	0.64	1374	1	3.3
600P_20.1	4.25	0.62	0.09	1.21	0.14	1.42	7.2	1.17	1343	2	3.2
600P_21	4.45	0.79	0.08	1.55	0.13	1.40	14.0	1.68	2619	3	6.2
600P_22	4.65	0.69	0.08	1.35	0.12	1.39	9.6	0.78	1798	1	4.3
600P_23	4.85	0.91	0.09	1.79	0.14	1.60	9.3	1.13	1728	2	4.1
600P_24	5.15	0.73	0.09	1.44	0.13	1.68	9.6	0.99	1797	2	4.3
600P_25	5.35	0.74	0.12	1.45	0.18	1.76	10.3	1.03	1923	2	4.6
600P_26	5.50	0.79	0.13	1.56	0.19	1.82	9.5	0.68	1779	1	4.2
600P_27	5.70	0.68	0.14	1.33	0.21	1.57	9.1	1.09	1703	2	4.0
600P_28	5.95	0.68	0.10	1.34	0.15	1.53	8.6	1.12	1602	2	3.8
600P_29	6.15	0.75	0.08	1.46	0.12	1.63	7.6	0.82	1413	1	3.4
600P_30	6.40	0.78	0.09	1.54	0.14	1.73	7.9	0.91	1474	1	3.5
600P_31	6.65	0.66	0.09	1.29	0.13	1.59	9.5	0.77	1771	1	4.2
600P_32	6.80	0.67	0.09	1.32	0.13	1.58	8.1	0.73	1512	1	3.6
600P_32.1	6.80	0.66	0.08	1.30	0.12	1.37	7.1	1.01	1320	1	3.1
600P_33	6.95	0.84	0.08	1.64	0.13	1.58	6.4	0.38	1192	9	2.8
600P_34	7.25	0.92	0.08	1.81	0.12	1.79	6.1	0.47	1134	1	2.7
600P_34.1	7.25	0.65	0.09	1.27	0.13	1.37	9.0	1.02	1683	2	4.0
600P_35	7.45	1.03	0.09	2.02	0.14	2.10	4.5	0.29	840	6	2.0

continued

analysis ID	dist. [mm]	$\delta^{29}Si$ [‰]	2SE	$\delta^{30}Si$ calc. [‰]	2SE calc	$\delta^{30}Si$ [‰]	$^{27}Al/^{28}Si$ $*10^{-3}$	2SE [a] $*10^{-3}$	Al [ppm]	± [b]	Al/Si $*10^{-3}$ [wt%/wt]
600P_36	7.65	0.90	0.08	1.76	0.13	1.91	4.8	0.32	892	7	2.1
600P_37	7.95	0.96	0.08	1.88	0.13	2.00	4.5	0.21	832	5	2.0
600P_38	8.15	0.89	0.07	1.74	0.11	1.80	5.0	0.40	928	8	2.2
600P_39	8.35	0.90	0.08	1.77	0.12	1.79	5.0	0.28	935	6	2.2
600P_40	8.60	0.91	0.08	1.79	0.12	1.78	4.5	0.21	838	5	2.0
600P_41	8.80	1.02	0.09	2.01	0.14	1.92	4.5	0.34	836	7	2.0
600P_42.1	9.00	0.94	0.07	1.84	0.11	1.88	4.3	0.21	809	5	1.9
600P_44	9.45	0.98	0.10	1.94	0.15	1.98	6.1	0.50	1138	1	2.7
600P_45	9.60	0.93	0.10	1.82	0.15	1.77	5.0	0.54	933	1	2.2
600P_46	9.85	0.91	0.10	1.79	0.15	1.76	4.5	0.41	832	8	2.0
600P_47	10.05	0.92	0.10	1.81	0.15	1.82	4.1	0.41	759	8	1.8
600P_48	10.25	0.97	0.09	1.90	0.13	1.92	4.7	0.37	885	8	2.1
600P_49	10.45	0.92	0.08	1.80	0.12	1.91	4.3	0.50	799	1	1.9
600P_50	10.70	0.95	0.08	1.87	0.13	1.85	3.6	0.39	675	7	1.6
600P_50.1	10.70	0.95	0.07	1.86	0.11	1.89	3.4	0.20	636	4	1.5
600P_51	10.95	0.98	0.08	1.93	0.13	1.86	3.4	0.34	629	7	1.5
600P_52	11.15	0.88	0.08	1.73	0.12	1.74	4.7	0.48	878	9	2.1
600P_53	11.35	0.92	0.08	1.80	0.11	1.75	3.9	0.37	732	7	1.7
600P_54	11.55	0.98	0.07	1.93	0.11	1.96	2.4	0.39	452	7	1.1
600P_55	11.75	1.04	0.08	2.05	0.12	2.05	3.5	0.35	650	7	1.5
600P_56	12.00	1.05	0.09	2.07	0.13	2.17	6.1	0.31	1147	7	2.7
600P_56.1	12.00	1.02	0.08	2.01	0.11	2.09	5.0	0.29	937	6	2.2
600P_57	12.20	1.03	0.07	2.02	0.11	2.11	2.4	0.19	447	4	1.1
600P_58	12.40	0.96	0.07	1.88	0.10	2.05	3.3	0.20	614	4	1.5
600P_59	12.65	0.97	0.08	1.91	0.11	1.92	3.4	0.20	641	4	1.5
600P_60	12.85	0.94	0.07	1.84	0.11	1.87	3.8	0.29	704	6	1.7
600P_61	13.05	0.93	0.08	1.82	0.12	1.81	3.2	0.18	605	4	1.4
600P_62	13.25	0.91	0.08	1.78	0.12	1.67	2.5	0.44	466	8	1.1
600P_62.1	13.25	0.87	0.07	1.71	0.11	1.81	3.5	0.18	646	4	1.5
600P_63	13.45	0.80	0.09	1.58	0.13	1.65	4.9	0.47	913	9	2.2
600P_64	13.65	0.84	0.08	1.66	0.12	1.56	4.7	0.40	871	8	2.1
600P_65	13.85	0.73	0.09	1.44	0.14	1.56	20.6	0.80	3843	2	9.1
600P_65.1	13.85	0.81	0.07	1.60	0.11	1.69	18.3	0.79	3415	2	8.1

[a] uncertainty estimated from error propagation of internal counting statistical error and repeatability on BHVO-2G

[b] uncertainty estimated from error propagation of internal counting statistical error, repeatability on BHVO-2G, measurement uncertainty on Al/Si (BHVO-2G GeoRem reference value), uncertainty on the silicon concentration in the sample, and the variability in the silicon concentration of the sample

Supplementary Table 2-3: fs-LA-MC-ICP-MS silicon isotope and Al/Si data of porcellanite layer PS2070-1-472P. The internal standard error of the mean (2SE) is given for each individual sample measurement (comprising n= 80 integrations á 1 second for sample and 2 bracketing standards). The uncertainty of the fs-LA-MC-ICP-MS method (external long-term repeatability) is ± 0.15‰ (2SD) for $\delta^{29}Si$ and ± 0.23‰ (2SD) for $\delta^{30}Si$, respectively.

analysis ID	dist. [mm]	$\delta^{29}Si$ [‰]	2SE	$\delta^{30}Si$ [‰]	2SE	$^{27}Al/^{28}Si$ $*10^{-3}$	2SE [a] $*10^{-3}$	Al [ppm]	± [b]	Al/Si $*10^{-3}$ [wt%/wt%]
472P_1	0.1	1.26	0.09	2.49	0.12	1.4	0.12	<350		0.8
472P_2	0.2	1.29	0.08	2.58	0.10	0.4	0.03	<350		0.2
472P_3	0.3	1.32	0.07	2.51	0.10	0.1	0.02	<350		0.1
472P_4	0.4	1.23	0.08	2.39	0.10	0.0	0.01	<350		0.0
472P_5	0.5	1.29	0.07	2.65	0.09	0.1	0.01	<350		0.1
472P_6	0.6	1.39	0.08	2.82	0.10	0.1	0.03	<350		0.0
472P_7	0.7	1.45	0.07	2.77	0.11	0.4	0.04	<350		0.2
472P_8	0.8	1.48	0.07	2.89	0.09	0.3	0.05	<350		0.2
472P_9	0.9	1.38	0.07	2.76	0.10	0.3	0.03	<350		0.2
472P_10	1.0	1.50	0.07	2.95	0.10	0.4	0.02	<350		0.2
472P_11	1.1	1.38	0.07	2.82	0.10	0.4	0.04	<350		0.2
472P_12	1.2	1.43	0.07	2.80	0.11	0.3	0.02	<350		0.1
472P_13	1.3	1.47	0.07	2.92	0.10	0.6	0.07	<350		0.3
472P_14	1.4	1.37	0.07	2.65	0.10	0.2	0.02	<350		0.1
472P_15	1.5	1.40	0.08	2.87	0.11	0.8	0.05	<350		0.4
472P_16	1.6	1.23	0.07	2.47	0.10	8.2	0.40	1897	189	4.5
472P_17	1.7	1.09	0.07	2.12	0.10	10.5	0.52	2438	243	5.8
472P_18	1.8	1.12	0.07	2.18	0.10	10.2	0.72	2365	264	5.6
472P_19	1.9	1.22	0.07	2.35	0.11	15.5	0.78	3603	361	8.6
472P_20	2.0	1.23	0.07	2.35	0.09	6.1	0.24	1405	134	3.3
472P_21	2.1	1.23	0.08	2.36	0.11	5.7	0.22	1333	126	3.2
472P_22	2.2	1.28	0.07	2.41	0.10	5.3	0.51	1236	160	2.9
472P_23	2.3	1.28	0.07	2.40	0.12	3.8	0.18	878	87	2.1
472P_24	2.4	1.17	0.09	2.27	0.12	5.3	0.28	1227	124	2.9
472P_25	2.5	1.20	0.08	2.33	0.12	5.4	0.19	1247	117	3.0
472P_26	2.6	1.22	0.08	2.33	0.13	4.0	0.36	939	116	2.2
472P_27	2.7	1.24	0.07	2.40	0.14	12.2	0.63	2837	286	6.7
472P_28	2.8	1.24	0.07	2.37	0.12	14.8	0.48	3442	319	8.2
472P_29	2.9	1.27	0.08	2.45	0.13	25.6	0.87	5931	552	14.1
472P_30	3.0	1.31	0.11	2.56	0.17	11.0	0.37	2563	238	6.1
472P_31	3.1	1.25	0.12	2.50	0.20	12.0	0.70	2787	291	6.6
472P_32	3.2	1.22	0.12	2.43	0.20	6.9	0.32	1603	157	3.8
472P_33	3.3	1.14	0.09	2.19	0.15	4.0	0.20	919	92	2.2

[a] uncertainty estimated from error propagation of internal counting statistical error and repeatability on BHVO-2G

[b] uncertainty estimated from error propagation of internal counting statistical error, repeatability on BHVO-2G, measurement uncertainty on Al/Si (BHVO-2G GeoRem reference value), uncertainty on the silicon concentration in the sample, and the variability in the silicon concentration of the sample

Supplementary Table 2-4: fs-LA-MC-ICP-MS silicon isotope and Al/Si data of a porcellanite-filled animal burrow (ichnofossil; PS-2070-1-472-bh) in the vicinity of the porcellanite in piston core PS2070-1. The internal standard error of the mean (2SE) is given for each individual sample measurement (comprising n= 80 integrations á 1 second for sample and 2 bracketing standards). The uncertainty of the fs-LA-MC-ICP-MS method (external long-term repeatability) is ± 0.15‰ (2SD) for $\delta^{29}Si$ and ± 0.23‰ (2SD) for $\delta^{30}Si$, respectively.

analysis ID	distance [mm]	$\delta^{29}Si$ [‰]	2SE	$\delta^{30}Si$ [‰]	2SE	$^{27}Al/^{28}Si$ $*10^{-3}$	2SE [a] $*10^{-3}$	Al [ppm]	± [b]	Al/Si $*10^{-3}$ [wt%/wt]
472P_bh6	0.5	1.18	0.1	2.21	0.25	8.4	0.40	671	112	1.53
472P_bh7	0.7	1.14	0.1	2.18	0.20	11.6	0.58	910	153	2.08
472P_bh8	0.8	1.14	0.1	2.20	0.17	6.9	0.27	557	92	1.27
472P_bh9	0.9	1.09	0.1	2.23	0.13	4.2	0.14	359	59	0.82
472P_bh10	1.1	1.17	0.1	2.41	0.15	6.5	0.16	533	87	1.22
472P_bh11	1.2	1.15	0.1	2.06	0.15	5.7	0.20	466	77	1.06
472P_bh12	1.3	1.10	0.1	2.21	0.15	6.6	0.21	535	87	1.22
472P_bh13	1.4	1.16	0.0	2.25	0.15	3.3	0.12	289	48	0.66
472P_bh14	1.6	1.09	0.0	2.21	0.13	1.2	0.09	<130		0.30
472P_bh15	1.8	1.13	0.1	2.21	0.14	1.2	0.08	<130		0.29
472P_bh16	1.9	1.11	0.0	2.23	0.13	1.2	0.08	<130		0.29
472P_bh17	2.1	1.21	0.0	2.41	0.14	2.7	0.13	242	41	0.55
472P_bh18	2.2	1.18	0.0	2.28	0.12	1.4	0.08	145	25	0.33
472P_bh19	2.4	1.15	0.1	2.32	0.14	1.4	0.06	146	24	0.33
472P_bh20	2.5	1.23	0.0	2.26	0.12	0.7	0.06	<130		0.20
472P_bh21	2.7	1.15	0.0	2.14	0.13	0.6	0.04	<130		0.19
472P_bh22	2.8	1.13	0.1	2.30	0.13	0.7	0.06	<130		0.20
472P_bh23	3.0	1.23	0.0	2.28	0.11	0.7	0.06	<130		0.20
472P_bh24	3.2	1.19	0.0	2.33	0.11	0.8	0.09	<130		0.21
472P_bh25	3.3	1.20	0.0	2.37	0.11	0.1	0.04	<130		0.10
472P_bh26	3.5	1.16	0.0	2.30	0.13	0.1	0.01	<130		0.08
472P_bh27	3.6	1.32	0.0	2.41	0.13	0.2	0.02	<130		0.11
472P_bh28	3.8	1.27	0.0	2.41	0.13	1.0	0.06	<130		0.25
472P_bh29	4.0	1.31	0.1	2.46	0.22	1.8	0.33	<130		0.43
472P_bh30	4.2	1.40	0.0	2.63	0.15	3.8	0.38	324	61	0.74
472P_bh31	4.3	1.36	0.1	2.60	0.12	1.8	0.22	166	34	0.38
472P_bh32	4.6	1.13	0.0	2.13	0.11	2.7	0.47	232	56	0.53
472P_bh33	5.0	1.17	0.0	2.22	0.12	0.9	0.07	<130		0.23
472P_bh34	5.3	1.20	0.0	2.43	0.15	0.7	0.06	<130		0.21
472P_bh35	5.4	1.23	0.0	2.45	0.13	1.1	0.06	<130		0.28
472P_bh36	5.6	1.27	0.0	2.35	0.16	1.2	0.04	<130		0.30
472P_bh39	6.2	1.19	0.0	2.44	0.14	3.6	0.15	304	50	0.69
472P_bh48	7.8	-0.03	0.1	-0.11	0.22	20.5	0.80	1580	261	3.61
472P_bh50	8.2	-0.07	0.1	-0.27	0.26	28.4	1.17	2181	362	4.98

[a] uncertainty estimated from error propagation of internal counting statistical error and repeatability on BHVO-2G

[b] uncertainty estimated from error propagation of internal counting statistical error, repeatability on BHVO-2G, measurement uncertainty on Al/Si (BHVO-2G GeoRem reference value), uncertainty on the silicon concentration in the sample, and the variability in the silicon concentration of the sample

Supplementary Table 2-5: Major- and trace element concentrations in bulk samples analyzed by ICP-OES (Varian 720-ES). Na concentrations were not measured because NaOH was used for sample digestion. The difference to 100% of the sum of the major oxides thus comprises Na, K, volatile compounds, organic matter as well as adhesively and structurally bound water in opal. The relative analytical uncertainty is estimated based on measurements of reference materials following the same dissolution protocol and is up to 15% relative.

		wt%					ppm			
sample	**sediment depth [cm]**	**SiO_2**	**Al_2O_3**	**Fe_2O_3**	**MgO**	**CaO**	**Mn**	**La**	**Ba**	**Sr**
2089-2 541	541	74.4	1.1	1.1	0.7	2.6	<12	176	543	104
2089-2 549	549	73.0	1.9	1.4	0.8	1.7	<12	189	536	83
2089-2 559	559	67.6	3.5	3.3	1.0	1.8	<12	237	562	99
2089-2 589	589	75.6	0.3	0.2	0.5	0.2	<12	<11	269	27
2089-2 596	596	73.6	2.2	1.4	0.8	0.3	587	108	4028	133
2089-2-600P1	600	87.3	1.9	1.3	0.4	0.6	<12	<11	193	27
2089-2-600P2	600	86.6	<0.3	<0.2	0.2	<0.1	<12	<11	<133	10
2089-2 617	617	72.4	0.3	0.8	0.8	0.3	<12	<11	268	37
2089-2 628	628	70.7	1.2	1.0	0.9	0.3	<12	134	327	47
2089-2 639	639	73.6	1.8	1.2	0.8	0.4	<12	156	469	48
2089-2 670	670	58.2	24.5	14.2	3.0	4.4	825	353	1031	170
2089-2 700	700	52.5	16.0	10.1	1.9	13.3	680	423	1191	378
2089-2 730	730	52.3	23.7	14.4	2.8	11.1	997	328	812	299
2070-1 423	423	73.9	3.0	2.1	0.8	0.3	594	175	6439	189
2070-1 428	428	70.8	3.1	2.1	0.8	0.3	562	179	6558	194
2070-1 432	432	72.4	2.9	2.1	0.8	0.3	599	171	6287	189
2070-1 438	438	71.4	2.6	1.8	0.7	0.3	414	158	5702	174
2070-1 443	443	73.0	1.8	1.3	0.6	0.2	296	121	4350	141
2070-1 448	448	73.4	1.2	0.7	0.5	0.2	148	107	3640	125
2070-1 453	453	71.9	1.0	0.6	0.6	0.2	<12	908	3275	117
2070-1 457	457	74.7	0.7	0.4	0.5	0.2	<12	583	2069	78
2070-1 463	463	73.5	0.8	0.5	0.5	0.2	<12	475	1619	61
2070-1 467	467	74.9	0.6	0.3	0.5	0.1	<12	321	1149	48
2070-1 471	471	75.5	0.5	0.4	0.5	0.1	<12	425	1452	59
2070-1 472P	472	92.3	0.4	0.2	0.1	<0.09	<12	324	1044	34
2070-1 475	475	74.4	0.8	0.6	0.6	0.3	<12	514	1714	71
2070-1 479	479	72.4	0.9	0.5	0.8	0.3	<12	438	1454	63
2070-1 483	483	73.3	1.0	0.5	0.7	0.2	<12	419	1449	64
2070-1 487	487	76.2	0.7	0.3	0.6	0.2	<12	279	923	44
2070-1 493	493	74.0	2.5	1.4	0.8	0.3	<12	945	3464	107
2070-1 498	498	73.5	2.9	1.8	0.9	0.3	<12	119	4356	127
2070-1 503	503	72.7	2.9	1.9	0.9	0.4	<12	104	3891	133
2070-1 508	508	71.2	3.1	2.0	1.0	0.4	<12	852	3126	112
2070-1 513	513	68.0	2.9	1.7	1.0	0.4	<12	976	3543	154
2070-1 517	517	71.9	4.7	3.0	1.1	0.6	<12	150	5514	187
2070-1 527	527	71.3	5.0	3.4	1.0	0.5	998	217	8082	236
2070-1 564	564	73.2	1.9	1.2	0.7	0.3	<12	757	2567	92
2070-1 613	613	71.6	2.8	1.8	0.9	0.4	226	113	4212	138

The quantification limits were determined taking sample dilution factors and lowest concentration of the calibration standards into account.

Supplementary Table 2-6: Solution MC-ICP-MS measurements of the silicon isotope composition of reference materials obtained during this study. Individual measurements from different analytical sessions are listed. Average δ-values and their 95% confidence interval (= *t*·SD/√n), are calculated (intermediate precision of the mass spectrometric method (instrument repeatability). The overall uncertainty of the solution MC-ICP-MS method is estimated to be ± 0.07‰ (2SD) for δ^{29}Si and ± 0.10‰ (2SD) for δ^{30}Si. Averages (± 1SD) of published values (Jochum et al., 2005) of reference materials measured relative to NIST8546 (aka. NBS 28) are as follows. Big Batch: -5.38 ± 0.08‰ δ^{29}Si (n= 8), -10.53 ± 0.19‰ δ^{30}Si (n= 12); IRMM-017: -0.69 ± 0.04‰ δ^{29}Si (n= 3), -1.33 ± 0.08‰ δ^{30}Si (n= 3); BHVO-2: -0.14 ± 0.04‰ δ^{29}Si (n= 12), -0.28 ± 0.05‰ δ^{30}Si (n= 17); Diatomite: 0.64 ± 0.02‰ δ^{29}Si (n= 9), 1.24 ± 0.06‰ δ^{30}Si (n= 15).

Big Batch	**δ^{29}Si**	**δ^{30}Si**	**date**
029-BigBatch	-5.41	-10.62	24.05.2012
039-BigBatch	-5.48	-10.68	24.05.2012
029-BigBatch	-5.47	-10.71	05.06.2012
065-BigBatch	-5.43	-10.72	05.06.2012
033-BigBatch	-5.44	-10.66	18.06.2012
063-BigBatch	-5.46	-10.70	18.06.2012
093-BigBatch	-5.50	-10.81	18.06.2012
033-BigBatch	-5.43	-10.68	30.07.2012
063-BigBatch	-5.44	-10.66	30.07.2012
017-BigBatch	-5.41	-10.64	30.07.2012
037-BigBatch	-5.41	-10.60	19.06.2012
073-BigBatch	-5.42	-10.67	19.06.2012
003-BigBatch	-5.42	-10.61	19.11.2012
059-BigBatch	-5.49	-10.76	19.11.2012
003-BigBatch	-5.48	-10.75	06.05.2013
085-BigBatch	-5.44	-10.74	06.05.2013
143-BigBatch	-5.44	-10.69	06.05.2013
187-BigBatch	-5.43	-10.67	06.05.2013
average	-5.45	-10.69	
95%CI	0.01	0.03	
2SD	0.06	0.11	

BHVO-2	**δ^{29}Si**	**δ^{30}Si**	**date**
039-BHVO	-0.15	-0.29	24.05.2012
005-BHVO	-0.21	-0.36	18.06.2012
035-BHVO	-0.15	-0.28	18.06.2012
065-BHVO	-0.13	-0.27	18.06.2012
095-BHVO	-0.19	-0.38	18.06.2012
005-BHVO	-0.12	-0.25	19.11.2012
061-BHVO	-0.11	-0.25	19.11.2012
average	-0.15	-0.30	
95%CI	0.03	0.05	
2SD	0.07	0.11	

IRMM-017	**δ^{29}Si**	**δ^{30}Si**	**date**
009-IRMM17	-0.72	-1.43	24.05.2012
039-IRMM17	-0.66	-1.31	24.05.2012
069-IRMM17	-0.65	-1.30	24.05.2012
099-IRMM17	-0.70	-1.30	24.05.2012
033-IRMM17	-0.66	-1.36	24.05.2012
041-IRMM17	-0.59	-1.25	24.05.2012
009-IRMM17	-0.72	-1.43	05.06.2012
039-IRMM17	-0.66	-1.31	05.06.2012
069-IRMM17	-0.65	-1.30	05.06.2012
099-IRMM17	-0.70	-1.30	05.06.2012
007-IRMM17	-0.71	-1.38	06.05.2013
091-IRMM17	-0.73	-1.33	06.05.2013
149-IRMM17	-0.69	-1.41	06.05.2013
191-IRMM17	-0.70	-1.39	06.05.2013
average	-0.68	-1.34	
95%CI	0.02	0.03	
2SD	0.07	0.11	

Diatomite	**δ^{29}Si**	**δ^{30}Si**	**date**
043-Diatomite	0.66	1.23	19.11.2012
077-Diatomite	0.64	1.19	19.11.2012
007-Diatomite	0.63	1.25	30.07.2012
037-Diatomite	0.64	1.24	30.07.2012
067-Diatomite	0.61	1.23	30.07.2012
021-Diatomite	0.66	1.28	30.07.2012
005-Diatomite	0.62	1.27	06.05.2013
087-Diatomite	0.63	1.26	06.05.2013
147-Diatomite	0.65	1.22	06.05.2013
189-Diatomite	0.63	1.19	06.05.2013
059-Diatomite	0.64	1.27	31.02.2013
119-Diatomite	0.63	1.23	31.02.2013
123-Diatomite	0.65	1.27	31.02.2013
average	0.64	1.24	
95%CI	0.01	0.02	
2SD	0.03	0.06	

Herasil	**$\delta^{29}Si$**	**$\delta^{30}Si$**	**date**
035-Herasil	-0.06	-0.14	24.05.2012
007-Herasil	-0.09	-0.16	18.06.2012
037-Herasil	-0.03	-0.17	18.06.2012
067-Herasil	-0.03	-0.07	18.06.2012
097-Herasil	-0.10	-0.19	18.06.2012
039-Herasil	-0.08	-0.22	19.06.2012
075-Herasil	-0.06	-0.17	19.06.2012
005-Herasil	-0.08	-0.13	30.07.2012
035-Herasil	-0.05	-0.18	30.07.2012
065-Herasil	0.00	-0.04	30.07.2012
019-Herasil	-0.04	-0.05	30.07.2012
011-Herasil	-0.08	-0.13	06.05.2013
093-Herasil	-0.11	-0.19	06.05.2013
151-Herasil	-0.10	-0.12	06.05.2013
195-Herasil	-0.03	-0.11	06.05.2013
average	-0.06	-0.14	
95%CI	0.02	0.03	
2SD	0.06	0.10	

Supplementary Table 2-7: fs-laser ablation MC-ICP-MS measurements of the silicon isotope composition of reference materials obtained during this study. The internal standard error of the mean (2SE) is given for each single sample measurements (comprising n= 80 integrations á 1 second for sample and 2 bracketing standards). The uncertainty of the fs-LA-MC-ICP-MS method (external long-term repeatability) is ± 0.15‰ (2SD) for δ^{29}Si and ± 0.23‰ (2SD) for δ^{30}Si, respectively. Averages (±1SD) of published values (Jochum et al., 2005) of reference materials measured relative to NIST8546 (aka. NBS 28) are as follows. IRMM-017: -0.69 ± 0.04‰ δ^{29}Si (n= 3), -1.33 ± 0.08‰ δ^{30}Si (n= 3); BHVO-2: -0.14 ± 0.04‰ δ^{29}Si (n= 12), -0.28 ± 0.05‰ δ^{30}Si (n= 17).

BHVO-2G	**δ^{29}Si [‰]**	**2SE**	**δ^{30}Si [‰]**	**2SE**	**date**
003-BHVO_1	-0.12	0.12	-0.29	0.23	03.08.2012
015-BHVO_2	-0.21	0.14	-0.40	0.26	03.08.2012
035-BHVO_3	-0.09	0.14	-0.34	0.26	03.08.2012
055-BHVO_4	-0.15	0.15	-0.35	0.24	03.08.2012
075-BHVO_5	-0.31	0.18	-0.63	0.35	03.08.2012
average	-0.18		-0.40		
95%CI	0.10		0.16		

BHVO-2G	**δ^{29}Si [‰]**	**2SE**	**δ^{30}Si (calc.) [‰]**		**date**
005-BHVO1	-0.25	0.16	-0.63	0.23	01.08.2012
029-BHVO2	-0.11	0.07	-0.36	0.11	01.08.2012
053-BHVO3	-0.16	0.08	-0.46	0.12	01.08.2012
077-BHVO4	-0.20	0.08	-0.30	0.11	01.08.2012
101-BHVO5	-0.16	0.10	-0.18	0.13	01.08.2012
125-BHVO6	-0.18	0.09	-0.25	0.13	01.08.2012
131-BHVO7	-0.20	0.10	-0.26	0.14	01.08.2012
average	-0.18		-0.35		
95%CI	0.04		0.14		

BHVO-2G	**δ^{29}Si [‰]**	**2SE**	**δ^{30}Si (calc.) [‰]**		**date**
011-BHVO	-0.09	0.07	-0.17	0.11	11.02.2013
013-BHVO	-0.06	0.08	-0.11	0.12	11.02.2013
015-BHVO	-0.04	0.07	-0.08	0.11	11.02.2013
057-BHVO	-0.01	0.08	-0.02	0.11	11.02.2013
059-BHVO	-0.06	0.08	-0.12	0.12	11.02.2013
061-BHVO	-0.04	0.08	-0.08	0.11	11.02.2013
103-BHVO	-0.09	0.07	-0.18	0.10	11.02.2013
105-BHVO	-0.09	0.08	-0.19	0.12	11.02.2013
107-BHVO	-0.02	0.07	-0.04	0.11	11.02.2013
149-BHVO	-0.17	0.08	-0.33	0.11	11.02.2013
151-BHVO	-0.14	0.08	-0.27	0.12	11.02.2013
153-BHVO	-0.09	0.08	-0.17	0.11	11.02.2013
189-BHVO	-0.07	0.08	-0.14	0.12	11.02.2013
191-BHVO	0.02	0.08	0.04	0.12	11.02.2013
average	-0.07		-0.13		
95%CI	0.03		0.06		

all BHVO-2G data		
average	-0.12	-0.24
2SD	0.15	0.34
95%CI	0.03	0.07

continued

IRMM-017	**$\delta^{29}Si$ [‰]**	**2SE**	**$\delta^{30}Si$ [‰]**	**2SE**	**date**
005-IRMM17_1	-0.67	0.07	-1.35	0.11	8/3/2012
025-IRMM17_2	-0.66	0.08	-1.20	0.12	8/3/2012
045-IRMM17_3	-0.65	0.07	-1.32	0.11	8/3/2012
065-IRMM17_4	-0.64	0.10	-1.34	0.13	8/3/2012
087-IRMM17_5	-0.75	0.08	-1.36	0.12	8/3/2012
average	-0.67		-1.31		
95%CI	0.05		0.08		
129-IRMM17	-0.61	0.11	-1.00	0.17	8/1/2012
017-IRMM17_2	-0.58	0.10	-1.15	0.16	8/1/2012
041-IRMM17_3	-0.64	0.09	-1.13	0.13	8/1/2012
065-IRMM17_4	-0.59	0.11	-1.26	0.13	8/1/2012
089-IRMM17_5	-0.55	0.12	-1.08	0.16	8/1/2012
average	-0.59		-1.12		
95%CI	0.04		0.11		

IRMM-017	**$\delta^{29}Si$ [‰]**	**2SE**	**$\delta^{30}Si$ (calc.) [‰]**		**date**
003-IRMM17	-0.71	0.08	-1.39	0.12	2/11/2013
005-IRMM17	-0.71	0.08	-1.39	0.12	2/11/2013
007-IRMM17	-0.69	0.07	-1.35	0.11	2/11/2013
009-IRMM17	-0.68	0.09	-1.34	0.14	2/11/2013
193-IRMM17	-0.67	0.08	-1.31	0.11	2/11/2013
195-IRMM17	-0.69	0.07	-1.35	0.11	2/11/2013
197-IRMM17	-0.76	0.08	-1.50	0.12	2/11/2013
average	-0.70		-1.37		
95%CI	0.03		0.05		

all IRMM-017 data

average	-0.66		-1.28
2SD	0.11		0.26
95%CI	0.03		0.07

Supplementary Table 2-8: Experimental conditions for leaching experiments

Experiment #	**I (sequential extraction)**	**II (batch extraction)**
sample	PS2070-1-423	IIa: PS2070-1-493 IIb: PS2089-2-639
sample mass [mg]	5.3	2.6 - 3
vol. 1.6 mm NaOH [ml]	50	25
increased to 1M NaOH	after 5 hours 1 aliquot of sample powder with continuous sampling from one tube	- 12 separate sample powder aliquots (+NaOH) sampled once after given time
T [°C]	≈ 70°C	20°C after 0.5, 1, 1.5, 2, 2.5, 3, 3.5, 4, 5, 6, 8 and 22.5 h; 70°C after 24 h
mixing	occasional shaking by hand	roller mixer for leaching experiment IIa at 20°C in PP tubes; exp. IIb convection in Teflon vials on hot plate for leaching experiments at 70°C
sampling interval	every 30 min for 5h, then after 6.5h, 22.5h, respectively	every 30 to 60 min for 5h, then after 6h, 8h, 22.5h, 24h, respectively

Supplementary Table 2-9: Solution MC-ICP-MS silicon isotope data of solutions sampled during leaching of siliceous sediments in NaOH. Leaching experiment I (on sample PS2070-1-423) was conducted using one solution that was repeatedly sampled. In experiments IIa (PS2070 1-493) and IIb (PS2089-2-639) twelve separate tubes were sampled separately. See main text and table S.8 for details. Samples V123a and V456a represent mixtures of samples with too low Si amounts for individual Si isotope analyses. Average δ-values of n replicate measurements and their 95% confidence intervals (= t·SD/√n) are reported. 95%CI indicates the intermediate precision of the mass spectrometric method (instrument repeatability). The overall uncertainty of the solution MC-ICP-MS method is estimated to be ± 0.07‰ (2SD) for δ29Si and ± 0.10‰ (2SD) for δ30Si, which should be used for data interpretation (also for analysis results with n= 1). Uncertainty in Al and Si concentration data measured by ICP-OES are estimated to be 5% relative.

sample	time [h]	T [°C]	NaOH [mM]	δ^{29}Si [‰]	95%CI	δ^{30}Si [‰]	95%CI	n	Al [ppm]	Si [ppm]	Al/Si
leaching experiment I (single aliquot extraction; sample PS2070-1-423)											
V123a	0.5 - 1.5	70	1.6	0.41	0.04	0.75	0.08	4	0.94	6.2	0.15
V456a	2 - 3	70	1.6	0.73	0.05	1.45	0.12	3	1.55	17.1	0.09
V7a	3.5	70	1.6	0.73	0.01	1.42	0.05	3	0.80	9.6	0.08
V8a	4	70	1.6	0.74	0.03	1.40	0.09	3	2.76	34.1	0.08
V9a	4.5	70	1.6	0.66	0.10	1.35	0.15	3	1.41	16.3	0.09
V10a	5	70	1.6	0.62	0.03	1.23	0.05	3	0.27	7.1	0.04
V12a	6.5	70	1000	0.45	0.02	0.88	0.12	3	0.07	18.1	0.00
V13a	22.5	70	1000	0.13	0.06	0.29	0.07	4	0.30	61.7	0.00
leaching experiment IIa (multiple aliquot extraction; sample PS2070-1-493)											
493_1	0.5	20	1.6	0.40		0.55		1	0.15	2.2	0.07
493_4	2	20	1.6	0.38		0.64		1	0.10	1.7	0.06
493_5	2.5	20	1.6	0.39		0.62		1	0.11	2.1	0.05
493_6	3	20	1.6	0.41		0.66		1	0.05	1.4	0.04
493_7	3.5	20	1.6	0.41	0.09	0.71	0.04	3	0.10	3.2	0.03
493_8	4	20	1.6	0.42	0.15	0.73	0.56	2	0.03	1.2	0.02
493_9	5	20	1.6	0.38	0.38	0.67	0.60	2	0.22	4.0	0.05
493_10	6	20	1.6	0.32	0.14	0.57	0.30	2	0.09	1.8	0.05
493_11	8	20	1.6	0.45	0.03	0.74	0.08	3	0.11	2.9	0.04
493_12	22.5	20	1.6	0.58	0.09	1.08	0.07	4	0.37	4.1	0.09
493_13	24	70	1.6	0.33	0.05	0.68	0.04	4	0.10	16.5	0.01
leaching experiment IIb (multiple aliquot extraction; PS2070-1-639)											
693_1	0.5	20	1.6	0.26		0.28		1	0.05	2.0	0.02
693_2	1	20	1.6	0.17		0.38		1	0.07	2.3	0.03
693_5	2.5	20	1.6	0.18		0.32		1	0.05	1.1	0.04
693_6	3	20	1.6	0.23		0.43		1	0.04	1.2	0.03
693_7	3.5	20	1.6	0.26	0.14	0.55	0.14	3	0.09	3.9	0.02
693_8	4	20	1.6	0.19	0.27	0.34	0.33	2	0.08	2.0	0.04
693_9	5	20	1.6	0.25		0.41		1	0.05	1.3	0.03
693_10	6	20	1.6	0.23	0.42	0.42	0.63	2	0.04	1.6	0.03
693_11	8	20	1.6	0.29	0.12	0.48	0.41	2	0.05	1.3	0.04
693_12	22.5	20	1.6	0.39	0.07	0.74	0.05	3	0.07	2.0	0.03
693_13	24	70	1.6	0.52	0.02	1.00	0.07	4	0.09	10.5	0.01

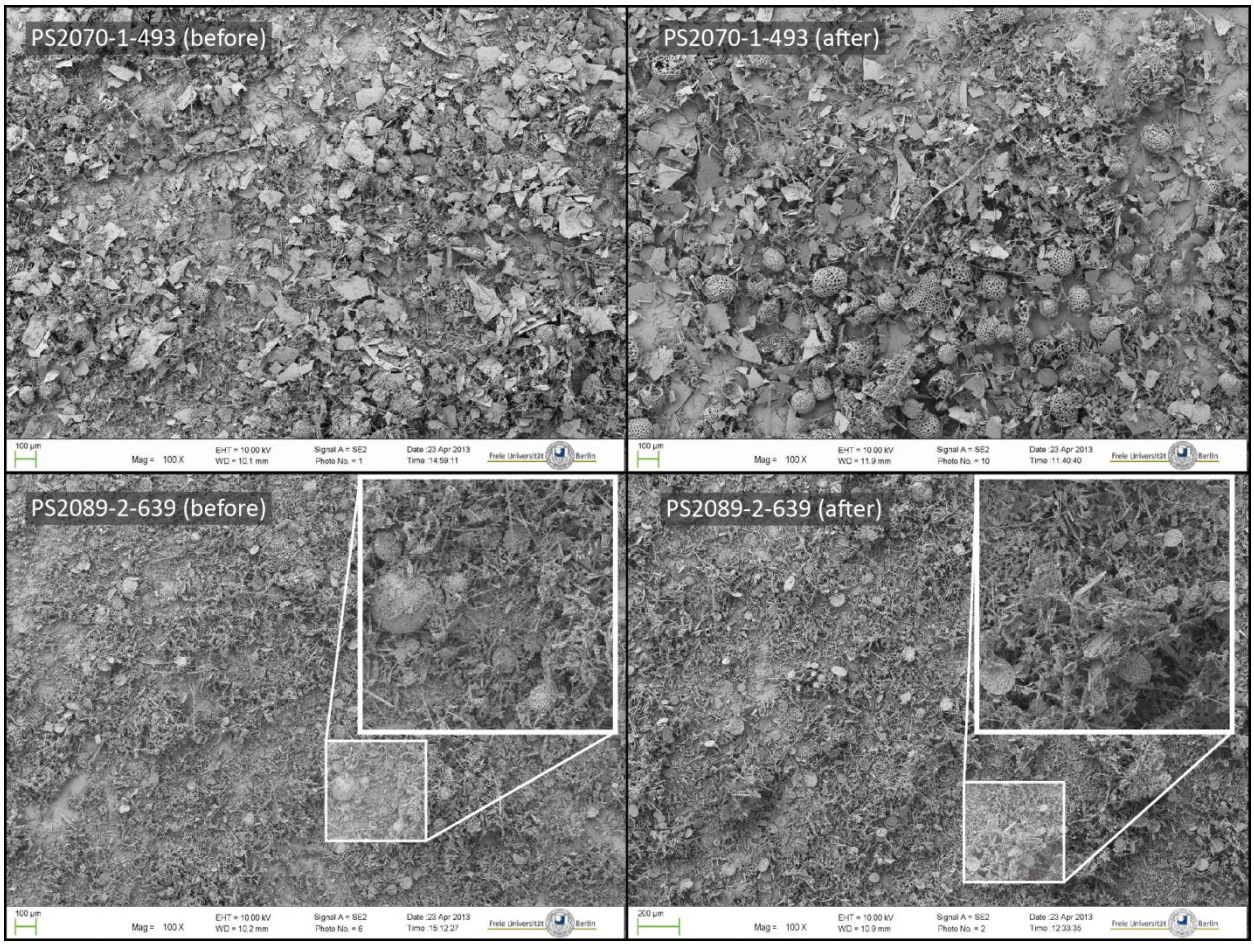

Supplementary Figure 2-1: Secondary electron microscopy (SEM) images obtained before and after the leaching treatment of samples PS2070-1-493 (experiment IIa) and PS2089-2-639 (experiment IIb) with 1.6 mm NaOH for 24 hours at 70°C. A relative increase of radiolarians is apparent in sample PS2070-1-493, after 43% of the total silica has been dissolved. Sample PS2089-2-639 almost exclusively contains diatoms and no obvious changes in composition occur after 27% of the total silicon has been dissolved.

3. Ecosystem engineering as driver for the Late Neoproterozoic ocean oxygenation

Abstract

The oxygen content of the world's ocean basins increased at the end of the Neoproterozoic (Canfield et al., 2007; Scott et al., 2008; Sperling et al., 2015) (circa 550 million years ago). Recent evidence shows that bottom water oxygenation occurred concomitantly with the Cambrian bioradiation, the appearance of almost all animal phyla on Earth (Chen et al., 2015). However, controversy exists about trigger mechanisms of this fundamental change in sea water redox state (Lenton et al., 2014). A common view holds that atmospheric oxygen built up first through increased primary productivity accompanied by decreased rates of organic carbon oxidation through enhanced burial (Derry et al., 1992; Des Marais et al., 1992; Kump, 2014; Planavsky et al., 2010). The alternative hypothesis suggests that the upper ocean was oxygenated by a shift of the oxygen demand away from shallow sea water induced by organic carbon filtration by sponges (Erwin and Tweedt, 2012). However, the test of this alternative hypothesis is hampered by hitherto lacking proxies for sponge abundance. Here, we employ the stable isotopes of silicon that distinguish between inorganic and biogenic Si precipitation in chert and siliceous shale to show that the abundance of siliceous sponge spicules increased across the transition from the Ediacaran to the Cambrian period. Seawater and benthos were oxygenated simultaneously, as reflected in increased relative cerium depletion and increased concentrations of phosphorus and barium. These data evidences that oxygenation of slope environments did not require increased atmospheric oxygen levels. The demonstration that continental slopes were colonized by siliceous sponges reveals that the ensuing 'ecosystem engineering' led to rising oxygen concentrations in shallow seawater, and, consequently facilitated the Cambrian 'explosion'.

3.1. Main text

A general assumption holds that the evolution of higher animal life forms in the Late Neoproterozoic required the availability of atmospheric oxygen (Canfield et al., 2007; Nursall, 1959). Hypothesised mechanisms for increasing atmospheric oxygen levels involve both increased oceanic primary production (Canfield et al., 2007; Planavsky et al., 2010) triggered by increased weathering fluxes (Canfield et al., 2007; Des Marais et al., 1992; Planavsky et al., 2010), and decreased oxidation rates of ferrous iron in primary bedrock minerals (Kump, 2014) and of organic carbon (Canfield et al., 2007; Des Marais et al., 1992; Planavsky et al., 2010). The competing hypothesis holds that an evolutionary innovation, namely the 'filter feeding' of benthic sponges, removed dissolved organic carbon (DOC) and fine particulate organic carbon (POC) from sea water (de Goeij et al., 2008), thereby reducing the respiratory oxygen consumption in shallow seawater (Lenton et al., 2014). Sponges selective feed upon the smaller, cyanobacteria-dominated plankton, and moreover promote the evolution of eukaryotic algae with larger average cell size (Lenton et al., 2014). Because of the resulting faster sinking rates of POC through the water column, this would have led to a lowering of the zone of maximum O_2 consumption (Lenton et al., 2014).

To test the hypothesis that ecosystem engineering by sponges caused the Late Neoproterozoic ocean oxygenation requires estimates of the variation of sponge biomass with time(Erwin and Tweedt, 2012). This estimate cannot be readily extracted from the fossil record because the preservation of sponge spicule textures is not complete. Spicules are even completely absent in the Precambrian record, despite molecular clock evidence for their evolution in the Cryogenian long before the Ediacaran (Sperling et al., 2010) (Supplementary Figure 3-1a). However, sponge spicules contain silicon with a distinct stable isotope composition (De La Rocha, 2003) that is preserved during their diagenetic recrystallisation (Supplementary Information SI 1).

Here we assess the relative amount of siliceous sponges in sedimentary strata, using a novel mass balance approach based on stable silicon isotope ratios. We furthermore reconstruct the ocean's and sediment's redox states using concentrations of proxy elements in sediment. We analysed bulk Late Ediacaran (the uppermost Neoproterozoic) to Cambrian bedded cherts and siliceous shales of the Liuchapo and Xiaoyanxi Formations in China, which were deposited in a continental slope- to basin setting at a few hundred meters water depth on the Yangtze Platform.

The normalised silicon stable isotope ratio, $\delta^{30}Si$, decreases from 1.1‰ at the base of the section to -0.5‰ at its top (Supplementary Figure 3-1b, Supplementary Table 3-4). We interpret the positive $\delta^{30}Si$ at the section's base to reflect inorganic precipitation of silicon dissolved in the ocean, consistent with $\delta^{30}Si$ of contemporaneously formed inorganic chert (Ramseyer et al., 2013). This isotope ratio reflects the ocean's dominant silicon source as slow precipitation of abiotic silica occurs in the absence of Si isotope fractionation

(Oelze et al., 2015) (Supplementary Information SI 1.4). The ocean's dissolved silicon is dominantly supplied by rivers (Tréguer et al., 1995) that carry silicon which was previously depleted in the light isotope ^{28}Si by clay formation (De La Rocha et al., 2000) during continental weathering. We see no evidence that Al/Si, or TOC/Al induce shifts in the fractionation factor (Oelze et al., 2015) during precipitation (Supplementary Information SI 1.3) and rare earth element (REE) patterns do not support increasing contribution of ^{28}Si-rich hydrothermal silicon (Supplementary Table 8). Instead, the decrease in δ^{30}Si most likely results from a continuously increasing contribution of opal from sponges that contain low δ^{30}Si (De La Rocha, 2003; Wille et al., 2010).

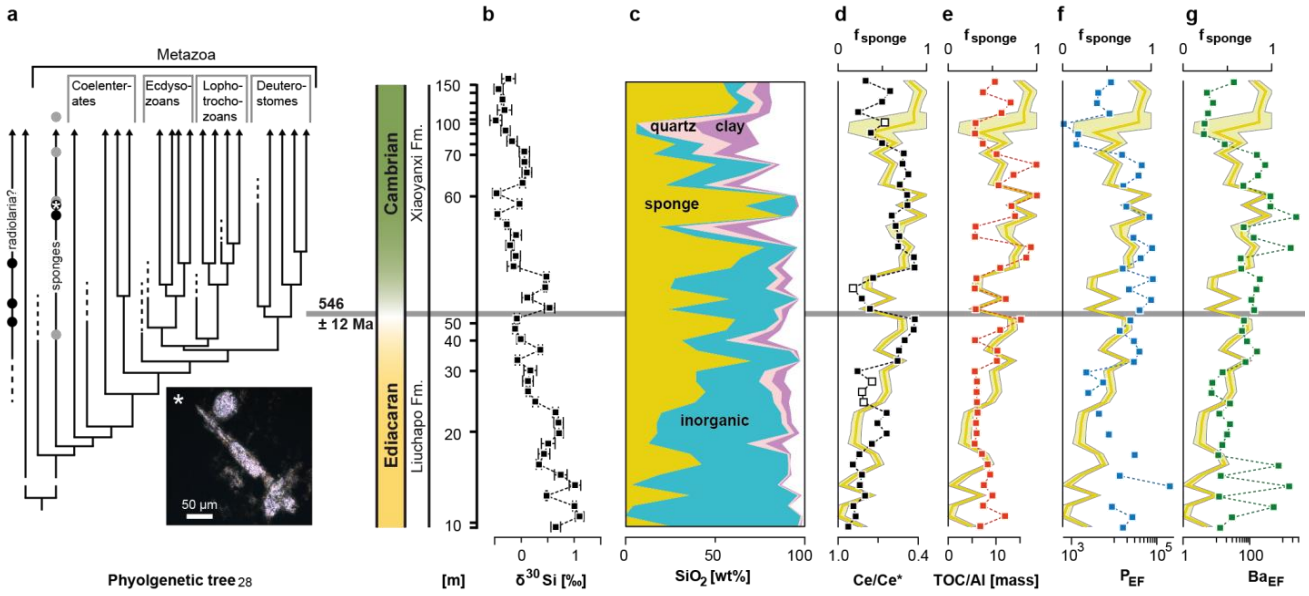

Figure 3-1: Metazoan evolution across the Precambrian-Cambrian boundary(Conway Morris, 2000) in relation to the silicon isotope- and redox record at 'Lijiatuo' section, South China. (a) Early evolution of Metazoans(Conway Morris, 2000). Circles indicate preserved sponge spicules and tentative radiolarians (black: our samples, grey: Guo et al., 2007(Guo et al., 2007b); * marks a siliceous sponge spicule shown below); (b) normalised bulk rock δ30Si; (c) calculated abundance of Si-bearing components from geochemical mass balance (see Methods Summary). For better visibility, samples are plotted with equidistant Y axis. (d) Ce/Ce*(Ce- anomalies); white symbols mark samples with Pr/Yb>1, indicating biased sea water REE pattern; and f_{sponge} (in yellow; d-g) is the abundance of Si in sponges relative to total non-detrital components; (e) TOC/Al ratios, indicating organic productivity or preservation relative to detrital mineral fluxes; (f) P- and (g) Ba-enrichment (Supplementary Information SI 2.3).

We use this trend in δ^{30}Si to quantify sponge productivity by mass balance and geochemical inversion (see Methods Summary). We assume that the isotope composition of both the inorganic seawater precipitate and the sponge end members have been constant during the investigated time interval. The oceanic Si reservoir was sufficiently large (Siever, 1992) that neither its concentration nor its δ^{30}Si was subject to detectable shifts induced by biogenic silica precipitation (Supplementary Information SI 1.4 in section 3.4.1). Thus the abundance of sponges in the sediment can be calculated (Figure 3-1c) and is defined here as a fraction f_{sponge} that does not depend on the amount of detrital mineral contents (Figure 3-1d-g) and is neither sensitive to the choice of the end member isotope composition (Supplementary Information SI 1.4 in section 3.4.1). Relative sponge abundance steadily increases from the base of the section in the Ediacaran towards

the ash layer. Following a short-term (representing circa 1.6 m in outcrop) decrease to lower abundances, relatively high abundances are maintained in the early Cambrian. Silicon isotopes thus testify to the expansion of sponges across the Ediacaran-Cambrian transition at this section.

With the appearance of filter-feeding benthic sponges, the biogeochemistry of marine ecosystems would have changed fundamentally (Erwin and Tweedt, 2012), in particular the redox state of both sea water and sediment, which are recorded by palaeo-redox proxies (Figure 3-2). Organic carbon filtration by sponges reduces the oxidation rate of organic carbon in sea water and thereby locally increases dissolved oxygen concentrations (Figure 3-2, process A). The removal of DOC and fine POC likely led to the evolution of larger, eukaryotic primary producers and thus faster organic carbon sinking rates and lower re-oxidation rates in the upper water column (Lenton et al., 2014) (Figure 3-2, process B). The resulting redox state of sea water at the water sediment interface is recorded by Ce-anomalies that express the oxidation of soluble Ce(III) to insoluble Ce(IV) (Bau and Koschinsky, 2009) relative to the adjacent REEs (Ce/Ce*). The more oxic the sea water, the lower Ce/Ce*. The overall trend shows decreasing Ce/Ce* with increasing sponge abundance (Figure 3-2d) where Ce/Ce* is circa 1 in the Ediacaran and drops to values as low as 0.42. This increasing seawater oxygen concentration over the Ediacaran is not a local feature, as confirmed by a similar evolution in Ce-anomalies in carbonates of the Ediacaran Dengying Formation (Ling et al., 2013). In the topmost part of the section Ce/Ce* increases to high values despite increasing sponge abundance. In this phase the commonly observed Cambrian transgression might have caused a local return to anoxic conditions (Zhuravlev and Wood, 1996). The resulting phytoplankton blooms together with a deeper water column overlying the benthos would have resulted in higher organic carbon concentrations that exceeded the filtering capacity of sponges.

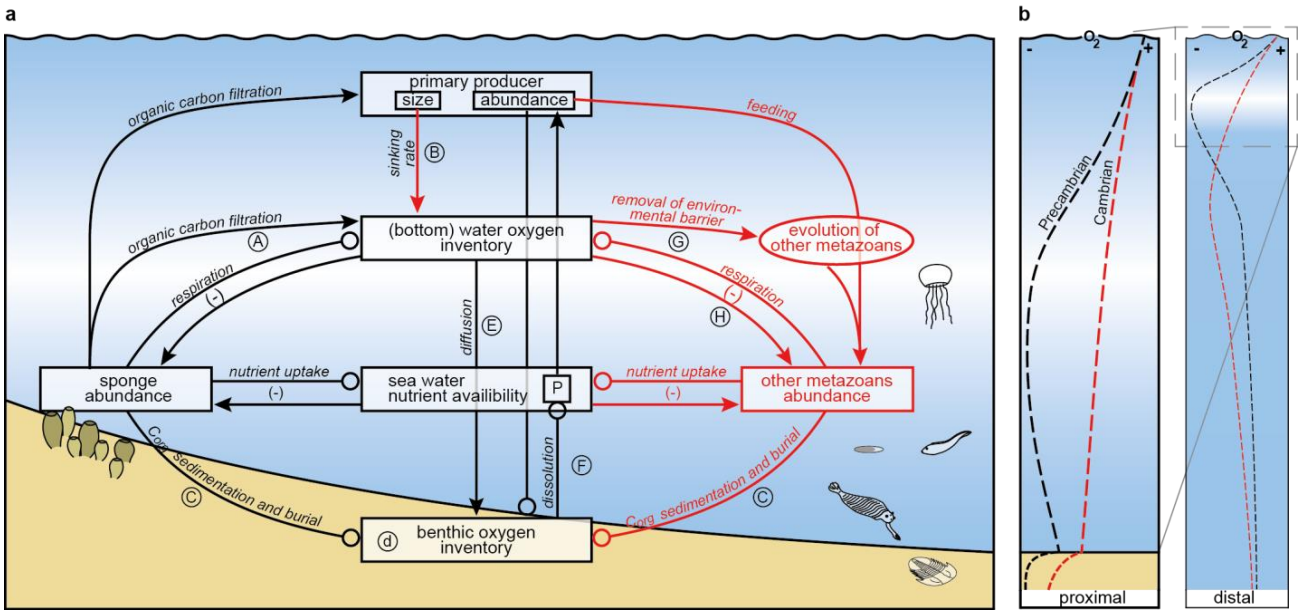

Figure 3-2: Couplings and feedbacks in the Late Neoproterozoic to Cambrian ocean ecosystem. (a) An environmental barrier in the form of insufficient oxygen concentrations was removed by filter-feeding sponges. This removal would have triggered the evolution of oxygen-respiring Metazoans; the Cambrian 'explosion'. Processes A-G are denoted by arrows and are detailed in the text. Compartments are shown by boxes, couplings and feedbacks related to sponge filtering in black and those resulting from the introduction of Metazoans in red. Arrows denote positive couplings and circles a negative couplings, together forming negative feedbacks (-). (b) The oxygen minimum zone shifted towards greater water depth, increased the benthic oxygen inventory at the continental slope (proximal), without necessarily affecting the ocean's total oxygen and carbon balance (distal).

The efficiency of organic carbon transfer from the water column to the benthos would depend on sponge abundance, too (Figure 3-2, process C). We estimate the carbon withdrawal from sea water from the TOC/Al ratio (Figure 3-1e). Even though post-depositional organic carbon oxidation potentially impairs the accuracy of this proxy, TOC/Al is well correlated with f_{sponge} after the Ediacaran/Cambrian boundary, suggesting enhanced organic carbon withdrawal from seawater with increasing sponge productivity.

Variations in the efficiency of organic carbon entrapment can further be estimated by scrutinising the benthic oxygen inventory (Figure 3-2, compartment d). The redox state of this sedimentary compartment depends on the diffusion of oxygen from bottom sea water (Figure 3-2, process E) that is balanced by organic carbon oxidation after burial. We employ two proxies: Ba is immobilized at the sulphate/sulphide redox interface in the mineral barite (Torres et al., 1996); P accumulates under (sub-) oxic conditions through the bacterial formation of refractory P-compounds (van Cappellen and Ingall, 1996). Therefore, both elements become enriched when the sediment becomes more oxic. First, the two proxies correlate well (Figure 3-1f, g), meaning that both indeed react sensitively to redox changes at the sea water-sediment interface, and that P accumulation is not primarily related to increases in productivity. Second, both proxies broadly anti-correlate with Ce/Ce* implying a link between seawater and sediment redox state. While Ba and P enrichment (Supplementary Information SI 2.3 in section 3.4.2) are relatively low in the Ediacaran, they

increase in the early Cambrian (Figure 3-1f, g). In the upper part of the section Ba and P enrichment factors return to low levels, which is consistent with increased Ce/Ce* observed in this part of the section (Figure 3-1d).

The increasing oxygen levels that were engineered by the growing sponge biomass constitute the removal of an environmental barrier that is believed to have restricted the evolution and distribution of animals with high oxygen demands (Mills and Canfield, 2014) (Figure 3-2, process G, and red arrows). The sponges inhabiting the continental shelves would have shifted the oxygen minimum zone to greater depth (Figure 3-2b) without necessarily inducing a major shift in the ocean's total oxygen and carbon balance. Shelf areas would become oxygenated and promote metazoan development.

One might argue that the appearance of oxygen-consuming Metazoans would have induced a negative feedback on dissolved oxygen concentrations (Figure 3-2, process H). However, oxygen concentrations remained at elevated levels in the Phanerozoic (Holland, 2006). Our results support the suggestion that phosphorous immobilization under (sub-)oxic bottom sea water conditions (Lenton et al., 2014) limited primary production and in turn metazoan productivity. Moreover, Metazoans introduced rapidly sinking faecal pellets that might have further inhibited carbon oxidation and supported seawater oxygenation (Logan et al., 1995). One could argue as well that our record is also compatible with radiolarians that also carry isotopically light Si in their ballasting tests, and which also lead to fast organic carbon sedimentation upon their death. However, even though radiolarians might have contributed to the recorded trends in δ^{30}Si and redox proxies, sponges have more likely been the decisive ecosystem engineers due to their low oxygen demand. One might finally argue that the inherently local nature of our record does not represent a global shift in marine biogeochemical systems, and is possibly unique. We emphasise that what we present is the hitherto lacking documentation of a trigger mechanism of these coupled systems. Due to its sensitivity to sea level and overall environmental conditions the shift might well have occurred asynchronously at different sites, or might have been obliterated elsewhere by competing processes on the Si isotope- and redox records. Such deviations and temporal shifts from this record would not invalidate the global significance of the mechanism.

It seems likely that sponge ecosystem engineering initiated substantial ecological changes in the Cambrian period and indirectly triggered the rapid expansion of animals with a higher oxygen demand. This finding implies that the Cambrian 'explosion' could proceed without increased atmospheric oxygen concentrations. In the new, Phanerozoic marine ecosystem bioproductivity was limited by reduced phosphorus recycling from sediment, a mechanism that allowed sea water- and atmospheric oxygen concentrations to reach and maintain permanently high levels.

3.2. Methods Summary

Samples were collected along the well-preserved, continuous section 'Lijiatuo' in Hunan, South China. Approximately 50 m of mostly black, Ediacaran cherts are overlain by circa 100 m of Lower- to Middle Cambrian black cherts and siliceous shales and two thin, intercalated nodular phosphorite layers. The two units are separated by a volcanic ash layer dated at 546 ± 12 Ma (Jiang et al., 2010). We estimate an approximately Middle Cambrian age for the samples highest in the section based on the assumption of constant detrital mineral depositional fluxes (Supplementary Information SI 3 in section 3.4.1). Some samples contain fragments of siliceous sponge spicules or 50-100 µm-sized spherical bodies that possibly represent radiolarians (siliceous zooplankton), the earliest appearances of which date back to the Early Cambrian (Figure 3-1a).

Sponge abundances reported in this study are calculated by mass balance and geochemical inversion. First, we built a set of mass balance equations based on Si stable isotopes and Al/Si ratios, consisting of five equations and 15 parameters, each of which has been assigned an *a priori* value and an *a priori* uncertainty (Supplementary Information SI 1.4 in section 3.4.1). We then solved this system using a full inversion procedure that iteratively seeks for the best solution to the system of equations in a least square sense. We then obtain a set of *a posteriori* values and associated uncertainties.

A priori values were estimated for four major compartments present in the chert samples that contain Si (inorganically precipitated silica, sponge silica, detrital quartz, and illite, see Supplementary Information SI 1.4 in section 3.4.1 for the choice of values). Illite abundances are estimated from Al/Si of bulk chert. We assume that equal amounts of detrital and authigenic illite were initially deposited and that silica released from the diagenetic reaction K-feldspar + K-smectite → illite, i.e. 2 moles SiO_2 per mole illite are conserved in the sediment. We estimate the detrital quartz fraction from a constant clay/detrital quartz ratio of 1.7 estimated from carbonate-poor shales. We assume $\delta^{30}Si$ of -0.1 ± 0.2‰ $\delta^{30}Si$ for quartz and -0.8‰ ± 0.3‰ for clay (in agreement with the measured isotope composition of a kaolinite-rich mudstone Li173 and the clay Si isotope composition extrapolated from the shale sample with the highest Al-content, Li31). The Si isotope composition of the sponge end member is constrained by a well-preserved sponge spicule from the early Cambrian Niutitang Fm. of 'Tongpengai' section, Guizhou Province. The spicule was analysed *in situ* by femtosecond UV laser ablation multi-collector inductively coupled plasma mass spectrometry (fs-LA-MC-ICP-MS) (Schuessler and von Blanckenburg, 2014) and yielded $\delta^{30}Si$ of -0.53 ± 0.33‰ (2SD, n= 13). The isotope composition of inorganically precipitated silica is estimated from the isotopic composition of dissolved silicon in modern river water to $\delta^{30}Si$= 1.1‰ ± 0.5‰. This silicon is assumed to dominate the ocean at the Cambrian/Precambrian boundary and to form inorganic opal in the absence of isotope fractionation during slow precipitation of inorganic silica (Oelze et al., 2015). This composition agrees with measurements of inorganic chert from this period (Ramseyer et al., 2013). We note that while the

inferred abundance depends on the choice of the isotope end member compositions, patterns of temporal changes are insensitive to these choices.

3.3. Acknowledgements

MT is grateful for funding provided by the DFG through research group FOR736 “The Precambrian-Cambrian Ecosphere (R)evolution: Insights from Chinese microcontinents” (grant no. BL 562/11-2). We thank J.A. Schuessler for continuous laboratory support, R. Naumann and C. Kotre for XRD analyses, B. Plessen for C and N isotope analyses, M. Steiner for the sponge spicule specimen, B. Kamber, S. Hohl, J. Payne, and K. Lau for discussions.

3.4. Supplementary Information

The supplementary information comprises details about the mass balance and inversion calculation (Supplementary Information 1), analytical methods including Si isotope analyses and major-and trace element analyses (Supplementary Information 2), the construction of the age model (Supplementary Information 3), and analytical results from complementary C- and N isotope analyses (Supplementary Information 4).

3.4.1. Si isotope mass balance and inversion (SI 1)

3.4.1.1. The preservation of the Si isotope record of Neoproterozoic chert (SI 1.1)

The silicon isotope record of Ediacaran to Cambrian cherts and siliceous shales provides information about silicon sources. This inference depends on the requirement that the silicon isotope composition of bulk sedimentary rock has not been altered during diagenesis. From an unaltered bulk rock Si isotope composition relative proportions of source components can be calculated using a mass balance approach.

Early diagenesis of amorphous silica precursors of these cherts has likely not significantly altered their silicon isotope composition. Early diagenesis of silica may bias the silicon isotope composition of siliceous sediments (Ziegler and Marin-Carbonne, 2012). However, these processes occur when seawater silicon concentrations are below the equilibrium solubility of the sediment, such as in modern ocean settings. In the Precambrian, seawater silicon concentration were much higher because organisms taking up dissolved silicon had not yet appeared (Holland, 1972). The seawater silicon concentration was controlled by the precipitation of clay minerals, zeolites, organic matter, and silica phases and is estimated to be ca. 28 ppm Si (Siever, 1992) or even >51 ppm Si (Grenne and Slack, 2003). These conditions caused diffusion of dissolved silicon into sediments (Siever, 1992) and allowed direct precipitation of opal-CT (minimum equilibrium concentration of ca. 12 ppm Si at 20°C; Walther and Helgeson, 1977; Williams et al., 1985). Sponges and radiolarians were the first organisms with siliceous skeletons and appeared when sea water silicon concentrations were still high, precluding the dissolution of these skeletons during early diagenesis. These conditions allow for the preservation of the Si isotope composition of bulk sediments in Late Neoproterozoic chert and siliceous shale. Their increasing abundance until the Ordovician led to a continuous decrease in the seawater Si concentration and consequently to declining importance of inorganic silicon withdrawal from seawater (Kidder and Erwin, 2001; Maliva and Siever, 1989). At that time, diagenetic effects that bias the silicon isotope composition of opal potentially became more important.

During later burial, diagenetic exchange of silicon between sedimentary layers through dissolution-reprecipitation during opal-to-quartz conversion can affect the isotope composition of the diagenetic product. However, later diagenetic exchange between layers of buried siliceous sediment is expected to be largely determined by the variability of detrital mineral contents between sediment layers, because detrital/opal ratios determine the depth of diagenetic transformation (Isaacs, 1982). Each sediment layer would have evolved isolated from the others, inhibiting the exchange of silicon isotopes. Furthermore, the overall high abundance of clay minerals impaired fluid flow and hence inter-layer Si mobility. While a high variability of δ^{30}Si at the micro-scale testifies to diagenetic dissolution-reprecipitation (Marin-Carbonne et al., 2012), bulk chert δ^{30}Si is preserved even under metamorphic conditions through the high abundance of Si in most rocks (André et al., 2006). We conclude that a diagenetic bias of the silicon isotope composition of our samples is negligible and that the bulk rock silicon isotope composition can be used to estimate relative abundances of silicon sources.

3.4.1.2. Preservation of the Si isotope composition of sponge spicules (SI 1.2)

We cannot exclude a bias in the isotope composition of the analysed Lower Cambrian sponge spicule (Supplementary Table 1) during phase transformations of biogenic silica into (opal-CT and) quartz. Its negative δ^{30}Si however agrees with the preferential uptake of light silicon by modern sponges. In support of preservation, Eocene/Oligocene sponge spicules were found to be resistant against early diagenetic Si exchange (De La Rocha, 2003).

Supplementary Table 3-1: Silicon isotope composition (‰) of sponge spicules from Early Cambrian 'Tongpengai' section, Guizhou Province as analyzed by femtosecond laser ablation MC-ICP-MS. The internal standard error of the mean (2SE) is given for each single sample measurement (n= 80 integrations á 1 second). The uncertainty of the fs-LA-MC-ICP-MS method (external long-term repeatability) is ±0.15‰ (2SD) for $\delta^{29}Si$ and ±0.23‰ (2SD) for $\delta^{30}Si$, respectively (Schuessler and von Blanckenburg, 2014).

Sample	$\delta^{29}Si$ [‰]	2SE	$\delta^{30}Si$ [‰]	2SE
b x l 1r	-0.26	0.09	-0.59	0.14
b x l 2l	-0.41	0.09	-0.89	0.14
b x l 2r	-0.19	0.10	-0.41	0.16
b x l 3l	-0.24	0.09	-0.53	0.12
b x l 3r	-0.18	0.09	-0.38	0.13
b x l 5l	-0.23	0.08	-0.41	0.14
b x l 5r	-0.15	0.08	-0.35	0.12
b x s 1	-0.13	0.08	-0.33	0.14
b x s 2o	-0.22	0.09	-0.46	0.16
b x s 2u	-0.34	0.09	-0.75	0.13
b x s 3o	-0.23	0.09	-0.59	0.15
b x s 4	-0.26	0.09	-0.59	0.12
b x c	-0.31	0.08	-0.60	0.15
Average	-0.24		-0.53	
95% CI	0.05		0.10	
2SD	0.16		0.33	

3.4.1.3. Constant Si isotope fractionation factor during silica precipitation (SI 1.3)

The decrease in the $\delta^{30}Si$ signature observed in the 'Lijiatuo' section might also be induced by an increasing fractionation factor related to a changing depositional setting. Major differences in host rock lithology are increased Al/Si and increased TOC/Al ratios, both of which potentially affect the rates of precipitation (Oelze et al., 2014; Siever, 1992) and hence fractionation factors. To test if bulk chert $\delta^{30}Si$ has been affected by such variations, we have sampled several chert samples from within the same level of two continuous chert layers at 'Longbizui' section, South China (28°30'0.00"N, 109°50'24.00"E) and analysed concentrations of Al, TOC, Si as well as the bulk chert silicon isotope composition. The bulk chert $\delta^{30}Si$ signature of all samples within one chert layer is analytically indistinguishable despite a large range of Al/Si and TOC/Al ratios observed (Supplementary Figure 1). Therefore we conclude that the fractionation factor during silica precipitation was not affected by varying Al/Si or TOC/Al ratios. We therefore interpret the changes of the $\delta^{30}Si$ signature in the 'Lijiatuo' section to denote changes in the abundance of sponge spicules deposited (main text, Figure 3-1).

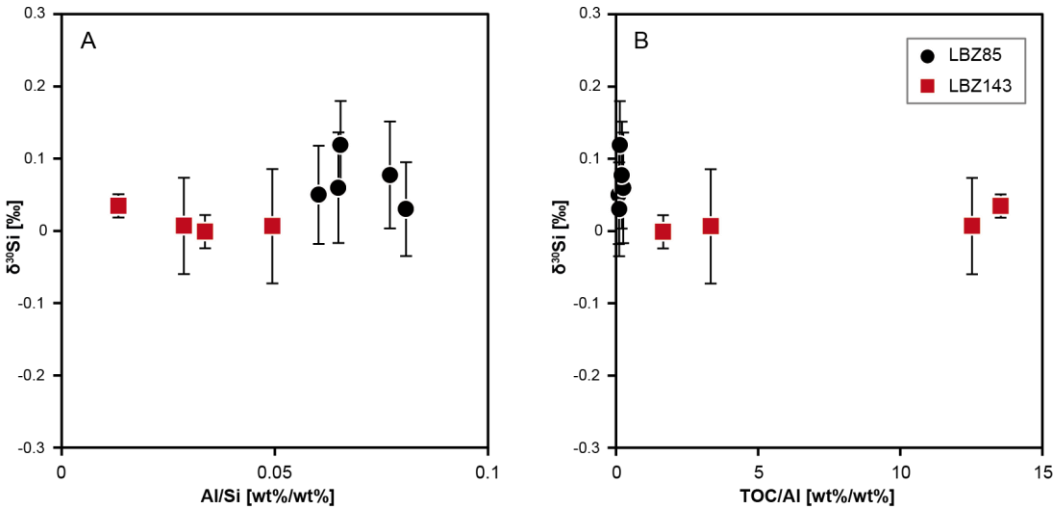

Supplementary Figure 3-1: Bulk chert silicon isotope composition of chert samples from two continuous chert layers (LBZ85, LBZ, 143). Samples were collected approximately 1 m apart from another along distinct chert beds at 'Longbizui' section, South China (a) Al/Si and (b) TOC/Al vary while δ^{30}Si remains constant, indicating that the silicon isotope fractionation factor during precipitation was not affected by variations thereof.

3.4.1.4. Geochemical mass balance and inversion (SI 1.4)

The sampled chert consists of silica inorganically precipitated from seawater, detrital minerals (clays: "detr" and quartz: "qtz", authigenic illite: "auth"), and silica from sponge spicules. Contribution of silicon from hydrothermal sources is negligible in our samples as suggested by typical sea water rare earth element (REE) patterns. Hydrothermal fluids typically carry silicon with δ^{30}Si≈ -0.3‰ (De La Rocha et al., 2000; Ding et al., 1996; Douthitt, 1982), where precipitation with α<1 from hot, Si saturated fluids would further significantly deplete the δ^{30}Si of the precipitate (Geilert et al., 2014a; Roerdink et al., 2015). Therefore, a dominating contribution from such source would shift the δ^{30}Si of chert towards overall higher values likely following a Rayleigh trend. However, the opposite trend is seen. Therefore, the chemical and Si isotope composition of bulk samples is a mixture between six end members (see below), the relative fractions of which are expressed here in Si mass fractions *f*. In order to calculate the contribution of sponge material in each sample, the following mass balance equations can be written:

$$\left(\frac{Al}{Si}\right)_{chert} = f(Si)_{detr} \cdot \left(\frac{Al}{Si}\right)_{detr} + f(Si)_{auth} \cdot \left(\frac{Al}{Si}\right)_{auth}$$

Supplementary Equation 3-1

The dominant detrital mineral of the siliceous shales and chert is illite (Supplementary Table 6) and thus for simplification we assume that Al is exclusively present in illite. This assumption is verified by exemplary quantitative XRD analyses show that this approximation yields calculated amounts of illite that are within uncertainty identical to measured amounts (Supplementary Table 2). Furthermore, we assume that detrital (*detr*) and authigenic illite (*auth*) are present (Supplementary Equation 3-1).

$$\delta^{30}Si_{chert} = (f(Si)_{detr} + f(Si)_{auth} + f(Si)_{sds}) \cdot \delta^{30}Si_{clay} + f(Si)_{qtz} \cdot \delta^{30}Si_{qtz} + f(Si)_{inorg} \cdot \delta^{30}Si_{inorg} + f(Si)_{sponge} \cdot \delta^{30}Si_{sponge}$$

Supplementary Equation 3-2

where $\left(\frac{Al}{Si}\right)_j$ and $\delta^{30}Si_j$ are the molar Al/Si ratio and Si isotope ratio, respectively, of the bulk sample (*j= chert*) or end member (quartz: *j= qtz*, detrital clays: *j= detr*, authigenic clays: *j= auth*, smectite-derived silica: *j= sds*, inorganically precipitated silica: *j= inorg*, and sponge silica: *j= sponge*), and $f(Si)_j$ is the fraction of bulk Si that is present in the end member *j*, such that:

$$f(Si)_{detr} + f(Si)_{auth} + f(Si)_{sds} + f(Si)_{qtz} + f(Si)_{inorg} + f(Si)_{sponge} = 1$$

Supplementary Equation 3-3

The smectite-derived silica end member ($f(Si)_{sds}$) accounts for the fact that the reaction of illite and K-feldspar to smectite during diagenesis releases two moles SiO_2 per mole of illite formed(Abercrombie et al., 1994).

Additional constraints can be used for this mass balance. As shown in Supplementary Equation 3-2, we assume that smectite-derived silica, detrital clays and authigenic clays have the same Si isotope composition (see discussion below). A fraction of the illite in the chert is likely of detrital origin rather than authigenic:

$$f(Si)_{detr} = r_1 \cdot f(Si)_{auth}$$

Supplementary Equation 3-4

with $r_1$the ratio between the number of Si moles carried by detrital illite and that carried by authigenic illite. The rest of the detrital material is formed of quartz:

$$f(Si)_{detr} + f(Si)_{auth} = r_2 \cdot f(Si)_{qtz}$$

Supplementary Equation 3-5

with r_2 the ratio between the number of Si moles carried by illite and that carried by quartz.

Our mass balance problem is thus a system of 5 equations and 15 parameters, that we solve using a full inversion procedure (Allègre and Lewin, 1989; Tarantola and Valette, 1982). The first step of the inversion procedure is the estimation of input values and associated uncertainties (‘*a priori*’). The input parameters are estimated assuming likely values for Al/Si ratios and silicon isotope composition of the respective compartments, measured bulk rock Al concentrations, bulk rock and sponge δ^{30}Si, and assumed detrital mineral chemical composition and isotope composition of end members. In a second step we solve this system using a full inversion procedure that iteratively seeks for the best solution to the system in a least square sense (Allègre and Lewin, 1989; Tarantola and Valette, 1982). This inversion is performed separately

for each sample, such that end members are allowed to be different from a sample to another. We then obtain a set of *a posteriori* values and associated uncertainties.

A priori values for $\left(\frac{Al}{Si}\right)_{chert}$ and $\delta^{30}Si_{chert}$ were taken from measurements and associated analytical uncertainties. We assume the Al/Si of detrital illite to be $\left(\frac{Al}{Si}\right)_{detr} = 0.791 \pm 0.158$ considering a typical stoichiometry of $K_{0.65}Al_{2.65}Si_{3.35}O_{10}(OH)_2$("www.mindat.org/min-2011.html," 2015) and assume a 20% uncertainty on this element ratio. As *a priori* Al/Si ratio of authigenic illite we assume $\left(\frac{Al}{Si}\right)_{auth} = 0.609 \pm 0.122$ (20%), accounting for the two moles SiO_2 that are generated during diagenetic smectite- to illite conversion(Abercrombie et al., 1994). As authigenic illite contains twice as much SiO_2 in mass compared to detrital illite, *a priori* $r_1 = 2 \pm 0.5$. Fine-grained clastic sediments also contain a fraction of detrital quartz, which is difficult to quantify. We assume that the clay/detrital quartz ratio is around 1.7 (Shaw and Weaver, 1965). In terms of the ratio of moles Si in illite over moles Si in quartz, this yields $r_2 = 1.0$ (with an assumed uncertainty of ± 0.5). For the sponge- $\delta^{30}Si_{sponge}$ and inorganic silica $\delta^{30}Si_{inorg}$ end-members we use -0.53 ± 0.33‰ δ^{30}Si and 1.1 ± 0.5‰ δ^{30}Si; for clay $\delta^{30}Si_{clay}$ and detrital quartz $\delta^{30}Si_{qtz}$ we use -0.80 ± 0.3‰ δ^{30}Si and -0.1 ± 0.3‰ δ^{30}Si, respectively. These values are justified in sections below. *A priori* values for the relative mass fraction of Si in each component $f(Si)_j$ are calculated from the above mass balance equations. For detrital ($f(Si)_{detr}$) and authigenic ($f(Si)_{auth}$) clays we assume 10% *a priori* uncertainty on the calculated values, for quartz ($f(Si)_{qtz}$) 50%, for sponge derived silica ($f(Si)_{sponge}$) and inorganically precipitated silica ($f(Si)_{inorg}$) 20%.

Supplementary Table 3-2: Illite mass fractions of some samples [wt%] as determined by quantitative XRD measurements and calculated from bulk rock Al/Si based on assumptions discussed in section 1.3. The uncertainty on calculated Al/Si is estimated to 7%; on quantitative XRD analyses to <10%.

	Illite[wt%]	
	XRD	**Calculated from Al/Si**
Li20a	12.5	14.7
Li24b	7.7	6.9
Li31	46.6	45
Li36	9.2	9.4

The silicon isotope composition of inorganically precipitated silica

Inorganically precipitated silica carries the isotopic signature of its sea water source if no fractionation occurs during precipitation (α=1). Such absence of fractionation is supported by recent experimental work on isotope fractionation during silica precipitation (Oelze et al., 2015; Roerdink et al., 2015) and adsorption (Oelze et al., 2014). Seawater is isotopically heavy because most of its Si ultimately derives from river water. Modern rivers consistently yield Si enriched in heavy isotopes: ca. 1.0‰ (the Congo River main branch;

Cardinal et al., 2010); ca. 1.6‰ (average value; tributaries draining into Lake Tanganyika; Alleman et al., 2005); 0.92‰ (the Amazon river; Hughes et al., 2013); and 0.7 to 3.4‰ (the Yangtze River; Ding et al., 2004). Si in rivers is isotopically heavy due to clay mineral formation(De La Rocha et al., 2000) and silica adsorption in the weathering zone on land, where light isotopes are preferentially incorporated into the solid (Delstanche et al., 2009; Oelze et al., 2014). Isotopically heavy residual waters are being supplied to river- and ground water and eventually to sea water, out of which inorganic precipitation can occur upon silica oversaturation in marine pore waters. Short-term fluctuations in the isotope composition of this component e.g. through variations in weathering intensity, changing drainage areas, or changing seawater circulation will not be recorded due to the high residence time of silicon in the Precambrian/Cambrian ocean that is estimated to be around 1 Ma (Chakrabarti et al., 2012). We assume that the heaviest isotope composition measured in chert represents that of the riverine input, and hence of the inorganic precipitate (before the introduction of sponges): *a priori* $\delta^{30}Si_{inorg}$ = 1.1‰ ± 0.5.

The silicon isotope composition of detrital quartz and clay

Detrital quartz and clay have comparably well-known Si isotope compositions. Because most detrital quartz has an igneous or metamorphic source, its isotope composition is relatively uniform whereas clay δ^{30}Si bears a greater variability, where clay δ^{30}Si is typically negative (Georg et al., 2009; Opfergelt and Delmelle, 2012; Opfergelt et al., 2012). The *a priori* $\delta^{30}Si_{qtz}$ was set to -0.1 ± 0.2‰ δ^{30}Si, overlapping with average values determined for loess (comprising both quartz and feldspar) of -0.22‰ δ^{30}Si (Savage et al., 2013); for clay we assume -0.8‰ δ^{30}Si, in agreement with the measured isotope composition of a kaolinite-rich mudstone (Li173; Supplementary Table 4) and the clay Si isotope composition extrapolated from the shale sample with the highest Al-content (Li 31; Supplementary Table 4). We assume a common δ^{30}Si *a priori* value for detrital and authigenic clay $\delta^{30}Si_{clay}$ = -0.8 ± 0.3‰.

The silicon isotope composition of sponge silica

Sponge silica is isotopically distinct from seawater through preferential uptake of light silicon. Modern sponges fractionate Si isotopes with up to $\alpha_{(sponge\text{-}seawater)}$= 0.995 (Hendry and Robinson, 2012; Wille et al., 2010) where Si isotope fractionation by modern sponges reveals a dependence on seawater silicon concentrations between ca. 1.7 ppm (ca. 60 µmol/L) (Wille et al., 2010) and ca. 4.2 ppm (150 µmol/L) (Hendry and Robinson, 2012). As Si concentrations were much higher in the Late Neoproterozoic, we predict that small variations in Si concentration would not affect the magnitude of Si isotope fractionation by sponges (Wille et al., 2010). We therefore assume a constant sponge Si δ^{30}Si in the 'Lijiatuo' section. For the inversion calculation we use the measured Si isotope composition of the Cambrian sponge spicule $\delta^{30}Si_{sponge}$ = -0.53 ± 0.33‰ δ^{30}Si (2SD) as *a priori* value for sponge silica. The assumed end member isotope compositions of inorganically precipitated silica (and hence sea water) and the measured sponge spicule suggest a minimum estimate for Si isotope fractionation by the first sponges of $\alpha_{(sponge\text{-}seawater)}$= 0.9984.

The calculated relative fraction of sponge-derived Si would be systematically reduced if sponges had lower δ^{30}Si values. Similarly, if $\delta^{30}Si_{inorg}$ was under- or overestimated, the calculated value of f_{sponge} would differ from the values obtained here. Nevertheless, relative trends with time are not sensitive on the choice of the end member composition. Additionally, we argue that changes in the sea water Si isotope composition induced by removing sponge Si itself are unlikely. Indeed, the Si inventory of the ancient ocean was so large that a comparatively small Si output flux by sponges was not able to significantly shift the sea water silicon isotope composition (we note that such a mass balance effect cannot be induced by inorganic silica precipitation as its α= 1, see above). However, even if there were a shift in sea water δ^{30}Si induced by sponge spicule formation, the resulting increase in seawater δ^{30}Si would actually result in underestimated sponge abundances. Such underestimate would be most pronounced in the upper layers where f_{sponge} is highest,

meaning we underestimate their contribution in our current analysis. Such underestimate would leave our results and interpretation unchanged.

3.4.2. Analytical methods (SI 2)

3.4.2.1. Si-isotope analyses (SI 2.1)

Solution MC-ICP-MS silicon isotope analyses

Silicon stable isotope ratios were determined on a Thermo Neptune multi-collector inductively coupled plasma mass spectrometer (MC-ICP-MS) equipped with a Neptune Plus Jet Interface at GFZ Potsdam following protocols detailed in Oelze et al. (2014). Samples were diluted to 0.4 to 1 ppm Si with identical concentrations of Mg added and introduced into an ESI APEX desolvator. Analyses were done in medium- or high resolution mode and yielded signal intensity of usually > 10 V on a Faraday cup (10^{11} Ω) for ^{28}Si; blank intensities were usually <5 mV. Mass bias correction was done by standard-sample bracketing after internal correction of mass bias drift by Mg isotope ratios. The ^{29}Si/^{28}Si and ^{30}Si/^{28}Si isotope ratios are reported as per mill deviation from the international reference material NIST 8546 *aka.* NBS 28, i.e. by multiplying Supplementary Equation 3-6 with 10^3:

$$\delta\left(30/28_{Si}\right)_{NBS28} = \left[\frac{\left(\frac{^{30}Si}{^{28}Si}\right)_{sample}}{\left(\frac{^{30}Si}{^{28}Si}\right)_{NBS28}} - 1\right]$$

Supplementary Equation 3-6

We abbreviate $\delta(^{30/28}Si)_{NBS\ 28}*10^3$ as δ^{30}Si and report average δ-values obtained from typically 4 to 7 replicate measurements of the same analyte solution and their 95% confidence interval (= t·SD/√n) which indicates instrument repeatability. Quality control standards were regularly measured and yielded results in agreement with published data (Supplementary Table 3). Results from solution Si isotope analyses are compiled in Supplementary Table 3.

Supplementary Table 3-3: Silicon isotope data of solution MC-ICP-MS measurements of reference materials obtained during this study. Individual measurements from different analytical sessions are listed. Average δ-values and their 95% confidence interval (= t·SD/√n), are calculated (intermediate precision of the mass spectrometric method, instrument repeatability). The uncertainty of the solution MC-ICP-MS method (external long-term repeatability) is estimated to be ± 0.07‰ (2SD) for δ^{29}Si and ± 0.10‰ (2SD) for δ^{30}Si. Published values of reference materials are within uncertainty identical to values measured during this study. BigBatch: δ^{29}Si= -5.35 ± 0.15‰ (1SD, average of 11 published average values (Reynolds et al., 2007)), δ^{30}Si= -10.48 ± 0.27‰ (1SD, average of 11 published average values (Reynolds et al., 2007)); Diatomite: δ^{29}Si= 0.64 ± 0.02‰ (1SD, average of 9 published average values reported on GeoREM (Jochum et al., 2005)), δ^{30}Si= 1.24 ± 0.06‰ (1SD, average of 15 published average values reported on GeoREM (Jochum et al., 2005)); IRMM17: δ^{29}Si= -0.69 ± 0.04‰ (1SD, average of 3 published average values reported on GeoREM (Jochum et al., 2005)), δ^{30}Si= -1.33 ± 0.08‰ (1SD, average of three published average values reported on GeoREM (Jochum et al., 2005)); BHVO-2: δ^{29}Si= -0.14 ± 0.04‰ (1SD, average of 12 published values(Reynolds et al., 2007)), δ^{30}Si= -0.28 ± 0.05‰ (1SD, average of 18 published average values (Reynolds et al., 2007)).

Big Batch	**δ^{29} Si**	**δ^{30} Si**
011-BigBatch	-5.47	-10.71
043-BigBatch	-5.47	-10.74
027-BigBatch	-5.43	-10.74
043-BigBatch	-5.46	-10.63
059-BigBatch	-5.39	-10.68
035-BigBatch	-5.51	-10.67
075-BigBatch	-5.46	-10.64
113-BigBatch	-5.40	-10.60
153-BigBatch	-5.44	-10.63
003-BigBatch	-5.33	-10.70
075-BigBatch	-5.49	-10.69
003-BigBatch	-5.44	-10.79
039-BigBatch	-5.46	-10.70
003-BigBatch	-5.45	-10.80
029-BigBatch	-5.45	-10.69
065-BigBatch	-5.47	-10.72
101-BigBatch	-5.43	-10.83
137-BigBatch	-5.49	-10.79
029-BigBatch	-5.46	-10.64
069-BigBatch	-5.49	-10.60
107-BigBatch	-5.43	-10.63
Average	-5.45	-10.70
95%CI	0.02	0.03

Diatomite	**δ^{29} Si**	**δ^{30} Si**
015-Diatomite	0.60	1.23
047-Diatomite	0.66	1.24
015-Diatomite	0.64	1.25
031-Diatomite	0.68	1.27
047-Diatomite	0.59	1.22
063-Diatomite	0.63	1.29
039-Diatomite	0.60	1.27
077-Diatomite	0.68	1.30
117-Diatomite	0.62	1.25
155-Diatomite	0.65	1.22
005-Diatomite	0.61	1.22
041-Diatomite	0.66	1.29
005-Diatomite	0.62	1.25
041-Diatomite	0.64	1.28
005-Diatomite	0.65	1.20
035-Diatomite	0.69	1.25
071-Diatomite	0.68	1.28
107-Diatomite	0.72	1.35
143-Diatomite	0.69	1.33
Average	0.65	1.26
95%CI	0.02	0.02

continued

IRMM-017	δ^{29} Si	δ^{30} Si
009-IRMM17	-0.65	-1.33
009-IRMM17	-0.73	-1.32
045-IRMM17	-0.65	-1.35
009-IRMM17	-0.73	-1.43
033-IRMM17	-0.73	-1.43
069-IRMM17	-0.71	-1.42
105-IRMM17	-0.69	-1.39
141-IRMM17	-0.74	-1.35
033-IRMM17	-0.67	-1.32
071-IRMM17	-0.73	-1.32
111-IRMM17	-0.76	-1.44
Average	-0.71	-1.37
95%CI	0.03	0.03

BHVO-2	δ^{29} Si	δ^{30} Si
009-BHVO	-0.07	-0.24
025-BHVO	-0.15	-0.29
041-BHVO	-0.18	-0.29
057-BHVO	-0.14	-0.26
025-BHVO	-0.14	-0.32
041-BHVO	-0.13	-0.25
057-BHVO	-0.13	-0.25
033-BHVO	-0.10	-0.23
071-BHVO	-0.15	-0.27
111-BHVO	-0.17	-0.25
149-BHVO	-0.14	-0.25
015-BHVO	-0.17	-0.34
051-BHVO	-0.14	-0.29
015-BHVO	-0.18	-0.37
039-BHVO	-0.14	-0.24
077-BHVO	-0.10	-0.18
117-BHVO	-0.15	-0.21
Average	-0.14	-0.27
95%CI	0.02	0.02

Supplementary Table 3-4: Silicon isotope composition (‰) of bulk chert and silicified shales of 'Lijiatuo' section as analyzed by MC-ICP-MS. Average δ-values of n replicate measurements and their 95% confidence intervals (= t·SD/√n) are reported. 95%CI indicates the intermediate precision of the mass spectrometric method (instrument repeatability). The uncertainty of the solution MC-ICP-MS method (external long-term repeatability) is estimated to be ± 0.07‰ (2SD) for $\delta^{29}Si$ and ± 0.10‰ (2SD) for $\delta^{30}Si$.

Sample	height above section base [m]	$\delta^{29}Si$	95%CI [‰]	$\delta^{30}Si$ [‰]	95%CI	n
Li1	0.20	0.33	0.08	0.65	0.09	4
Li2	9.45	0.56	0.04	1.10	0.08	6
Li-11.5-12	11.50	0.51	0.04	1.00	0.04	4
Li3	12.50	0.25	0.02	0.48	0.01	23
Li-13.5-12	13.50	0.53	0.03	1.01	0.11	4
Li-15-12	15.00	0.39	0.09	0.75	0.12	4
Li-16.2-15-	15.60	0.15	0.02	0.33	0.05	4
Li-16.2-12	16.20	0.21	0.05	0.43	0.11	4
Li-17.5-12	17.50	0.26	0.07	0.51	0.13	4
Li4	18.50	0.36	0.05	0.71	0.08	4
Li-20.5-12	20.50	0.34	0.06	0.71	0.09	4
Li-21.4-12	21.40	0.31	0.04	0.65	0.05	4
Li-24.5-12	24.50	0.15	0.06	0.27	0.05	4
Li5	24.50	0.04	0.06	0.13	0.03	4
Li-26.5-12	26.50	0.05	0.04	0.12	0.10	4
Li-28.5-12	28.50	0.08	0.07	0.17	0.12	4
Li6	30.50	-0.05	0.04	-0.07	0.04	4
Li7b	31.00	0.19	0.05	0.36	0.04	5
Li7a	36.50	-0.01	0.03	-0.01	0.07	5
Li9a	46.50	-0.03	0.03	-0.11	0.05	5
Li9b	46.60	-0.04	0.04	-0.08	0.05	5
Li12a	52.00	0.27	0.02	0.53	0.10	4
Li12b	52.05	0.07	0.03	0.11	0.10	4
Li16	53.06	0.24	0.06	0.45	0.02	4
Li18	53.60	0.25	0.08	0.48	0.05	5
Li19a	53.87	-0.09	0.08	-0.14	0.12	4
Li19b	54.04	-0.04	0.06	-0.10	0.09	4
Li20b	54.5	-0.11	0.06	-0.21	0.08	4
Li20a	54.6	-0.05	0.03	-0.10	0.10	5
Li21B-hr	55.13	-0.12	0.02	-0.27	0.03	7
Li22	55.52	-0.21	0.08	-0.45	0.05	5
Li23a	56.42	-0.02	0.06	-0.03	0.04	4
Li23b	56.52	-0.26	0.03	-0.47	0.08	4
Li24a	60.93	0.01	0.03	0.02	0.06	4
Li24b	60.98	0.06	0.07	0.11	0.09	5
Li25b	61.5	0.06	0.07	0.06	0.09	4
Li25a	61.6	0.05	0.03	0.06	0.10	4
Li29	77	-0.10	0.07	-0.17	0.10	5
Li30	87.25	-0.16	0.05	-0.3	0.09	5
Li31	96.5	-0.21	0.06	-0.48	0.11	5
Li33	117.5	-0.16	0.04	-0.32	0.14	4
Li34	128	-0.18	0.04	-0.35	0.02	5
Li35	138.5	-0.23	0.05	-0.43	0.09	4
Li36	149	-0.11	0.04	-0.24	0.13	4
Li 173	173	-0.41	0.06	-0.77	0.08	4

Femtosecond laser ablation MC-ICP-MS silicon isotope analyses

The silicon isotope composition of the siliceous sponge spicule was determined by UV femtosecond laser ablation MC-ICP-MS (UV fs-LA-MC-ICP-MS) at GFZ Potsdam. Analytical conditions and instrumental specification are briefly reported below and are detailed in Schuessler and von Blanckenburg (2014). Together with the shale host-rock, the sponge spicule sample was embedded into epoxy resin. A polished thin section of ca. 40 µm thickness was prepared and placed together with epoxy grain mounts of the calibration standard and external reference materials into the ablation cell for analysis. Ablation was done in line scanning mode with individual ablation paths (24 to 27 µm spot diameter, ca. 10 µm depth, 22 to 42 Hz repetition rate). Helium was used as carrier gas for the ablated material to which Ar and Milli-Q-H_2O were added before introduction into the plasma. Analytical conditions yielded intensities of ca. 4 to 5.5 V on a Faraday cup for ^{28}Si (10^{11} Ω) and gas blank intensities of ca. 40 mV; signal intensity matching was better than 14%. Data evaluation and quality control criteria were performed according to Schuessler and von Blanckenburg (2014). Analyses of calibration and quality control standards (NBS 28 quartz, USGS BHVO-2G basalt glass and IRMM-017 Si single crystal) yielded $\delta^{30}Si$= -0.10 ± 0.16‰ (2SD, n= 3) for BHVO-2G and -1.21 ± 0.24‰ (2SD, n= 3) for IRMM-017 (Supplementary Table 5), in agreement with previously published values (Chmeleff et al., 2008; Reynolds et al., 2007; Savage et al., 2014; Schuessler and von Blanckenburg, 2014).

Supplementary Table 3-5: Silicon isotope data of fs-laser ablation MC-ICP-MS measurements of reference materials obtained during this study. The internal standard error of the mean (2SE) is given for each single sample measurements (n= 80 integrations á 1 second), obtained in the same analytical session together with unknown sponge samples. The uncertainty of the fs-LA-MC-ICP-MS method (external long-term repeatability) is ±0.15‰ (2SD) for $\delta^{29}Si$ and ±0.23‰ (2SD) for $\delta^{30}Si$, respectively. Published values of reference materials are within uncertainty identical to values measured during this study. IRMM17: $\delta^{29}Si$= -0.69 ± 0.04‰ (1SD, average of 3 published average values reported on GeoREM (Jochum et al., 2005)), $\delta^{30}Si$= -1.33 ± 0.08‰ (1SD, average of three published average values reported on GeoREM (Jochum et al., 2005)); BHVO-2: $\delta^{29}Si$= -0.14 ± 0.04‰ (1SD, average of 12 published values (Reynolds et al., 2007)), $\delta^{30}Si$= -0.28 ± 0.05‰ (1SD, average of 18 published average values(Reynolds et al., 2007)); BHVO-2G: $\delta^{29}Si$= -0.17 ± 0.04‰ (1SD, average of 5 LA analyses (Schuessler and von Blanckenburg, 2014)), $\delta^{30}Si$= -0.35 ± 0.07‰ (1SD, average of 5 LA analyses (Schuessler and von Blanckenburg, 2014).

BHVO-2G	**$\delta^{29}Si$ [‰]**	**2SE**	**$\delta^{30}Si$ [‰]**	**2SE**
BHVO-2G	-0.09	0.09	-0.11	0.14
BHVO-2G	-0.02	0.08	-0.08	0.14
BHVO-2G	-0.11	0.10	-0.11	0.16
Average	-0.07		-0.10	
95% CI	0.40		0.16	
2SD	0.10		0.04	

IRMM17	**$\delta^{29}Si$ [‰]**	**2SE**	**$\delta^{30}Si$ [‰]**	**2SE**
IRMM17	-0.68	0.08	-1.27	0.12
IRMM17	-0.55	0.09	-1.07	0.13
IRMM17	-0.69	0.09	-1.29	0.13
Average	-0.64		-1.21	
95% CI	0.63		0.96	
2SD	0.16		0.24	

3.4.2.2. Mineralogical composition (SI 2.2)

X-ray diffraction analyses (XRD) were carried out at the Institute of Applied Geosciences at the Technical University Berlin and GFZ Potsdam. Powdered samples were analyzed using an Iso-Debyeflex Philips PW 1050 diffractometer, and a Panalytical Empyrean, both equipped with Cu-sources. XRD patterns were measured between 5-80° 2-theta and 2.5-80° 2-theta, respectively. Mineral phase composition and quantification were evaluated with the software X'Pert HighScore, and Autoquan. Uncertainties are estimated to <10 wt% for major mineral constituents.

3.4.2.3. Major- and trace element geochemistry (SI 2.3)

Major, trace and rare earth elements were determined using (a) X-ray fluorescence analysis (XRF) as well as (b) inductively-coupled plasma mass spectrometry (ICP-MS). XRF analyses were made on powdered and fused samples using a Philips Panalytical PW2400 at the Institute of Applied Geosciences at the Technical University Berlin. The accuracy of XRF analyses was better than 5% RSD for most elements estimated using reference materials JR-1 and JR-2 (rhyolite). The uncertainty on trace element concentrations determined by ICP-MS (Actlabs, Canada) was estimated <10% based on analyses of reference materials DNC-1 (dolerite), W-

2a (diabase), and BIR-1a (basalt). Uncertainty of REE+Y analyses is typically <10% RSD, estimated from analyses of reference materials DNC-1, W-2a, BIR-1a and NCS DC70014 8 (ore).

We calculate Ce* for Ce-anomalies (Ce/Ce*) according to equation (7) in Lawrence et al. (2006):

$$Ce^* = Pr_n \cdot \left(\frac{Pr_n}{Nd_n}\right) \qquad \textbf{Equation 3-1}$$

Using Nd and Pr to calculate Ce* precludes artificial anomalies that may arise from elevated La concentrations that result from the higher stability of La relative to other REE in solution(Alibo and Nozaki, 1999).

Ba and P concentrations are redox proxies, but as absolute concentrations can also be influenced by the abundance of other Ba- and P-free phases such as detrital clay. Therefore, we calculated normalized concentrations as enrichment factors of Ba and P, defined as:

$$X_{EF} = \frac{X/_{Al_{sample}}}{X/_{Al_{PAAS}}} \qquad \textbf{Equation 3-2}$$

The second normalization to the X/Al ratio of the PAAS (Mclennan, 1989) (Post-Archean Australian Shale) allows for obtaining numbers on the same order of magnitude for both elements.

3.4.2.4. The Total organic carbon content (SI 2.4)

The total organic carbon content (TOC) was measured using an elemental analyser NA1500 at GFZ Potsdam. Samples were weighed into silver capsules and 20% HCl were added to achieve complete decarbonation. Before analysis, samples were heated to dryness at 75°C. The analytical uncertainty for TOC content is <2%.

Results from major element and TOC analyses together with results from XRD analyses are compiled in Supplementary Table 6. Results from trace element analyses and rare earth element analyses are compiled in Supplementary Table 3-7 and Supplementary Table 3-8.

Supplementary Table 3-6: Concentration (wt%) of major elements (XRF) and TOC (elemental analyzer) as well as mineral composition (XRD) in bulk chert and silicified shales of the 'Lijiatuo' section. *XRD analyses: quartz is present as main component in all samples. Ba= barite, Kfs= K-feldspar, Il= illite, Py= pyrite, Ba-Fs= Ba-feldspar, 15Å = 15Å clay mineral. Brackets indicate abundances < 5 wt%. The uncertainty of XRF analyses was better than 5% RSD for most elements and <22% for MgO and TiO_2 estimated using reference materials JR-1 and JR-2.

Sample	Height above section base [m]	SiO_2	Al_2O_3	Fe_2O_3	MnO	MgO	CaO	Na_2O	K_2O	TiO_2	P_2O_5	L.O.I.	TOC	XRD*
Li1	0.20	98.1	0.43	<0.50	<0.040	<0.05	<0.40	<0.10	0.14	0.06	0.02	0.58	0.29	
Li2	9.45	98.9	0.26	0.06	0.002	0.03	0.03	0.01	0.07	0.01	0.02	1.51	0.89	
Li-11.5-12	11.50	95.4	0.39	0.19	0.003	0.05	0.05	0.01	0.08	0.02	0.01	1.46	0.38	
Li3	12.50	98.2	0.47	0.13	0.002	0.07	0.02	0.01	0.13	0.02	<0.01	1.50	0.95	(Ba, Kfs)
Li-13.5-12	13.50	90.7	0.48	0.27	0.003	0.07	0.31	0.01	0.12	0.02	0.28	3.09	0.51	
Li-15-12	15.00	95.4	0.51	0.16	0.004	0.07	0.04	0.04	0.2	0.05	0.02	1.61	0.90	
Li-16.2-15.0-12	15.60	95.3	0.37	0.09	0.003	0.04	0.03	0.01	0.09	0.02	<0.01	1.69	0.55	
Li-16.2-12	16.20	96.3	0.57	0.30	0.003	0.08	0.06	<0.01	0.15	0.03	0.05	1.16	0.48	
Li-17.5-12	17.50	87.5	5.48	0.75	0.003	0.49	0.02	0.03	1.39	0.28	<0.01	2.41	0.29	
Li4	18.50	97.1	1.39	0.27	0.002	0.14	0.02	0.01	0.39	0.06	0.03	1.06	0.38	
Li-20.5-12	20.50	95.8	1.06	0.49	0.003	0.09	0.03	0.01	0.27	0.05	<0.01	1.05	0.21	
Li-21.4-12	21.40	94.8	1.58	0.28	0.003	0.18	0.02	<0.01	0.41	0.06	0.02	1.50	0.56	
Li-24.5-12	24.50	94.5	2.09	0.37	0.003	0.23	0.03	0.01	0.62	0.09	<0.01	2.02	0.61	
Li5	24.50	92.5	2.82	0.31	<0.040	0.28	<0.40	<0.10	0.85	0.15	0.02	2.03	0.74	(Il, Ba, Kfs, Py)
Li-26.5-12	26.50	91.5	3.78	0.33	0.006	0.42	0.03	0.05	1.16	0.17	0.06	2.96	1.12	
Li-28.5-12	28.50	92.7	3.10	0.61	0.003	0.31	0.02	0.02	0.92	0.16	0.02	1.62	0.19	
Li6	30.50	97.6	0.24	0.10	<0.040	<0.05	<0.40	<0.10	0.05	<0.10	0.02	1.19	0.60	(Ba)
Li7b	31.00	95.7	0.80	0.28	0.002	0.09	0.03	0.01	0.23	0.04	0.09	3.38	2.05	Ba, (Il, Kfs)
Li7a	36.50	78.9	5.99	3.33	0.003	0.68	0.03	0.02	1.88	0.28	0.50	5.00	0.42	Il, Ba
Li9a	46.50	86.4	2.04	0.14	0.002	0.26	0.04	0.03	0.59	0.13	0.08	8.22	5.86	Il, Ba
Li9b	46.60	89.3	1.01	0.12	0.002	0.12	0.04	0.02	0.28	0.07	0.07	7.06	5.21	Ba, (Il)
Li12a	52.00	91.5	2.19	0.90	0.003	0.07	0.04	0.04	0.67	0.12	0.25	2.20	0.36	(Ba, Kfs, Ba-Fs)
Li12b	52.05	97.0	0.33	0.16	<0.040	<0.05	<0.40	<0.10	<0.10	<0.10	0.07	1.34	1.15	(Ba, Kfs)
Li16	53.06	88.4	2.80	1.34	<0.040	<0.05	<0.40	<0.10	0.51	0.38	0.18	2.75	0.17	(Ba, Kfs)
Li18	53.60	93.5	1.98	0.60	0.003	0.02	0.55	0.02	0.56	0.06	0.46	1.66	0.49	Ba, Kfs, (Py)

continued

Sample	Height above section base [m]	SiO_2	Al_2O_3	Fe_2O_3	MnO	MgO	CaO	Na_2O	K_2O	TiO_2	P_2O_5	L.O.I.	TOC	XRD*
Li19a	53.87	87.2	1.96	0.16	0.002	0.29	2.25	0.08	0.57	0.13	0.09	7.88	5.64	Il, Ba
Li19b	54.04	91.9	0.91	0.16	0.002	0.11	0.04	0.02	0.23	0.06	0.11	7.20	5.24	Ba, (Il)
Li20b	54.50	96.0	0.18	0.15	0.002	0.02	0.03	<0.10	0.04	0.02	0.04	2.07	1.13	Ba
Li20a	54.60	80.8	5.16	3.02	0.002	0.62	0.04	0.02	1.58	0.25	0.42	4.59	0.37	Il, Ba
Li21B-hr	55.13	67.2	10.26	0.91	0.005	1.45	0.07	0.1	3.07	0.59	<0.01	7.39	1.38	
Li22	55.52	92.9	0.31	0.11	0.002	0.03	0.02	0.01	0.07	0.01	0.06	2.74	1.40	
Li23a	56.42	96.7	0.36	0.24	0.002	0.03	0.02	0.01	0.06	0.01	0.02	3.00	1.48	Ba
Li23b	56.52	94.9	0.26	0.13	0.002	0.05	0.02	<0.10	0.05	0.02	0.00	3.14	1.80	Ba
Li24a	60.93	63.4	5.28	2.17	0.004	0.65	0.06	0.04	1.61	0.44	0.25	22.44	14.29	Il, Ba, (Kfs, Py)
Li24b	60.98	75.2	2.41	1.29	0.002	0.25	0.06	0.04	0.75	0.22	0.26	16.24	10.47	Il, Ba, (Kfs, Py)
Li25b	61.50	86.3	1.10	0.29	0.002	0.13	0.06	0.03	0.31	0.14	0.14	10.44	7.57	Il, Ba
Li25a	61.60	60.4	6.11	0.48	0.003	0.72	0.05	0.04	1.86	0.49	0.27	22.21	15.15	Il, Ba, (Kfs, 15Å)
Li29	77.00	74.7	8.01	0.5	0.003	0.93	0.03	0.05	2.14	0.70	0.03	11.54	7.58	Il, (Ba)
Li30	87.25	70.8	14.62	0.77	0.004	1.81	0.03	0.04	3.67	1.03	0.06	6.11	1.29	Il
Li31	96.50	67.1	15.78	0.67	0.004	1.71	0.03	0.1	3.81	0.97	0.03	8.07	2.50	Il
Li33	117.50	80.5	3.57	0.62	0.003	0.35	0.03	0.03	0.82	0.21	0.08	14.53	10.80	Il, (15Å)
Li34	128.00	81.7	2.63	0.16	0.002	0.32	0.02	0.03	0.68	0.17	0.03	13.82	10.59	Il, (15Å)
Li35	138.50	80.4	4.91	0.29	0.003	0.55	0.03	0.04	1.19	0.28	0.06	8.28	4.69	Il
Li36	149.00	80.4	3.31	0.21	0.003	0.31	0.06	0.03	0.8	0.30	0.08	12.38	7.58	Il, (Ba)

Supplementary Table 3-7: Concentration (ppm) of trace elements in bulk chert and silicified shales of 'Lijiatuo' section as analyzed by ICP-MS (Actlabs, Canada). The uncertainty on trace element concentrations determined by ICP-MS was estimated <10% based on analyses of reference materials DNC-1, W-2a, and BIR-1a.

Sample	Height above section base [m]	Ba	Cr	Cs	Cu	Ga	Ge	Hf	Mo	Nb	Ni	Pb	Rb	Sr	Th	Tl	U	V	Zr
Li1	0.20	235	380	0.3	40	2	0.8	0.9	8	2.3	<20	23	4	12	1.4	<0.05	10.8	456	64
Li2	9.45	315	40	0.2	10	<1	<0.5	0.3	7	<0.2	<20	<5	2	6	0.37	<0.05	2.1	153	13
Li-11.5-12	11.50	8583	100	0.3	10	1	0.6	0.3	12	0.8	< 20	28	3	58	0.62	0.06	3.3	239	14
Li3	12.50	234	100	0.3	<10	3	<0.5	0.3	18	0.6	<20	6	4	6	0.67	<0.05	4.0	320	18
Li-13.5-12	13.50	30970	170	0.3	20	2	<0.5	0.4	9	8.9	< 20	14	4	240	1.3	0.07	6.3	240	19
Li-15-12	15.00	285	140	0.6	10	3	0.6	0.4	20	0.7	< 20	8	8	7	0.77	0.06	5.7	380	30
Li-16.2-15-12	15.60	11410	70	0.3	10	2	<0.5	0.2	8	0.6	< 20	<5	3	63	0.54	< 0.05	4.7	156	13
Li-16.2-12	16.20	268	120	0.4	10	3	0.6	0.4	13	0.7	< 20	10	6	9	1.14	0.06	9.6	326	30
Li-17.5-12	17.50	3389	70	2.2	10	11	0.8	1.8	5	5	< 20	7	44	12	6.62	0.2	9.1	87	69
Li4	18.50	1194	30	0.5	<10	2	0.7	0.4	3	1	<20	0	9	7	1.17	<0.05	13.6	67	18
Li-20.5-12	20.50	1128	50	0.6	20	2	0.5	0.3	5	1	< 20	10	8	13	1.1	0.1	35.3	69	17
Li-21.4-12	21.40	802	50	0.6	<10	2	0.6	0.3	<2	1.1	< 20	<5	12	9	1.31	0.07	2.3	66	15
Li-24.5-12	24.50	2219	30	1.2	<10	4	0.6	0.5	<2	1.7	< 20	<5	19	16	1.58	0.08	0.8	30	20
Li5	24.50	825	18	1.7	<10	5	0.7	1.1	<2	3.4	<20	11	17	6	3.22	0.07	1.3	39	40
Li-26.5-12	26.50	1171	40	3	<10	6	0.8	0.7	<2	2.5	< 20	10	30	9	3.76	0.28	1.0	46	33
Li-28.5-12	28.50	1964	40	2	<10	5	0.9	1	2	3.1	< 20	5	29	11	3.5	0.14	1.4	40	42
Li6	30.50	747	57	0.3	26	<1	<0.5	0.6	2	1.4	<20	5	1	5	0.29	<0.05	10.7	166	53
Li7b	31.00	5551	90	0.6	50	2	<0.5	0.3	8	0.6	<20	12	6	26	1.01	0.17	6.4	1060	11
Li7a	36.50	20640	1440	4.5	180	16	1.5	1.8	52	7.3	20	37	49	96	6.62	1.35	27.0	8065	84
Li9a	46.50	4928	470	2.1	30	6	1	1.4	8	4.7	30	38	24	61	3.81	0.73	18.2	7139	109
Li9b	46.60	2840	200	0.9	20	3	<0.5	0.6	7	2	<20	14	10	39	1.74	0.49	8.8	3375	42
Li12a	52.00	12520	80	0.6	30	3	0.7	0.8	11	4.1	<20	35	11	53	2.03	0.36	153.0	525	39
Li12b	52.05	1542	21	0.1	17	<1	<0.5	0.2	<2	1.3	<20	5	<1	15	0.35	<0.05	33.3	104	8
Li16	53.06	18531	41	0.4	59	<1	<0.5	0.9	6	5.6	5	37	7	51	3.97	0.24	9.0	525	34
Li18	53.60	16690	20	0.2	160	2	<0.5	0.4	4	1.4	<20	13	8	124	0.98	0.49	114.0	65	19

continued

Sample	Height above section base [m]	Ba	Cr	Cs	Cu	Ga	Ge	Hf	Mo	Nb	Ni	Pb	Rb	Sr	Th	Tl	U	V	Zr
Li19a	53.87	4515	430	2.1	20	5	0.8	1.3	7	4.3	20	32	22	65	3.53	0.59	17.2	6488	98
Li19b	54.04	2030	190	0.9	20	3	0.6	0.6	8	1.9	20	14	9	32	1.53	0.23	8.3	2765	51
Li20b	54.50	12930	15	0.2	30	<1	<0.5	0.2	7	0.3	<20	23	<1	96	0.3	<0.05	3.1	74	8
Li20a	54.60	28270	1300	3.6	200	16	1.4	1.6	45	5.4	<20	42	41	191	7.5	0.98	30.8	6951	73
Li21B-hr	55.13	28140	1720	11.2	220	32	4.1	5.3	14	18.9	<20	525	122	185	10.5	3.24	38.2	>10000	172
Li22	55.52	32870	15	0.2	50	<1	<0.5	0.1	5	0.3	<20	<5	<1	268	0.2	0.11	4.1	221	4
Li23a	56.42	6360	40	0.2	120	2	<0.5	0.7	7	0.5	<20	8	<1	47	0.41	<0.05	5.9	564	26
Li23b	56.52	4580	20	0.3	40	<1	<0.5	0.1	4	0.8	<20	6	<1	29	0.2	0.08	3.0	405	6
Li24a	60.93	14190	1220	4.5	300	17	2.9	4.2	48	16.2	270	92	51	95	9.54	1.71	31.7	10000	292
Li24b	60.98	17750	610	1.9	150	9	1.1	1.7	31	7.6	100	74	24	155	5.89	0.79	34.6	4359	321
Li25b	61.50	13450	200	0.6	20	3	<0.5	0.9	30	4.2	<20	34	11	40	2.94	<0.05	17.2	1849	85
Li25a	61.60	41780	1390	7.4	60	17	1.7	3.5	58	12.8	50	123	76	67	10.2	1.12	32.5	9578	417
Li29	77.00	5910	100	6	<10	16	1.7	3.4	11	12.7	<20	18	81	25	9.72	0.78	12.4	298	137
Li30	87.25	2518	90	12.6	<10	21	2.7	4.3	0	16.5	20	9	129	16	11.9	1.44	5.1	145	160
Li31	96.50	2843	120	9.9	10	25	3	4.3	6	20.4	<20	19	137	15	14.9	1.21	6.8	117	151
Li33	117.50	821	40	3	10	7	0.9	1.9	41	5	20	28	32	15	4.26	0.48	19.7	474	79
Li34	128.00	856	140	2	<10	10	4	1.2	36	4.4	<20	121	31	11	3.01	0.34	9.3	1981	48
Li35	138.50	1046	240	4.4	20	11	1.1	1.9	11	5.4	<20	16	45	113	4.52	0.6	12.0	3533	75
Li36	149.00	4546	40	1.8	40	7	1.2	2.3	26	5.9	30	39	30	312	5.64	0.53	21.4	360	96

Supplementary Table 3-8: Concentration (ppm) of rare earth elements in bulk chert and silicified shales of 'Lijiatuo' section as analyzed by ICP-MS (Actlabs, Canada). Ce/Ce*, Eu/Eu*, and Pr/Yb are calculated according to Lawrence et al.(Lawrence et al., 2006) from PAAS-normalized(Mclennan, 1989) element concentrations. The uncertainty of REE+Y analyses is typically <10%, estimated from analyses of reference materials DNC-1, W-2a, BIR-1a and NCS DC70014.

Sample	Height above section base [m]	La	Ce	Pr	Nd	Sm	Eu	Gd	Tb	Dy	Ho	Er	Tm	Yb	Lu	Y	ΣREEY	Ce/Ce^*_N	Eu/Eu^*_N	Pr/Yb_N
Li1	0.20	7.96	17.80	2.39	10.30	2.05	0.41	2.38	0.44	3.01	0.72	2.35	0.36	2.22	0.34	41.5	94.2	0.93	0.88	0.34
Li2	9.45	0.31	0.52	0.09	0.47	0.19	0.06	0.34	0.08	0.62	0.15	0.50	0.08	0.53	0.09	6.5	10.5	0.87	1.16	0.05
Li-11.5-12	11.50	2.71	4.32	0.67	3.19	0.79	0.09	0.91	0.15	0.94	0.21	0.69	0.11	0.68	0.12	10.1	25.7	0.89	0.53	0.31
Li3	12.50	2.02	3.45	0.53	2.25	0.47	0.13	0.64	0.12	0.86	0.20	0.67	0.11	0.78	0.12	8.3	20.7	0.80	1.19	0.22
Li-13.5-12	13.50	3.11	4.88	0.93	5.15	2.71	0.43	3.25	0.47	2.82	0.57	1.72	0.25	1.49	0.22	24.8	52.8	0.84	0.76	0.20
Li-15-12	15.00	1.96	3.38	0.44	1.63	0.42	0.17	0.71	0.15	1.16	0.31	1.14	0.18	1.33	0.20	12.7	25.9	0.82	1.49	0.11
Li-16.2-15-12	15.60	2.35	4.08	0.55	2.29	0.53	0.06	0.61	0.11	0.69	0.15	0.48	0.08	0.57	0.09	6.7	19.3	0.89	0.54	0.31
Li-16.2-12	16.20	2.08	3.73	0.59	2.72	0.89	0.25	1.12	0.21	1.41	0.32	1.02	0.16	1.04	0.17	14.3	30.0	0.84	1.20	0.18
Li-17.5-12	17.50	18.30	26.60	3.70	13.30	1.72	0.26	1.11	0.25	1.82	0.42	1.37	0.23	1.54	0.24	15.0	85.9	0.75	0.78	0.77
Li4	18.50	5.46	7.70	1.43	5.83	1.08	0.17	0.81	0.15	1.01	0.22	0.71	0.11	0.77	0.12	6.5	32.1	0.63	0.81	0.59
Li-20.5-12	20.50	3.22	4.80	0.83	3.50	0.74	0.16	0.65	0.13	0.91	0.20	0.61	0.10	0.68	0.09	6.5	23.1	0.70	1.05	0.39
Li-21.4-12	21.40	6.41	8.66	1.47	5.48	0.98	0.18	0.73	0.12	0.77	0.16	0.50	0.08	0.59	0.09	5.6	31.8	0.63	1.00	0.80
Li-24.5-12	24.50	12.10	18.80	2.20	7.22	0.84	0.07	0.37	0.06	0.42	0.10	0.31	0.05	0.33	0.05	2.9	45.8	0.81	0.54	2.13
Li5	24.50	43.20	72.70	8.17	26.10	2.40	0.35	0.94	0.11	0.66	0.14	0.48	0.08	0.51	0.07	4.0	159.9	0.82	1.10	5.12
Li-26.5-12	26.50	10.10	15.50	1.95	6.33	0.93	0.22	0.79	0.12	0.76	0.17	0.54	0.09	0.55	0.09	4.6	42.7	0.75	1.24	1.13
Li-28.5-12	28.50	5.13	8.87	1.07	3.83	0.80	0.15	0.79	0.15	1.02	0.22	0.70	0.12	0.78	0.11	7.3	31.0	0.86	0.89	0.44
Li6	30.50	2.11	2.50	0.70	3.74	1.38	0.42	2.14	0.40	2.66	0.61	1.94	0.32	2.26	0.40	23.4	45.0	0.55	1.22	0.10
Li7b	31.00	4.98	5.04	1.09	4.41	0.93	0.14	0.99	0.16	1.03	0.22	0.71	0.11	0.73	0.11	7.7	28.4	0.54	0.72	0.48
Li7a	36.50	51.20	49.20	11.80	48.80	9.82	1.58	10.70	2.00	13.70	3.22	10.40	1.55	9.31	1.35	123.0	347.6	0.50	0.73	0.40
Li9a	46.50	44.50	38.20	11.70	53.20	11.40	2.35	12.10	2.21	15.00	3.51	11.40	1.74	10.70	1.63	129.0	348.6	0.43	0.95	0.35
Li9b	46.60	26.00	22.00	6.73	30.00	5.98	1.22	6.36	1.18	7.87	1.86	5.89	0.91	5.73	0.84	64.6	187.2	0.42	0.93	0.38
Li12a	52.00	7.00	9.98	1.43	5.40	0.97	0.05	0.81	0.16	1.06	0.24	0.84	0.14	0.96	0.14	8.2	37.4	0.76	0.26	0.48
Li12b	52.05	1.59	2.57	0.37	1.52	0.37	0.06	0.40	0.07	0.51	0.11	0.37	0.05	0.34	0.05	3.9	12.3	0.82	0.72	0.35
Li16	53.06	24.90	43.90	4.62	15.00	1.68	0.13	1.12	0.13	0.78	0.18	0.62	0.11	0.83	0.14	5.7	99.8	0.89	0.48	1.78
Li18	53.60	3.93	8.79	1.58	7.25	1.83	0.22	2.18	0.40	2.69	0.58	1.80	0.27	1.80	0.29	18.6	52.2	0.74	0.54	0.28

continued

Sample	Height above section base [m]	La	Ce	Pr	Nd	Sm	Eu	Gd	Tb	Dy	Ho	Er	Tm	Yb	Lu	Y	ΣREEY	Ce/Ce^*_N	Eu/Eu^*_N	Pr/Yb_N
Li19a	53.87	38.30	32.80	10.10	45.60	10.00	2.09	10.90	2.04	13.50	2.97	9.87	1.50	9.49	1.47	111.0	301.6	0.42	0.95	0.34
Li19b	54.04	22.30	19.10	5.81	26.20	5.43	1.12	5.87	1.10	7.61	1.76	5.49	0.83	5.12	0.76	63.7	172.2	0.43	0.94	0.36
Li20b	54.50	4.24	4.57	0.97	3.91	0.94	0.03	1.38	0.26	1.84	0.42	1.34	0.20	1.25	0.19	17.5	39.0	0.55	0.13	0.25
Li20a	54.60	31.80	31.30	7.63	34.70	8.79	1.63	11.90	2.30	15.60	3.57	11.60	1.72	10.40	1.59	137.0	311.5	0.54	0.77	0.23
Li21B-hr	55.13	84.50	86.50	17.40	68.70	14.90	2.54	15.20	2.13	12.00	2.41	7.29	1.10	7.10	1.13	90.0	412.9	0.57	0.87	0.78
Li22	55.52	2.27	2.13	0.47	2.14	0.52	0.004	0.57	0.08	0.43	0.09	0.30	0.05	0.30	0.04	4.0	13.4	0.60		0.50
Li23a	56.42	5.57	3.66	0.98	4.33	0.95	0.15	1.19	0.17	1.08	0.26	0.87	0.14	0.90	0.14	11.8	32.2	0.48	0.76	0.35
Li23b	56.52	3.92	3.35	0.90	4.01	0.80	0.08	0.82	0.13	0.83	0.18	0.56	0.08	0.54	0.08	7.0	23.3	0.48	0.47	0.53
Li24a	60.93	61.50	60.50	15.70	75.50	20.20	4.05	28.80	5.05	32.50	7.05	22.10	3.26	19.80	3.04	292.0	651.1	0.54	0.85	0.25
Li24b	60.98	75.30	80.20	21.00	89.50	21.00	4.31	28.00	5.26	35.30	8.15	25.00	3.62	21.60	3.20	321.0	742.4	0.47	0.87	0.31
Li25b	61.50	13.00	12.40	3.03	13.20	3.85	0.73	6.42	1.22	8.57	2.06	6.57	0.97	6.00	0.90	85.0	163.9	0.52	0.74	0.16
Li25a	61.60	37.10	37.70	10.50	51.10	19.80	4.05	35.30	6.84	45.50	10.40	32.70	4.77	28.30	4.29	417.0	745.4	0.50	0.78	0.12
Li29	77.00	31.80	43.30	6.29	21.20	3.07	0.53	2.36	0.46	3.30	0.79	2.76	0.46	3.14	0.53	25.2	145.2	0.67	0.86	0.64
Li30	87.25	31.10	52.50	7.58	28.60	5.63	1.17	5.28	0.91	5.43	1.05	3.05	0.44	2.70	0.41	32.0	177.8	0.76	1.02	0.90
Li31	96.50	47.50	57.20	8.60	29.00	4.17	0.65	2.67	0.45	2.82	0.62	1.92	0.30	1.97	0.30	19.4	177.6	0.65	0.87	1.39
Li33	117.50	8.61	14.80	2.11	8.87	2.05	0.45	2.42	0.49	3.32	0.71	2.16	0.30	1.89	0.29	26.5	75.0	0.85	0.94	0.36
Li34	128.00	10.60	14.50	2.36	8.91	1.51	0.28	1.38	0.23	1.59	0.38	1.30	0.21	1.43	0.23	15.3	60.2	0.67	0.93	0.53
Li35	138.50	14.00	17.90	3.23	12.30	2.46	0.49	3.08	0.55	3.68	0.85	2.67	0.39	2.52	0.41	32.6	97.1	0.61	0.88	0.41
Li36	149.00	16.60	25.20	3.49	13.30	2.52	0.40	1.59	0.22	1.33	0.31	1.13	0.20	1.40	0.23	11.6	79.5	0.80	0.96	0.80

3.4.3. Age model for the 'Lijiatuo' section (SI 3)

The only absolute geochronological constraint of the age of 'Lijiatuo' section is one ash layer dated to 546± 12 Ma (Jiang et al., 2010). Without more geochronological information, any age estimate of the section must be considered with caution. We attempt to derive a rough age model of the section by the following approach which is based on four assumptions: (1) The base of the section represents the lowermost Liuchapo Formation, which is equivalent to the Doushantuo/Dengying boundary at 551 Ma (Condon et al., 2005), (2) the section is continuous and does not contain significant hiatuses, (3) detrital minerals were deposited at a constant rate with constant zirconium concentrations where zirconium is exclusively present in zircon and hence is exclusively detrital and most resistant to post-depositional changes; hence (4) relative sedimentation rates are expressed in bulk rock zirconium concentrations.

If the lowermost section is 551 Ma and the ash layer is 546 Ma in age, the average post-compaction sedimentation rate is around 10 mm/ka for this time frame that is represented by the 50 m in outcrop. Deviations from this average rate are expressed in variations in Zr concentrations where higher concentrations of Zr indicate lower sedimentation rates and vice versa. From sedimentation rates and sampling height of samples in the section we calculate the time between two subsequent samples. The cumulative time yields the estimated age of the section after 551 Ma. Under these assumptions the estimated age at the top of the sampled section is 515 Ma and which is approximately Middle Cambrian.

3.4.4. Carbon and Nitrogen isotopes (SI 4)

The stable isotope composition of organic carbon ($\delta^{13}C_{org}$) depends on a number of factors including i) the C isotope composition and quantity of the inorganic, dissolved inorganic carbon ($\delta^{13}C_{DIC}$) source, and ii) isotope fractionation between DIC and primary producers ($\Delta^{13}C_{DIC\text{-}org}$) that results from carbon assimilation, metabolism and synthesis (Hayes, 1993). The isotope composition of carbon can be shifted i) during early diagenesis where $\delta^{13}C_{org}$ might decrease by up to 2‰ (e.g. Lehmann et al., 2002), and ii) during thermal alteration that can increase the $\delta^{13}C$ value of the residual organic matter by 2 to 3‰ due to the extraction of isotopically light hydrocarbons (Burwood et al., 1988). The carbon isotope record of organic matter is used to study the global carbon cycle (e.g. Des Marais et al., 1992; Krissansen-Totton et al., 2015), and is commonly used in the correlation of sedimentary successions.

During consumption from seawater, the nitrogen isotope composition is set in organic matter, derived from primary producers (Altabet and Francois, 1994). It is to only minor extents modified by early diagenetic organic matter remineralization and ammonium fixation in clay minerals (Robinson et al., 2012). Changes in the seawater biogeochemical cycle of nitrogen depend on the ocean redox structure and are recorded in the nitrogen isotope composition of organic matter (e.g. Boyle et al., 2013). Therefore, $\delta^{15}N$ of

organic matter can reflect the redox state of the water column. Under oxygen-poor conditions, nitrate cannot form and nitrogen fixation will be the dominant process that produces bio-available nitrogen. This process is characterized by slightly negative $\delta^{15}N$ (Quan et al., 2008). Under oxygen-rich conditions, incomplete denitrification of the nitrate pool shifts $\delta^{15}N$ towards higher values ranging between 1 and 15‰ (Somes et al., 2010). This dependence of the organic matter $\delta^{15}N$ value on the seawater redox condition is shown in a conceptual model by Quan et al. (2008) (inset in Supplementary Figure 3-4): in the absence of oxygen, no nitrate forms, and $\delta^{15}N$ will be around 0‰ $\delta^{15}N$. Increasing oxygen levels result in increased nitrate concentrations and increased denitrification, such that $\delta^{15}N$ shifts towards higher values with increasing oxygen levels until ≈30 µM O_2. Higher oxygen concentrations inhibit the nitrogenase enzyme, and hence suppress denitrification and cause a negative correlation of oxygen concentration with $\delta^{15}N$ (Quan et al., 2008).

Results from C- and N- concentration and isotope analyses are summarized in Supplementary Table 3-9. The concentration of organic carbon is increasing towards the top of the section and reaches up to ≈15wt% (Supplementary Figure 3-2b). The isotope composition of organic carbon ranges from ca. -35 to ca. -29‰ $\delta^{13}C_{org}$ and overall increases throughout the section (Supplementary Figure 3-2c). Samples with high detrital mineral contents have systematically higher $\delta^{13}C_{org}$ values and have usually lower TOC concentrations. Nitrogen concentrations range from 0.01wt% to 0.45wt% with an increasing trend upsection (Supplementary Figure 3-2d). The nitrogen isotope composition ranges from -1.5 to 6.5 $\delta^{15}N$. At the bottom of the section most samples range between 1 and 4‰ $\delta^{15}N$. The overlying samples increase up to 6.5‰ $\delta^{15}N$, where some samples have distinctly lower $\delta^{15}N$ of between 1 and 2‰. The top part of the section is characterized by overall decreasing values from ca. 2 to -1.5‰ $\delta^{15}N$ (Supplementary Figure 3-2).

Supplementary Table 3-9: Bulk rock Carbon and Nitrogen concentration and isotope composition in 'Lijiatuo' as analyzed by an elemental analyzer (NA1500) coupled via a ConFlow III to an isotopic ratio mass spectrometer (DELTAplusXL). The analytical uncertainty on $\delta^{13}C_{org}$ is ca. 0.3‰.; uncertainties on TOC and N concentrations are <2%.

sample	height above section base [m]	$\delta^{13}C_{org}$ [‰]	$\delta^{13}C_{bulk}$ [‰]	$\delta^{15}N$ [‰]	1SD	n	TC [wt%]	TOC [wt%]	N [wt%]
Li 01	0.20	-33.9	-33.7	4.47	1.04	3	0.31	0.29	0.01
Li 02	9.45	-34.5	-34.8	-0.02	0.24	2	0.93	0.89	0.01
Li11.5-12	11.50	-33.8	-33.7	1.35	0.39	3	0.39	0.38	0.01
Li 03	12.50	-34.2	-34.6	1.07	0.52	4	0.95	0.95	0.02
Li13.5-12	13.50	-33.8	-33.5	1.99	0.17	2	0.55	0.51	0.02
Li15-12	15.00	-35.0	-34.7	1.54	0.48	4	0.90	0.90	0.02
Li16.20-15-12	15.60	-34.7	-34.2	0.35	0.49	3	0.56	0.55	0.01
Li16.20-12	16.20	-34.5	-34.2	1.10	0.18	2	0.49	0.48	0.01
Li17.5-12	17.50	-34.0	-32.9	3.48	0.41	2	0.29	0.29	0.04
Li 04	18.50	-33.6	-33.3	2.64	0.00	2	0.40	0.38	0.02
Li20.5-12	20.50	-33.9	-33.4	2.38	0.48	4	0.20	0.21	0.02
Li21.4-12	21.40	-34.2	-33.8	2.28	0.44	3	0.56	0.56	0.04
Li24.5-12	24.50	-34.1	-33.6	2.61	0.38	2	0.63	0.63	0.05
Li 05	24.50	-32.5	-32.9	2.46	0.48	3	0.73	0.74	0.06
Li26.5-12	26.50	-34.2	-34.0	2.18	0.01	2	1.12	1.12	0.09
Li28.5-12	28.50	-33.2	-33.0	2.26	0.19	2	0.20	0.19	0.06
Li 06	30.50	-33.6	-33.4	1.19	0.04	2	0.62	0.6	0.01
Li 07b	31.00	-34.7	-35.1	2.78	0.53	3	2.02	2.05	0.06
Li 07a	36.50	-33.0	-32.8	5.17	0.25	2	0.45	0.42	0.15
Li 09a	46.50	-33.3	-32.9	6.47	0.05	2	6.06	5.9	0.19
Li 09b	46.60	-33.2	-32.7	4.29	0.40	2	5.41	5.2	0.12
Li 12 a	52.00	-32.3	-31.9	4.82	0.65	3	0.36	0.36	0.03
Li 12 b	52.05	-33.2	-32.5	0.51	0.49	3	0.94	1.15	0.01
Li 16	53.06	-31.6	-31.2	5.28	1.30	3	0.18	0.17	0.02
Li 18	53.60	-33.5	-32.9	2.35	0.13	2	0.48	0.49	0.03
Li 19a	53.87	-33.2	-32.9	5.44	0.35	2	5.90	5.6	0.21
Li 19b	54.04	-33.3	-32.9	4.58	0.07	2	5.42	5.2	0.11
Li 20b	54.50	-33.4	-32.9	-0.25	0.26	2	1.20	1.13	0.02
Li 20a	54.60	-32.2	-32.3	4.58	0.29	2	0.39	0.37	0.13
Li 21B-hr	55.13	-32.7	-32.2	5.11	0.50	2	1.47	1.38	0.34
Li 22	55.52	-33.5	-33.5	-0.18	0.02	2	1.36	1.40	0.02
Li 23a	56.42	-33.3	-33.3	1.26		1	1.68	1.48	0.03
Li 23b	56.52	-33.5	-33.5	1.18		1	1.57	1.80	0.02
Li 24a	60.93	-33.9	-33.6	1.87	0.45	2	15.64	14.3	0.32
Li 24b	60.98	-33.7	-33.4	1.09	0.14	2	10.85	10.5	0.20
Li 25b	61.50	-33.5	-33.2	-0.50	0.38	2	8.07	7.6	0.12
Li 25a	61.60	-33.4	-33.1	2.01	0.46	3	15.35	15.1	0.33
Li 29	77.00	-31.0	-30.7	-0.04	0.60	3	7.62	7.6	0.27
Li 30	87.25	-29.1	-29.2	-1.37	0.22	2	1.34	1.29	0.42
Li 31	96.50	-30.3	-30.2	0.23	0.35	2	2.37	2.50	0.45
Li 33	117.50	-33.4	-33.3	-1.21	0.16	2	11.33	10.8	0.16
Li 34	128.00	-33.0	-33.1	-1.49	0.57	2	10.88	10.6	0.18
Li 35	138.50	-33.3	-33.5	-0.30	0.16	2	4.82	4.7	0.22
Li 36	149.00	-33.4	-33.5	-1.48	0.23	2	7.84	7.6	0.16

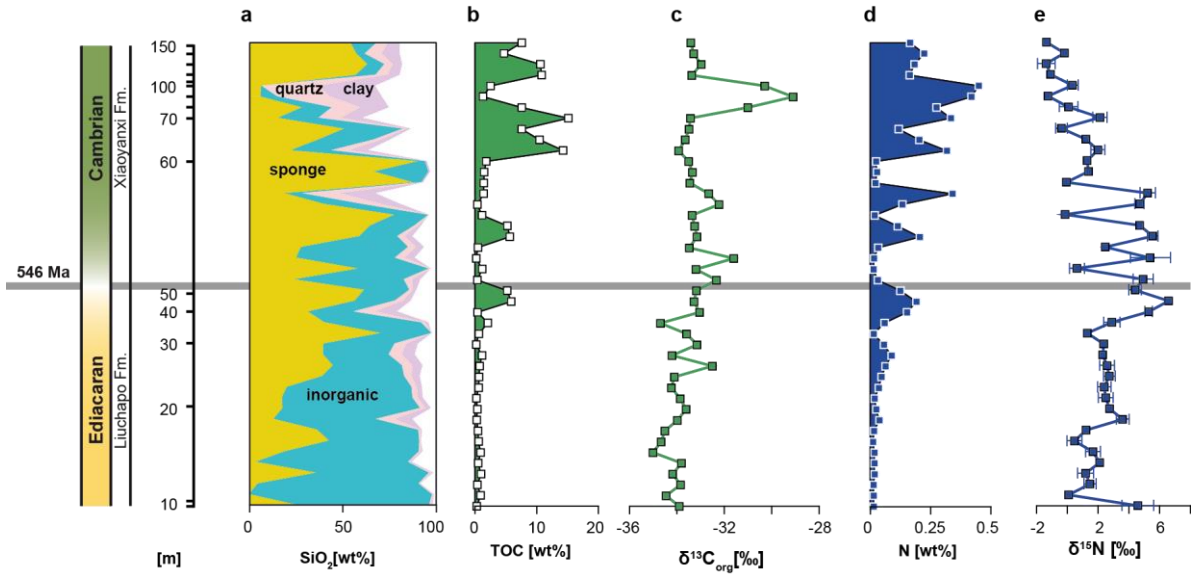

Supplementary Figure 3-2: (a) The calculated abundance of sponges, inorganically precipitated silica, and silica from quartz and clay (see main text) in relation to (b) the TOC concentration, (c), the carbon isotope composition, (d) the N concentration, and (e) the N isotope composition at Lijiatuo section.

It cannot be ruled out that bulk sediment carbon isotope composition has shifted during early diagenesis or thermal maturation. However, we observe an increasing trend of $\delta^{13}C$ through this time interval that coincides with increased abundance of siliceous sponges as calculated from the mass balance. The shift of $\delta^{13}C$ from around -35‰ to -33‰ can be explained by i) change in phytoplanctonic producers with variable $\Delta^{13}C_{DIC\text{-}org}$ between (Hayes et al., 1999) or by ii) increased efficiency of organic carbon burial. The latter explanation is suggested by mass balance in that burial of ^{12}C-enriched organic matter shifts seawater to higher $\delta^{13}C$ values. The calculated relative sponge abundance f_{sponge} overall correlates with $\delta^{13}C_{org}$ (Supplementary Figure 3-3). This finding suggests that seawater filtration by sponges is a plausible mechanism that increased carbon burial efficiency and/or that the clearing of turbid water caused a change in the assemblage of primary producers (Lenton et al., 2014) with slightly different carbon isotope fractionation factors.

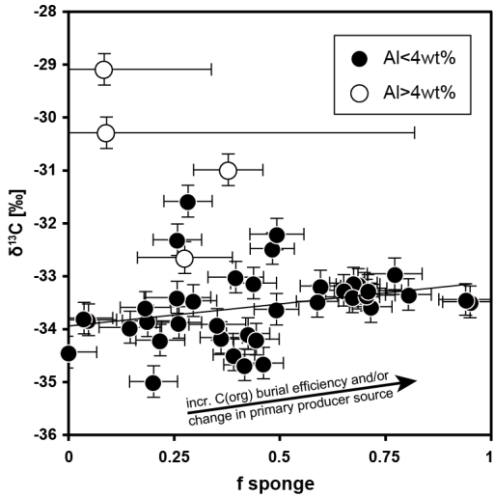

Supplementary Figure 3-3: The organic carbon isotope composition $\delta^{13}C_{org}$ increases with calculated relative abundance of sponges. Samples with high detrital mineral contents are represented by higher Al concentrations (open symbols) and likely carry recycled organic carbon with a different δ^{13}Corg.

The nitrogen isotope composition overall correlates with the Ce-anomaly (Supplementary Figure 3-4), suggesting that it is dominantly controlled by redox-dependent nitrate formation and denitrification in the water column. In the framework of the conceptual relation between seawater oxygenation and organic matter $\delta^{15}N$ (Quan et al., 2008), this inference suggests bottom water oxygen concentrations reaching ≈10 µM O_2 in the latest Ediacaran at Lijiatuo. This inferred oxygen concentration is in the range of suggested threshold concentrations between ≈5 and 20 µM O_2 that was necessary to trigger ecological responses for the evolution of larger organisms that developed during the Cambrian bioradiation (Sperling et al., 2015).

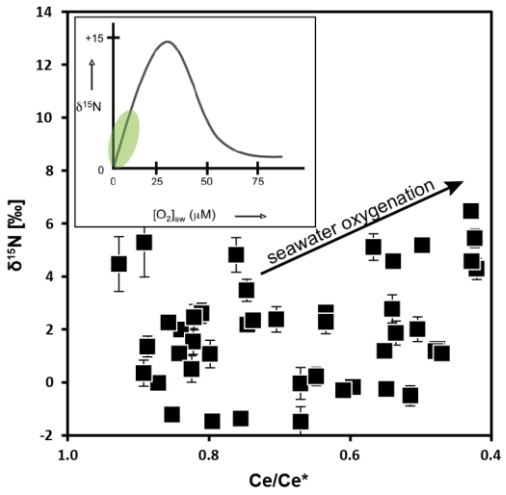

Supplementary Figure 3-4: Nitrogen isotope composition vs. Ce-anomaly. Only samples with a large Ce-anomaly (low Ce/Ce*) have high $\delta^{15}N$. The inset conceptually shows the nitrogen isotope composition as function of seawater oxygen concentration after Quan et al. (2008). The green shaded area marks the range of measured $\delta^{15}N$-values in samples from Lijiatuo section and suggest seawater oxygen concentrations reaching ≈ 10µM.

Complementary C- and N isotope data support the paleoenvironmental implications drawn from the Si isotope and geochemical record at 'Lijiatuo' section. The carbon- isotope record of organic matter is compatible with the interpretation of increased organic carbon burial and/or a change in the composition of primary producers. The latter is suggested to be induced by the preferential filtration of DOC and small particulate organic matter by siliceous sponges, exerting evolutionary pressure in favor of larger phytoplankton (Lenton et al., 2014). Inferences from the nitrogen isotope record agree with the interpretation that Ce-anomalies of bulk chert/siliceous shale track the seawater oxygenation, which occurs concomitantly with the colonisation of siliceous sponges on the continental slope.

4. The chert oxygen isotope composition as a recorder of the geothermal gradient

Abstract

The oxygen isotope composition of chert reveals an increasing trend through Earth's history. The most common explanations are decreasing seawater temperatures, increasing $\delta^{18}O$ of seawater, or overprinting of the rock record. These hypotheses are challenged by recent evidence for constant seawater $\delta^{18}O$ and temperatures <40°C in the Archean. Here, I present evidence that $\delta^{18}O$ of chert depends on heating rates during diagenesis and that chert faithfully preserves diagenetic conditions in its $\delta^{18}O$ record despite burial to prehnite-pumpellyite facies conditions. I suggest that the Proterozoic secular trend of increasing $\delta^{18}O$ in chert between the Proterozoic and today stems from decreasing geothermal gradients through the cooling of the solid Earth. Evidence is provided by the oxygen isotope composition of cherts and siliceous shales from a stratigraphic section of Ediacaran to Cambrian age that has highly variable detritus contents. I have calculated the $\delta^{18}O$ composition of authigenic quartz by mass balance and results were confirmed by micro-scale oxygen isotope analyses using secondary ion mass spectrometry. Detritus contents are correlated with the $\delta^{18}O$ of authigenic quartz, revealing the strong control of the geochemical environment on silica phase transformation rates, and the memory of chert for diagenetic conditions of chert formation. Diagenetic peak temperatures of around 260°C, as determined by Raman spectrometry of carbonaceous material, show that chert likely preserves the diagenetic $\delta^{18}O$ signature. Modeled temperature- controlled rates of chert formation show that quartz forms at lower average temperatures and greater depths when the geothermal gradient decreases from 90°C km^{-1} to 10°C km^{-1}. I estimate that an increase of approximately 9‰ $\delta^{18}O$ is the resulting natural consequence of the cooling Earth. However, the lowest $\delta^{18}O$ values found in the Archean cannot be explained by the presented model and might be due to hydrothermal alteration of chert or to extremely high temperatures of chert formation at the time before the onset of accelerated heat loss from Earth through plate tectonics.

4.1. Introduction

The global record of the oxygen isotope composition of chert over Earth's history reveals a secular trend towards higher $\delta^{18}O$ values of about 15‰ in younger sediment (Figure 1-1; Knauth, 2005). Several suggestions have been made for i) the underlying causes for this secular shift and ii) the relatively high scatter in $\delta^{18}O$ values within a given time slice that amounts to about 10‰. Carbonate sediment shares this trend of increasing $\delta^{18}O$ (Jaffrés et al., 2007), suggesting that carbonates and chert document a common process.

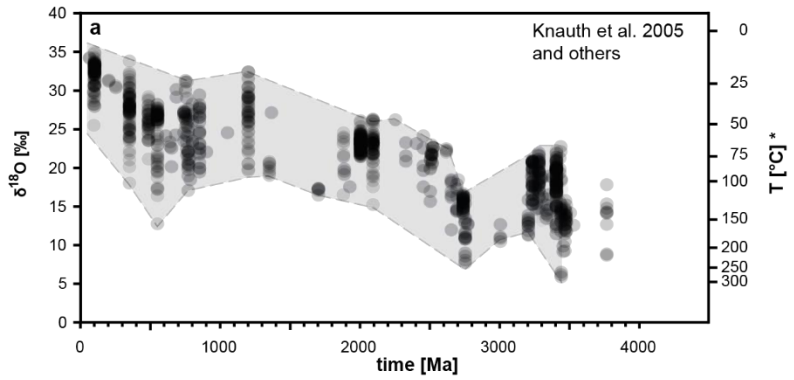

Figure 4-1: Compilation of chert oxygen isotope data (Beeunas and Knauth, 1985; Force et al., 1986; Gao and Land, 1991; Heck et al., 2011; Jones and Knauth, 1979; Kenny and Knauth, 1992; Knauth and Lowe, 2003, 1978; Knauth, 2005; Levin et al., 2014; Marin et al., 2010; Marin-Carbonne et al., 2012; Ramseyer et al., 2013; Suchecki and Hubert, 1984; Winter and Knauth, 1992). $\delta^{18}O$ values reveal an increase over Earth history. The temperature scale refers to the $\delta^{18}O$ calibration of Knauth and Epstein (1976) assuming a constant seawater $\delta^{18}O_{water}$ of -1.1‰ (Cummins et al., 2014).

Given that oxygen in most carbonate and opal (the precursor of chert) sediment is sourced in seawater, the hypotheses for the secular shift to higher $\delta^{18}O$ of carbonates and cherts include 1) age-dependent alteration through interaction with ^{16}O-rich groundwater (Degens and Epstein, 1962), 2) decreasing seawater temperatures (Knauth and Lowe, 2003, 1978; Knauth, 2005; Kolodny and Epstein, 1976; Robert and Chaussidon, 2006), and 3) an increase in seawater oxygen isotope composition (Jaffrés et al., 2007; Kasting et al., 2006; Wallmann, 2001). The scatter in the record is explained for carbonates by primary variations in the depositional setting, post-depositional alteration (Kah, 2000) and by local variations in sea surface temperatures of between 10 and 33°C (Jaffrés et al., 2007). In contrast, the scatter in the chert record is thought to result from the variability of temperatures during diagenesis (Knauth, 2005; Kolodny and Epstein, 1976; Matheney and Knauth, 1993; Murata and Larson, 1975; Murata et al., 1977; Pisciotto, 1981). This consideration emphasizes the difference between opal and carbonates, namely that opal must undergo a diagenetic lithification process that transforms it into quartz chert. Thus, whether $\delta^{18}O$ of chert does indeed record the same processes as carbonates is questionable.

Chert generally forms from amorphous silica (Kastner et al., 1977; Knauth, 1994), regardless of whether the deposited opal has a sedimentary or a hydrothermal source. Hence almost all chert underwent diagenetic phase transformations. Lithification occurs over the temperature range experienced during burial diagenesis where commonly two successive diagenetic reactions transform opal-A via an intermediate opal-CT stage (Kastner et al., 1977; Williams et al., 1985) to quartz. Both silica polymorph transformation steps (opal-A to opal-CT and opal-CT to quartz) occur via dissolution-reprecipitation reactions where Si-O bonds are broken and later reformed (Williams et al., 1985).

Besides the seawater $\delta^{18}O$ composition also the temperatures of silica phase transformation reactions set $\delta^{18}O$ ratios of chert. It was observed that $\delta^{18}O$-values of quartz are lower by about 1-2‰ compared to coexisting opal-CT, suggesting that $\delta^{18}O$ of quartz records a higher (trans)formation temperature (Kolodny and Epstein, 1976). This interpretation is supported by a stepwise decrease in $\delta^{18}O$-values at the silica polymorph boundaries of opal-A to opal-CT and opal-CT to quartz in a sedimentary succession (Mizutani, 1977; Pisciotto, 1981).

The rate of the diagenetic polymorph transformation reactions of silica depends predominantly on temperature (Ernst and Calvert, 1969; Kano and Taguchi, 1982). The phase transformations of silica polymorphs proceed fast at high temperature and much slower under the low temperature prevailing at shallow burial depth (Hesse and Schacht, 2011; Riech and von Rad, 1979). At a burial depth of 500 m, chert formation takes 30-40 Ma, but can take up to 120 Ma at shallow burial depth where low temperatures prevail (Riech and von Rad, 1979). Therefore, both the thermal gradient and the burial rate affect the heating rate of sediment and thus the rate of quartz formation, and in consequence the depth and temperature at which silica phase transformations occur.

Besides temperature, rates of chert formation depend on the host sediment's properties (Hinman, 1990; Isaacs, 1982; Kastner et al., 1977). These include the specific surface area of silica, detrital mineral-, and carbonate contents, organic matter type- and contents, the salt concentration, the pore water pH, and, subordinately, pressure (Kastner et al., 1977; Williams and Crerar, 1985; Williams et al., 1985). The detrital mineral content has a particularly strong effect on the rate of silica diagenesis (Isaacs, 1982) as it exerts the main control on the Si equilibrium solubility of siliceous sediment (Dixit et al., 2001).

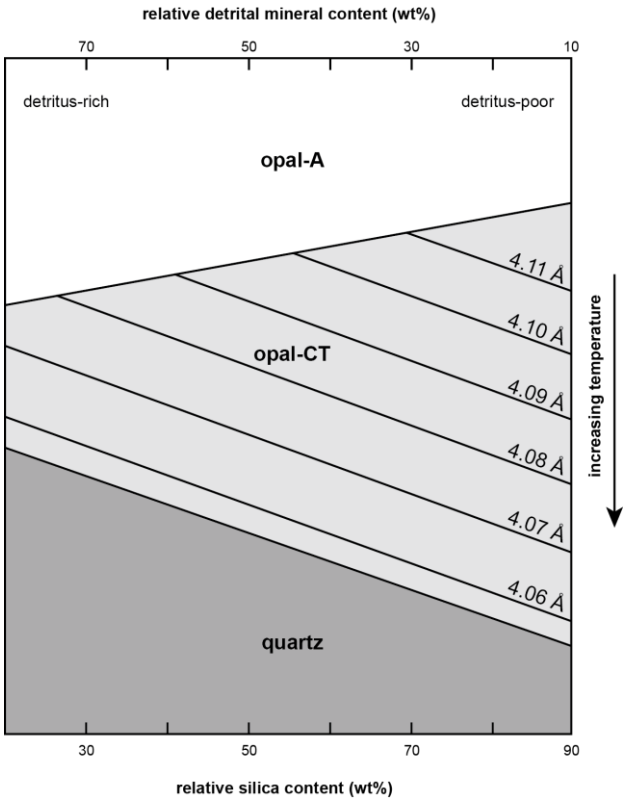

Figure 4-2: Diagenetic silica phase transformation as function of detrital mineral content (redrawn after Isaacs (1982). Quartz chert that contains high detritus contents forms at lower temperature and depth during burial diagenesis compared to pure quartz chert. The underlying cause is that prior to quartz formation opal-CT must first have matured to obtain a high degree of crystallographic order (i.e., a low d-101-spacing of ca. 4.06 Å). In detritus-poor siliceous sediments, opal-A transforms to opal-CT during early diagenesis and obtains an initially low degree of crystallographic order (high d101-spacing), entailing a prolonged maturation time during diagenesis. With increasing detritus content the degree of initial crystallographic order increases (d-101-spacing decreases) and the maturation time of opal-CT is reduced.

Opal-CT will form only when this equilibrium solubility is exceeded. Detritus-poor siliceous sediment releases Si readily and the solubility is fast exceeded during the incipient stages of silica diagenesis. Opal-CT can thus form at low temperatures (Bohrmann et al., 1994; Botz and Bohrmann, 1991; Tatzel et al., 2015). In detritus-rich siliceous sediment the equilibrium Si solubility is not exceeded during early diagenesis and opal-CT forms later during burial when elevated temperature raises the silica solubility. The opal-CT that forms in detritus-rich sediment obtains an initially higher crystallographic order (Figure 4-2). Therefore, the next step, the conversion to quartz occurs earlier and at lower temperature, too (Isaacs, 1982). Conversely, opal-CT that forms from detritus-poor siliceous sediment has initially a lower crystallographic order and is being converted to quartz at higher temperature and thus later during burial diagenesis (Figure 4-2). Thus it is i) the degree of initial crystallographic order in opal-CT that is controlled by detritus contents and ii) the rates of maturation that couple detritus contents and rates of quartz formation (Isaacs, 1982).

In addition to detrital minerals, organic matter and carbonates are important modifiers of the rates of quartz formation. At higher pH values MgOH nucleus formation is favored. These MgOH nuclei serve as

sites for opal-CT lepisphere (microcrystalline, blade-shaped cristobalite-tridymite crystals) growth by attraction of silanol groups (a functional group consisting of SiOH) (Williams and Crerar, 1985). The presence of carbonates increases pH and thus strongly enhances opal-CT formation (Kastner et al., 1977). However, the Mg^{2+} and OH^- are also taken up by clay minerals, the presence of which therefore suppresses opal-CT formation (Kastner et al., 1977). Opal-CT formation is also suppressed in organic-rich siliceous sediment, possibly due to the chelatization of Mg through oxalic acid (Hinman, 1990). Overall, the effect of organic matter on the rates of silica diagenesis depends on type- and amount of organic matter as well as volume fraction of carbonates and detritus (Hinman, 1990). These differences in the rate of opal-CT formation result in a range of possible initial crystallographic order of the opal-CT. The result is that the time required for the opal-CT maturation is variable and depends on the composition of the host sediment. A corollary is that quartz forms at different temperatures and thus depths during diagenesis, and that this depth is dictated by the chemical properties of the sediment.

Oxygen isotope evidence in quartz documents the above predictions in the geological record: the temperature of quartz precipitation controls the oxygen isotope composition because oxygen equilibrium isotope fractionation is temperature-dependent. Unlike is the case for Si, oxygen isotope fractionation does commonly not depend on mass balance due to virtually infinite oxygen supply in both fluid and quartz (Knauth and Epstein, 1976). Isotopic evidence for the suggested chemical control on the temperature of mineral formation and hence on the chert $\delta^{18}O$ record is documented by the systematically higher $\delta^{18}O$ in carbonate-hosted Paleozoic cherts as compared to carbonate-free facies. This result was interpreted to imply lower temperatures, higher rates and shallower depths of silica diagenesis (Jones and Knauth, 1979). Such dependence of $\delta^{18}O$ in chert on the bulk sediment composition shows that quartz chert retains a temperature-dependent $\delta^{18}O$ signature acquired during diagenesis. Furthermore, substantial decreases in $\delta^{18}O$ at the lithological boundary between siliceous sediment and porcellanite (opal-A/opal-CT) and between porcellanite and quartz chert (opal-CT/quartz) in the Miocene Monterrey Formation, California, document the temperature increase at the silica phase boundaries (Murata et al., 1977).

In this study I evaluate how the oxygen isotope record of chert depends on and varies with the rate of quartz formation during burial diagenesis. In order to do so, chert samples from a single stratigraphic section featuring highly variable amounts of detrital minerals were analyzed, i.e., samples in which quartz has presumably formed at variable rates. I present $\delta^{18}O$ data together with SiO_2, Al_2O_3- and TOC concentrations of Ediacaran to Cambrian bedded cherts and siliceous shales of the Lichapo and Xiaoyanxi Formations deposited in a continental slope- to basin setting at 'Lijiatuo' section on the Yangtze Platform, China (Guo et al., 2007a). I have determined the mass fraction of detrital minerals in these samples, and calculated $\delta^{18}O$ of authigenic quartz. The $\delta^{18}O$ of authigenic quartz in three detritus-rich samples was measured by secondary ion mass spectrometry. If $\delta^{18}O$ in quartz indeed reflects the temperature, rate, and depth of diagenetic quartz formation I assume that these temperatures will be set earlier and hence be lower

than peak diagenetic temperatures. To evaluate whether this is the case the peak diagenetic temperatures were determined by Raman spectrometry of carbonaceous material. Moreover, given that the temperature of diagenetic quartz formation and thus its oxygen isotope fractionation depends on the rate of quartz formation, I quantify the magnitude of the $\delta^{18}O$ increase in chert that is expected for decreasing geothermal gradients on Earth through time.

The results suggest that the chert's $\delta^{18}O$ is locked in at the ambient temperatures experienced during diagenesis, and that this signature is preserved despite subsequent burial to prehnite-pumpellyite-facies conditions. The presence of variable contents of detrital minerals in chert can account for a large part of the scatter observed in the global chert $\delta^{18}O$ compilation. Model results suggest that the secular shift observed in the chert oxygen isotope record results from decreasing temperatures and decreasing rates of quartz formation due to decreasing geothermal gradients that result from the cooling of the Earth's crust.

4.1. Materials and Methods

Samples were taken at the well-preserved, marine section 'Lijiatuo' in Hunan, South China (28°24.519, 110°27.926). This section comprises ca. 50 m of mostly black, Ediacaran cherts that are divided by a volcanic ash layer dated by U/Pb at 546 Ma ± 12 Ma (Jiang et al., 2010) from ca. 100 m of Lower- to Middle Cambrian black cherts and metal-rich, siliceous shales with two intercalated nodular phosphorite layers.

Bulk chert oxygen isotope analyses were carried out by laser fluorination gas source mass spectrometry (Sharp, 1990) at the University of Göttingen. Oxygen is liberated from solid samples by the reaction of 0.2 mg powdered rock with purified F_2 using a CO_2-laser. Samples are purified in a gas extraction line and a Thermo Gas Bench-II. Sample O_2 is then analyzed using a Thermo MAT 253 mass spectrometer operating in continuous flow mode (for method details see section 4.6.1.1).

The oxygen isotope composition of authigenic quartz I estimate by a mass balance (Equation 4-10). First, I derive the relative contribution of detrital minerals from bulk rock Al/Si ratios and the Al/Si ratio of stoichiometric illite ($K_{0.65}Al_{2.65}Si_{3.35}O_{10}(OH)_2$; "mindat.org," 2015). This calculation is based on the assumption that all Al in the bulk rock is exclusively present in illite. That this assumption is a valid approximation is shown by exemplary quantitative XRD analyses (Supplementary Table 3-2). Furthermore, I assume a constant clay to detrital quartz ratio between 1.5 and 10 to account for the presence of detrital quartz (for details see section 4.6.2).

Calculated $\delta^{18}O$ of authigenic quartz of detritus-rich samples were confirmed by micro-scale oxygen isotope analyses by secondary ion mass spectrometry using a Cameca 1280-HR at GFZ Potsdam. A 2.5 nA Gaussian $^{133}Cs^+$ primary ion beam is focused onto a solid sample surface to produce secondary ions that are detected in Faraday cups (for method details see section 4.6.1.2). Raman spectra of carbonaceous matter

were acquired using a Horiba Jobin Yvon HR800-UV spectrometer equipped with a 488 nm Ar^+ laser at the University of Göttingen. The laser beam is focused through the objective of the connected microscope onto the sample surface and the backscattered light passes through a 100 µm confocal hole and is diffracted by a 600 lines/mm grating onto a CCD detector to generate Raman spectra (for method details see section 4.6.1.3).

Al_2O_3 and SiO_2 concentrations were determined by x-ray fluoresence (XRF) of powdered and fused samples using a Philips Panalytical PW2400 X-ray at the Institute of Applied Geosciences at the Technical University Berlin. The total organic carbon content (TOC) was measured using an elemental analyser NA1500 at GFZ Potsdam.

4.2. Results

All samples are composed predominantly of SiO_2, Al_2O_3 and organic carbon (Table 4-1). Bulk rock SiO_2 concentrations vary between 60 and 99 wt%, Al_2O_3 concentrations between 0.2 and 15.8 wt%, TOC concentrations between 0.2 to 15.1 wt%. Other major- and trace element concentrations are reported in chapter 3. Quartz is the dominant component in all rocks with illite being the second most abundant mineral phase and the major carrier of Al. Some samples contain barite, K-feldspar and other minor phases (Table 4-1).

The oxygen isotope composition of bulk samples (consisting of 0.2 mg of material) ranges from 12.6 to 24.0‰ $\delta^{18}O$ (Table 4-1). The detrital mineral content is estimated to range between 1 and 75 wt%. The oxygen isotope composition of authigenic quartz, $\delta^{18}O_{a\text{-}qtz}$ (excluding detritus-bound O) is estimated by mass balance to range from 17.1 to 29.8‰ (Table 4-1, Figure 4-3, Figure 4-4). Analytical results from secondary ion mass spectrometric analyses of authigenic quartz are reported in Table 4-1 and Appendix Table 4-2. The preparation quality of the samples was aggravated by high clay contents and only few analyses yielded sufficiently high ^{16}O count rates. The morphology of sample pits frequently shows irregularities, analyses of multiple phases, fluid inclusions, and broken off edges. We report all analyses with ^{16}O count rates $>1.7 \cdot 10^9$ cps and highlight $\delta^{18}O$ values of sampled spots with the best morphology. The analyses yield $\delta^{18}O$-values between 14.4 and 25.4‰, where spots with the cleanest crater morphology yield mostly higher $\delta^{18}O$ values. One analyses yielded 10.7‰ $\delta^{18}O$ and likely represents detrital quartz.

I have calculated temperatures from $\delta^{18}O_{a\text{-}qtz}$ based on the calibration of O-isotope fractionation between quartz and water by Knauth and Epstein (1976) assuming that $\delta^{18}O_{water} = \delta^{18}O_{seawater} = -1.1$ (Cummins et al., 2014). Calculated quartz precipitation temperatures vary between 30°C to 155°C assuming clay/quartz= 1.5 (Table 4-1).

Analytical results from Raman spectrometry are summarized in Appendix Table 4-1. Temperatures were calculated by means of a new approach, using integrated peak areas of specific wavelength ranges (Lünsdorf, in prep.). Peak diagenetic temperatures calculated based on this method yield 254 ± 1.9°C (sample Li 02), 265.6 ± 7.8°C (sample Li 23A), and 261.6 ± 2.8°C (Li 33). Peak diagenetic temperatures can also be estimated by the calibration of Lahfid et al. (2010). Using their calibration, peak temperatures are in the range of 250 to 310°C. This approach, however, yields higher uncertainties, because their calibration was made on different type of organic matter and a Raman Spectrometer equipped with a different laser wavelength.

Table 4-1: Concentrations of SiO_2, Al_2O_3, TOC, and the O-Isotope composition of bulk chert and silicified shales of the 'Lijiatuo' section. Two estimates of detrital mineral contents and $\delta^{18}O$ of silica are reported (see Supplementary Information). The oxygen isotope composition of authigenic quartz was calculated based on the estimated detrital mineral abundances. Temperatures were calculated for authigenic quartz, assuming a clay/quartz ratio of 1.5†. See text for details. *Quartz is present as main component in all samples. Ba= barite, Kfs= K-feldspar, Il= illite, Py= pyrite, Ba-Fs= Ba-feldspar, 15Å= 15Å clay mineral. Brackets indicate abundances <5 wt%. ** $\delta^{18}O$ calculated from $\delta^{17}O$ assuming an equilibrium isotope fractionation factor of 0.53052.

sample	height above section base	SiO_2	Al_2O_3	TOC	minerals XRD*	$\delta^{17}O$	$\delta^{18}O$	detritus clay/quartz= 10	$\delta^{18}O_{silica}$	detritus clay/quartz= 1.5	$\delta^{18}O_{silica}$	T
	[m]	[wt%]	[wt%]	[wt%]		[‰]	[‰]	[wt%]	[‰]	[wt%]	[‰]	[°C]
Li 01	0.20	98.1	0.4	0.3		9.11	17.1	2.0	17.1	1.3	17.2	108
Li 02	9.45	98.9	0.3	0.9		9.04	17.1	1.2	17.1	0.8	17.2	108
Li 03	12.50	98.2	0.5	0.9	(Ba, Kfs)	10.14	19.3	2.2	19.3	1.5	19.4	89
Li 04	18.50	97.1	1.4	0.4		10.69	20.4	6.6	20.6	4.4	20.8	79
Li 05	24.50	92.5	2.8	0.7	(Il, Ba, Kfs, Py)	11.35	21.4**	13.4	22.0	8.8	22.6	67
Li 06	30.50	97.6	0.2	0.6	(Ba)	10.37	19.5	1.1	19.5	0.8	19.5	88
Li 07a	36.50	78.9	6.0	0.4	Il, Ba	11.99	22.8**	28.5	24.6	18.8	26.9	44
Li 12a	52.00	91.5	2.2	0.4	(Ba, Kfs, Ba-Fs)	11.43	21.8	10.4	22.2	6.9	22.7	67
Li 16	53.06	88.4	2.8	0.2	(Ba, Kfs)	12.65	24.0	13.3	24.9	8.8	25.7	50
Li 18	53.60	93.5	2.0	0.5	Ba, Kfs, (Py)	12.36	23.3	9.4	23.8	6.2	24.3	57
Li 22	55.52	92.9	0.3	1.4		9.81	18.6	1.5	18.7	1.0	18.7	95
Li 23b	56.52	94.9	0.3	1.8	Ba	6.71	12.6	1.2	12.6	0.8	12.6	155
Li 25b	61.50	86.3	1.1	7.6	Il, Ba	12.30	23.6	5.2	23.9	3.4	24.2	58
Li 25a	61.60	60.4	6.1	15.1	Il, Ba, (Kfs, 15Å)	9.09	17.3	29.0	18.0	19.2	19.8	86
Li 29	77.00	74.7	8.0	7.6	Il, (Ba)	11.94	22.8	38.0	25.7	25.1	29.8	30
Li 31	96.50	67.1	15.8	2.5	Il	8.55	16.2	75.0	17.2	49.5	29.2	33
Li 33	117.50	80.5	3.6	10.8	Il, (15Å)	10.54	20.1	17.0	20.8	11.2	21.7	74
Li 34	128.00	81.7	2.6	10.6	Il, (15Å)	10.49	20.0	12.5	20.4	8.2	21.0	78
Li 35	138.50	80.4	4.9	4.7	Il	11.02	21.0	23.3	22.2	15.4	23.6	61

† The temperature of quartz formation is calculated using the calibration of temperature-dependent oxygen isotope fractionation by Knauth and Epstein (1976) assuming $\delta^{18}O$ (water)= -1.1‰ (Cummins et al., 2014). The $\delta^{18}O$ of authigenic quartz (a-qtz) is calculated by mass balance where Al/Si ratios of bulk rock and of stoichiometric illite, as well as a constant detrital quartz (d-qtz) to clay ratio of 1.5 are assumed.

Table 4-2: Analytical results from SIMS analyses of samples Li 29, Li 31 and Li35. All measurements reported yielded ^{16}O count rates >1.7 10^9 cps and clean sample spots. The uncertainty on absolute $\delta^{18}O_{SMOW}$ is estimated to 0.37‰.

Analysis	^{16}O cps	$^{18}O/^{16}O$ measured	1SD [‰]	$^{18}O/^{16}O$ imf corrected	$\delta^{18}O$ SMOW [‰]	comment
Li29@12	2.32E+09	0.00204242	0.087	0.00205603	25.35	nice hole, slight overlap with other
Li31@02	2.24E+09	0.00201316	0.071	0.00202659	10.67	nice hole
Li31@19	2.14E+09	0.00203896	0.111	0.00205256	23.62	nice, clean hole, minor cracks
Li35@13	2.11E+09	0.00202943	0.117	0.00204296	18.83	nice hole
Li35@14	2.08E+09	0.00203956	0.083	0.00205315	23.92	nice hole, slightly irregular surface
Li35@16	2.12E+09	0.00202212	0.103	0.00203560	15.16	nice hole, slightly irregular surface
Li35@17	2.11E+09	0.00203502	0.086	0.00204859	21.64	nice hole, slightly irregular surface
Li35@18	2.10E+09	0.00202576	0.088	0.00203926	16.99	nice hole, slightly irregular surface
Li35@19	2.06E+09	0.00203817	0.085	0.00205176	23.22	slightly irregular surface
Li35@20	2.06E+09	0.00203814	0.073	0.00205173	23.20	slightly irregular hole, mixed analysis

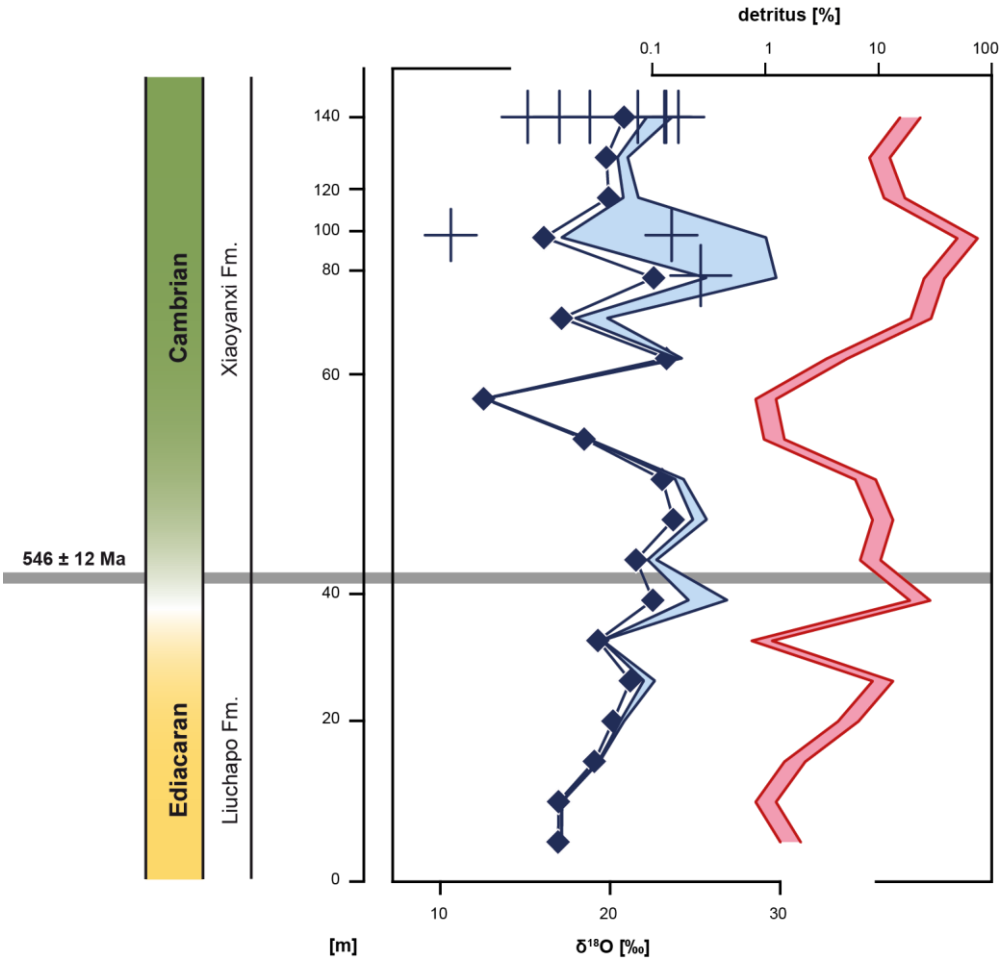

Figure 4-3: Stratigraphic variation of the chert oxygen isotope composition and detritus contents. The measured oxygen isotope composition of bulk samples $\delta^{18}O_{bulk}$ (diamonds) and calculated $\delta^{18}O$ of authigenic quartz, $\delta^{18}O_{a\text{-}qtz}$ (blue envelope) is shown in relation to calculated contents of detrital minerals (red envelope). The range of $\delta^{18}O_{a\text{-}qtz}$ estimates results from the end-member estimates of detritus contents. Two 'end-member' estimates for the detrital quartz contents are clay/quartz= 1.5 (high end) and clay/quartz= 10 (low end). The blue crosses show results from SIMS analysis of authigenic quartz (Table 4-2), where the best analyses, characterized by high ^{16}O count rates >$1.7 \cdot 10^9$ cps and clean crater morphology are highlighted (big crosses). Samples are plotted against stratigraphic age with equidistant spacing for better visibility. Thus the y-axis is not uniform.

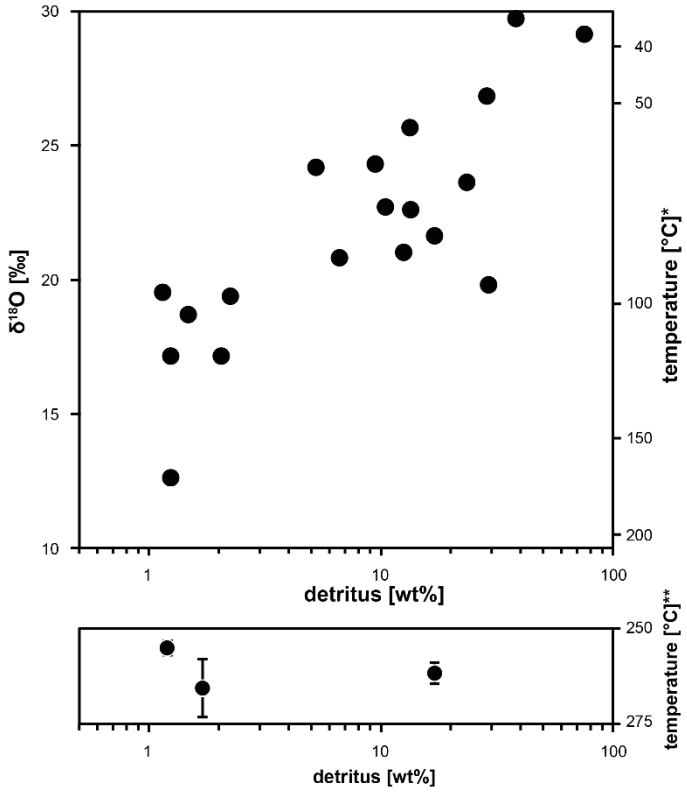

Figure 4-4: The calculated oxygen isotope composition of authigenic quartz in chert and corresponding temperatures of quartz formation (a) and diagenetic peak temperatures from Raman spectroscopy of carbonaceous matter (b) vs. the calculated detritus content. a) $\delta^{18}O$ of authigenic quartz increases with increasing detritus contents. * The temperature scale corresponds to the calibration of O-isotope fractionation between quartz and water by Knauth and Epstein (1976) assuming $\delta^{18}O_{water}$= -1.1 (Cummins et al., 2014). b) diagenetic peak temperatures are invariant at variable detritus contents. ** Diagenetic peak temperatures are estimated from Raman spectra of carbonaceous matter (section 4.6.1.3).

4.3. Discussion

Temperatures calculated from $\delta^{18}O$ of quartz range between 30 and 155°C (assuming $\delta^{18}O_{water}$ = -1.1; Cummins et al., 2014). These $\delta^{18}O$ signatures were preserved despite high peak diagenetic temperatures of ca. 260°C as indicated by Raman spectroscopy (Table 4-1, Figure 4-4b), indicating an overall high robustness of the chert $\delta^{18}O$ record through hundreds of million years. That these $\delta^{18}O$ temperatures calculated from chert reveal an early diagenetic fingerprint is suggested by a strong correlation between $\delta^{18}O_{silica}$ and the detrital content. Specifically, this observation supports existing evidence that the timing, and the temperature of quartz formation (from opal-CT) in the sediment is highly variable and depends on detritus contents (Isaacs, 1982). Therefore, the large range of $\delta^{18}O$ observed within a single stratigraphic section can result from variations in the quartz formation temperatures. Even small variations in detrital mineral contents in chert can explain a part of the scatter in $\delta^{18}O$ that is observed in the global compilation. Because the early diagenetic fingerprint is preserved, it follows that age-dependent alteration (hypothesis 1; see section 4.1)

through interaction with ^{16}O-rich groundwater (Degens and Epstein, 1962) is an unlikely explanation for the secular trend in chert.

If decreasing seawater temperatures caused the secular shift (Knauth and Lowe, 2003, 1978; Knauth, 2005; Kolodny and Epstein, 1976; Robert and Chaussidon, 2006), then seawater temperatures (derived from chert samples with the highest $\delta^{18}O$ values found) must have been as high as 55 to 85°C at 3.5 Ga (Knauth and Lowe, 2003). This inference is challenged by recent estimates for Archean seawater temperatures <40°C as derived from phosphate $\delta^{18}O$ (Blake et al., 2010) and serpentine $\delta^{18}O$ and δD (Pope et al., 2012). Based on this evidence and given that I attribute a diagenetic nature to the chert $\delta^{18}O$ record, I consider this explanation (hypothesis 2) unlikely.

Hypothesis 3) states that the seawater $\delta^{18}O$ has increased over Earth history (Jaffrés et al., 2007; Kasting et al., 2006; Wallmann, 2001). Mass balance calculations suggest that $\delta^{18}O$ of seawater has increased through the Phanerozoic due to higher emission of water from hydrothermal and volcanic sources relative to the fixation of ^{18}O through low-temperature water/rock interaction (Wallmann, 2001). On billion-year time scales, models suggest that the decreasing heat flow over Earth's history led to greater water column overlying ridge crests, entailing increased hydrothermal penetration depth, and hence increasing seafloor alteration temperatures, shifting the seawater $\delta^{18}O$ value by up to 10‰ (Kasting et al., 2006). Recently, it was suggested that the critical average ridge depth for a shift towards higher $\delta^{18}O$ of seawater was attained in the early Paleozoic and amounts approximately 6‰ (Veizer and Prokoph, 2015). Besides reduced high-temperature alteration, enhanced weathering in the Precambrian was suggested to decrease seawater by up to 13‰ (Jaffrés et al., 2007).

These models were recently challenged by evidence from clumped isotope data that suggests a relatively constant Phanerozoic seawater $\delta^{18}O$ at -1.1 ± 1‰ (Cummins et al., 2014; Finnegan et al., 2011; Muehlenbachs et al., 2003). The constancy of this value is explained by buffering through interaction of seawater and oceanic crust (Muehlenbachs and Clayton, 1976). Recent oxygen isotope evidence of phosphates (Blake et al., 2010) and serpentines (Pope et al., 2012) supports the view that even Archean seawater had a similar $\delta^{18}O$ to that in the modern ocean. These new findings suggests that the large shift of ca. 6‰ $\delta^{18}O$ observed in Phanerozoic marine carbonates (Veizer and Prokoph, 2015; Veizer et al., 1999) is not due to large long-term changes in seawater $\delta^{18}O$ either, but instead result from post-depositional alteration. That carbonates are prone to isotope exchange with fluids during diagenetic dissolution-reprecipitation is indicated by increasing $\delta^{18}O$ in pore water of modern deep sea carbonates where elevated temperatures drive the $\delta^{18}O$ of carbonate towards lower values (Swart, 2015). Such shift has also been observed in apparently well-preserved Ediacaran carbonates (Hohl et al., 2015). Nevertheless, as far as the secular $\delta^{18}O$ shift over the Phanerozoic is concerned, a high number (>57000) of alteration-resistant Low-

Magnesium Calcite shells of Bivalves, Brachiopods, Belemnites and Foraminifera suggest that a secular change in seawater $\delta^{18}O$ is tracked in such shells (Veizer and Prokoph, 2015).

The indicated robustness of the chert oxygen isotope composition (beyond the Phanerozoic) on the other hand suggests that the secular $\delta^{18}O$ trends in carbonates and cherts are caused by different processes. This evidence calls for a new explanation for the secular trend in $\delta^{18}O$ of chert that involves crustal temperatures. It was noted earlier that the thermal history of siliceous sediment controls silica phase transformation rates (Mizutani, 1977, 1970). Thermal histories are controlled by the geothermal gradient (Becker and Clayton, 1976; Knauth and Lowe, 2003) and sedimentation rates both of which affect the oxygen isotope composition of chert through burial heating (Pisciotto, 1981). Knauth and Lowe (2003) ascribe a 6 to 7‰ $\delta^{18}O$ range in Archean samples to locally high geothermal gradients resulting from the emplacement of interbedding volcanic rocks. Here, I thus suggest that the secular increase in $\delta^{18}O$ of chert stems from decreasing quartz formation temperatures as consequence of changing heat flow. Changes in the geothermal gradient lead to shifts in $\delta^{18}O$ of chert that I explore below.

4.3.1. Crustal cooling as driver for the oxygen isotope record of chert

Cooling of the crust will lead to a decreased geothermal gradient that causes reduced heating rates and therefore causes i) overall lower temperatures of quartz formation. The heating rate of sediments also depends on the sediment burial rate. Therefore, ii) variations in sedimentation rate will also affect the temperature and depth of quartz formation, as demonstrated for siliceous rocks from the Monterrey Formation (Pisciotto, 1981). A lower geothermal gradient will lead to iii) an increasing depth of quartz formation caused by lower quartz formation rates and hence to a decreasing water/rock ratio during the phase formation from opal-CT to quartz. All of these will affect $\delta^{18}O$ of silica.

4.3.1.1. The temperature and depth of chert formation

In a simple model, I explore the influence of changing geothermal gradient and sedimentation rate on the temperature and depth of quartz chert formation. In this model I assume a pure silica system where quartz formation is based on temperature-dependent reaction rates for opal-A to opal-CT transformation (Mizutani, 1970), opal-CT maturation (Kano and Taguchi, 1982), and opal-CT to quartz transformation (Ernst and Calvert, 1969). The maturation process comprises three subsequent processes where first opal-A is being transformed into opal-CT, second opal-CT matures to obtain a high degree of crystallographic order, and third quartz forms from highly ordered opal-CT. The temperature dependence of the reaction rate constants of these mineral transformation reactions can be described by the Arrhenius equation:

$$k = A \cdot e^{\frac{-E_a}{RT}}$$ **Equation 4-1**

Where *k* is the reaction rate constant of the reaction and has the unit 1/time [h^{-1}] (in a first order reaction), *A* is the pre-exponential factor [h^{-1}], E_a is the activation energy [kcal/mol], *R* is the gas constant [J/(mol K)], and *T* is the temperature [K]. 1/*k* gives the time constant corresponding to the time required to increase the fractional amount of a product (opal-CT, quartz) by $1\text{-}e^{-1}$ ≈63% over that of the precursor at a given temperature and activation energy. The three maturation processes have different activation energies and pre-exponential factors. To calculate the rates of opal-A to opal-CT transformation, I have used values given in Mizutani (1970) of: *A*= 23700 h^{-1}, and E_a= 16 kcal/mole.

To calculate the time for opal-CT maturation I use the equation given in Kano and Taguchi (1982):

$$S = S_0 \cdot e^{-kt}$$ **Equation 4-2**

Where *S* is the difference in d(101) spacing from an ideal opal-CT [Å] (with d(101) spacing= 4.05 Å) following opal-CT maturation, S_0 [Å] is the difference in d(101) spacing from an ideal opal-CT before the maturation process, *k* is the rate constant and *t* is time [h]. Combining the Arrhenius equation (Equation 4-1) with Eq. 2, the time needed to mature opal-CT with a given initial and final d(101) spacing at a given temperature and activation energy can be calculated:

$$t = \frac{\ln\left(\frac{S}{S_0}\right)}{-A \cdot e^{\frac{-E_a}{RT}}}$$ **Equation 4-3**

I assume an initial d(101) spacing of 4.12, and a final d(101) spacing of 4.06 Å, values that correspond to opal-CT that forms and matures in a pure silica systems (Isaacs, 1982). S, the difference in d(101) spacing, cannot be zero and here I assume S_0= 4.0599. S_0 is 4.12 - 4.0599 = 0.0601 Å. For the preexponential factor *A*= $1.519 \cdot 10^6$ is used. This value was extracted from the Arrhenius plot reported in Kano and Taguchi (1982). The activation energies for opal-CT maturation are poorly constrained and range between 19 and 23 kcal/mol. To calculate opal-CT maturation rates I use E_a= 23 kcal/mol.

The opal-CT to quartz transformation rate is calculated according to the experimental work by Ernst and Calvert (1969) assuming a nucleation and growth model (Stein and Kirkpatrick, 1976). Using the Arrhenius equation (Equation 4-1) with *A*= $9.762\ 10^6$ [$1/h^{-n}$], n= 1.3, and E_a= 30.54 kcal/mole (Dralus, 2013),

I calculate the temperature dependence of the reaction rate constant. To estimate the total time needed to form chert at a given temperature, $t_{chert(T)}$, I sum up the calculated durations needed for the opal-A to opal-CT transformation, the opal-CT maturation, and the opal-CT to quartz transformation at given temperatures during burial.

$$t_{chert}(T)\,[Ma] = t_{A-CT\,(T)} + t_{CT-CT\,(T)} + t_{CT-Q\,(T)} \qquad \textbf{Equation 4-4}$$

Where $t_{A\text{-}CT(T)}$ is the time needed to convert opal-A into opal-CT, $t_{CT\text{-}CT(T)}$ is the time needed for opal-CT maturation, and $t_{CT\text{-}Q(T)}$ is the time needed to convert opal-CT into quartz at given temperature. This way of calculating the duration of chert formation is a simplification and gives a maximum estimate for the chert formation time, because the diagenetic silica phase transformations are not strictly temporally and spatially separated. This is so because successive diagenetic silica phases start forming prior to the completion of the precursor phase transformation. Calculated fractions of quartz within a depth increment, f_{quartz} relate to quartz that forms within one mean time (63%).

The fraction of quartz formed during the time interval Δt spent at a depth increment Δz during burial depends on the temperature (given by the geothermal gradient) and time (given by the rate of sediment burial). The time Δt is derived from the thickness of a given depth increment Δz and the sedimentation rate S [m yr^{-1}].

$$\Delta t = \frac{\Delta z}{S \cdot \frac{\rho(z)}{\rho(0)}} \qquad \textbf{Equation 4-5}$$

Equation 4-5 includes a correction term for sediment compaction, where a density at a given depth $\rho(z)$ [kg m^{-3}] was corrected relative to the sediment surfaces density $\rho(0)$= 1650 kg m^{-3} using the minimum density curve of water saturated clastic sediments (McCulloh, 1967) that is approximated by a logarithmic function. To obtain a total samples recorded temperatures and depth of chert formation, temperatures and depths in each depth increment are weighted according to calculated fractions of quartz, f_{quartz} that formed at the respective condition during burial.

The depth and temperature of quartz formation was calculated for different sedimentation rates of 5, 50, and 500 mm kyr^{-1}, assuming that the geothermal gradient remains constant for the highest sedimentation rate. I further calculate the temperature and depth of quartz formation for different geothermal gradients of 10, 30, 50, 70 and 90°C/km.

Figure 4-5 summarizes the results of the modeling, which show that if the geothermal gradient decreases, quartz will form at lower temperature (Figure 4-5, a-c) and greater depth (Figure 4-5, d-f). Average quartz formation temperatures shift from ca. 39°C (90°C/km) to ca. 23°C (10°C/km) at 5 mm kyr^{-1} sedimentation rate (Figure 4-5 a). The average depth of quartz formation decreases from ca. 0.9 km to 0.3 km when the thermal gradient decreases from 90°C km^{-1} to 10° C km^{-1} at 5 mm kyr^{-1} sedimentation rate (Figure 4-5 d). When sedimentation rates are as high as 50 mm kyr^{-1}, quartz forms at higher average temperature (33°C – 52°C) and at greater average depths (2 – 0.5 km). When sedimentation rates are 500 mm kyr^{-1}, quartz forms between 51 and 73°C and of 3.3 – 0.6 km depth.

These temperature estimates from the model agree well with temperatures reported for the opal-CT to quartz conversion in Cenozoic silica deposits. Siliceous sediments of the Miocene Monterrey formation in the 'Temblor range' location transform to quartz at temperatures between 55 and 110°C as estimated from chert $\delta^{18}O$ (Murata et al., 1977). In the 'Santa Maria Valley' location, quartz formation temperatures were estimated based on chert $\delta^{18}O$ to between 35 and 61°C (Pisciotto, 1981). However, calculated temperatures for the intermediate and low sedimentation rate are at the lower end of reported temperature ranges, possibly indicating that the rates calculated here are faster than in nature.

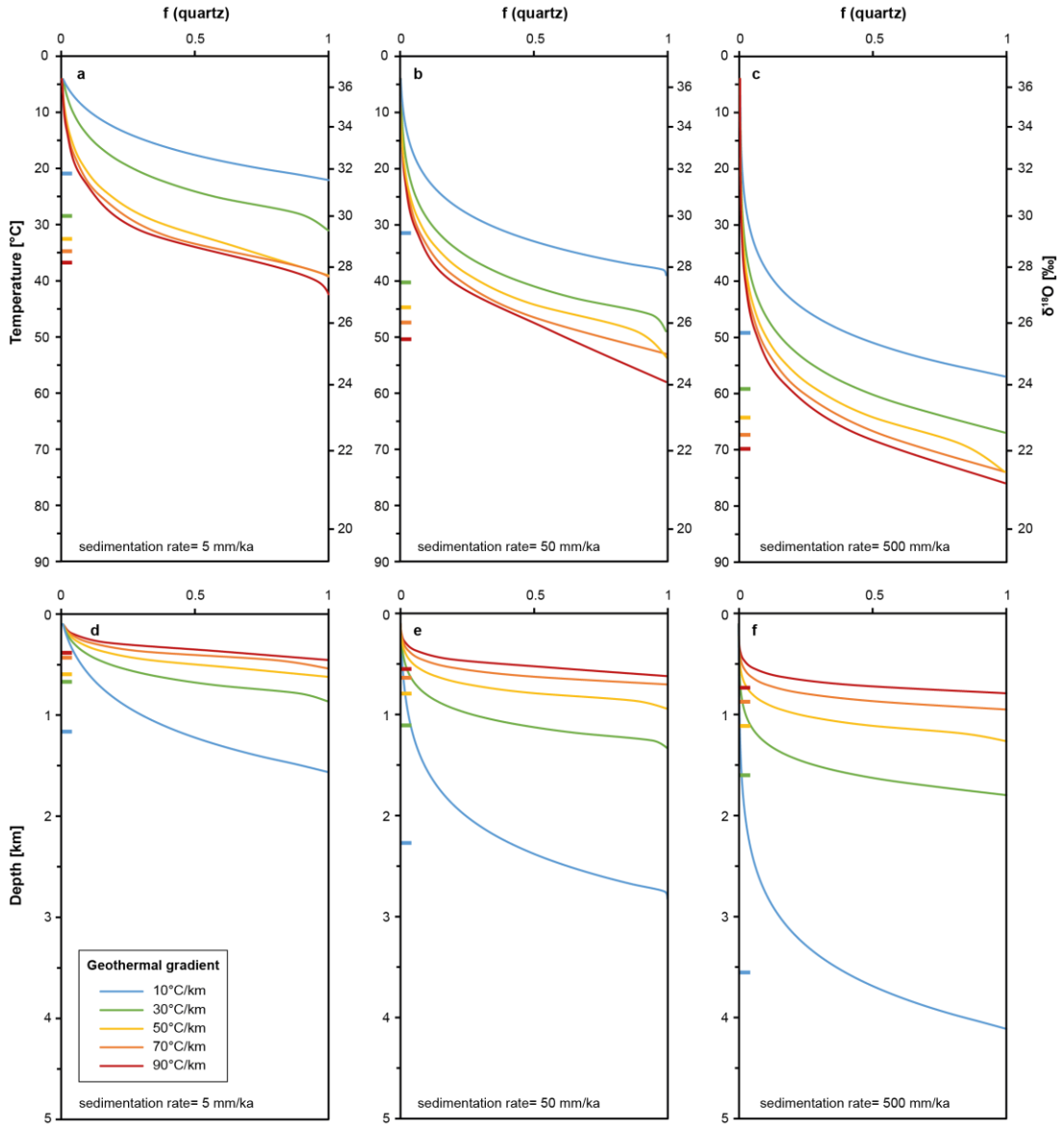

Figure 4-5: Model temperature and depth of diagenetic quartz formation for different geothermal gradients and sedimentation rates. In the model for a pure silica system and constant sedimentation rates temperature-dependent reaction rates were calculated from opal-A to opal-CT transformation, opal-CT maturation, and opal-CT to quartz transformation. The temperature scale corresponds to the calibration of O-isotope fractionation between quartz and water by Knauth and Epstein (1976) assuming $\delta^{18}O_{water}$= -1.1 (Cummins et al., 2014). The temperature of quartz formation decreases with decreasing geothermal gradient (a-c). The depth of quartz formation increases with decreasing geothermal gradient (d-f). Increasing sedimentation rates result in quartz formation at higher temperatures and greater depth. The marks at the side of the panels indicate the weighted average values.

4.3.1.2. The depth-time relation

From calculated depth and duration of quartz chert formation, a depth-time relation can be constructed for different geothermal gradients and sedimentation rates. A comparison with depths and ages of diagenetically formed quartz chert found in sediments of the Atlantic and Pacific Oceans (Riech and von Rad, 1979) allows estimating how well the calculated quartz formation rates (based on experimentally-derived transformation rates) agree with natural observations (Figure 4-6).

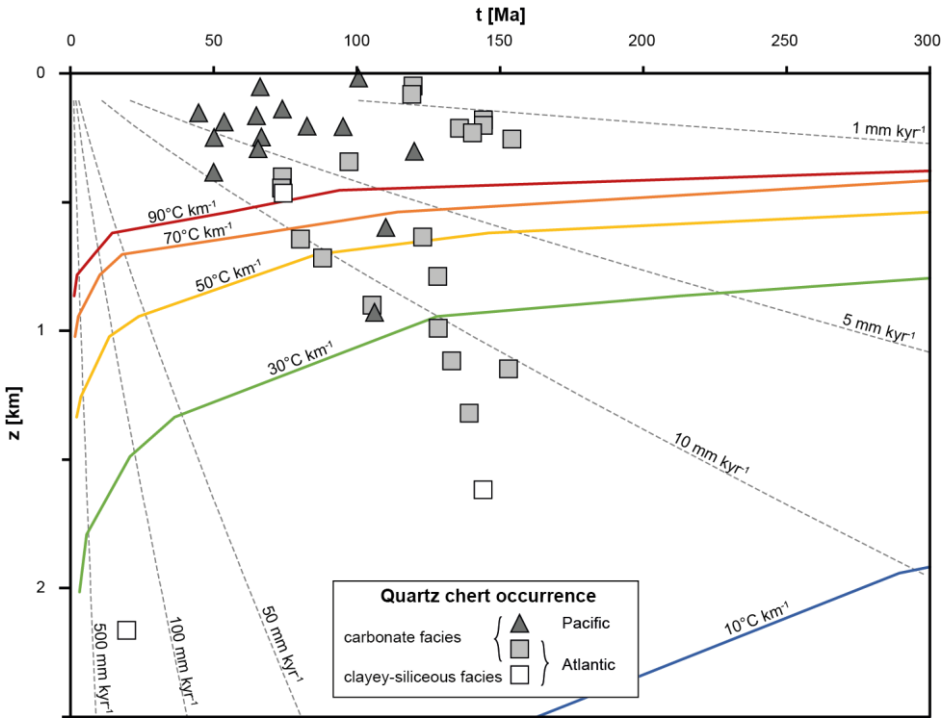

Figure 4-6: Model curves showing the mean time of quartz formation for a given geothermal gradient and burial rate. Contour lines show the compaction-corrected depth to which sediment is buried after a time t at a given sedimentation rate. Symbols show quartz chert occurrences in the Atlantic (squares) and Pacific Oceans (triangles) (Riech and von Rad, 1979). Gray symbols indicate chert in a carbonatic facies and white symbols represent cherts from clayey-siliceous facies. The age at which these data are plotted is the sediment age and therefore represents a maximum age for quartz formation.

Among the cherts from carbonate facies, those of the Pacific are found at shallower depths compared to those of the Atlantic. One explanation is that in Atlantic cherts sediment ages exceed the age of quartz formation (note that the sediment ages used provide a maximum time for quartz formation). Another explanation is that the Pacific seafloor has an average younger age and is hence characterized by a higher heat flow. The sediments overlying young (<20 Ma) oceanic crust are expected to have thermal gradients of ca. 40 to 120°C km^{-1} assuming a high heat flow of ca. 0.1 to 0.25 W m^{-2} (Sclater et al., 1980) and thermal conductivities of shale and carbonate of 2.1 W m^{-1} K^{-1} and 3.1 W m^{-1} K^{-1} (Reiter and Tovar, 1982). However, quartz chert formation can only run to completion in such short time when sedimentation rates are accordingly high (100-500 mm kyr^{-1}).

On the other hand, siliceous sediment from the clayey-siliceous facies has not been transformed to quartz chert and is mostly still porcellanite (opal-CT; not shown). That the modeled mean time of quartz formation is shorter than the actual age of diagenetic quartz in deep sea sediments means that the experimental data (describing diagenetic rates based on hydrothermal experiments conducted at >200°C) fail at predicting the rates of silica diagenesis at lower temperatures. This in mind, I proceed using the laboratory data based calibration to calculate the effect of changing geothermal gradients on the $\delta^{18}O$ of quartz chert.

4.3.1.3. The influence of changing geothermal gradients on chert $\delta^{18}O$

Variations in geothermal gradients affect the oxygen isotope composition of chert by changes in the temperature and depth of quartz formation. Temperature affects $\delta^{18}O$ ratios by temperature-dependent isotope fractionation and depth affects $\delta^{18}O$ by depth-dependent changes in the water/rock ratio.

Temperature dependence

To evaluate the effect of the sediment's thermal evolution on the $\delta^{18}O$ record of chert, I have calculated the $\delta^{18}O$ of quartz from the temperature at depth and a fluid isotope composition of $\delta^{18}O$= -1.1‰ (Cummins et al., 2014) assuming temperature dependent isotope fractionation described by:

$$1000 \cdot \ ln\ \alpha = A \cdot 10^6 \cdot \ T^{-2} + B \qquad \textbf{Equation 4-6}$$

with *A*= 3.09 and *B*= -3.29 according to the calibration of Knauth and Epstein (1976).

The relationship Knauth and Epstein (1976) applies only for a constant fluid oxygen isotope composition. This condition is only achieved when water supply is unlimited. However, quartz chert precipitation occurs over a depth range during diagenesis (Figure 4-5 d-f) suggesting that quartz precipitation occurs under variable supply of water.

The water/rock ratio

The oxygen isotope composition of chert is not only dependent on temperature and source fluid $\delta^{18}O$ when the water availability is limited (Knauth and Lowe, 2003). When chert forms close to the surface, Water/rock (W/R) ratios are very high due to continuous water replenishment, and consequently, a temperature-dependent isotopic equilibrium will establish (Knauth and Lowe, 2003). With increasing depth of quartz formation, W/R ratios decrease due to compaction and dewatering and quartz will remain closer to the initial $\delta^{18}O$ value of the amorphous precursor silica. To account for the dependence of $\delta^{18}O$ on W/R ratios that decrease with depth, I have assumed an exponential decrease of W/R ratios with depth:

$$W/R_{(z)} = \ W/R_{(0)} \cdot \ e^{-z \cdot a} \qquad \textbf{Equation 4-7}$$

Where *a* is a scaling factor. The initial water/rock ratio, $(W/R)_0$, is assumed to be 50 in the uppermost depth increment of sediment (100 m). The ambient W/R ratio during chert formation at temperatures between 85 and 105°C was estimated to be 3.5 based on fluid inclusion data (Knauth and Lowe, 2003; Winter and Knauth, 1992). I use a scaling factor of a= 2 in order to let W/R approach zero at the maximum depth for quartz formation. Using $(W/R)_0$= 50 and a= 2, the W/R ratio is reaching 3.5 at ca. 1.3 km depth, i.e., a depth where most quartz formation takes place for a geothermal gradient between 10 and 30°C/km (Figure 4-5 d-f).

The W/R ratio and the oxygen isotope composition are related in a closed system by the difference in isotope composition of silica and the fluid (Sheppard et al., 1969):

$$\frac{W}{R} = \frac{\delta^{18}O_{silica}(final) - \delta^{18}O_{silica}(initial)}{\delta^{18}O_{water}(initial) - \delta^{18}O_{water}(final)} \qquad \textbf{Equation 4-8}$$

Where *initial* and *final* refer to before and after isotope exchange between water and silica. This equation can be incorporated into the standard equation for temperature dependent oxygen isotope fractionation (Equation 4-6) and be rearranged for $\delta^{18}O_{silica(final)}$ to yield the temperature- and W/R dependent oxygen isotope composition of chert.

The seawater temperature

Opal precipitated from seawater attains an oxygen isotope composition that depends on the seawater temperature. But does the oxygen isotope composition of chert still reflect this temperature? Seawater temperatures were likely higher in the geological past than today and potentially affect chert $\delta^{18}O$ values. Recent estimates for paleo seawater temperatures are 33 ± 7°C in the Silurian (Cummins et al., 2014), 37-52°C at 1.9 Ga (Marin et al., 2010; Marin-Carbonne et al., 2012), 26-35°C between 3.5 and 3.2 Ga (Blake et al., 2010) and <40°C at 3.42 Ga (Hren et al., 2009). To evaluate the effect of different seawater temperatures on chert $\delta^{18}O$, I have calculated two scenarios where opal formed in equilibrium with seawater at 10°C and 40°C. I assume a temperature of 4°C at the seafloor in both scenarios. Modeled average $\delta^{18}O$ values of bulk chert were calculated by weighing $\delta^{18}O$ values of quartz with calculated fractions of quartz, f_{quartz} that formed at the respective depth increment during burial.

The model results show that the oxygen isotope composition of quartz decreases when geothermal gradients increase and/or when sedimentation rates increase (Figure 4-7). For a very low geothermal gradient (10°C km^{-1}), quartz formation will occur at great depth between ca. 1 and 4 km (Figure 4-5 d-f), where water/rock ratios are low, such that chert forms under rock-buffered conditions and the oxygen isotope composition of chert remains close to that of the precursor opal. With increasing geothermal

gradient, quartz precipitation occurs at higher temperature and shallower depth, and thus quartz formation occurs under higher W/R ratios. It follows that quartz will obtain an oxygen isotope composition that is determined dominantly by the fractionation factor prescribed by the ambient temperature.

When sedimentation rates increase, quartz formation shifts to greater depth (Figure 4-5 d-f, Figure 4-7) where lower W/R ratios prevail and where ambient temperatures are higher (Figure 4-5 a-c). Hence, for higher sedimentation rates, changes in the geothermal gradient impose larger decreases in chert $\delta^{18}O$.

With respect to the potential of chert $\delta^{18}O$ to serve as paleo seawater temperature proxy, the results indicate that paleo seawater temperatures might be preserved in the $\delta^{18}O$ record of chert which formed under low water/rock ratios, i.e., when the geothermal gradient was low and sedimentation rates were high (Figure 4-7). However, if silica diagenesis occurred under conditions of high geothermal gradients, the initial oxygen isotope composition of opal (that once equilibrated with colder seawater) would not have been preserved.

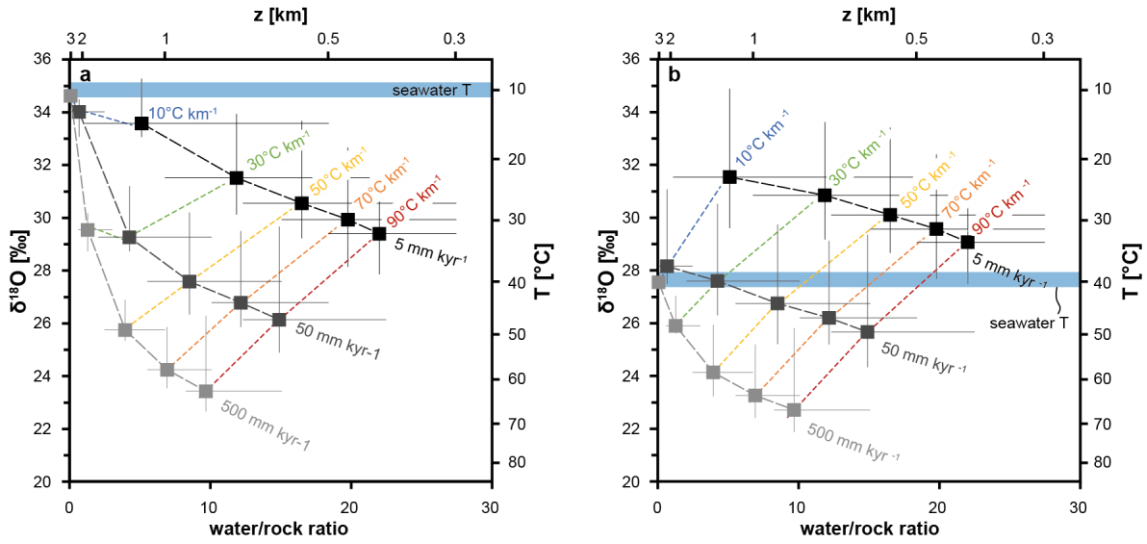

Figure 4-7: Modeled oxygen isotope composition of chert formed under different geothermal gradients and sedimentation rates with opal that initially precipitated from seawater at 10°C (a) and 40°C (b) against water/ rock ratios. The data points show weighted average $\delta^{18}O$ values and the error bars show ranges in which ≈95% of quartz formation takes place. The contour lines show geothermal gradients (colored) and sedimentation rates (gray scales). When the geothermal gradient is low, chert is predicted to form at high $\delta^{18}O$ values because quartz formation occurs at great burial depth where water/rock ratios are low. When sedimentation rates are sufficiently high, chert potentially preserves the $\delta^{18}O$ of opal that formed in equilibrium with seawater (blue bars). With increasing geothermal gradient, chert forms at higher temperatures, at shallower depth, higher water/rock ratios and hence with lower $\delta^{18}O$. When sedimentation rates increase, chert forms at increasing temperatures due to increased heating rates, at greater depth, lower water/rock ratios, and therefore obtains overall lower $\delta^{18}O$ values.

4.3.1.4. The influence of the geochemical environment on chert $\delta^{18}O$

Rates of quartz formation are determined not only by the sediment's heating rate, but also by the chemical composition of the precursor siliceous sediment (section 4.1). Quartz formation rates are higher in carbonate-rich siliceous sediment (Jones and Knauth, 1979) and in detritus-rich siliceous sediment (Isaacs, 1982; Figure 4-2, Figure 4-4) and are expressed by higher bulk chert $\delta^{18}O$ values.

Compositional variations in chert will hence introduce scatter in the global $\delta^{18}O$ record (additional to the scatter introduced by spatial variations in sedimentation rates and geothermal gradients). Therefore, gradual temporal change in the geochemical environment of silica deposition potentially contributes to a secular trend in $\delta^{18}O$ that could be superimposed on the $\delta^{18}O$ trend that is proposed to result from decreasing geothermal gradients. In this respect, the shifting locus of silica deposition from peritidal environments (where silica precipitation occurred abiotically) to subtidal environments (through the development of siliceous sponges in the Late Neoproterozoic), to deep sea settings (through increasingly pelagic deposition of radiolaria and diatoms) (Maliva et al., 1989) has potentially led to a unidirectional shift in chert $\delta^{18}O$. A secular shift in the environment of chert formation implies possible changes in sedimentation rates and the local geothermal gradient, which might contribute to a secular $\delta^{18}O$ shift.

Regarding the magnitude of $\delta^{18}O$ shifts related to variations in detritus contents, the samples from the Lijiatuo section suggest a maximum 7‰ variability on the bulk chert scale for detritus contents between 1 and ca. 10 wt% (neglecting the sample with the lowest $\delta^{18}O$ measured at 12.6‰). If this variability is caused by differences in temperature of quartz formation alone, this $\delta^{18}O$ range should be reproduced in the model by assuming initial d(101) spacing values (Equation 4-2) (corresponding to variable amounts of detritus and hence variable rates of quartz chert formation). However, the model predicts a shift of less than 1‰ for variable initial d(101) spacing values. There are two possible reasons for this shortcoming of the model. First, silica transformation rate laws based on laboratory experiments conducted at T>200°C do not adequately describe reaction rates at low temperatures where chemical controls become important. Second, the observed $\delta^{18}O$ variation is not only the result of variable rates and temperatures of quartz formation, but also depends on variations in W/R ratios on the cm-scale. Layers with high detritus contents (here dominantly illite) might have much lower W/R ratios than surrounding layers of pure silica as a result of higher compaction and lower permeability. If this is the case, the $\delta^{18}O$ of detritus-rich chert layers remains closer to the initial value of the deposited opal. Additionally, the oxygen isotope fractionation factor might depend on the rates of quartz formation. In summary, variable detrital mineral contents in chert lead to a large range of bulk chert $\delta^{18}O$ values that reflect a combination of variations in rates, temperature and W/R ratios during diagenesis.

4.3.2. Implications for the global chert $\delta^{18}O$ trend

If the oxygen isotope composition of bulk chert is sensitive to changes in the geothermal gradient, secular changes in the heat flow through the Earth's crust should be mirrored in the secular $\delta^{18}O$ trend in chert.

Constraints for the thermal history of the Earth come from petrological estimates of mantle temperatures that have been inferred from the chemical composition of primary magmas as deduced from MgO and FeO contents of non-arc basalts (Herzberg et al., 2010) and suggest that the mantle temperature has increased in the Hadean and Archean, followed by cooling over the Proterozoic (Figure 4-8). This thermal evolution of the mantle can be reconciled with an increase in mantle heat flow from ca. 20 TW on the early Earth to modern values of ≈38 TW between 3 and 2 Ga (Korenaga, 2013). The proposed change in heat flow is suggested to result from a switch from stagnant lid mantle convection (characterized by mantle heating exceeding surface heat loss) to the onset of plate tectonics (where mantle heat loss increased by the subduction of cold crustal material) (Herzberg et al., 2010; Korenaga, 2013). Provided that the thermal evolution of mantle and crust were coupled, the crust was also subjected to secular cooling. The decrease in radioactive heat production from ca. 100 TW to ca. 20 TW through Earth history (e.g. Arevalo et al., 2009) has likely contributed to decreasing heat flow through time, where the distribution of radioactive elements in the crust and the crustal thickness might have played a subsidiary role.

I suggest that the chert $\delta^{18}O$ record reflects the long-term cooling of the Earth's crust. A decreasing geothermal gradient from 90°C km^{-1} to 10°C km^{-1} entails an approximate 9‰ shift in the $\delta^{18}O$ record of chert (for sedimentation rates up to 50 mm kyr^{-1}). This range can account for the long-term increase in $\delta^{18}O$ observed over the Proterozoic. However, the apparently higher rate of $\delta^{18}O$ increase over the Phanerozoic (Figure 4-1) has likely other causes, including a shift in the seawater $\delta^{18}O$ ratio by 6‰ since the Paleozoic (Veizer and Prokoph, 2015) (supposing that the new clumped isotope system is not yet sufficiently explored). The very low oxygen isotope composition of Archean cherts, however, cannot be explained by the presented model. I suspect that the explanation for the very low $\delta^{18}O$ values of Archean cherts lies in a different mode of their formation. This view is supported by the occurrence of interbedded volcanic rocks that suggest locally very high temperatures during chert precipitation in the crust (Knauth and Lowe, 2003). Moreover, narrow ranges in $\delta^{18}O$ values on the micro scale provide evidence for re-equilibration of the chert $\delta^{18}O$ signature through hydrothermal alteration at 200-300°C (Marin-Carbonne et al., 2011). These high-temperature conditions during chert formation in the Archean might be related to the heating of the mantle as result of stagnant lid mantle convection (Figure 1-8; Herzberg et al., 2010; Korenaga, 2013).

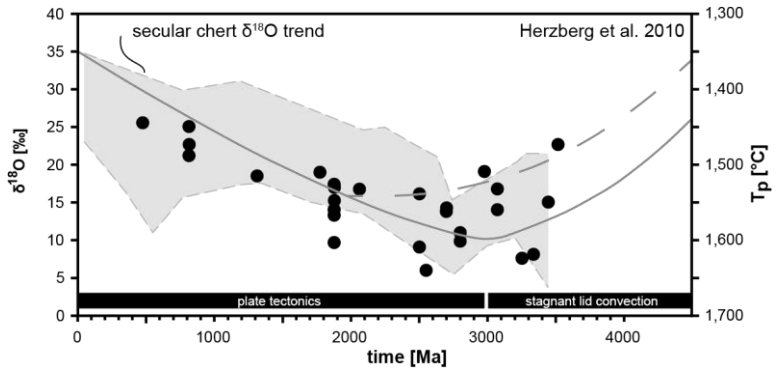

Figure 4-8: The secular O-Isotope trend in chert (gray band, cf. Figure 4-1) compared with modelled and calculated mantle potential temperatures (T_P) through Earth history. Modeled thermal histories of the Earth's mantle (lines), estimated based on a switch from stagnant lid convection to plate tectonics at 3 Ga (solid line) and at 2 Ga (dashed line) are shown together with petrological estimates of the mantle potential temperatures (Herzberg et al., 2010) (circles).

4.4. Conclusions

Correlated detritus contents and $\delta^{18}O$ of authigenic quartz in approximately 550 Ma chert and siliceous shales disclose i) that $\delta^{18}O$ of chert records diagenetic temperatures and ii) that rates of quartz formation depend on detritus contents. Raman spectra of carbonaceous material reveal that peak diagenetic temperatures exceeded the temperatures recorded in $\delta^{18}O$ of chert, implying that iii) the chert $\delta^{18}O$ is resistant against isotopic exchange during diagenesis. These results suggest that the bulk chert $\delta^{18}O$ is a robust indicator for the quartz chert formation temperature in the shallow Earth crust. Bulk chert averages over $\delta^{18}O$ of quartz that has formed with a transiently changing isotope composition during burial diagenesis, and hence the micro scale $\delta^{18}O$ records the detailed diagenetic history (Marin et al., 2010).

Computed shifts in chert $\delta^{18}O$ through decreasing geothermal gradients from 90°C km^{-1} to 10°C km^{-1} and sedimentation rates between 5 and 500 mm kyr^{-1} are ca. 12‰ (and approximately 9‰ for sedimentation rates up to 50 mm kyr^{-1}). The Proterozoic chert $\delta^{18}O$ record reveals a secular shift at the same magnitude, suggesting that this secular increase in the chert oxygen isotope record is a resulting corollary of decreasing geothermal gradients related to the cooling of the Earth. An additional control over the $\delta^{18}O$ record during the Phanerozoic eon is suggested by a steep increase in chert $\delta^{18}O$ that potentially relates to a shift in seawater $\delta^{18}O$ by ca. 6‰ triggered by overstepping a critical depth of mid oceanic ridge crests in the Paleozoic (Veizer and Prokoph, 2015). The large scatter of ca. 10‰ in the global record stems from variations in detrital mineral contents and other non-silica components in siliceous sediment that modify rates of quartz precipitation, as well as from spatial variations in sedimentation rates, geothermal gradients and differences in how the water/rock ratios change with depth.

This new interpretational framework for chert $\delta^{18}O$ suggests that the long-term covariation of mantle potential temperatures (Herzberg et al., 2010), and the bulk chert $\delta^{18}O$ (Knauth, 2005 and others) are

dominantly controlled by the decreasing heat flow in the Earth's mantle and crust that stems from the initiation of plate tectonics between 2.5 and 3 Ga.

4.5. Acknowledgements

I am grateful for funding provided by the DFG through research group FOR736 "The Precambrian-Cambrian Ecosphere (R)evolution: Insights from Chinese microcontinents" (grant no. BL 562/11-2). Many thanks to Marcus Oelze for discussions. Thanks to Michael Wiedenbeck and Fréderic Couffignal for SIMS analyses, Daniel Herwartz for laser fluorination analyses and Keno Lünsdorf for Raman analyses. Uwe Dittmann is thanked for preparation of shale samples, Christa Kotré for XRD analyses and Birgit Plessen for TOC analyses.

4.6. Appendix

The appendix comprises details about the analytical methods, the mass balance to estimate detritus contents and the O-isotope composition of silica, and data tables with analytical results from Raman Spectroscopy and SIMS analyses.

4.6.1. Analytical methods

4.6.1.1. Laser fluorination multi-collector gas mass spectrometry

Oxygen isotope analyses by laser fluorination gas source mass spectrometry (Sharp, 1990) were performed in continuous flow mode at the University of Göttingen. Following evacuation and heating of the sample chamber to 70°C overnight, sample and NBS 28 standard powders were fused in a 18-pit Ni sample holder to glass beads using a SYNRAD 50 W CO_2-laser. Oxygen is liberated from solid samples by the reaction of 0.2 mg ground rock with ≈10 mbar purified F_2 using the same laser. Condensable reaction products (e.g. SiF_4) are trapped in a first liquid nitrogen cold trap. Excess F_2 is reacted with NaCl at 180°C, where the Cl2 produced is removed in a second liquid nitrogen cold trap. Oxygen is trapped in a liquid nitrogen- cooled U-trap containing a 5 Å molecular sieve. Following O_2 collection for 8 to 10 minutes, the sample is heated to ca. 120°C and transported by He-carrier gas into a final 5 Å molecular sieve trap, where a fraction of the sample was cryofocused at -196°C. Oxygen was released by rapid heating in a water bath at ca. 92°C and transported with the carrier gas stream to a Thermo Gas Bench-II where the O_2 gas is purified in a ca. 10 m capillary gas chromatography column lined with a 5 Å molecular sieve to remove residual trace gasses other than O_2. Sample O_2 is then analyzed using a Thermo MAT 253 mass spectrometer operating in continuous flow mode. Two reference O_2 gas peaks were injected prior to the sample peak and used as internal reference. Oxygen isotopes were simultaneously detected on m/z 32 ($^{16}O^{16}O$) and m/z 34 ($^{16}O^{18}O$) on Faraday cups and yielded signal intensities of ca. 25V for the sample peak. Absolute $\delta^{18}O$ values are calibrated from measurements of NBS 28 quartz standard. $\delta^{18}O$ is reported as per mil deviation from SMOW (standard mean ocean water), i.e., by multiplying Equation 4-9 with 10^3:

$$\delta^{(x/16)}O = \left[\frac{\left(\frac{^{x}O}{^{16}O} \right)_{sample}}{\left(\frac{^{x}O}{^{16}O} \right)_{SMOW}} - 1 \right] \qquad \textbf{Equation 4-9}$$

where x denotes either 17 or 18. We abbreviate $\delta(^{x/16}O)_{SMOW} \cdot 10^3$ as $\delta^{x}O$ and report δ-values obtained from one measurement.

4.6.1.2. Secondary Ion Mass Spectrometry

Oxygen isotope analyses by secondary ion mass spectrometry were conducted on a Cameca 1280-HR at GFZ Potsdam. In SIMS, secondary ions, produced by sputtering primary ions onto a solid sample surface are measured using mass spectrometry. A primary 2.5 nA Gaussian $^{133}Cs^{+}$ beam was focused to a beam diameter of ca. 8 µm on the sample surface. Charge compensation on the surface is accomplished by low energy electron flooding. The secondary ion beam is transmitted through an analyzer system and ions are detected with Faraday cups, similarly to MC-ICP-MS. During data acquisition, a 10 x 10 µm area is rastered to reduce drift in isotopic composition. To resolve isobaric interferences, the mass spectrometer is operated at mass resolution of $\Delta m/m \approx 2000$. ^{16}O is measured on the L2 Faraday cup connected to an amplifier with a 10^{10} Ω resistor; ^{18}O is measured on the H2 cup connected to an amplifier with a 10^{11} Ω resistor. Drift in mass bias is corrected for by measurement of 'drift monitors' between sample measurements, i.e., homogenous standard materials with known isotope composition. For analysis of quartz samples, NBS 28 quartz is used to monitor and correct mass bias drift and to calibrate absolute $\delta^{18}O$ values.

This material has a published value of $\delta^{18}O_{VSMOW}$ = 9.57 ± 0.10‰ (1SD) (IAEA, 2007). We have used an absolute value for the zero-point on the SMOW delta-scale was set at $^{18}O/^{16}O \equiv 0.00200520$ (Baertschi, 1976), which we have directly transferred to the zero-point value for the VSMOW scale. We detected a significant dispersion in the $^{18}O^{-}/^{16}O^{-}$ data from NBS 28 (n= 24 analyses on n= 14 grains), leading to repeatabilites of ± 0.37‰. A subset of NBS 28 data from another analytical yielded ± 0.10‰ for n= 15 analyses on one single grain. This suggests that there is significant inter-grain isotopic heterogeneity in the NBS 28 quartz sand reference material. In order to achieve an absolute calibration of our analyses we thus reverted to taking the mean value derived from an equal weighting of each grain of NBS 28 that was analysed during the analytical sequence. As such, we believe differences between our data values are reliable to ± 0.14‰ (1SD) based on the square-root of the sum-of-squares using the repeatability of ± 0.10‰ as the assigned uncertainty. With regards to the absolute delta-values, we believe our results are reliable to ± 0.35‰, which is the best that could be achieved in light of the apparent isotopic heterogeneity of our reference material at the sub-nanogram sampling scale. The high abundance of clay minerals and the small grain size of authigenic quartz aggravated sample preparation and analysis. Analyses with ^{16}O count rates 1.7 10^{9} cps were neglected. Analysis spots were screened for sample homogeneity and crater morphology where mixed analyses (mostly clay and quartz) and analyses with uneven craters and holes were rejected (Appendix Figure 4-1b).

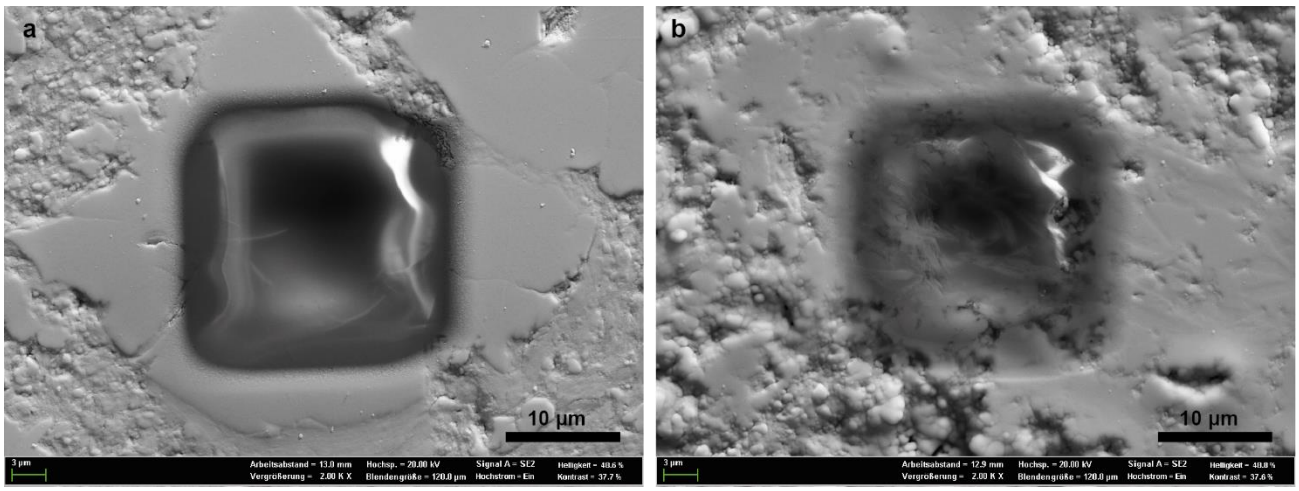

Appendix Figure 4-1: SEM image of the sample surface after SIMS analysis of a) an analysis where pure quartz was analyzed (sample Li23@19) that yielded a clean crater morphology and b) an analysis where multiple phases were analyzed (sample Li35@15) and where the sample surface is uneven.

4.6.1.3. Raman spectrometry of carbonaceous material

Raman spectra were acquired using a Horiba Jobin Yvon HR800-UV spectrometer connected to an Olympus BX41 microscope. The system is setup in 180° backscattering geometry where the Raman scattered light passes through the same 100x objective (numerical aperture of 0.9) through which the sample is visualized. The laser beam of the 488 nm Ar^+ laser line is operated at 10 mW where neutral density filters attenuate the signal intensity to 0.3 – 0.5 mW to prevent thermal alteration of the sample. The laser beam is focused through the objective onto the sample surface and the backscattered light passes through a 100 µm confocal hole and is diffracted by a 600 lines/mm grating onto a 1024x256 pixel CCD detector. Each spectrum analyzed represents the average of three measurement intervals with 10 to 30 s acquisition time, depending on signal intensities. Calibration of Raman bands was done using the Raman band of silicon at 520.4 cm^{-1}.

4.6.2. Oxygen isotope mass balance

The oxygen isotope composition of bulk chert or siliceous shales is determined by the oxygen isotope composition from different mineral components and their relative abundance in the bulk rock.

In the samples investigated here, the dominant authigenic, oxygen-bearing component is SiO_2 (a-qtz) derived from biogenic silica, inorganically precipitated silica, and likely also silica released during the diagenetic smectite-to illite conversion (see chapter 3). The dominant detrital component is illite (ill). It is likely that also detrital quartz (d-qtz) is present in an abundance estimated to clay/quartz≈ 1.7 (Shaw and Weaver, 1965). Feldspar is present in minor amounts and either has a detrital or authigenic origin.

To determine the oxygen isotope composition of authigenic quartz, we estimate the relative abundance of detrital minerals in bulk rock and the $\delta^{18}O$ of non-detrital silica.

The oxygen isotope composition of authigenic quartz, $\delta^{18}O_{a\text{-}qtz}$, is calculated according to:

$$^{18/16}O_{bulk} = {}^{18/16}O_{a-qtz} \cdot f_{a-qtz} + {}^{18/16}O_{illite} \cdot f_{illite} + {}^{18/16}O_{d-qtz} \cdot f_{d-qtz} \quad \textbf{Equation 4-10}$$

To calculate $\delta^{18}O_{a\text{-}qtz}$ I assume $\delta^{18}O_{d\text{-}qtz}$= 10‰ (Savin and Epstein, 1970) and $\delta^{18}O$(ill)= 16‰ (Lynch et al., 1997). I have calculated two endmember scenarios to report a range of estimates for detrital mineral contents present and a range of $\delta^{18}O_{a\text{-}qtz}$. Endmember scenario (a) assumes illite/quartz= 1.5 and (b) illite/quartz= 10. I assume that the illite/quartz ratio is constant for all samples. Therefore, illite/quartz cannot be <1.5 because then the fraction of detrital minerals would exceed 1 for the most detritus-rich sample (Li31). The estimated range of detrital mineral contents and $\delta^{18}O_{a\text{-}qtz}$ is shown in Figure 4-3 in the main text.

Appendix Table 4-1: Intensity of Raman bands, characteristic intensity ratios, and calculated peak temperature of samples Li2, Li23A, and Li33.

sample	spectrum	RAR (mean)	RAR (1SD)	D_STA (mean)	D_STA (1SD)	G_STA (mean)	G_STA (1SD)	D-band center [cm^{-1}] (mean)	D-band center [cm^{-1}] (1SD)	G-band center [cm^{-1}] (mean)	G-band center [cm^{-1}] (1SD)	D/G int. ratio (mean)	D/G int. ratio (1SD)	Temperature ± (1SD) [°C]
Li2	Li_2_1	0.569	0.004	174.007	0.043	146.652	0.032	1345.886		1605.425		0.841	0	254.5
	Li_2_2	0.615	0.002	178.423	0.029	147.781	0.027	1338.187		1603.493		0.826	0	250.8
	Li_2_3	0.611	0.021	170.405	0.333	143.902	0.393	1340.1		1603.484		0.847	0.001	257.5
	Li_2_4	0.564	0.014	170.616	0.088	142.527	0.442	1345.849		1607.31		0.836	0.003	257.3
	Li_2_5	0.582	0.006	170.664	0.17	145.409	0.452	1341.977		1603.438		0.852	0.001	257.3
	Li_2_6	0.571	0.005	171.62	0.063	145.497	0.193	1340.046		1603.429		0.847	0	256.5
	Li_2_7	0.586	0.004	174.202	0.067	149.148	0.081	1343.873		1605.335		0.858	0	254.3
	Li_2_8	0.591	0.016	175.216	0.425	147.494	0.665	1345.788		1603.404		0.84	0.002	253.5
	Li_2_9	0.57	0.001	175.085	0.031	149.094	0.068	1341.926		1603.387		0.852	0	253.6
	Li_2_10	0.582	0.008	174.084	0.338	143.735	0.592	1334.228		1605.302		0.818	0.002	254.4
	Li_2_11	0.58	0.007	173.146	0.124	147.512	0.409	1345.74		1603.356		0.85	0.001	255.2
	Li_2_12	0.549	0.007	173.796	0.151	147.974	0.166	1343.802		1605.264		0.852	0.002	254.6
	Li_2_13	0.577	0.005	173.82	0.229	146.463	0.496	1343.788		1603.327		0.842	0.001	254.6
	Li_2_14	0.605	0.003	176.35	0.036	149.635	0.057	1339.936		1605.242		0.848	0	252.5
	Li_2_15	0.561	0.002	171.333	0.051	145.611	0.081	1339.909		1605.215		0.848	0	256.7
		0.581	**0.019**	**173.518**	**2.290**	**146.562**	**2.113**	**1342.069**	**3.372**	**1604.427**	**1.228**	**0.844**	**0.011**	**254.9 ± 1.9**
Li23A	Li_23A_1	0.718	0.004	144.256	0.117	150.346	0.682	1353.271		1603.198		1.039	0.004	281.6
	Li_23A_2	0.622	0.003	149.737	0.018	145.554	0.022	1349.42		1605.113		0.974	0	276.2
	Li_23A_3	0.605	0.004	159.301	0.029	148.289	0.013	1349.416		1601.265		0.933	0	267.2
	Li_23A_4	0.583	0.001	162.784	0.067	148.384	0.043	1347.485		1603.179		0.912	0	264.1
	Li_23A_5	0.631	0.01	162.684	0.16	144.551	0.357	1349.403		1607.019		0.893	0.003	264.2
	Li_23A_6	0.56	0.002	171.312	0.048	150.48	0.051	1353.244		1605.093		0.872	0	256.7
	Li_23A_7	0.618	0.003	175.446	0.144	153.234	0.088	1353.24		1603.167		0.866	0.001	253.3
	Li_23A_8	0.587	0.017	160.173	0.011	142.368	0.379	1351.315		1605.086		0.889	0.002	266.4
	Li_23A_9	0.577	0.01	153.135	0.161	144.034	0.114	1347.469		1603.163		0.939	0	272.9
	Li_23A_10	0.582	0.005	158.553	0.05	143.514	0.06	1353.234		1603.161		0.904	0	267.9
	Li_23A_11	0.6	0.004	170.35	0.12	150.56	0.608	1345.543		1603.16		0.884	0.003	257.5
	Li_23A_12	0.625	0.066	165.268	0.439	148.848	0.195	1347.465		1605.082		0.901	0.001	261.9
	Li_23A_13	0.584	0.012	166.1	0.337	146.864	0.131	1347.466		1605.082		0.884	0.003	261.2
	Li_23A_14	0.577	0.003	167.378	0.092	150.849	0.039	1347.466		1603.16		0.901	0	260.1
	Li_23A_15	0.599	0.009	153.051	0.562	147.839	0.542	1351.313		1603.162		0.966	0.001	273.0
		0.605	**0.038**	**161.302**	**8.593**	**147.714**	**3.165**	**1349.783**	**2.643**	**1603.939**	**1.415**	**0.917**	**0.046**	**265.6 ± 7.8**
Li33	Li_33_1	0.63	0.003	171.366	0.177	146.924	0.118	1347.489		1601.261		0.855	0.001	256.7
	Li_33_2	0.651	0.055	168.8	0.099	152.063	0.468	1349.422		1599.348		0.896	0.001	258.9
	Li_33_3	0.633	0.015	170.006	0.226	151.329	0.1	1343.658		1601.274		0.895	0.002	257.8
	Li_33_4	0.644	0.013	162.977	0.273	136.418	0.178	1343.662		1601.278		0.84	0.001	263.9
	Li_33_5	0.579	0.004	164.817	0.113	149.289	0.135	1339.825		1597.442		0.901	0	262.3
	Li_33_6	0.59	0.009	163.42	0.503	140.364	0.281	1345.602		1601.296		0.859	0.001	263.5
	Li_33_7	0.623	0.004	160.98	0.075	137.749	0.072	1347.53		1601.301		0.855	0	265.7
	Li_33_8	0.598	0.002	167.299	0.056	148.202	0.045	1343.69		1599.384		0.886	0	260.1
	Li_33_9	0.613	0.003	171.054	0.055	148.938	0.041	1349.468		1601.317		0.867	0	256.9
	Li_33_10	0.612	0.022	164.897	0.37	145.185	0.115	1343.707		1601.323		0.88	0.002	262.2
	Li_33_11	0.62	0.01	164.009	0.242	138.794	0.214	1349.486		1601.335		0.843	0	263.0
	Li_33_12	0.625	0.002	162.062	0.088	138.582	0.038	1347.584		1599.433		0.857	0	264.7
	Li_33_13	0.605	0.012	163.821	0.459	146.534	0.737	1345.676		1601.37		0.898	0.002	263.2
	Li_33_14	0.583	0.009	164.296	0.231	148.444	0.866	1347.606		1597.532		0.902	0.004	262.8
	Li_33_15	0.628	0.005	164.765	0.325	144.141	0.178	1338.009		1599.47		0.871	0	262.4
		0.616	**0.021**	**165.638**	**3.276**	**144.864**	**5.209**	**1345.494**	**3.438**	**1600.291**	**1.418**	**0.874**	**0.022**	**261.6 ± 2.8**

Appendix Table 4-2: Analytical results from SIMS analyses of samples Li 29, Li 31 and Li35. All measurements are reported that yielded ^{16}O count rates >1.7 10^9 cps. Bold values highlight samples with the best morphology of sample spots (Table 4-2). The uncertainty on absolute $\delta^{18}O_{SMOW}$ is estimated to 0.37‰.

Analysis	time after start [h]	stage pos x [µm]	stage pos y [µm]	^{16}O cps	$^{18}O/^{16}O$ measured	1SD [‰]	$^{18}O/^{16}O$ imf corrected	DT-FA-x bits	DT-FA-y bits	$\delta^{18}O$ SMOW [‰]	comment
Li29											
Li29@01	3.80	209	6957	1.72E+09	0.00203107	0.101	0.00204461	-21	-20	19.66	irregular hole
Li29@08	4.25	-2335	4942	1.79E+09	0.00202889	0.106	0.00204241	-22	-19	18.56	very irregular hole
Li29@09	4.32	-2102	4891	2.76E+09	0.00202261	0.111	0.00203609	-23	-19	15.41	very irregular hole, rim broken off
Li29@10	4.38	865	3558	2.07E+09	0.00202713	0.093	0.00204065	-19	-16	17.68	very irregular hole
Li29@12	4.58	1391	3168	2.32E+09	0.00204242	0.087	0.00205603	-18	-16	**25.35**	nice hole, slight overlap with other phase
Li29@19	5.03	36	2872	1.84E+09	0.00202921	0.104	0.00204274	-20	-14	18.72	irregular bottom, likely multiple phases
Li31											
Li31@02	5.70	-3417	-515	2.24E+09	0.00201316	0.071	0.00202659	-11	-21	**10.67**	nice hole, slight overlap with other phases
Li31@06	6.03	-6151	-177	2.12E+09	0.00203397	0.089	0.00204753	-20	-18	21.11	very irregular hole, mixed analysis
Li31@10	6.28	-2344	-869	1.82E+09	0.00203296	0.095	0.00204652	-14	-25	20.61	multiple phases
Li31@19	6.95	-5219	-1780	2.14E+09	0.00203896	0.111	0.00205256	-20	-14	**23.62**	nice, clean hole
Li31@27	7.53	-7111	-3957	1.91E+09	0.00204072	0.078	0.00205433	-30	1	24.50	nice pit, slight layering
Li31@35b	8.18	-3354	-4891	1.96E+09	0.00203460	0.097	0.00204817	-19	-5	21.43	mixed analysis: clay and quartz
Li31@37b	8.45	-3637	-5009	1.95E+09	0.00203685	0.076	0.00205043	-21	-5	22.56	mixed analysis: clay and quartz
Li35											
Li35@02	8.90	3450	1963	2.17E+09	0.00202063	0.077	0.00203410	-21	-17	14.41	impurity in hole
Li35@07	9.23	4257	1089	1.99E+09	0.00202622	0.119	0.00203973	-22	-16	17.22	very irregular hole
Li35@08	9.28	5611	639	1.92E+09	0.00203481	0.111	0.00204838	-22	-17	21.53	very irregular hole
Li35@10	9.42	5967	588	1.77E+09	0.00203040	0.136	0.00204393	-20	-17	19.32	very irregular hole
Li35@11	9.48	5031	342	1.94E+09	0.00203205	0.121	0.00204560	-21	-16	20.15	irregular hole
Li35@12	9.62	5838	18	1.97E+09	0.00203218	0.103	0.00204573	-21	-18	20.21	irregular hole
Li35@13	9.68	2015	-4107	2.11E+09	0.00202943	0.117	0.00204296	-20	-9	**18.83**	nice hole
Li35@14	9.75	2452	-5189	2.08E+09	0.00203956	0.083	0.00205315	-19	-8	**23.92**	nice hole, slightly irregular
Li35@15	9.82	2532	-4431	2.06E+09	0.00203907	0.093	0.00205267	-19	-9	23.67	very irregular hole
Li35@16	9.88	5006	-4064	2.12E+09	0.00202212	0.103	0.00203560	-17	-4	**15.16**	nice hole, slightly irregular edge
Li35@17	9.95	5527	-3384	2.11E+09	0.00203502	0.086	0.00204859	-17	-5	**21.64**	nice hole, slightly irregular
Li35@18	10.02	5972	-1908	2.10E+09	0.00202576	0.088	0.00203926	-20	-9	**16.99**	irregular hole
Li35@19	10.08	5642	-798	2.06E+09	0.00203817	0.085	0.00205176	-21	-13	**23.22**	slightly irregular hole
Li35@20	10.15	6594	114	2.06E+09	0.00203814	0.073	0.00205173	-19	-16	**23.20**	

References

Abelmann, A., Gersonde, R., 1991. Biosiliceous particle flux in the Southern Ocean. Mar. Chem. 35, 503–536. doi:10.1016/S0304-4203(09)90040-8

Abercrombie, H.J., Hutcheon, I.E., Bloch, J.D., de Caritat, P., 1994. Silica activity and the smectite-illite reaction. Geology.

Abraham, K., Hofmann, A., Foley, S.F., Cardinal, D., Harris, C., Barth, M.G., André, L., 2011. Coupled silicon–oxygen isotope fractionation traces Archaean silicification. Earth Planet. Sci. Lett. 301, 222–230. doi:10.1016/j.epsl.2010.11.002

Alibo, D.S., Nozaki, Y., 1999. Rare earth elements in seawater: Particle association, shale-normalization, and Ce oxidation. Geochim. Cosmochim. Acta 63, 363–372.

Allègre, C.J., Lewin, E., 1989. Chemical structure and history of the Earth: evidence from global non-linear inversion of isotopic data in a three-box model. Earth Planet. Sci. Lett. 96, 61–88.

Alleman, L.Y., Cardinal, D., Cocquyt, C., Plisnier, P.-D., Descy, J.-P., Kimirei, I., Sinyinza, D., André, L., 2005. Silicon Isotopic Fractionation in Lake Tanganyika and Its Main Tributaries. J. Great Lakes Res. 31, 509–519. doi:10.1016/S0380-1330(05)70280-X

Altabet, M.A., Francois, F., 1994. Sedimentary nitrogen isotopic ratio as a recorder for surface ocean ntirate utilization. Biogeochem. Cycles. 8, 103–116.

Anbar, A.D., Knoll, A.H., 2002. Proterozoic ocean chemistry and evolution: a bioinorganic bridge? Science 297, 1137–1142. doi:10.1126/science.1069651

André, L., Cardinal, D., Alleman, L.Y., Moorbath, S., 2006. Silicon isotopes in ~3.8 Ga West Greenland rocks as clues to the Eoarchaean supracrustal Si cycle. Earth Planet. Sci. Lett. 245, 162–173. doi:10.1016/j.epsl.2006.02.046

Arevalo, R., McDonough, W.F., Luong, M., 2009. The K/U ratio of the silicate Earth: Insights into mantle composition, structure and thermal evolution. Earth Planet. Sci. Lett. 278, 361–369. doi:10.1016/j.epsl.2008.12.023

Baah, C. a., Baah, J.I., 2002. Polypropylene degradation in NaOH environments. Mater. Des. 23, 341–343. doi:10.1016/S0261-3069(01)00091-7

Baertschi, P., 1976. Absolute18O content of standard mean ocean water. Earth Planet. Sci. Lett. 31, 341–344. doi:10.1016/0012-821X(76)90115-1

Barker, P.F., Kennett, J.P. et al., 1988. Proc. ODP, Initial Reports 113. College Station. doi:doi:10.2973/odp.proc.ir.113.106.1988

Barling, J., Weis, D., 2012. An isotopic perspective on mass bias and matrix effects in multi-collector inductively-coupled-plasma mass spectrometry. J. Anal. At. Spectrom. 27, 653. doi:10.1039/c2ja10382f

Basile-Doelsch, I., Meunier, J.D., Parron, C., 2005. Another continental pool in the terrestrial silicon cycle. Nature 433, 399–402. doi:10.1038/nature03217

Bau, M., Koschinsky, A., 2009. Oxidative scavenging of cerium on hydrous Fe oxide: Evidence from the distribution of rare earth elements and yttrium between Fe oxides and Mn oxides in hydrogenetic ferromanganese crusts. Geochem. J. 43, 37–47. doi:10.2343/geochemj.1.0005

Beauchemin, D., Mclaren, J.W., Herman, S.S., 1987. Study of the effects of concomitant elements in inductively coupled plasmamass spectrometry. Spectrochim. Acta Part B At. Spectrosc. 42, 467–490. doi:10.1016/0584-8547(87)80024-1

Becker, R.H., Clayton, R.N., 1976. Oxygen isotope study of a Precambrian banded iron-formation, Hamerslay

Range, Western Australia. Geochim. Cosmochim. Acta 40, 1153–1154. doi:10.1016/0016-7037(76)90151-4

Beeunas, M.A., Knauth, L.P., 1985. Preserved stable isotopic signature of subaerial diagenesis in the 1.2-b.y. Mescal Limestone, central Arizona: Implications for the timing and development of a terrestrial plant cover. Geol. Soc. Am. Bull. 96, 737–745.

Blake, R.E., Chang, S.J., Lepland, A., 2010. Phosphate oxygen isotopic evidence for a temperate and biologically active Archaean ocean. Nature 464, 1029–1032. doi:10.1038/nature08952

Bohrmann, G., Abelmann, A., Gersonde, R., Hubberten, H., Kuhn, G., 1994. Pure siliceous ooze, a diagenetic environment for early chert formation. Geology 22, 207–210.

Bohrmann, G., Kuhn, G., Abelmann, A., Gersonde, R., Fütterer, D., 1990. A young porcellanite occurrence from the Southwest Indian Ridge. Mar. Geol. 92, 155–163. doi:10.1016/0025-3227(90)90034-H

Bohrmann, G., Spiel, V., Hinze, H., Kuhn, G., 1992. Reflector " Pc " a prominent feature in the Maud Rise sediment sequence (eastern Weddell Sea): Occurrence, regional distribution and implications to silica diagenesis. Mar. Geol. 106, 69–87.

Botz, R., Bohrmann, G., 1991. Low-temperature opal-CT precipitation in Antarctic deep-sea sediments: evidence from oxygen isotopes. Earth Planet. Sci. Lett. 107, 612–617. doi:10.1016/0012-821X(91)90105-Q

Boyle, R.A., Clark, J.R., Poulton, S.W., Shields-Zhou, G.A., Canfield, D.E., Lenton, T.M., 2013. Nitrogen cycle feedbacks as a control on euxinia in the mid-Proterozoic ocean. Nat. Commun. 4, 1533. doi:10.1038/ncomms2511

Bramlette, M.N., 1946. Monterrey Formation of California and origin of its siliceous rocks. USGS Prof. Pap. 212, 57.

Brzezinski, M.A., Nelson, D.M., 1995. The annual silica cycle in the Sargasso Sea near Bermuda. Deep. Res. Part I Oceanogr. Res. Pap. 42, 1215–1237. doi:10.1016/0967-0637(95)93592-3

Budd, G.E., Jensen, S., 2000. A critical reappraisal of the fossil record of the bilaterian phyla. Biol. Rev. Camb. Philos. Soc. 75, 253–295. doi:10.1111/j.1469-185X.1999.tb00046.x

Burwood, R., Drozd, J., Halpern, H.I., Sedivy, R.A., 1988. Carbon isotopic variations of kerogen pyrolyzates. Org. Geochem. 12, 195–205.

Butterfield, N.J., 2009. Oxygen, animals and oceanic ventilation: an alternative view. Geobiology 7, 1–7. doi:10.1111/j.1472-4669.2009.00188.x

Calvert, S.E., 1974. Deposition and diagenesis of silica in marine sediments. Spec. Publs. int. Ass. Sediment 1, 273–299.

Canfield, D.E., Poulton, S.W., Narbonne, G.M., 2007. Late-Neoproterozoic Deep-Ocean Oxygenation and the Rise of Animal Life. Science 315, 3–6. doi:10.1126/science.1135013

Cardinal, D., Alleman, L.Y., de Jong, J., Ziegler, K., André, L., 2003. Isotopic composition of silicon measured by multicollector plasma source mass spectrometry in dry plasma mode. J. Anal. At. Spectrom. 18, 213–218. doi:10.1039/b210109b

Cardinal, D., Alleman, L.Y., Dehairs, F., Savoye, N., Trull, T.W., André, L., 2005. Relevance of silicon isotopes to Si-nutrient utilization and Si-source assessment in Antarctic waters. Global Biogeochem. Cycles 19. doi:10.1029/2004GB002364

Cardinal, D., Gaillardet, J., Hughes, H.J., Opfergelt, S., André, L., 2010. Contrasting silicon isotope signatures in rivers from the Congo Basin and the specific behaviour of organic-rich waters. Geophys. Res. Lett. 37, L12403. doi:10.1029/2010GL043413

Chakrabarti, R., Fischer, W.W., Knoll, A.H., Jacobsen, S.B., 2012. Si isotope variability in Proterozoic cherts.

Geochim. Cosmochim. Acta 91, 187–201. doi:10.1016/j.gca.2012.05.025

Chen, X., Ling, H.-F., Vance, D., Shields-Zhou, G.A., Zhu, M., Poulton, S.W., Och, L.M., Jiang, S.-Y., Li, D., Cremonese, L., Archer, C., 2015. Rise to modern levels of ocean oxygenation coincided with the Cambrian radiation of animals. Nat. Commun. 6, 7142. doi:10.1038/ncomms8142

Chmeleff, J., Horn, I., Steinhoefel, G., von Blanckenburg, F., 2008. In situ determination of precise stable Si isotope ratios by UV-femtosecond laser ablation high-resolution multi-collector ICP-MS. Chem. Geol. 249, 155–166. doi:10.1016/j.chemgeo.2007.12.003

Condon, D.J., Zhu, M., Bowring, S., Wang, W., Yang, A., Jin, Y., 2005. U-Pb ages from the neoproterozoic Doushantuo Formation, China. Science 308, 95–98. doi:10.1126/science.1107765

Conway Morris, S., 2000. The Cambrian "explosion": slow-fuse or megatonnage? Proc. Natl. Acad. Sci. U. S. A. 97, 4426–4429. doi:10.1073/pnas.97.9.4426

Cornelis, J.T., Weis, D., Lavkulich, L., Vermeire, M.L., Delvaux, B., Barling, J., 2014. Silicon isotopes record dissolution and re-precipitation of pedogenic clay minerals in a podzolic soil chronosequence. Geoderma 235-236, 19–29. doi:10.1016/j.geoderma.2014.06.023

Cummins, R.C., Finnegan, S., Fike, D.A., Eiler, J.M., Fischer, W.W., 2014. Carbonate clumped isotope constraints on Silurian ocean temperature and seawater d18O. Geochim. Cosmochim. Acta 140, 241–258. doi:10.1016/j.gca.2014.05.024

de Goeij, J.M., van den Berg, H., van Oostveen, M.M., Epping, E.H.G., van Duyl, F.C., 2008. Major bulk dissolved organic carbon (DOC) removal by encrusting coral reef cavity sponges. Mar. Ecol. Prog. Ser. 357, 139–151. doi:10.3354/meps07403

De La Rocha, C.L., 2003. Silicon isotope fractionation by marine sponges and the reconstruction of the silicon isotope composition of ancient deep water. Geology 31, 423–426.

De La Rocha, C.L., Brzezinski, M.A., DeNiro, M.J., 2000. A first look at the distribution of the stable isotopes of silicon in natural waters. Geochim. Cosmochim. Acta 64, 2467–2477.

De La Rocha, C.L., Brzezinski, M.A., DeNiro, M.J., 1997. Fractionation of silicon isotopes by marine diatoms during biogenic silica formation. Geochim. Cosmochim. Acta 61, 5051–5056.

Degens, E.T., Epstein, S., 1962. Relationship between O18/O16 ratios in coexisting carbonates, cherts, and diatomites. Am. Assoc. Pet. Geol. Bull. 46, 534–542.

Delstanche, S., Opfergelt, S., Cardinal, D., Elsass, F., André, L., Delvaux, B., 2009. Silicon isotopic fractionation during adsorption of aqueous monosilicic acid onto iron oxide. Geochim. Cosmochim. Acta 73, 923–934. doi:10.1016/j.gca.2008.11.014

Demarest, M.S., Brzezinski, M.A., Beucher, C.P., 2009. Fractionation of silicon isotopes during biogenic silica dissolution. Geochim. Cosmochim. Acta 73, 5572–5583. doi:10.1016/j.gca.2009.06.019

DePaolo, D.J., 2011. Surface kinetic model for isotopic and trace element fractionation during precipitation of calcite from aqueous solutions. Geochim. Cosmochim. Acta 75, 1039–1056. doi:10.1016/j.gca.2010.11.020

Derry, L.A., 2006. Fungi, Weathering, and the Emergence of Animals. Science 311, 1386–1387.

Derry, L.A., Kaufman, A.J., Jacobsen, S.B., 1992. Sedimentary cycling and environmental change in the Late Proterozoic: Evidence from stable and radiogenic isotopes. Geochim. Cosmochim. Acta 56, 1317–1329. doi:10.1016/0016-7037(92)90064-P

Des Marais, D.J., Strauss, H., Summons, R.E., Hayes, J.M., 1992. Carbon isotope evidence for the stepwise oxidation of the Proterozoic environment. Nature 359, 605–609. doi:10.1038/359605a0

Ding, T., Jiang, S.-Y., Wan, D., Li, Y., Li, J., Song, H., Liu, Z., Yao, X., 1996. Silicon Isotope Geochemistry. Geological Publishing House, Beijing.

Ding, T., Wan, D., Wang, C., Zhang, F., 2004. Silicon isotope compositions of dissolved silicon and suspended matter in the Yangtze River, China. Geochim. Cosmochim. Acta 68, 205–216. doi:10.1016/S0016-7037(03)00264-3

Dixit, S., Van Cappellen, P., van Bennekom, A.J., 2001. Processes controlling solubility of biogenic silica and pore water build-up of silicic acid in marine sediments. Mar. Chem. 73, 333–352. doi:10.1016/S0304-4203(00)00118-3

Douthitt, C.B., 1982. The geochemistry of the stable isotopes of silicon. Geochim. Cosmochim. Acta 46, 1449–1458.

Dralus, D., 2013. Chemical interactions between silicates and their pore fluids: how they affect rock physics properties from atomic to reservoir scales. Stanford University.

Egan, K.E., Rickaby, R.E.M., Leng, M.J., Hendry, K.R., Hermoso, M., Sloane, H.J., Bostock, H., Halliday, A.N., 2012. Diatom Silicon Isotopes as a Proxy for Silicic Acid Utilisation : a Southern Ocean Core Top Calibration. Geochim. Cosmochim. Acta 96, 174–192. doi:10.1016/j.gca.2012.08.002

Ehlert, C., Grasse, P., Mollier-Vogel, E., Böschen, T., Franz, J., de Souza, G.F., Reynolds, B.C., Stramma, L., Frank, M., 2012. Factors controlling the silicon isotope distribution in waters and surface sediments of the Peruvian coastal upwelling. Geochim. Cosmochim. Acta 99, 128–145. doi:10.1016/j.gca.2012.09.038

Engström, E., Rodushkin, I., Baxter, D.C., Ohlander, B., 2006. Chromatographic purification for the determination of dissolved silicon isotopic compositions in natural waters by high-resolution multicollector inductively coupled plasma mass spectrometry. Anal. Chem. 78, 250–7. doi:10.1021/ac051246v

Ernst, W.G., Calvert, S.E., 1969. An experimental study of the recrystallization of porcelanite and its bearing on the origin of some bedded cherts. Am. J. Sci. 267A, 114–133.

Erwin, D.H., Tweedt, S., 2012. Ecological drivers of the Ediacaran-Cambrian diversification of Metazoa. Evol. Ecol. 26, 417–433. doi:10.1007/s10682-011-9505-7

Fan, H., Wen, H., Zhu, X., Hu, R., Tian, S., 2013. Hydrothermal activity during Ediacaran–Cambrian transition: Silicon isotopic evidence. Precambrian Res. 224, 23–35. doi:10.1016/j.precamres.2012.09.004

Fike, D.A., Grotzinger, J.P., Pratt, L.M., Summons, R.E., 2006. Oxidation of the Ediacaran ocean. Nature 444, 744–747. doi:10.1038/nature05345

Finnegan, S., Bergmann, K., Eiler, J.M., Jones, D.S., Fike, D.A., Eisenman, I., Hughes, N.C., Tripati, A.K., Fischer, W.W., 2011. The Magnitude and Duration of Late Ordovician–Early Silurian Glaciation. Science 3, 903–907.

Force, E.R., Back, W., Spiker, E.C., Knauth, L.P., 1986. A ground-water mixing model for the origin of the Imini manganese deposit (Cretaceous) of Morocco. Econ. Geol. 81, 65–79. doi:10.2113/gsecongeo.81.1.65

Gao, Q., Land, L.S., 1991. Nodular chert from the Arbuckle Group, Slick Hills, SW Oklahoma: a combined field, petrographic and isotopic study. Sedimentology 38, 857–870.

Gehlen, M., Beck, L., Calas, G., Flank, A.-M., van Bennekom, A.J., Van Beusekom, J.E.E., 2002. Unraveling the atomic structure of biogenic silica: Evidence of the structural association of Al and Si in diatom frustules. Geochim. Cosmochim. Acta 66, 1601–1609.

Geilert, S., Vroon, P.Z., Roerdink, D.L., Cappellen, P. Van, van Bergen, M.J., 2014a. Silicon isotope fractionation during abiotic silica precipitation at low temperatures: inferences from flow-through experiments. Geochim. Cosmochim. Acta. doi:10.1016/j.gca.2014.07.003

Geilert, S., Vroon, P.Z., van Bergen, M.J., 2014b. Silicon isotopes and trace elements in chert record early Archean basin evolution. Chem. Geol. 386, 133–142. doi:10.1016/j.chemgeo.2014.07.027

Georg, R.B., Reynolds, B.C., Frank, M., Halliday, A.N., 2006. New sample preparation techniques for the determination of Si isotopic compositions using MC-ICPMS. Chem. Geol. 235, 95–104. doi:10.1016/j.chemgeo.2006.06.006

Georg, R.B., Zhu, C., Reynolds, B.C., Halliday, A.N., 2009. Stable silicon isotopes of groundwater, feldspars, and clay coatings in the Navajo Sandstone aquifer, Black Mesa, Arizona, USA. Geochim. Cosmochim. Acta 73, 2229–2241. doi:10.1016/j.gca.2009.02.005

Grenne, T., Slack, J.F., 2003. Paleozoic and Mesozoic silica-rich seawater: Evidence from hematitic chert (jasper) deposits. Geology 31, 319–322.

Guo, Q., Shields, G.A., Liu, C., Strauss, H., Zhu, M., Pi, D., Goldberg, T., Yang, X., 2007a. Trace element chemostratigraphy of two Ediacaran–Cambrian successions in South China: Implications for organosedimentary metal enrichment and silicification in the Early Cambrian. Palaeogeogr. Palaeoclimatol. Palaeoecol. 254, 194–216. doi:10.1016/j.palaeo.2007.03.016

Guo, Q., Strauss, H., Liu, C., Goldberg, T., Zhu, M., Pi, D., Heubeck, C., Vernhet, E., Yang, X., Fu, P., 2007b. Carbon isotopic evolution of the terminal Neoproterozoic and early Cambrian: Evidence from the Yangtze Platform, South China. Palaeogeogr. Palaeoclimatol. Palaeoecol. 254, 140–157. doi:10.1016/j.palaeo.2007.03.014

Hayes, J.M., 1993. Factors controlling 13C contents of sedimentary organic compounds: Principles and evidence. Mar. Geol. 113, 111–125. doi:10.1016/0025-3227(93)90153-M

Hayes, J.M., Strauss, H., Kaufman, A.J., 1999. The abundance of in marine organic matter and isotopic fractionation in the global biogeochemical cycle of carbon during the past 800 Ma. Chem. Geol. doi:10.1016/S0009-2541(99)00083-2

Heck, P.R., Huberty, J.M., Kita, N.T., Ushikubo, T., Kozdon, R., Valley, J.W., 2011. SIMS analyses of silicon and oxygen isotope ratios for quartz from Archean and Paleoproterozoic banded iron formations. Geochim. Cosmochim. Acta 75, 5879–5891. doi:10.1016/j.gca.2011.07.023

Hendry, K.R., Robinson, L.F., 2012. The relationship between silicon isotope fractionation in sponges and silicic acid concentration: Modern and core-top studies of biogenic opal. Geochim. Cosmochim. Acta 81, 1–12. doi:10.1016/j.gca.2011.12.010

Herzberg, C., Condie, K.C., Korenaga, J., 2010. Thermal history of the Earth and its petrological expression. Earth Planet. Sci. Lett. 292, 79–88. doi:10.1016/j.epsl.2010.01.022

Hesse, R., 1988. Origin of chert: Diagenesis of biogenic siliceous sediments. J. Geol. Assoc. Canada 15, 171–192.

Hesse, R., Schacht, U., 2011. Early diagenesis of deep-sea sediments, 1st ed, Developments in Sedimentology. Elsevier B.V. doi:10.1016/B978-0-444-53000-4.00009-3

Hinman, N.W., 1998. Sequences of silica phase transitions: effects of Na, Mg, K, Al, and Fe ions. Mar. Geol. 147, 13–24. doi:10.1016/S0025-3227(98)00002-4

Hinman, N.W., 1990. Chemical factors influencing the rates and sequences of silica phase transitions : Effects of organic constituents. Geochim. Cosmochim. Acta 54, 1563–1574.

Hoefs, J., 2009. Stable Isotope Geochemistry, 6th ed. Springer, Berlin/Heidelberg.

Hoffman, P.F., Kaufman, A.J., Halverson, G.P., Schrag, D.P., 1998. A Neoproterozoic Snowball Earth. Science 281, 1342–1346.

Hohl, S., Becker, H., Herzlieb, S., Guo, Q., 2015. Multiproxy constraints on alteration and primary compositions of Ediacaran deep-water carbonate rocks, Yangtze Platform, South China. Geochim. Cosmochim. Acta 163, 262–278.

Holland, H.D., 2006. The oxygenation of the atmosphere and oceans. Philos. Trans. R. Soc. Lond. B. Biol. Sci.

361, 903–15. doi:10.1098/rstb.2006.1838

Holland, H.D., 1972. The geologic history of sea water-an attempt to solve the problem. Geochim. Cosmochim. Acta 36, 637–651.

Howarth, R.W., 2013. Nutrient Limitation of Net Primary Production in Marine Ecosystems 19, 89–110. doi:10.1146/annurev.ecolsys.19.1.89

Hren, M.T., Tice, M.M., Chamberlain, C.P., 2009. Oxygen and hydrogen isotope evidence for a temperate climate 3.42 billion years ago. Nature 462, 205–8. doi:10.1038/nature08518

Hughes, H.J., Sondag, F., Santos, R.V., André, L., Cardinal, D., 2013. The riverine silicon isotope composition of the Amazon Basin. Geochim. Cosmochim. Acta 121, 637–651. doi:10.1016/j.gca.2013.07.040

Hurd, D.C., 1973. Interactions of biogenic opal, sediment and seawater in the Central Equatorial Pacific. Geochim. Cosmochim. Acta 37, 2257–2282. doi:10.1016/0016-7037(73)90103-8

IAEA, 2007. Reference sheet for reference materials: NBS28 & NBS30 5. doi:http://nucleus.iaea.org/rpst/Documents/NBS28_NBS30.pdf

Isaacs, C.M., 1982. Influence of rock composition on kinetics of silica phase changes in the Monterey Formation, Santa Barbara area, California. Geology 10, 304.

Jaffrés, J.B.D., Shields, G.A., Wallmann, K., 2007. The oxygen isotope evolution of seawater: A critical review of a long-standing controversy and an improved geological water cycle model for the past 3.4 billion years. Earth-Science Rev. 83, 83–122. doi:10.1016/j.earscirev.2007.04.002

Jiang, S.-Y., Pi, D.-H., Schoene, B., 2010. Ages of the key boundaries during the Precambrian-Cambrian Interval in South China, in: GSA Denver Annual Meeting.

Jochum, K.P., Nohl, U., Herwig, K., Lammel, E., Stoll, B., Hofmann, A.W., 2005. GeoReM: A New Geochemical Database for Reference Materials and Isotopic Standards. Geostand. Geoanalytical Res. 29, 333–338. doi:10.1111/j.1751-908X.2005.tb00904.x

Johnson, C.M., Beard, B.L., Albarède, F., 2004. Overview and General Concepts. Rev. Mineral. 55, 1–24.

Jones, D.L., Knauth, L.P., 1979. Oxygen isotopic and petrographic evidence relevant to the origin of the Arkansas Novaculite. J. Sediment. Petrol. 49, 581–598.

Kah, L.C., 2000. Depositional δ18O signatures in Proterozoic dolostones: constraints on seawater chemistry and early diagenesis, in: Carbonate Sedimentation and Diagenesis in the Evolving Precambrian World. Tulsa, pp. 345–360.

Kano, K., Taguchi, K., 1982. Experimental study on ordering of opal-CT. Geochem. J. 16, 33–41.

Kasting, J.F., Howard, M.T., Wallmann, K., Veizer, J., Shields, G.A., Jaffrés, J.B.D., 2006. Paleoclimates, ocean depth, and the oxygen isotopic composition of seawater. Earth Planet. Sci. Lett. 252, 82–93. doi:10.1016/j.epsl.2006.09.029

Kastner, M., Keene, J.B., Gieskes, J.M., 1977. Diagenesis of siliceous oozes-I. Chemical controls on the rate of opal-A to opal-CT transformation- an experimental study. Geochim. Cosmochim. Acta 41, 1041–1059.

Kennedy, M.J., Droser, M.L., Mayer, L.M., Pevear, D., Mrofka, D., 2006. Late Precambrian Oxygenation; Inception of the Clay Mineral Factory. Science 311, 1446–1449.

Kenny, R., Knauth, L.P., 1992. Continental paleoclimates from δD and δ18O secondary silica in paleocarst chert lags. Geology 20, 219–222.

Kidder, D.L., Erwin, D.H., 2001. Secular Distribution of Biogenic Silica through the Phanerozoic : Comparison of Silica-Replaced Fossils and Bedded Cherts at the Series Level. J. Geol. 109, 509–522.

Kirschvink, J.L., 1992. Late Proterozoic low-latitude global glaciation: the snowball Earth, in: The Proterozoic

Biosphere: A Multidisciplinary Study. Cambridge University Press, New York, pp. 51–52.

Knauth, L.P., 2005. Temperature and salinity history of the Precambrian ocean: implications for the course of microbial evolution. Palaeogeogr. Palaeoclimatol. Palaeoecol. 219, 53–69. doi:10.1016/j.palaeo.2004.10.014

Knauth, L.P., 1994. Petrogenesis of chert. In silica: physical behavior. Rev. Mineral. Geochemistry 29, 233–258.

Knauth, L.P., Epstein, S., 1976. Hydrogen and oxygen isotope ratios in nodular and bedded cherts. Geochim. Cosmochim. Acta 40, 1095–1108.

Knauth, L.P., Lowe, D.R., 2003. High Archean climatic temperature inferred from oxygen isotope geochemistry of cherts in the 3.5 Ga Swaziland Supergroup, South Africa. Geol. Soc. Am. Bull. 115, 566–580. doi:10.1130/0016-7606(2003)115<0566

Knauth, L.P., Lowe, D.R., 1978. Oxygen isotope geochemistry of cherts from the Onverwacht Group (3.4 Billion years), Transvaal, South Africa, with implications for secular variations in the isotopic composition of cherts. Earth Planet. Sci. Lett. 41, 209–222.

Kolodny, Y., Epstein, S., 1976. Stable isotope geochemistry of deep sea cherts. Geochim. Cosmochim. Acta 40, 1195–1209.

Korenaga, J., 2013. Initiation and Evolution of Plate Tectonics on Earth: Theories and Observations. Annu. Rev. Earth Planet. Sci. 41, 117–151. doi:10.1146/annurev-earth-050212-124208

Krissansen-Totton, J., Buick, R., Catling, D.C., 2015. A statistical analysis of the carbon isotope record from the Archean to Phanerozoic and implications for the rise of oxygen. Am. J. Sci. 315, 275–316. doi:10.2475/04.2015.01

Kump, L.R., 2014. Hypothesized link between Neoproterozoic greening of the land surface and the establishment of an oxygen-rich atmosphere. Proc. Natl. Acad. Sci. U. S. A. 111. doi:10.1073/pnas.1321496111

Kurzweil, F., Drost, K., Pašava, J., Wille, M., Taubald, H., Schoeckle, D., Schoenberg, R., 2015. Coupled sulfur, iron and molybdenum isotope data from black shales of the Teplá-Barrandian unit argue against deep ocean oxygenation during the Ediacaran. Geochim. Cosmochim. Acta 171, 121–142. doi:10.1016/j.gca.2015.08.022

Lahfid, A., Beyssac, O., Deville, E., Negro, F., Chopin, C., Goffé, B., 2010. Evolution of the Raman spectrum of carbonaceous material in low-grade metasediments of the Glarus Alps (Switzerland). Terra Nov. 22, 354–360. doi:10.1111/j.1365-3121.2010.00956.x

Lawrence, M.G., Greig, A., Collerson, K.D., Kamber, B.S., 2006. Rare Earth Element and Yttrium Variability in South East Queensland Waterways. Aquat. Geochemistry 12, 39–72. doi:10.1007/s10498-005-4471-8

Lehmann, M.F., Bernasconi, M., Barbieri, A., McKenzie, J.A., 2002. Preservation of organic matter and alteration of its carbon and nitrogen isotope composition during simulated and in situ early sedimentary diagenesis. Geochim. Cosmochim. Acta 66, 3573–3584.

Lenton, T.M., Boyle, R.A., Poulton, S.W., Shields-Zhou, G.A., Butterfield, N.J., 2014. Co-evolution of eukaryotes and ocean oxygenation in the Neoproterozoic era. Nat. Geosci. 7, 257–265. doi:10.1038/ngeo2108

Levin, N.E., Raub, T.D., Dauphas, N., Eiler, J.M., 2014. Triple oxygen isotope variations in sedimentary rocks. Geochim. Cosmochim. Acta 139, 173–189. doi:10.1016/j.gca.2014.04.034

Li, C., Love, G.D., Lyons, T.W., Fike, D.A., Sessions, A.L., Chu, X., 2010. A stratified redox model for the Ediacaran ocean. Science 328, 80–3. doi:10.1126/science.1182369

Ling, H.-F., Chen, X., Li, D., Wang, D., Shields-Zhou, G.A., Zhu, M., 2013. Cerium anomaly variations in

Ediacaran–earliest Cambrian carbonates from the Yangtze Gorges area, South China: Implications for oxygenation of coeval shallow seawater. Precambrian Res. 225, 110–127. doi:10.1016/j.precamres.2011.10.011

Logan, G.A., Hayes, J.M., Hieshima, G.B., Summons, R.E., 1995. Terminal Proterzoic reorganization of biogeochemical cycles. Nature 376, 53–56.

Lynch, F.L., Mack, L.E., Land, L.S., 1997. Burial diagenesis of illite/smectite in shales and the origins of authigenic quartz and secondary porosity in sandstones. Geochim. Cosmochim. Acta 61, 1995–2006. doi:10.1016/S0016-7037(97)00066-5

Lyons, T.W., Reinhard, C.T., Planavsky, N.J., 2014. The rise of oxygen in Earth's early ocean and atmosphere. Nature 506, 307–15. doi:10.1038/nature13068

Maliva, R.G., Knoll, A.H., Siever, R., 1989. Secular Change in Chert Distribution: A Reflection of Evolving Biological Participation in the Silica Cycle. Palaios 4, 519–532.

Maliva, R.G., Siever, R., 1989. Nodular chert formation in carbonate rocks. J. Geol. 97, 421–433.

Marin, J., Chaussidon, M., Robert, F., 2010. Microscale oxygen isotope variations in 1.9Ga Gunflint cherts: Assessments of diagenesis effects and implications for oceanic paleotemperature reconstructions. Geochim. Cosmochim. Acta 74, 116–130. doi:10.1016/j.gca.2009.09.016

Marin-Carbonne, J., Chaussidon, M., Boiron, M.-C., Robert, F., 2011. A combined in situ oxygen, silicon isotopic and fluid inclusion study of a chert sample from Onverwacht Group (3.35Ga, South Africa): New constraints on fluid circulation. Chem. Geol. 286, 59–71. doi:10.1016/j.chemgeo.2011.02.025

Marin-Carbonne, J., Chaussidon, M., Robert, F., 2012. Micrometer-scale chemical and isotopic criteria (O and Si) on the origin and history of Precambrian cherts: Implications for paleo-temperature reconstructions. Geochim. Cosmochim. Acta 92, 129–147. doi:10.1016/j.gca.2012.05.040

Marin-Carbonne, J., Faure, F., Chaussidon, M., Jacob, D., Robert, F., 2013. A petrographic and isotopic criterion of the state of preservation of Precambrian cherts based on the characterization of the quartz veins. Precambrian Res. 231, 290–300. doi:10.1016/j.precamres.2013.03.019

Marin-Carbonne, J., Robert, F., Chaussidon, M., 2014. The silicon and oxygen isotope compositions of Precambrian cherts: A record of oceanic paleo-temperatures? Precambrian Res. 247, 223–234. doi:10.1016/j.precamres.2014.03.016

Matheney, R.K., Knauth, L.P., 1993. New isotopic temperature estimates for early silica diagenesis in bedded cherts. Geology 21, 519–522. doi:10.1130/0091-7613(1993)021<0519:NITEFE>2.3.CO

McCulloh, T.H., 1967. Mass Properties of Sedimentary Rocks and Gravimetric Effects of Petroleum and Natural-Gas Reservoirs. Geol. Surv. Prof. Pap. 528-A.

Mclennan, S.M., 1989. Rare earth elements in sedimentary rocks; influence of provenance and sedimentary processes. Rev. Mineral. Geochemistry 21, 169–200.

Michalopoulos, P., Aller, R.C., 2004. Early diagenesis of biogenic silica in the Amazon delta: alteration, authigenic clay formation, and storage. Geochim. Cosmochim. Acta 68, 1061–1085. doi:10.1016/j.gca.2003.07.018

Michalopoulos, P., Aller, R.C., Reeder, R.J., 2000. Conversion of diatoms to clays during early diagenesis in tropical, continental shelf muds. Geology 28, 1095–1098. doi:10.1130/0091-7613(2000)28<1095:CODTCD>2.0.CO;2

Mills, D.B., Canfield, D.E., 2014. Oxygen and animal evolution: Did a rise of atmospheric oxygen "trigger" the origin of animals? BioEssays 36, 1145–1155. doi:10.1002/bies.201400101

Mizutani, S., 1977. Progressive ordering of cristobalitic silica in the early stage of diagenesis. Contrib. to Mineral. Petrol. 61, 129–140.

Mizutani, S., 1970. Silica minerals in the early stage of diagenesis. Sedimentology.

Muehlenbachs, K., Clayton, R.N., 1976. Oxygen isotope composition of the oceanic crust and its bearing on seawater. J. Geophys. Res. 81, 4365. doi:10.1029/JB081i023p04365

Muehlenbachs, K., Furnes, H., Fonneland, H.C., Hellevang, B., 2003. Ophiolites as faithful records of the oxygen isotope ratio of ancient seawater: the Solund-Stavfjord Ophiolite Complex as a Late Ordovician example. Geol. Soc. London, Spec. Publ. 218, 401–414. doi:10.1144/GSL.SP.2003.218.01.20

Murata, K.J., Friedman, I., Gleason, J.D., 1977. Oxygen isotope relations between diagenetic silica minerals in Monterey Shale, Temblor Range, California. Am. J. Sci. 277, 259–272.

Murata, K.J., Larson, R.R., 1975. Diagenesis of Miocene siliceous shales, Temblor range, California. U.S. Geol. Surv. Jour. Res 3, 553–566.

Murata, K.J., Nakata, J.K., 1974. Cristobalitic stage in the diagenesis of diatomaceous shale. Science 184, 567–568. doi:10.1126/science.184.4136.567

Narbonne, G.M., 2005. THE EDIACARA BIOTA: Neoproterozoic Origin of Animals and Their Ecosystems. Annu. Rev. Earth Planet. Sci. 33, 421–442. doi:10.1146/annurev.earth.33.092203.122519

Nursall, J.R., 1959. Oxygen as a prerequisite to the origin of the Metazoa. Nature 183, 1170–1172.

Oelze, M., von Blanckenburg, F., Bouchez, J., Hoellen, D., Dietzel, M., 2015. The effect of Al on Si isotope fractionation investigated by silica precipitation experiments. Chem. Geol. 397, 94–105. doi:10.1016/j.chemgeo.2015.01.002

Oelze, M., von Blanckenburg, F., Hoellen, D., Dietzel, M., Bouchez, J., 2014. Si stable isotope fractionation during adsorption and the competition between kinetic and equilibrium isotope fractionation: implications for weathering systems. Chem. Geol. 380, 161–171.

Opfergelt, S., Delmelle, P., 2012. Silicon isotopes and continental weathering processes: Assessing controls on Si transfer to the ocean. Comptes Rendus Geosci. 344, 723–738. doi:10.1016/j.crte.2012.09.006

Opfergelt, S., Georg, R.B., Delvaux, B., Cabidoche, Y.-M., Burton, K.W., Halliday, A.N., 2012. Silicon isotopes and the tracing of desilication in volcanic soil weathering sequences, Guadeloupe. Chem. Geol. 326-327, 113–122. doi:10.1016/j.chemgeo.2012.07.032

Pisciotto, K.A., 1981. Diagenetic trends in the siliceous facies of the Monterey Shale in the Santa Maria region, California. Sedimentology 28, 547–571.

Planavsky, N.J., Reinhard, C.T., Wang, X., Thomson, D., Mcgoldrick, P., Rainbird, R.H., Johnson, T., Fischer, W.W., Lyons, T.W., 2014. Low Mid-Proterozoic atmospheric oxygen levels and the delayed rise of animals. Science 346, 635–638.

Planavsky, N.J., Rouxel, O.J., Bekker, A., Lalonde, S. V, Konhauser, K.O., Reinhard, C.T., Lyons, T.W., 2010. The evolution of the marine phosphate reservoir. Nature 467, 1088–1090. doi:10.1038/nature09485

Pogge von Strandmann, P.A.E., Stüeken, E.E., Elliott, T., Poulton, S.W., Dehler, C.M., Canfield, D.E., Catling, D.C., 2015. Selenium isotope evidence for progressive oxidation of the Neoproterozoic biosphere. Nat. Commun. 6, 10157. doi:10.1038/ncomms10157

Pope, E.C., Bird, D.K., Rosing, M.T., 2012. Isotope composition and volume of Earth's early oceans. Proc. Natl. Acad. Sci. 109, 4371–4376. doi:10.1073/pnas.1115705109

Quan, T.M., van de Schootbrugge, B., Field, M.P., Rosenthal, Y., Falkowski, P.G., 2008. Nitrogen isotope and trace metal analyses from the Mingolsheim core (Germany): Evidence for redox variations across the Triassic-Jurassic boundary. Global Biogeochem. Cycles 22, n/a–n/a. doi:10.1029/2007GB002981

Racki, G., Cordey, F., 2000. Radiolarian palaeoecology and radiolarites: is the present the key to the past? Earth-Science Rev. 52, 83–120.

Ragueneau, O.G., Tréguer, P.J., Leynaert, A., Anderson, R.F., Brzezinski, M.A., DeMaster, D.J., Dugdale, R.C., Dymond, J., Fischer, G., Francois, R., Heinze, C., Maier-Reimer, E., Martin-Jézéquel, V., Nelson, D.M., Quéguiner, B., 2000. A review of the Si cycle in the modern ocean: recent progress and missing gaps in the application of biogenic opal as a paleoproductivity proxy. Glob. Planet. Change 26, 317–365.

Ramseyer, K., Amthor, J.E., Matter, A., Pettke, T., Wille, M., Fallick, A.E., 2013. Primary silica precipitate at the Precambrian/Cambrian boundary in the South Oman Salt Basin, Sultanate of Oman. Mar. Pet. Geol. 39, 187–197. doi:10.1016/j.marpetgeo.2012.08.006

Reiter, M., Tovar, R.J.C., 1982. Estimates of terrestrial heat flow in northern Chihuahua, Mexico, based upon petroleum bottom-hole temperatures. Geol. Soc. Am. Bull. 93, 613–624. doi:10.1130/0016-7606(1982)93<613:eothfi>2.0.co;2

Reynolds, B.C., Aggarwal, J., André, L., Baxter, D., Beucher, C., Brzezinski, M.A., Engström, E., Georg, R.B., Land, M., Leng, M.J., Opfergelt, S., Rodushkin, I., Sloane, H.J., van den Boorn, S.H.J.M., Vroon, P.Z., Cardinal, D., 2007. An inter-laboratory comparison of Si isotope reference materials. J. Anal. At. Spectrom. 22, 561–568. doi:10.1039/b616755a

Reynolds, B.C., Frank, M., Halliday, A., 2006. Silicon isotope fractionation during nutrient utilization in the North Pacific. Earth Planet. Sci. Lett. 244, 431–443. doi:10.1016/j.epsl.2006.02.002

Rickert, D., Schlüter, M., Wallmann, K., 2002. Dissolution kinetics of biogenic silica from the water column to the sediments. Geochim. Cosmochim. Acta 66, 439–455.

Riech, V., von Rad, U., 1979. Silica diagenesis in the Atlantic ocean: Diagenetic potential and transformations, in: Talwani, M., Hay, W., Ryan, W.B.F. (Eds.), Deep Drilling Results in the Atlantic Ocean: Continental Margins and Paleoenvironment. American Geophysical Union, pp. 315–341.

Robert, F., Chaussidon, M., 2006. A palaeotemperature curve for the Precambrian oceans based on silicon isotopes in cherts. Nature 443, 969–72. doi:10.1038/nature05239

Robinson, R.S., Kienast, M., Luiza Albuquerque, A., Altabet, M.A., Contreras, S., De Pol Holz, R., Dubois, N., Francois, R., Galbraith, E.D., Hsu, T.C., Ivanochko, T., Jaccard, S., Kao, S.J., Kiefer, T., Kienast, S., Lehmann, M.F., Martinez, P., McCarthy, M., Möbius, J., Pedersen, T., Quan, T.M., Ryabenko, E., Schmittner, A., Schneider, R., Schneider-Mor, A., Shigemitsu, M., Sinclair, D., Somes, C.J., Studer, A., Thunell, R., Yang, J.Y., 2012. A review of nitrogen isotopic alteration in marine sediments. Paleoceanography 27. doi:10.1029/2012PA002321

Roerdink, D.L., van den Boorn, S.H.J.M., Geilert, S., Vroon, P.Z., van Bergen, M.J., 2015. Experimental constraints on kinetic and equilibrium silicon isotope fractionation during the formation of non-biogenic chert deposits. Chem. Geol. 402, 40–51. doi:10.1016/j.chemgeo.2015.02.038

Russo, R.E., Mao, X., Gonzalez, J.J., Mao, S.S., 2002. Femtosecond laser ablation ICP-MS. J. Anal. At. Spectrom. 17, 1072–1075. doi:10.1039/B202044K

Savage, P.S., Armytage, R.M.G., Georg, R.B., Halliday, A.N., 2014. High temperature silicon isotope geochemistry. Lithos 190-191, 500–519. doi:10.1016/j.lithos.2014.01.003

Savage, P.S., Bastian Georg, R., Williams, H.M., Halliday, A.N., 2013. The silicon isotope composition of the upper continental crust. Geochim. Cosmochim. Acta 109, 384–399. doi:10.1016/j.gca.2013.02.004

Savin, S.M., Epstein, S., 1970. The oxygen and hydrogen isotope geochemistry of clay minerals. Geochim. Cosmochim. Acta 34, 25–42. doi:10.1016/0016-7037(70)90149-3

Schlich, R., Wise, S.W. et al., 1989. Proc. ODP, Initial Reports 120. College Station. doi:doi:10.2973/odp.proc.ir.120.1989

Schoenberg, R., von Blanckenburg, F., 2005. An assessment of the accuracy of stable Fe isotope ratio measurements on samples with organic and inorganic matrices by high-resolution multicollector ICP-MS. Int. J. Mass Spectrom. 242, 257–272. doi:10.1016/j.ijms.2004.11.025

Schuessler, J.A., von Blanckenburg, F., 2014. Testing the limits of micro-scale analyses of Si stable isotopes by femtosecond laser ablation multicollector inductively coupled plasma mass spectrometry with application to rock weathering. Spectrochim. Acta Part B At. Spectrosc. 98, 1–18. doi:10.1016/j.sab.2014.05.002

Sclater, J.G., Jaupart, C., Galson, D., 1980. The Heat Flow Through Oceanic and Continental Crust and the Heat Loss of the Earth 18.

Scott, C., Lyons, T.W., Bekker, A., Shen, Y., Poulton, S.W., Chu, X., Anbar, A.D., 2008. Tracing the stepwise oxygenation of the Proterozoic ocean. Nature 452, 456–459. doi:10.1038/nature06811

Sharp, Z.D., 1990. A laser-based microanalytical method for the in situ determination of oxygen isotope ratios of silicates and oxides. Geochim. Cosmochim. Acta. doi:10.1016/0016-7037(90)90160-M

Shaw, D.B., Weaver, C.E., 1965. The mineralogical composition of shales. J. Sediment. Petrol. 35, 213–222.

Sheppard, S.M.F., Nielsen, R.L., Taylor, H.P., 1969. Oxygen and hydrogen isotope ratios of clay minerals from porphyry copper deposits. Econ. Geol. 64, 755–777. doi:http://dx.doi.org/10.2113/gsecongeo.64.7.755

Siever, R., 1992. The silica cycle in the Precambrian. Geochim. Cosmochim. Acta 56, 3265–3272. doi:10.1016/0016-7037(92)90303-Z

Somes, C.J., Schmittner, A., Galbraith, E.D., Lehmann, M.F., Altabet, M. a., Montoya, J.P., Letelier, R.M., Mix, A.C., Bourbonnais, A., Eby, M., 2010. Simulating the global distribution of nitrogen isotopes in the ocean. Global Biogeochem. Cycles 24, 1–16. doi:10.1029/2009GB003767

Sperling, E.A., Robinson, J.M., Pisani, D., Peterson, K.J., 2010. Where's the glass? Biomarkers, molecular clocks, and microRNAs suggest a 200-Myr missing Precambrian fossil record of siliceous sponge spicules. Geobiology 8, 24–36. doi:10.1111/j.1472-4669.2009.00225.x

Sperling, E.A., Wolock, C.J., Morgan, A.S., Gill, B.C., Kunzmann, M., Halverson, G.P., Macdonald, F.A., Knoll, A.H., Johnston, D.T., 2015. Statistical analysis of iron geochemical data suggests limited late Proterozoic oxygenation. Nature 523, 3–6. doi:10.1038/nature14589

Stein, C.L., Kirkpatrick, R.J., 1976. Experimental Porcelanite Recrystallization Kinetics: A Nucleation and Growth Model.

Steinhoefel, G., Horn, I., von Blanckenburg, F., 2009. Micro-scale tracing of Fe and Si isotope signatures in banded iron formation using femtosecond laser ablation. Geochim. Cosmochim. Acta 73, 5343–5360. doi:10.1016/j.gca.2009.05.037

Steinhoefel, G., von Blanckenburg, F., Horn, I., Konhauser, K.O., Beukes, N.J., Gutzmer, J., 2010. Deciphering formation processes of banded iron formations from the Transvaal and the Hamersley successions by combined Si and Fe isotope analysis using UV femtosecond laser ablation. Geochim. Cosmochim. Acta 74, 2677–2696. doi:10.1016/j.gca.2010.01.028

Suchecki, R.K., Hubert, J.F., 1984. Stable isotopic and elemental relationships of ancient shallow-marine and slope carbonates, Cambro-Ordovician Cow Head Group, Newfoundland: Implications for fluid flux. J. Sediment. Petrol. 54, 1062–1080.

Sutton, J.N., Varela, D.E., Brzezinski, M.A., Beucher, C.P., Varela, D.E., Brzezinski, M.A., Beucher, C.P., 2013. Species-dependent silicon isotope fractionation by marine diatoms. Geochim. Cosmochim. Acta 104, 300–309. doi:10.1016/j.gca.2012.10.057

Swart, P.K., 2015. The geochemistry of carbonate diagenesis: The past, present and future. Sedimentology 62, 1233–1304. doi:10.1111/sed.12205

Tarantola, A., Valette, B., 1982. Inverse Problems = Quest for Information. J. Geophys. 50, 159–170. doi:10.1038/nrn1011

Tatzel, M., von Blanckenburg, F., Oelze, M., Schuessler, J.A., Bohrmann, G., 2015. The silicon isotope record

of early silica diagenesis. Earth Planet. Sci. Lett. 428, 293–303.

Torres, M.E., Brumsack, H.J., Bohrmann, G., Emeis, K.C., 1996. Barite fronts in continental margin sediments: a new look at barium remobilization in the zone of sulfate reduction and formation of heavy barites in diagenetic fronts. Chem. Geol. 127, 125–139. doi:10.1016/0009-2541(95)00090-9

Tréguer, P.J., Nelson, D.M., van Bennekom, A.J., De Master, D.J., Leynaert, A., Quéguiner, B., 1995. The Silica Balance in the World Ocean: A Reestimate. Science 268, 375–379.

van Bennekom, A.J., Buma, A.G.J., Nolting, R.F., 1991. Dissolved aluminium in the Weddell-Scotia Confluence and effect of Al on the dissolution kinetics of biogenic silica. Mar. Chem. 35, 423–434. doi:10.1016/S0304-4203(09)90034-2

van Beusekom, J.E.E., van Bennekom, A.J., Tréguer, P.J., Morvan, J., 1997. Aluminium and silicic acid in water and sediments of the Enderby and Crozet Basins. Deep. Res. II 44, 987–1003.

van Cappellen, P., Ingall, E.D., 1996. Redox stabilization of the atmosphere and oceans by phosphorus-limited marine productivity. Science 271, 493–496. doi:10.1126/science.275.5298.406

Van Cappellen, P., Qiu, L., 1997a. Biogenic silica dissolution in sediments of the Southern Ocean. I. Solubility. Deep. Res. II 44, 1109–1128.

Van Cappellen, P., Qiu, L., 1997b. Biogenic silica dissolution in sediments of the Southern Ocean. II. Kinetics. Deep Sea Res. Part II Top. Stud. Oceanogr. 44, 1129–1149. doi:10.1016/S0967-0645(96)00112-9

van den Boorn, S.H.J.M., van Bergen, M.J., Nijman, W., Vroon, P.Z., 2007. Dual role of seawater and hydrothermal fluids in Early Archean chert formation: Evidence from silicon isotopes. Geology 35, 939. doi:10.1130/G24096A.1

van den Boorn, S.H.J.M., van Bergen, M.J., Vroon, P.Z., de Vries, S.T., Nijman, W., 2010. Silicon isotope and trace element constraints on the origin of ~3.5Ga cherts: Implications for Early Archaean marine environments. Geochim. Cosmochim. Acta 74, 1077–1103. doi:10.1016/j.gca.2009.09.009

van der Heide, P., 2014. Secondary Ion Mass Spectrometry: An Introduction to Principles and Practices. John Wiley & Sons Inc., Hoboken, New Jersey.

Veizer, J., Ala, D., Azmy, K., Bruckschen, P., Buhl, D., Bruhn, F., Carden, G.A.F., Diener, A., Ebneth, S., Godderis, Y., Jasper, T., Korte, C., Pawellek, F., Podlaha, O.G., Strauss, H., 1999. 87Sr/86Sr, δ13C and δ18O evolution of Phanerozoic seawater. Chem. Geol. 161, 59–88. doi:10.1016/S0009-2541(99)00081-9

Veizer, J., Prokoph, A., 2015. Temperatures and oxygen isotopic composition of Phanerozoic oceans. Earth-Science Rev. 146, 92–104. doi:10.1016/j.earscirev.2015.03.008

Wallmann, K., 2001. The geological water cycle and the evolution of marine delta 18O values. Geochim. Cosmochim. Acta 65, 2469–2485. doi:10.1016/s0016-7037(01)00603-2

Walther, J. V., Helgeson, H.C., 1977. Calculation of the thermodynamic properties of aqueous silica and the solubility of quartz and its polymorphs at high pressures and temperatures. Am. J. Sci. 277, 1315–1351.

Weaver, F.M., Wise, S.W., 1973. Early diagenesis of deep sea bedded chert. Antarct. J. Sep.-Oct., 298–300.

Wen, H., Fan, H., Zhang, Y., Cloquet, C., Carignan, J., 2015. Reconstruction of early Cambrian ocean chemistry from Mo isotopes. Geochim. Cosmochim. Acta 164, 1–16. doi:10.1016/j.gca.2015.05.008

Wetzel, F., de Souza, G.F., Reynolds, B.C., 2014. What controls silicon isotope fractionation during dissolution of diatom opal? Geochim. Cosmochim. Acta 131, 128–137. doi:10.1016/j.gca.2014.01.028

Wille, M., Sutton, J.N., Ellwood, M.J., Sambridge, M., Maher, W., Eggins, S., Kelly, M., 2010. Silicon isotopic fractionation in marine sponges: A new model for understanding silicon isotopic variations in sponges. Earth Planet. Sci. Lett. 292, 281–289. doi:10.1016/j.epsl.2010.01.036

Williams, L.A., Crerar, D.A., 1985. Silica Diagenesis, II. General Mechanisms. J. Sediment. Petrol. 55, 312–321.

Williams, L.A., Parks, G.A., Crerar, D.A., 1985. Silica Diagenesis, I. Solubility Controls. J. Sediment. Petrol. 55, 301–311.

Winter, B.L., Knauth, L.P., 1992. Stable isotope geochemistry of cherts and carbonates from the 2.0 Ga gunflint iron formation: implications for the depositional setting, and the effects of diagenesis and metamorphism. Precambrian Res. 59, 283–313. doi:10.1016/0301-9268(92)90061-R

www.mindat.org/min-2011.html [WWW Document], 2015. URL http://www.mindat.org/ (accessed 3.25.15).

Zambardi, T., Poitrasson, F., 2011. Precise Determination of Silicon Isotopes in Silicate Rock Reference Materials by MC-ICP-MS. Geostand. Geoanalytical Res. 35, 89–99. doi:10.1111/j.1751-908X.2010.00067.x

Zhang, S., Wang, X., Wang, H., Bjerrum, C.J., Hammarlund, E.U., Costa, M.M., Connelly, J.N., Zhang, B., Su, J., Canfield, D.E., 2016. Sufficient oxygen for animal respiration 1,400 million years ago. Proc. Natl. Acad. Sci. 201523449. doi:10.1073/pnas.1523449113

Zhuravlev, A.Y., Wood, R.A., 1996. Anoxia as the cause of the mid-Early Cambrian (Botomian) extinction event. Geology 24, 311–314. doi:10.1130/0091-7613(1996)024<0311:AATCOT>2.3.CO

Ziegler, K., Chadwick, O.A., Brzezinski, M.A., Kelly, E.F., 2005. Natural variations of δ30Si ratios during progressive basalt weathering, Hawaiian Islands. Geochim. Cosmochim. Acta 69, 4597–4610. doi:10.1016/j.gca.2005.05.008

Ziegler, K., Dodd, J.P., Sharp, Z.D., Brearley, A.J., Young, E.D., 2011. Silicon and oxygen isotope values of cherts and their precursors, in: Goldschmidt Conference Abstracts. p. 2284.

Ziegler, K., Marin-Carbonne, J., 2012. Silicon and oxygen isotopes during diagenesis of the Monterey chert, in: Goldschmidt Conference Abstracts. p. 2603.